626938
212p.

Blade-Mounted Trailing Edge Flap Control for BVI Noise Reduction

A. A. Hassan, B. D. Charles,
H. Tadghighi, and L. N. Sankar

NASA

NASA Contractor Report 4426

Blade-Mounted Trailing Edge Flap Control for BVI Noise Reduction

A. A. Hassan, B. D. Charles,
and H. Tadghighi
McDonnell Douglas Corporation
McDonnell Douglas Helicopter Company
Mesa, Arizona

L. N. Sankar
Georgia Institute of Technology
School of Aerospace Engineering
Atlanta, Georgia

NASA

National Aeronautics and
Space Administration

Office of Management

Scientific and Technical
Information Program

1992

SUMMARY

Numerical procedures have been developed to investigate the effects of leading and trailing edge flap motions on the aerodynamics of parallel airfoil-vortex interactions and the effects of a trailing edge flap on the aerodynamics and acoustics of the more general self-generated rotor blade vortex interactions (BVI). Special emphasis was placed on the unsteady flap motion effects which result in alleviating the interaction(s) and hence the attendant acoustic signature. The two-dimensional solution procedures described here are based on the implicit finite-difference solutions to the unsteady full potential equation and the unsteady full Reynolds-averaged Navier-Stokes equations. In both formulations, the vortex flow field was computed using the Biot-Savart Law with allowance for a finite core radius. The vortex-induced velocities at the surface of the airfoil were incorporated into the potential flow model via the use of the efficient velocity "transpiration" approach. The more comprehensive "perturbation" approach was adopted in the Navier-Stokes formulation to simulate the flow field resulting from the head-on collision between the vortex and the airfoil. In the two-dimensional full potential formulation, leading and trailing edge flap motion effects were also modeled using the transpiration approach. In the Navier-Stokes formulation, trailing edge flap motion effects were locally accounted for through the use of a zonal time-dependent sheared grid which emulates the unsteady motion of the flap.

To model the more complex self-generated blade vortex interactions, the velocity field was obtained through a nonlinear decomposition of the rotor flowfield, computed using the unsteady three-dimensional full potential rotor flow solver RFS2.BVI, and the rotational vortex flow field computed using the Law of Biot-Savart. In this model, vortex and trailing edge flap induced effects were also simulated using the velocity "transpiration" approach. For a given user-specified trailing edge flap schedule, rotor advance ratio, and tip Mach number, potential blade-vortex encounters were identified and tracked in time at equal increments of rotor azimuth using the lifting-line helicopter/rotor trim code CAMRAD/JA. This information was then utilized in an interpolation routine within RFS2.BVI to compute the instantaneous position of the interaction vortex elements relative to the blade for the time-accurate potential calculation. The predicted surface pressures where then utilized in the acoustic prediction code WOPWOP to determine the impact of the unsteady trailing edge flap motions on the acoustics of BVI.

For subcritical interactions, our two-dimensional results indicate that the trailing edge flap can be used to alleviate the impulsive loads experienced by the airfoil. For

supercritical interactions, our results demonstrate the necessity of using a leading edge flap, rather than a trailing edge flap, to alleviate the interaction. Results for various time-dependent flap motions and their effect on the predicted temporal sectional loads, differential pressures, and the free vortex trajectories are presented.

For the baseline two-bladed model OLS rotor (i.e., with no trailing edge flap), reasonable correlation with the experimental wind tunnel blade surface pressure data was obtained for conditions representative of low speed descent flight. Numerical results have indicated that significant changes in the temporal gradients of the pressures in the vicinity of the blade's leading edge can be achieved with the careful deployment of the trailing edge flap. The temporal pressure gradients indicative of the BVI acoustic levels are shown to be highly dependent on the flap deflection rate, azimuthal angle of the maximum deflection, and on the rotor azimuth angles where the deployment of the flap is initiated and terminated respectively. The RFS2.BVI predicted surface pressures were utilized as input to the acoustic analysis program WOPWOP. The BVI noise prediction model is based on Farassat's formulation 1A. The noise signatures associated with the baseline and flapped OLS model rotors in descent flight conditions were computed for a range of trailing edge flap schedules. Contours of a BVI noise metric were employed to quantify the effects of the trailing edge flap on the size and on the directivity of the high/low intensity noise region(s). Average reductions in the BVI noise levels on the order of 5 dB (over a rectangular grid representative of near and farfield observer positions) with moderate power penalties (on the order of 18% for a four-bladed rotor and 58% for a two-bladed rotor) were obtained for a number of flap schedules. Examples illustrating the acoustic benefits arising from the use of the trailing edge flap for the OLS model rotor and for a generic four-bladed model rotor are presented.

TABLE OF CONTENTS

LIST OF ILLUSTRATIONS

LIST OF ILLUSTRATIONS (Cont'd)

LIST OF ILLUSTRATIONS (Cont'd)

<u>Figure</u>

LIST OF ILLUSTRATIONS (Cont'd)

LIST OF TABLES

NOMENCLATURE

a : normalized local speed of sound

$A_{1,2,3}$: coefficients in the discretized full potential equation

A : Jacobian matrix of the flux vector E in the 2-D Navier-Stokes formulation, and
         : coeff. in the expression for the ξ-direction contravariant velocity U (3-D)

B : Jacobian matrix of the flux vector F in the 2-D Navier-Stokes formulation, and
         : coeff. in the expression for the ξ-direction contravariant velocity U (3-D)

C : airfoil's chord length, and coeff. in the expression for the ξ-direction
         : contravariant velocity U (3-D)

CMBR   : normalized camber as measured fom the mean chord line

CMBRP : derivative of CMBR with respect to x (normalized chordwise location)

C_p : pressure coefficient

D : coeff. in the expression for the η-direction contravariant velocity V (3-D)

e : total energy per unit volume

E : flux vector in the x-coordinate direction, and coeff. in the expression for the
         : η-direction contravariant velocity V (3-D)

F : flux vector in the y-coordinate direction, and coeff. in the expression for the
         : η-direction contravariant velocity V (3-D)

G : coeff. in the expression for the ζ-direction contravariant velocity W (3-D)

H : coeff. in the expression for the ζ-direction contravariant velocity W (3-D)

i : grid point index for the streamwise direction (2-D, 3-D),

I : coeff. in the expression for the ζ-direction contravariant velocity W (3-D)

I : identity matrix

j : grid point index in the approximate normal direction (2-D), and grid point index
         : in the spanwise direction (3-D)

J : Jacobian of the algebraic coordinate transformation

k : grid point index for the approximate normal direction to the blade (3-D)

l_i : local force per unit area on the fluid in the i direction

M : local Mach number

M_r : Mach number in radiation direction

Mtip   : hover tip Mach number (rotation tip speed / free stream speed of sound)

Mu   : rotor advance ratio (helicopter forward velocity / tip rotational velocity)

N-S   : Navier-Stokes equations

n : unit vector normal to the airfoil's or blade's surfaces

NOMENCLATURE (cont'd)

p : normalized local pressure

p' : acoustic pressure $(p-p_0)$

q : normalized velocity, also vector of the dependent variables in the N-S equations

r : position vector

r v : normalized vortex core radius

R : Vector containing viscous terms in the N-S equations

RBAR : nondimensional blade radial station (= local radius / blade tip radius)

RHS : right hand side function in the transformed full potential equation

Rtip : blade tip radius

s : entropy

S : Vector containing viscous terms in the 2-D N-S equations, and function
: containing terms related to blade grid motion velocities

SIP : Strongly Implicit Procedure

t : time

TPP : blade tip path plane angle (degrees)

u,v : velocity components in the physical x, y directions respectively

U : contravariant velocity in the ξ - direction (2-D, 3-D)

V : contravariant velocity in the η - direction (2-D, 3-D)

Vn : local normal velocity to airfoil's and blade's surfaces

W : complex position vector in the mapped circle plane (W = x + i y), and
: contravariant velocity in the ζ-direction (3-D)

x : normalized airfoil (or blade) chordwise Cartesian coordinate

x v : normalized instantaneous vortex position along the x-coordinate direction

y : normalized airfoil normal Cartesian coordinate, and spanwise Cartesian
: coordinate in blade-fixed coordinate system

y v : normalized vortex position along the y-coordinate direction (miss distance)

z : normalized normal Cartesian coordinate in blade-fixed coordinate system

Subscripts:

n : unit vector normal to the airfoil's surface

N : designates airfoil's leading edge singular point

o : implies initial conditions

T : designates airfoil's trailing edge point

I : induced

Subscripts (cont'd):

ret   : evaluated at retarded or emission time

∞ : freestream conditions

Superscripts:

n   : index for time step

$-$: modified

Greek Symbols:

γ : ratio of specific heats (= 1.4)

Γ : normalized strength of interaction vortex segment

$\bar{\delta}$: one-sided finite-difference operator

δ : central difference operator, also trailing edge flap deflection angle (degrees)

$\dot{\delta}$: angular rate of flap deflection

Δ : differential change in quantity in two consecutive time steps

Δt : increment of time for advancing numerical solution towards a steady state

ρ : normalized local flow density

ϕ : velocity potential function

ξ : transformed streamwise airfoil (or blade) surface coordinate

η : transformed approximately normal airfoil coordinate, blade spanwise coordinate

ζ : transformed approximately normal blade-fixed coordinate

τ : transformed time or source time for acoustic calculations

ε : airfoil's included trailing edge angle

$\varepsilon^2, \varepsilon^4$: coefficients for the 2nd and 4th order damping terms in the 2-D N-S formulation

α : Alpha, airfoil's angle of attack

ω : magnitude of local vorticity, also rotor angular velocity of rotation (radians/sec)

Ψ : temporary solution vector in the solution of the 2-D full potential equation

Φ : temporary solution vector in the solution of 2-D the Navier-Stokes equations

σ_{ij} : pressure gradient sensing function

κ : von Karman's constant (= 0.4)

μ_t : turbulent eddy viscosity coefficient

1. INTRODUCTION

Over the past years researchers have embarked on investigating the aerodynamics of two-dimensional airfoil-vortex interactions experimentally [1-4] and numerically [5-8]. This interest was spurred primarily by the numerous similarities between the physics associated with this simple model problem and those arising from the more complex three-dimensional problem of a helicopter rotor blade encountering the trailing tip vortex (or vortices) of the preceding blade (or blades). These encounters, referred to as blade-vortex interactions, or BVI, are most commonly found in forward flight during low speed decent flight conditions where the blade tip vortices are convected towards the rotor disk by virtue of the flow direction normal to the tip path plane. The close blade-vortex encounters result in significant impulsive changes in the rotor blade aerodynamic surface pressures which subsequently give rise to vibration and noise levels [9]. To date, a large number of experimental setups [10-12] have successfully mimicked idealized conditions for these interactions in the controlled environment of the wind tunnel. For example, in Ref. [12] parallel and oblique-type BVI were simulated using an upstream-generated vortex which interacts with a nonlifting rotor (i.e., in the absence of a rotor generated wake) at a predetermined azimuth and a known miss distance. In these experiments, unlike self-generated interactions where the rotor interacts with elements of its own generated wake, experimental parameters relating to the vortex such as the vortex strength, core radius, and orientation with respect to the blade are all well defined through local flow measurements and visualization techniques.

In recent years, a vision for developing a viable technique to reduce the helicopter BVI noise contribution has stimulated great interest within the aeroacoustics research community. The acoustic intensity of BVI noise can be significantly reduced by minimizing the aerodynamic response to the vortex at both its generation (affecting vortex strength) and its interaction location(s) (affecting blade-vortex separation distances). Motivated by the need to meet FAA certification requirements for allowable BVI noise levels, researchers attempted to alleviate the response of the airfoil (or rotor blade) to the vortex passage by disrupting the natural mechanisms which are responsible for promoting these encounters. To minimize the response of the aerodynamic surface (i.e., airfoil or rotor blade) to the vortex, active and/or passive means must be adopted to reduce the strength of the vortex. This can be readily accomplished through the use of trailing edge devices which alter the structure of the tip vortex core and hence the vortex strength. The reduction in the vortex strength could also be an outcome of the merging of two vortices of opposite strength (or

circulation) or even through the postponement of the vortex roll-up process. In the latter case, the strength of the vortex is lower than the maximum bound circulation on the rotor blade. The results of the comprehensive experimental investigation by Wagner [13] also indicate that a rotor blade with an Ogee tip produces a tip vortex whose strength is, on the average, less than those produced by blades having rectangular, sweptback, or trapezoidal tips.

An alternative option for alleviating the impulsive response of the helicopter rotor blade during BVI is through diverting the vortex farther away from the blade. This approach was adopted by researchers at ONERA [14] through the use of a large anhedral angle in the blade tip region. The favorable effects of using downward-pointing blade tip "winglets" on the aerodynamics of blade-vortex interactions in forward flight were also demonstrated by Muller [15,16].

Thus far, we have only addressed the need to alter parameters which are associated with the vortex. However, the geometric parameters of the airfoil, and hence the blade, are also equally important in affecting the overall outcome of the interaction. The most important parameters are the airfoil's leading edge radius, maximum thickness, maximum camber, positions of maximum thickness and maximum camber, and thickness and camber distributions. These parameters should be optimized to minimize the airfoil's response to the interaction without resulting in poor aerodynamic performance at "other" operating conditions. For example, it is well known that improved transonic aerodynamic characteristics can only be achieved using an airfoil section with a maximum camber that is located far aft the leading edge. A small leading edge radius will also guarantee poor aerodynamic performance at low speeds and high angles of attack which are typical of the flow conditions on the retreating blade. It is thus obvious that an optimum airfoil configuration would be one which involves a "compliant" surface to meet the BVI requirements, the transonic high speed requirements, and the low speed high lift requirements. An airfoil section having both leading and trailing edge plain flaps would fulfil these conflicting requirements providing, of course, that the synchronization of the unsteady flap motions is carefully carried out.

The leading edge flap would provide the "droop nose" effect by moving the position of the maximum camber closer to the airfoil's leading edge. The trailing edge flap on the other hand would alter the maximum camber and tend to shift its position towards the hinge point location. In any event, with either flap being deployed, the zero-lift angle of the section is

varied (equivalent to imparting twist on a rotor blade) and the effective angle of attack for the section is altered. Caution however must be exercised in the deployment of either flap since uncoordinated motions can result in local flow conditions which enhance, rather than alleviate, the interaction between the vortex and the airfoil.

In our studies we have adopted two approaches for modeling the effects of the convecting vortex in the mathematical formulations (two- and three-dimensional full potential formulations, and the two-dimensional Navier-Stokes formulation). The velocity "transpiration" approach of Sankar and Malone [17] was used to model the vortex-induced effects as well as the flap-induced effects in the unsteady two- and three-dimensional full potential formulations. This approach was selected among others [5] due to its simplicity, demonstrated accuracy, and minimal computer CPU and memory requirements [18,19]. In the Navier-Stokes formulation, the "perturbation" approach of Sankar and Tang [20] was selected for modeling the more complex head-on collision between the vortex and the airfoil.

This report addresses the effects of the unsteady leading and trailing edge flap motions on the aerodynamics of airfoil-vortex interactions, and the effects of using a plain trailing edge flap on the aerodynamics and acoustics of rotor self-generated BVI. In the two-dimensional studies, special emphasis is being placed on the effects of varying the rates of deflection and maximum amplitude of the deflection on the aerodynamics of the two-dimensional interactions for subcritical and supercritical onset flows. In the three-dimensional study, emphasis is again placed on the effects of varying the rates of deflection and maximum amplitude of the deflection in addition to the azimuthal positions along the rotor disk where the flap motion is initiated and terminated, on the aerodynamics and acoustics of BVI. The discrete frequency BVI noise (no broadband noise) predictions were performed using a modified version of the WOPWOP code based on Farassat's formulation 1A [21]. Details of the modifications necessary for the accurate prediction of BVI noise for a flapped rotor configuration are presented. For contrast, all the results obtained for the airfoil (or blade) with the flap in the neutral position, referred to throughout this report as the baseline problem, are also presented.

2. TWO-DIMENSIONAL FULL POTENTIAL FORMULATION

The governing equation expressing conservation of mass for a two-dimensional, unsteady, compressible flow is given by

$$\rho_t + (\rho \, \phi_x)_x + (\rho \, \phi_y)_y = 0 \tag{1}$$

In Eq. (1), ϕ is the velocity potential function, ρ is the density normalized by the free stream density, and subscripts denote partial differentiation with respect to the independent variables. We assume that any shock waves originally present or resulting from the interactions are weak and hence do not represent a source of vorticity in the flow. Under these assumptions, the energy equation can be written as

$$a^2 = 1 - 0.5 \, (\gamma - 1) \, [2\phi_t + \phi_x^2 + \phi_y^2] \tag{2}$$

The isentropic gas relation for a calorically perfect gas is, viz.,

$$\rho = (a^2)^{1/(\gamma-1)} \tag{3}$$

where a is the normalized (using the free stream speed of sound) local speed of sound. By combining Eqs. (1,2,3) we obtain the familiar hyperbolic equation for the velocity potential

$$(\rho/a^2) \, [\phi_{tt} + \phi_x \, \phi_{xt} + \phi_y \, \phi_{yt}] = [(\rho\phi_x)_x + (\rho\phi_y)_y] \tag{4}$$

To facilitate the application of surface boundary conditions, we consider a coordinate transformation from the physical (x,y) coordinate system to the body-fitted (ξ, η) coordinate system, i.e.,

$$\xi = \xi \, (x,y)$$

$$\eta = \eta \, (x,y)$$

where the ξ coordinate is measured along the surface of the airfoil and the η coordinate is measured in the direction normal to the airfoil's surface. In this study, an O-type computational grid (141 nodes on the airfoil's surface, 51 nodes in the direction normal to

the surface) was generated using the Karman-Trefftz complex mapping function [22] given by

$$\left(\frac{Z - Z_T}{Z - Z_n}\right)^{\frac{1}{2 - \varepsilon/\pi}} = \left(\left|\frac{W - c}{W + c}\right|\right) \tag{5}$$

In Eq. (5), Z represents the complex position vector in the physical x-y plane (airfoil's plane), W is the complex position vector in the circle plane (i.e., transformed ξ-η plane), c is an arbitrary constant which determines the radius of the circle in the transformed plane, Z_T and Z_n are the position vectors for the airfoil's trailing edge and the leading edge singular point respectively, and ε is the airfoil's included trailing edge angle. Figure (1) depicts a close-up view of the computational grid (141x51) in the physical domain. The far-field outer boundary was located approximately 15 chords away from the airfoil's surface. With ξ, η as new independent variables we express Eq. (4) as

$$\left(\frac{\rho U}{J}\right)_\xi + \left(\frac{\rho V}{J}\right)_\eta = -\frac{\rho}{a^2 J}\left(\phi_{tt} + U \phi_{\xi t} + V \phi_{\eta t}\right) \tag{6}$$

Here, J is the Jacobian of the algebraic coordinate transformation, viz.,

$$J = \frac{\partial (x, y)}{\partial (\xi, \eta)} = (x_\xi y_\eta - x_\eta y_\xi) \tag{7}$$

U and V are the contravariant velocity components given by

$$\begin{aligned} U &= u\,\xi_x + v\,\xi_y \\ V &= u\,\eta_x + v\,\eta_y \end{aligned} \tag{8}$$

u, v are the physical plane velocity components in the x and y directions respectively, and $\xi_x, \xi_y, \eta_x, \eta_y$ are the metrics of the coordinate transformation. These metrics are related to the physical plane coordinates x,y via the following relationship

$$\begin{bmatrix} \xi_x & \xi_y \\ \eta_x & \eta_y \end{bmatrix} = \begin{bmatrix} x_\xi & x_\eta \\ y_\xi & y_\eta \end{bmatrix}^{-1}$$

2.1. <u>SOLUTION ALGORITHM</u>

Let $\Delta\phi\,(i,j)$ represent the change in the solution vector (or correction) in two consecutive time steps n, (n+1) or (n-1), n, i.e.,

$$\Delta\phi^{n+1}(i,j) = \phi^{n+1}(i,j) - \phi^{n}(i,j)$$

The first term on the right hand side of Eq. (6) is evaluated using a second-order central differencing expression

$$\phi_{tt}\,(i,j) = \frac{1}{\Delta t^2}\{\phi^{n+1}(i,j) -2\,\phi^{n}(i,j) + \phi^{n-1}(i,j)\}$$

or

$$\phi_{tt}\,(i,j) = [\Delta\phi^{n+1}(i,j) - \Delta\phi^{n}(i,j)]\,/\,\Delta t^2 \tag{9}$$

The mixed space-time partial derivatives, second and third terms on the right hand side of Eq. (6), are discretized using upwind-differencing expressions for the spatial partial derivatives and two-point backward-differences for the temporal derivative. That is,

$$U\,\phi_{\xi t} = U^{n}(i,j)\,[\overline{\delta_\xi}\,\Delta\phi^{n+1}(i,j)]\,\frac{1}{\Delta t} \tag{10}$$

and

$$\overline{\delta_\xi}\,\Delta\phi^{n+1}(i,j) = \Delta\phi^{n+1}(i,j) - \Delta\phi^{n+1}(i-1,j) \qquad \text{for } U > 0$$

$$\overline{\delta_\xi}\,\Delta\phi^{n+1}(i,j) = \Delta\phi^{n+1}(i+1,j) - \Delta\phi^{n+1}(i,j) \qquad \text{for } U < 0$$

Similarly,

$$V\,\phi_{\eta t} = V^{n}(i,j)\,[\overline{\delta_\eta}\,\Delta\phi^{n+1}(i,j)]\,\frac{1}{\Delta t} \tag{11}$$

and

$$\overline{\delta_\eta}\,\Delta\phi^{n+1}(i,j) = \Delta\phi^{n+1}(i,j) - \Delta\phi^{n+1}(i,j-1) \qquad \text{for } V > 0$$

$$\overline{\delta_\eta}\,\Delta\phi^{n+1}(i,j) = \Delta\phi^{n+1}(i,j+1) - \Delta\phi^{n+1}(i,j) \qquad \text{for } V < 0$$

6

In Eqs. (10,11) $\bar{\delta}$ is a one-sided difference operator. We have also assumed that the mesh spacing in the ξ, η directions are equal to unity.

The first of equations (8) imply that

$$U = \{\phi_x + \cos(\alpha)\} \, \xi_x + \phi_y \, \xi_y$$

In terms of ξ, η the above expression can be reduced to

$$U = \phi_\xi \, (\xi_x^2 + \xi_y^2) + \phi_\eta (\, \xi_x \eta_x + \xi_y \eta_y) + \xi_x \cos(\alpha)$$

$$U^{n+1}(i,j) = \phi_\xi^{n+1} \, A_1 + \phi_\eta^n \, A_2 + \xi_x \cos(\alpha) \tag{12}$$

Rearranging terms we obtain

$$U^{n+1}(i,j) = \delta_\xi \, \Delta\phi^{n+1}(i,j) \; A_1 + U^n(i,j) \tag{13}$$

Similarly, we consider the second of Eqs. (8) where

$$V = \{\phi_x + \cos(\alpha)\} \, \eta_x + \phi_y \, \eta_y$$

$$V^{n+1}(i,j) = \delta_\eta \, \Delta\phi^{n+1}(i,j) \; A_3 + V^n(i,j) \tag{14}$$

In Eqs. (12-14) the coefficients A_1, A_2, A_3 are functions of the transformation metrics, viz.,

$$A_1 = \xi_x^2 + \xi_y^2$$

$$A_2 = \xi_x \, \eta_x + \xi_y \, \eta_y$$

$$A_3 = \eta_x^2 + \eta_y^2$$

Substituting Eqs. (13,14) into the left hand side of Eq. (6) and the expressions given by Eqs. (9-11) into the right hand side of Eq. (6) and equating we obtain

$$\{ I + \Delta t \, U^n(i,j) \, \delta_\xi + \Delta t \, V^n(i,j) \, \delta_\eta + \Delta t^2 \delta_\xi A_1 \delta_\xi + \Delta t^2 \delta_\eta A_3 \delta_\eta \} \, \Delta \phi^{n+1}(i,j) =$$

$$\Delta \phi^n(i,j) + J \, a^2 \Delta t^2 \{ (\tfrac{\rho U}{J})_\xi + (\tfrac{\rho V}{J})_\eta \}^n \frac{1}{\rho^n} \tag{15}$$

In Eq. (15) I is the identity matrix. The Beam and Warming [23] approximate factorization scheme is then used to approximate the two-dimensional spatial differential operator appearing on the left hand side of Eq. (15) as the product of two one-dimensional spatial differential operators in the ξ, η directions, viz.,

$$[I + \Delta t \, U^n(i,j) \, \delta_\xi + \Delta t^2 \, \delta_\xi A_1 \delta_\xi] \cdot [I + \Delta t \, V^n(i,j) \, \delta_\eta +$$

$$\Delta t^2 \, \delta_\eta A_3 \delta_\eta] \, \Delta \phi^{n+1}(i,j) = [RHS]^n \tag{16}$$

where

$$[RHS]^n = \Delta \phi^n(i,j) + J \, a^2 \Delta t^2 \{ (\tfrac{\rho U}{J})_\xi + (\tfrac{\rho V}{J})_\eta \}^n$$

The solutions to Eqs. (16) are then obtained using a two-step procedure where we first solve for a temporary solution vector ψ, i.e.,

$$(I + \Delta t \, U^n(i,j) \, \delta_\xi + \Delta t^2 \delta_\xi A_1 \delta_\xi) \, \psi(i,j) = [RHS]^n$$

Having solved for ψ, we then solve for the correction in the potential function $\Delta \phi$ using the following equation

$$(I + \Delta t \, V^n(i,j) \, \delta_\eta + \Delta t^2 \delta_\eta A_3 \delta_\eta) \, \Delta \phi^{n+1}(i,j) = \psi(i,j)$$

At this juncture, it is noteworthy to mention that the above factorization procedure is applicable to both quasi-steady as well as unsteady flowfield calculations. In the former case, the temporal derivatives of ϕ are set equal to zero and the solution procedure can be regarded as an iterative relaxation procedure. In the latter case, the solution procedure is regarded as a one-step non-iterative time-accurate marching procedure.

2.2. NUMERICAL BOUNDARY CONDITIONS

The present formulation require boundary conditions to be specified along the airfoil's surface, the far-field, and the periodic boundary due to the use of an O-type grid. On the airfoil's surface, the familiar "zero-flux" condition, i.e.,

$$\mathbf{V} \cdot \mathbf{n} = 0 \tag{17}$$

was enforced throughout the computations. Here, $\mathbf{n}$ is outward unit normal to the surface and $\mathbf{V}$ is the local velocity vector normalized by the free stream velocity. In this study, two modifications to Eq. (17) were necessary to reflect the modeling of the unsteady leading and trailing edge flap motions, and the vortex-induced effects. These modifications, to a large extent, facilitated the unsteady computations by allowing for the use of a fixed, rather than a time-varying, computational grid which would have been necessary to accommodate the time-dependent flap motion(s). This approach to solving the problem, commonly referred to in the literature as the "velocity transpiration" approach, has been previously used by Sankar and Malone [17], and Bharadvaj [19] to study the unsteady effects resulting from the use of two- and three-dimensional flaps respectively. The approach has also been used to simulate the three-dimensional blade-vortex interactions for helicopter rotor blades [18,24].

Consider a point P on the surface of the trailing edge flap, see Fig. (2). If the instantaneous angular rate of deflection is $\dot{\delta}_1$ one can compute a surface grid velocity V_P which is associated with the motion of point P, i.e.,

$$\mathbf{V}_P = \dot{\delta}_1 \ \mathbf{x} \ \mathbf{r}_P$$

To maintain the surface tangency boundary condition for the two-dimensional potential solution, Eq. (17) is rewritten as

$$(\mathbf{V} - \mathbf{V}_P) \cdot \mathbf{n} = 0 \qquad \text{for } x > x_{h1}$$

where x_{h1} is the normalized (using the airfoil's chord length C) hinge point position of the trailing edge flap (fixed at 0.75 C). For an airfoil having a leading edge flap (see inset

sketch in Fig. 2), a similar boundary condition at a point Q on the flap surface can also be written, viz.,

$$(V - V_Q) \cdot n = 0 \qquad \text{for } x < x_{h2}$$

where

$$V_Q = \dot{\delta}_2 \times r_Q$$

x_{h2} is the normalized hinge point position of the leading edge flap (fixed at 0.1 C), and $\dot{\delta}_2$ is the angular rate of deflection of the leading edge flap. A more general boundary condition for an airfoil having leading and trailing edge integral flaps is given by

$$(V - V_P - V_Q) \cdot n = 0 \qquad (18)$$

with

$$V_P = 0 \qquad \text{(trailing edge flap effects not modeled)}$$
$$V_Q = 0 \qquad \text{(leading edge flap effects not modeled)}$$

In a similar manner, vortex-induced effects can also be accounted for through an additional modification to the surface boundary condition given by Eq. (18). More precisely, if we assume a Lamb-type vortex [25], then the vortex-induced velocity at a point on the surface of the airfoil is given by

$$V_v = \frac{\Gamma}{2 \pi r} (1 - e^{-r^2 / a_0^2})$$

Here, r is the position vector connecting the center of the vortex and any point on the surface of the airfoil, a_0 is the normalized vortex core radius (taken as 0.05 C), and Γ is the normalized vortex strength (using the product of the free stream velocity and the airfoil's chord length C). The above expression is used to compute the vortex-induced velocities at all grid points lying on the surface of the airfoil. To maintain the surface tangency boundary condition in the presence of vortex effects we must further modify Eq. (18), i.e.,

$$(V - V_P - V_Q - V_v) \cdot n = 0 \qquad (19)$$

To allow for the free convection of the vortex in the computational domain (i.e.,

10

allowing for an unrestricted vortex path), the computations are first started assuming an initial position for the vortex, say (x_0, y_0). Having determined the potential flow solution we then advance the vortex to its new position (x_n, y_n) using the following expressions

$$x_n = x_0 + \Delta x = x_0 + \bar{u} \, \Delta t$$
$$y_n = y_0 + \Delta y = y_0 + \bar{v} \, \Delta t \qquad\qquad (20)$$

In Eqs. (20), $\bar{u}, \bar{v}$ are respectively the average velocities of the Cartesian x, y velocity components at the four corners of the cell enclosing the center of the vortex. Equations (20) when repeatedly applied for two consecutive time steps n, (n+1), provide the time varying free vortex path.

3. TWO-DIMENSIONAL FULL POTENTIAL RESULTS

In these studies, solutions were obtained to illustrate the effects of the unsteady leading and trailing edge flap motions on the aerodynamics of airfoil-vortex interactions. For convenience, the results of this study will be presented in three sections. In the first we will address the effects of using the trailing edge flap on the airfoil-vortex interactions. In the second section, the motivation for the need to use a leading edge flap for supercritical onset flows will be discussed. In the third section, the combined effects of using leading and trailing edge flaps will be presented. For contrast, in all our results depicting the influence of the flap(s), we will also include the results for the baseline airfoil-vortex interaction problem.

3.1. Airfoil-Vortex Interactions (baseline problem)

In this study, emphasis was placed on assessing the accuracy of the full potential flow solver in modeling the interaction between a Lamb vortex having a clockwise sense of rotation and a NACA 0012 airfoil. The Euler results of Ref. [26] using the perturbation approach were utilized for this purpose. The interaction conditions simulated a free stream Mach number of 0.8, a free stream angle of attack of 0.5 degrees, a nondimensional vortex strength of 0.2, a vortex core radius (rv/C) equal to 0.05, and an initial vortex position equal to -6 chord lengths ahead of the airfoil's leading edge (i.e., $x_0/C = -6$), and a vortex

miss distance equal to -0.26 (i.e., y_O/C). In the time-dependent computations of Ref. [26], the vortex was allowed to travel on a linear path described by

$$y_v = y_o - (x_v - x_o) \ \tan(\alpha) \tag{21}$$

The vortex was allowed to travel along the x-coordinate direction with a velocity equal to that of the free stream rather than the local velocity. Therefore, for each time step, x_v was known and Eq. (21) was utilized to compute the instantaneous miss distance y_v, and hence the vortex-induced velocity field necessary for the perturbation solution approach.

Figures (3,4) depict comparisons between the predicted sectional lift and moment coefficients using the Euler formulation of Ref. [26] and the present full potential formulation employing the surface transpiration approach. As seen, good agreement is obtained. The rapid variations in the lift and moment coefficients as the vortex approaches the airfoil's leading edge and continues to move beyond the trailing edge are well captured. The full potential results however indicate higher lift values once the vortex moves beyond the airfoil's trailing edge (i.e., $x_v/C > 1$). The moment coefficients on the other hand are slightly under-predicted as the vortex approaches the airfoil's leading edge and convects beyond the trailing edge. The maximum and minimum moment coefficients are also slightly overpredicted.

The ability of the full potential solver with the adopted transpiration approach to capture Tijdeman's type-C shock motion [27] which result from the interaction between the vortex and the airfoil is shown in Fig. (5). Here, we illustrate the predicted variations in the size of the embedded supersonic flow regions (obtained by limiting Mach contour plots to Mach number values equal to and larger than one) as a function of streamwise vortex position (or equivalently time). The results shown were obtained for a free stream Mach number of 0.8, an angle of attack of zero degrees, a vortex core radius of 0.05, a nondimensional vortex strength of 0.2, and an initial vortex position of $x_O/C = -6$, and $y_O/C = -0.26$. Unlike the previous simulation, the vortex was allowed here to follow a free path which was dictated by the computed local velocity field. Note the slight asymmetry which appear in the positions of the upper and lower surface shocks when the vortex is located five chords ahead of the airfoil (i.e., for $xv/C = -5$). This asymmetry, as expected, increases as the vortex approaches the airfoil's leading edge. When the vortex is at $xv/C = 0.4$ (i.e., at the 40% chordwise position), the upper surface supersonic region has completely

12

disappeared. As the vortex continues to move towards the trailing edge, the upper surface supersonic region gradually appears and continues to increase in size with the shock moving aft. This type of shock motion has also been predicted by George and Chang [7] in their studies of airfoil-vortex interactions using the VTRAN small disturbance potential solver. Note also that a significant asymmetry in the flow exists when the vortex is at a position 1.2 chord lengths downstream from the trailing edge (i.e., xv/C = 2.2). This asymmetry, as reported in Refs. [7,26] and evident from our numerical results, slowly disappears and the symmetric flow is recovered when the vortex position is approximately 10-11 chords downstream of the airfoil's trailing edge.

3.2. Effects of the Trailing Edge Flap

Figures (6a-e) depict, respectively, three user-specified trailing edge flap schedules (referred to here as A1, A2, A3), the predicted free vortex trajectories, predicted differential pressures at the 2% chordwise position, and the predicted sectional lift and moment coefficients for a free stream Mach number 0.8 and an angle of attack of zero degrees. In our simulations, the vortex (having a clockwise sense of rotation with a strength equal to 0.2 and a radius equal to 0.05) was introduced at a distance equal to 10 chord lengths upstream of the airfoil's leading edge (i.e., x_0/C = -10). The vortex initial miss distance was equal to -0.25 C below the airfoil (i.e., y_0/C = -0.25). In Fig. (6a) the two non-zero flap schedules reflect moderate and fast rates of deflection which are carried over a time period equivalent to that required by the vortex to travel a distance equal to 3.5 chord lengths. For clarity, the airfoil location has been highlighted on the horizontal axis representing the instantaneous vortex position. Note that the initial deployment of the flap takes place when the vortex is located at a distance equal to 1.25 C ahead of the airfoil (i.e., xv/C = -1.25). The deployment of the flap is terminated when the vortex is located at xv/C = 2.25. The flap schedules represent a complete cycle where initially a positive deflection (i.e., flap down) is simulated. The flap returns to the neutral position (i.e., the undeflected position) when the vortex is located at the mid-chord streamwise position. The motion of the flap then continues to provide a negative deflection (i.e., flap up) which is followed again by a return to the neutral position. For schedules A2 and A3, the maximum and minimum simulated angles of deflection were +/- 5 degrees and +/-10 degrees respectively. Examination of Fig. (6b) reveals that initially, the vortex path seems to be independent of the rate of deflection and the maximum deflection angle. However, as the vortex continues to move beyond the mid-chord position, noticeable differences are seen. More precisely, for schedule A3, the vortex seems to be drawn more towards the airfoil with the minimum

separation distance attained when the vortex is located approximately at a distance of one chord length downstream from the airfoil's trailing edge. This behavior is contrary to that predicted for the baseline airfoil-vortex interaction problem (schedule A1) where the vortex tends to move away from, rather than towards, the airfoil as it passes the trailing edge. It is conjectured here that during the upstroke portion of the motion described by schedule A3, a low pressure region is created in the vicinity of the lower surface of the flap. This region, in turn, results in "attracting" the vortex closer to the flap and thus yielding the observed smallest airfoil-vortex separation distance. The continuous decrease in the airfoil-vortex separation distances beyond the position of minimum flap deflection (i.e., $xv/C = 1$) and up to $xv/C \cong 2$, is only a consequence of the unsteady flap motion effects.

The temporal variations of the differential pressures near the airfoil's leading edge ($x/C = 0,02$), thought by researchers [28,29] to be indicative of the intensity of BVI noise levels, are depicted in Fig. (6c) for the three flap schedules of Fig. (6a). Note that no differences can be seen as a consequence of the flap motions. Obviously, the insensitivity of the leading edge pressures to the events taking place at the trailing edge must be attributed to the existence of the upper and lower surface supersonic flow regions which tend to "mask" the downstream unsteady motion effects.

In Figs. (6d,6e) we illustrate a comparison between the predicted lift and moment coefficients, as a function of vortex position, for the three flap schedules of Fig. (6a). For schedule A3, when the vortex is approximately at the mid chord position, the lift reaches a peak value of 0.215. This peak value is a direct consequence of the 10 degrees positive flap deflection (i.e., flap down) which took place when the vortex was at $xv/C = 0.0$. Note the shift in the vortex chordwise positions which correspond to maximum flap deflection and the computed peak lift value. This observed shift is attributed to the unsteady effects being simulated during the downstroke portion of the flap motion. Note also that the initial increase in the lift, rather than the observed decrease for the baseline case, occurs instantly with the deployment of the flap. For the three flap schedules considered, our results indicate an increase in the lift coefficients at a constant rate which seems to be independent of the maximum flap deflection and the flap deflection rate. The maximum lift values are however dependent on the maximum positive flap deflections.

To further emphasize the limited upstream influence of the trailing edge flap motion for conditions simulating a supercritical onset flow, we consider six observer positions fixed in space relative to the airfoil, see Fig. (7). As seen, the six positions fall along a straight line

which emanates from the airfoil's leading edge. The line is inclined at 40 degrees to the chordwise direction. Figure (8) illustrates the scaled predicted perturbation pressures, as a function of flap schedule, at the selected six observer positions. The perturbation pressures, in this context, represent the differences between the computed unsteady local pressures (accounting for all unsteady effects) minus the computed steady local pressures for the flow past the airfoil at the onset flow conditions. A multiplicative scaling factor, equal to the square root of the distance between the leading edge point and the point in question, was then used to magnify the computed perturbation pressures which tend to decay with the increase in distance from the leading edge.

For the three flap schedules of Fig. (6a), Figs. (9a-d) depict similar results for conditions simulating a subcritical onset flow with a free stream Mach number of 0.2. Aside from the expected differences in the lift and moment levels, striking differences now exist in the computed differential pressures at $x/C = 0.02$, see Fig. (9b). The computed flowfields are now everywhere subcritical and the trailing edge flap motion effects are immediately felt upstream near the airfoil's leading edge. The free vortex trajectories, unlike those predicted for supercritical onset flow, reflect path changes which simultaneously take place with the initial stages of flap deployment.

In Fig. (10) we illustrate the predicted unscaled temporal pressure perturbations, as a function of the trailing edge flap schedules given in Fig. (6a), at the observer positions of Fig. (7). As seen, the use of the flap results in the elimination of the high frequency oscillations which are visible for all nondimensional times less than 4.0 (i.e., prior to the deployment of the flap). It is conjectured here that the elimination process is one where a constructive interaction takes place between the disturbances introduced by the flap and those inherently present in the flow field due to the interaction between the airfoil and the vortex. Note also the formation of a secondary peak near the nondimensional time of 8. Our numerical results have indicated that the magnitude of this peak is directly proportional to the maximum deflection of the trailing edge flap.

For supercritical onset flow, the results of Fig. (8), as well as those of Fig. (6c), illustrate that no disturbances resulting from the motion of the trailing edge flap were propagated upstream. In the vicinity of the leading edge, and irrespective of the flap schedule being considered, the flow was entirely dominated by the vortex-induced velocity field. As a result, it was felt that any further variations in the leading edge flow characteristics can only be achieved through the use of a leading edge device which must be

positioned upstream of the embedded supersonic flow regions. A leading edge flap with a hinge point at the 10% chordwise position seemed to achieve this goal.

3.3. Effects of the Leading Edge Flap

Figure (11) illustrates the temporal variations of the predicted scaled perturbation pressures at the six observer positions of Fig. (7) for three leading edge flap schedules simulating minimum and maximum deflections of -/+ 1.5 degrees, -/+ 2.5 degrees, and -/+ 5 degrees (respectively referred to here as schedules 1, 2 and 3). Similar to the notation adopted for the trailing edge flap deflections, positive leading edge flap deflections imply flap down, and negative deflections imply flap up. A noticeable difference from the general features of the results shown in Fig. (8) is the appearance of a secondary peak which is evident between the nondimensional times of 6 and 8. This secondary peak reflects the increase in the disturbance levels as a consequence of the leading edge flap motion. As seen, the amplitude of the peak disturbances at all observer positions are highly dependent on the maximum deflection of the control surface. Note also that the results of Fig. (11) were obtained for flap schedules that reflect an initial negative deflection followed by a return to the neutral position and then positive deflections which are again followed by a return to the neutral position. In our numerical experimentation with what constituted a suitable flap deflection schedule it was apparent that by reversing this schedule (i.e., having initially positive deflections which are followed by negative deflections) very high disturbance levels were introduced into the vicinity of the leading edge. For these conditions, Fig. (12) depicts the computed disturbance levels at the six observer positions for a leading edge flap motion schedule simulating maximum and minimum deflections of +/- 5 degrees. A quick comparison between the results of Fig. (12) and those of Fig. (11) reveal that the temporal gradients are considerably higher than those for the baseline airfoil-vortex interaction problem. From an acoustics point of view, schedule 3 is therefore favored.

Figure (13a-e) depict, respectively, three user-specified leading edge flap schedules (A, B, C), the predicted free vortex trajectories, the differential pressures at the 2% chord position, and the sectional lift and moment coefficients for a free stream Mach number of 0.8 and an angle of attack of zero degrees. Aside from the noticeable variations in the differential pressures at the 2% chord position, very slight deviations from the baseline results occur for the vortex path and the lift and moment coefficients. This, of course, is a consequence of the small deflections and the relatively small leading edge flap chord of 10%

C. For a free stream Mach number of 0.2, i.e., subcritical onset flow, similar results were also obtained with the associated different levels for the predicted lift and moment coefficients.

3.4. Effects of the Leading and Trailing Edge Flaps

In light of the results presented in the previous two sections, it is clear that for subcritical onset flows, the use of the trailing edge flap significantly alters the temporal rates of variation of the pressures in the vicinity of the airfoil's leading edge. As a result, one would expect associated changes in the resulting acoustic signatures. Whether these changes decrease (or increase) noise levels will depend, to a large extent, on the specific flap schedule being prescribed. We have illustrated that the deflection rate as well as the maximum and minimum amplitudes are key factors in altering the aerodynamics, and hence the acoustics, of the baseline airfoil-vortex interaction problem. For supercritical onset flows, we have also illustrated the necessity of using a leading edge flap if one needs to alter the local flow characteristics, especially the temporal variations of pressure, in the vicinity of the airfoil's leading edge. A question may then arise as to how would the use of both leading and trailing edge flaps affect the basic airfoil-vortex interactions?

To address this question, two simulations were conducted for a supercritical onset flow with a free stream Mach number of 0.8 and an angle of attack of zero degrees. The simulated two leading edge flap schedules are denoted by B and C in Fig. (13a). In these simulations, the trailing edge flap schedules were identical to schedule A3 shown in Fig. (6a). Figures (14,15) depict the effects of the simulated flap motions on the predicted size of the embedded supersonic flow regions as a function of the instantaneous vortex position. As seen, for all vortex positions less than $x_v/C = -0.6$, no noticeable differences are evident in the size and chordwise extent of the embedded supersonic flow regions. For $x_v/C = -0.6$ (where the initial stages of flap deployment take place) flap schedule B results in the stretching of the lower surface supersonic flow region towards the airfoil's leading edge. More precisely, the sonic conditions are first reached at $x/C = 0.12$ for schedule B rather than at $x/C = 0.18$ for schedule C. For schedule B, as the vortex continues to propagate downstream, the lower surface supersonic flow region continues to increase in size with the shock wave moving aft. By comparison, the upper surface supersonic flow regions are smaller than those predicted for schedule C (see the results for $x_v/C = -0.2, 0.0, 0.2$). For both flap schedules, secondary supersonic regions can also be observed near the position of the trailing edge flap hinge as a consequence of the unsteady flap motion. No significant

differences however can be seen in their relative size and position. For schedule C, a secondary supercritical region can also be seen near the location of the leading edge flap hinge point, x/C = 0.1.

As the vortex continues to propagate beyond the airfoil's mid-chord position, an opposite effect to that described above takes place. That is, for schedule B, a gradual increase in the size of the upper surface supersonic flow region, as compared to that predicted for schedule C, takes place as the vortex continues to move towards and beyond the airfoil's trailing edge. The near symmetric flow conditions, resembling those predicted for xv/C = -5.0, are slowly recovered when the vortex is located approximately 13 chord lengths downstream of the airfoil's trailing edge.

Figure (16a-e) depict the simulated leading and trailing edge flap schedules, the predicted free vortex paths, the differential pressures at x/C = 0.02, and the variations in the sectional lift and moment coefficients. Comparison of the results of Fig. (16) with those of Fig. (13) reveal that simultaneous changes in the leading edge differential pressures and the sectional loads can only be achieved through the use of both leading and trailing edge flaps. Note that despite the relatively comparable peak lift values obtained with the leading edge flap schedules B and C, big differences exist in the temporal rates of variations of the differential pressures at x/C = 0.02. We have mentioned earlier that the temporal rates of variations of the leading edge pressures are, to a large extent, indicative of the noise levels associated with the airfoil-vortex interaction. Referring to Fig. (16c), one can therefore infer that the use of the leading edge flap schedule B in conjunction with the trailing edge flap schedule A3 is more favorable, from an acoustic point of view, than the combined use of the leading and trailing edge flap schedules C and A3 respectively. This is primarily due to the "milder" temporal rate of variation of the leading edge differential pressures for the combination of flap schedules B and A3 as contrasted with the more rapid or "steep" temporal variations obtained for schedules C and A3.

At this juncture, it is noteworthy to re-emphasize that throughout this study, the simulated flap schedules were only meant to illustrate their impact on the aerodynamics of the baseline airfoil-vortex interaction problem. These schedules should, by no means, be inferred as being representative of what constitutes the "optimum" deflection rates or amplitudes. For example, in our simulations, we have fixed the time interval for the deployment of the leading and the trailing edge flaps. From a practical point of view, the deployment of either flap can be linked directly to a preset differential pressure level once

1 8

it has been reached near the airfoil's leading edge. Further, the duration of the unsteady motions need not be identical for both the leading and the trailing edge flaps. Indeed, once all these factors are considered, one is then more likely to be able to speculate as to what constitutes the "optimum" combination of leading and trailing edge flap schedules necessary to alleviate the interaction.

4. TWO-DIMENSIONAL NAVIER-STOKES FORMULATION

We consider two-dimensional, unsteady, compressible flow of a perfect gas. The flow field is determined by the solution of the full Reynolds-averaged Navier-Stokes equations. In nondimensional conservation vector form, they may be written as

$$\partial_t q + \partial_x E + \partial_y F = Re^{-1}(\partial_x R + \partial_y S)$$

(22)

where

$$q = \begin{bmatrix} \rho \\ \rho u \\ \rho v \\ e \end{bmatrix}, \quad E = \begin{bmatrix} \rho u \\ \rho u^2 + p \\ \rho v u \\ u(e+p) \end{bmatrix}, \quad F = \begin{bmatrix} \rho v \\ \rho u v \\ \rho v^2 + p \\ v(e+p) \end{bmatrix}, \quad R = \begin{bmatrix} 0 \\ \tau_{xx} \\ \tau_{xy} \\ R_4 \end{bmatrix}, \quad S = \begin{bmatrix} 0 \\ \tau_{xy} \\ \tau_{yy} \\ S_4 \end{bmatrix}$$

(23)

and

$$\tau_{xx} = \mu(\lambda + 2\mu)u_x + \lambda v_y \ ,$$

$$\tau_{xy} = \mu(u_y + v_x) \ ,$$

$$\tau_{yy} = (\lambda + 2\mu)v_y + \lambda u_x \ ,$$

$$R_4 = u\,\tau_{xx} + v\,\tau_{xy} + \mu\,Pr^{-1}(\gamma - 1)^{-1}\partial_x a^2 \ ,$$

$$S_4 = u\,\tau_{xy} + v\,\tau_{yy} + \mu\,Pr^{-1}(\gamma - 1)^{-1}\partial_y a^2 \ .$$

(24)

In Eqs. (23) the density ρ, velocity components u, v are normalized by the free stream density and speed of sound respectively; the length scales x, y by the airfoil chord length C; time t by the ratio of the free stream speed of sound to the chord; and the total energy per unit volume e by the dynamic pressure based on the free stream speed of sound. In Eqs. (22), Re is the Reynolds number (based on the airfoil's chord length C, the free stream speed of sound and free stream density), and in Eqs. (24) Pr is the Prandtl number (set equal to 0.9 in the present analyses). Under Stoke's hypothesis, the bulk viscosity λ is taken as $-(2/3)\mu$. For a calorically perfect gas, the equation of state may be written in nondimensional form as

$$p = (\gamma - 1)[e - 0.5\,\rho\,(u^2 + v^2)].$$

(25)

Moreover, the local speed of sound a, can be written as

$$a^2 = \gamma p \rho^{-1}$$

or after utilizing Eq. (25) as

$$a^2 = \gamma (\gamma - 1) [e / \rho - 0.5 (u^2 + v^2)].$$ (26)

To properly represent the physical domain of interest, and to facilitate the application of the physical boundary conditions on the different segments of the airfoil's surface, it is important that the airfoil's surface coincide with one of the coordinate family of lines. In this respect, a body-fitted nonorthogonal coordinate system, referred to here as the $\xi - \eta$ coordinate system, was utilized in the present formulation of the problem. The body fitted grid was generated using an algebraic procedure [30] viz.,

$$W = \xi + \eta = \sqrt{Z - Z_n}$$

which results in a sheared parabolic C-type grid , see Fig. (17). To resolve the details of the flow in the developing boundary layer, an exponential stretching was used in the η direction yielding a minimum normal grid spacing of 0.00005 C between the surface grid points and the grid points in the flow field just off the surface of the airfoil. This normal spacing, equivalent to a nondimensional law-of-the-wall coordinate $y^+ = 4$, have been shown to yield accurate results [31] when used in conjunction with the Baldwin-Lomax turbulence model [32].

The results reported here were obtained on a grid having 161 nodes in the wrap-around direction with 99 nodes on the surface of the airfoil, and 61 nodes in the normal direction with approximately 25 points submerged in the developing boundary layer. The outer far-field boundary was located at a distance approximately 5 airfoil chord lengths away from the surface. With ξ and η as new independent variables, we recast Eqs. (22) in the strongly conservative form given by

$$\partial_\tau \overline{q} + \partial_\xi \overline{E} + \partial_\eta \overline{F} = Re^{-1} (\partial_\xi \overline{R} + \partial_\eta \overline{S})$$ (27)

Here,

$$\bar{q} = J^{-1} q \ ,$$

$$\bar{E} = J^{-1} (\xi_x E + \xi_y F) \ ,$$

$$\bar{F} = J^{-1} (\eta_x E + \eta_y F) \ ,$$

$$\bar{R} = J^{-1} (\xi_x R + \xi_y S) \ ,$$

$$\bar{S} = J^{-1} (\eta_x R + \eta_y S) \ .$$

(28)

In Eqs. (28), J is the Jacobian of the numerical coordinate transformation, Eq. (7), and $\xi_x, \eta_x, \xi_y, \eta_y$ are the metrics of the coordinate transformation. For convenience, the grid increments $\Delta\xi, \Delta\eta$ are set equal to 1 in the rectangular computational plane.

4.1. SOLUTION ALGORITHM

Equations (27) are discretized in time using first-order two-point backward differencing and in space using three-point second-order central differencing , i.e.,

$$\delta_\tau \bar{q} + \Delta\tau (\delta_\xi \bar{E}^{n+1} + \delta_\eta \bar{F}^{n+1}) = \Delta\tau Re^{-1} (\delta_\xi \bar{R}^{n+1} + \delta_\eta \bar{S}^{n+1})$$

(29)

Equations (29) are nonlinear since the flux terms E and F are functions of the dependent variable q. Application of a Taylor series expansion to these terms results in the following linearized expressions for E and F at the new time level (n+1), viz.,

$$\bar{E}^{n+1} = \bar{E}^n + A^n \Delta\bar{q}^n \ ,$$

$$\bar{F}^{n+1} = \bar{F}^n + B^n \Delta\bar{q}^n \ ,$$

(30)

Here, $A^n = (\partial_{\bar{q}}\bar{E})^n$, $B^n = (\partial_{\bar{q}}\bar{F})^n$, and $\Delta\bar{q}$ represents the change in the dependent variables $\rho, \rho u, \rho v, e$ at two successive time steps n, n+1. In Eqs. (30), A, and B are commonly referred to as the Jacobian matrices of the flux vectors E, F. Rewriting Eqs. (29) after utilizing the expressions given in Eqs. (30) and rearranging, we obtain the following

system of linear equations for Δq ,

$$[I + \Delta\tau(\delta_\xi A^n + \delta_\eta B^n)]\Delta\overline{q}^n = -\Delta\tau(\delta_\xi \overline{E}^n + \delta_\eta \overline{F}^n) + \Delta\tau Re^{-1}(\delta_\xi \overline{R}^n + \delta_\eta \overline{S}^n) \ . \tag{31}$$

As mentioned earlier, an approximate factorization scheme, Ref. [23], was used in the present formulation to approximate the two-dimensional spatial differential operator appearing on the left hand side of Eq. (31) as the product of two one-dimensional spatial operators in the ξ, η directions respectively, i.e.,

$$
\begin{aligned}
[I + \Delta\tau\delta_\xi A^n][I + \Delta\tau\delta_\eta B^n]\Delta\overline{q}^n = &-\Delta\tau(\delta_\xi \overline{E}^n + \delta_\eta \overline{F}^n) + \\
&\Delta\tau Re^{-1}(\delta_\xi \overline{R}^n + \delta_\eta \overline{S}^n) - \\
&(\Delta\tau)^2 \delta_\xi A^n \delta_\eta B^n \Delta\overline{q}^n
\end{aligned} \tag{32}
$$

In Eqs. (32), we further simplify the right hand side by neglecting the third term which is of $O(\Delta\tau)^2$ as compared to the first and second terms which are of $O(\Delta\tau)$. As a result, Eqs. (32) can be written as

$$[I + \Delta\tau\delta_\xi A^n][I + \Delta\tau\delta_\eta B^n]\Delta\overline{q}^n = \Delta\tau[RHS]^n \ , \tag{33}$$

where

$$[RHS]^n = \Delta\tau[Re^{-1}(\delta_\xi \overline{R}^n + \delta_\eta \overline{S}^n) - (\delta_\xi \overline{E}^n + \delta_\eta \overline{F}^n)] \ . \tag{34}$$

The solutions to Eqs. (33) are then obtained using a two-step process through the introduction of an intermediate solution vector $\Delta\Phi$. Let

$$\Delta\Phi = [I + \Delta\tau\delta_\eta B^n]\Delta\overline{q}^n \ , \tag{35}$$

then Eqs. (33) can be expressed as

$$[I + \Delta\tau \, \delta_\xi \, A^n] \, \Delta\Phi = \Delta\tau \, [RHS]^n \; . \tag{36}$$

Application of Eqs. (35) and (36) at grid nodes inside the computational domain results in a matrix system with a block tridiagonal structure (having 4x4 coefficient matrices) which is then solved efficiently using a lower-upper (LU) matrix decomposition procedure. Assuming that the dependent variables are known at time level n (or equivalently the corrections or delta quantities) , the solution then proceeds by first solving Eqs. (36) for $\Delta\Phi$, then Eqs. (35) for $\Delta\bar{q}$. For steady state solutions, the equations are advanced in time at each grid node using a time step $\Delta\tau$ which is a function of the local transformation Jacobian, i.e.,

$$\Delta\tau = \frac{1}{1 + \sqrt{J(i,j)}} \; .$$

For time-accurate computations, a time step on the order of one-tenth that found using a von-Neuman stability analysis of the equations is used.

4.2. ARTIFICIAL DISSIPATION

To prevent the odd-even point decoupling which results from the use of central difference operators on the left hand side of Eqs. (33), and to suppress the appearance of spurious solution oscillations in the vicinity of shock waves and stagnation points, 2nd and 4th-order dissipation terms are added to these equations. More precisely, implicit second-order dissipation terms in the ξ, η directions [33] are added to the left hand side of Eqs. (33), and a blend of "solution adaptive" second and fourth-order explicit dissipation terms, in the manner suggested by Jameson, Schmidt, and Turkel [34], are added to the right hand side of Eqs. (33), viz.,

$$[I + \Delta\tau \, \delta_\xi A^n + \varepsilon_I D_{I_\xi}][I + \Delta\tau \, \delta_\eta B^n + \varepsilon_I D_{I_\eta}] \, \Delta\bar{q}^n = \Delta\tau \, [(RHS)^n - \varepsilon_E D_E], \tag{37}$$

In the above equations, the second-order dissipation operators are expressed as

$$D_{I_\xi} = -J^{-1}(\nabla_\xi \, \Delta_\xi \, J)$$

$$D_{I_\eta} = -J^{-1}(\nabla_\eta \, \Delta_\eta \, J)$$

and the explicit dissipation terms are expressed as

$$D_E = - \nabla_\xi [J^{-1} (\varepsilon_{ij}^2 \Delta_\xi q^n - \varepsilon_{ij}^4 \Delta_\xi \nabla_\xi \Delta_\xi q^n)] - \varepsilon_E (\nabla_\eta \Delta_\eta) q^n$$

As seen, the added dissipation terms are usually of a higher-order (i.e., on the order of $\Delta\xi^4$, $\Delta\eta^4$ and as such do not affect the formal second-order spatial accuracy of the numerical solutions. The coefficients $\varepsilon_{ij}^2, \varepsilon_{ij}^4$ are adaptive coefficients which depend on the local pressure gradient determined using a "sensing" function σ_{ij}

$$\sigma_{ij} = \frac{| P_{i+1} - 2 P_i + P_{i-1} |}{| P_{i+1} + 2 P_i + P_{i-1} |}$$

For example, near shock waves, the influence of the second-order explicit dissipation terms will be more dominant as compared to the fourth-order dissipation terms. Near the leading edge, the opposite is true, with the fourth-order dissipation terms becoming more dominant. In Eqs. (37), the constants $\varepsilon_I, \varepsilon_E$ are used to control the amount of dissipation introduced in the solution. ε_E is usually on the order of 1, and ε_I is typically 2 to 5 times larger. The numerical values of these coefficients is directly related to the free stream Mach number being considered. It should be mentioned here that the primary function of the implicit dissipation terms, when used in conjunction with explicit fourth-order dissipation, is to allow for the use of a larger time step and to increase the diagonal dominance of the coefficient matrices appearing on the left hand side of Eqs. (37).

4.3. NUMERICAL BOUNDARY CONDITIONS

Referring to Fig. (18) we notice that the present time-dependent formulation requires boundary conditions to be specified along the coordinate lines $\xi_{max}, \xi_{min}, \eta_{max}, \eta_{min}$, and initial conditions (chosen to be those of the free stream) at grid nodes within the computational domain. In our solution approach, explicit boundary conditions are specified. That is, the delta quantities $\Delta\Phi$, $\Delta\bar{q}$ (or the flow field corrections) are set to zero during the advancement of the solution by one time step. The flow field variables as well as some flow variables at the boundaries are then computed as explained below. In this respect, the updated boundary conditions lag the solution by one time step.

Airfoil Surface (Boundary B-C-D)

On the airfoil, the no-slip boundary condition was enforced by setting the u and v components of the velocity vector **V** , or equivalently the contravariant velocities U, V, to zero. The density ρ and pressure p were computed using the following three-point difference expressions,

$$\rho\,(i,1) = 2\,\rho\,(i,2) - \rho\,(i,3) \ ,$$

$$p\,(i,1) = (\,4\,p\,(i,2) - p\,(i,3))\,/3\ .$$

The first expression implies that the density at the surface is extrapolated using the density values at the two grid nodes just off the surface. The second difference expression for the surface pressure is an approximation for a vanishing pressure gradient on the stationary solid wall. In our computations, an adiabatic wall condition was assumed at all grid nodes on the airfoil's surface. The surface total energy was determined using Eq. (25) once the surface pressure was computed.

Wake Branch Cut (segments A-B, D-E)

Continuity of the physical flow properties across the branch cut A-B, D-E, require that

$$q\,(\xi_A \leq \xi \leq \xi_B, \eta_{min}) = q\,(\,\xi_D \leq \xi \leq \xi_E, \eta_{min})\ .$$

In the present formulation, the above condition was satisfied by averaging linear extrapolates of the computed flow field variables from above and below the branch cut.

Far-Field Boundary (A-H-G-F-E)

We take advantage of the characteristic features of a subsonic inflow and/or outflow boundary [35]. At the computational domain boundary representing the far-field, i.e. $\eta = \eta_{max}$ in Fig. (18), the characteristics of the inviscid one-dimensional Euler equations a priori determine the number and type of variable(s) (e.g., ρ , u, v, e) which can be specified at this boundary. That is, for subsonic free stream Mach numbers, the nonreflecting boundary condition is based on the local, one-dimensional Riemann invariants expressed by

$$R^- = V_n - 2 \frac{a}{(\gamma - 1)}$$

$$R^+ = V_n + 2 \frac{a}{(\gamma - 1)}$$

Here, a is the local speed of sound and V_n is the velocity normal to the outermost grid line representing the far-field, viz.,

$$V_n = \frac{\eta_x u + \eta_y v}{\sqrt{\eta_x^2 + \eta_y^2}}$$

The local tangential velocity, V_t, is given by

$$V_t = \frac{\eta_x u - \eta_y v}{\sqrt{\eta_x^2 + \eta_y^2}}$$

The Riemann invariants R^-, R^+ and V_t provide three equations for three of the four unknown flow variables. An additional equation is therefore needed to uniquely define the boundary values for the four flow variables ρ, u, v, e. The entropy, s, can be easily computed using the following expression

$$s = \ln(p / \rho^\gamma)$$

and is used here to provide the fourth equation. The normal direction is taken positive outward from the outer boundary. The sign of V_n is used to determine whether the local flow conditions represent inflow or outflow through the boundary segment. For example, at locations where inflow exists, i.e., $V_n < 0$, the Riemann invariant R^- is constant along a wave which originates at an interior grid point and terminates at the outer boundary. Therefore, the three quantities R^-, V_t, and s can be specified at their free stream values. The remaining variable R^+ is extrapolated from the interior grid information. On the other hand, for conditions were outflow exists (i.e., $V_n > 0$), R^- is based on the free stream conditions. For supersonic onset flow, though not of practical interest in this study, all flow variables need to be specified where inflow exists, and all flow variables are extrapolated from the interior flowfield data for an outflow boundary.

Modeling of Vortex-Induced Effects:

In the Navier-Stokes formulation, the "perturbation" approach [36] was used to model the contribution of the vortex flow field to the total flow. This approach requires initially the computation of the vortex flowfield at each grid point in the computational domain which, in turn, requires a priori knowledge of the vortex core size and the instantaneous position of the vortex with respect to the airfoil. Once the vortex flowfield is computed (assuming a Lamb vortex), it is then added to the mean flowfield. Thereafter, the fluid dynamic phenomena convects the vortex. It is noteworthy to mention that in order to minimize excessive smearing of the captured vortex, the artificial viscosity terms were applied to the vector containing the difference between the instantaneous total field values and the vortex flowfield values rather than the commonly utilized approach of applying the artificial viscosity terms to the solution vector. In this respect, the dissipation terms have a minimal influence near the vortex and, as a result, the characteristics of the vortex-induced velocity field are preserved. The reader is referred to Ref. [20] for additional details. This approach was used here to investigate the more complex problem of simulating the encounter between the airfoil and the vortex when the miss distance is on the same order of the vortex core radius.

Modeling of Trailing Edge Flap Motions:

In the Navier-Stokes formulation, a comprehensive approach was adopted where the computational grid (extending between the surfaces of the flap and the farfield boundary) downstream of the flap hinge point was sheared in the y-direction to accommodate the motion of the trailing edge flap. The no-slip boundary condition was then enforced at the grid points lying on the actual instantaneous position of the flap surface. The grid velocities in the y-direction for all points lying on the flap surfaces were then computed using first-order time differencing of the known grid point positions at two consecutive time steps. Note that the time-dependent position of the flap surface is known a priori through the knowledge of the trailing edge flap schedule which is prescribed by the user.

4.4. TURBULENCE MODEL

The Baldwin-Lomax [32] turbulence model was used to calculate the turbulent viscosity for the wall-bounded shear layers. The model is patterned after the well known Cebeci-Smith [37] model, and have been extensively used in the prediction of separated

turbulent flows. A two-layer formulation is used to model the eddy viscosity. In the inner layer, the eddy viscosity is assumed to be proportional to the product of the mixing length,ℓ, and a turbulent velocity scale. The mixing length ℓ is selected to be proportional to the product of the Prandtl-Van Driest damping factor [38] and the normal distance from the wall. The velocity scale is chosen as the magnitude of the local vorticity $|\omega|$ times the mixing length, i.e.,

$$\mu_t = \rho \, \ell \, |\omega|$$

and

$$\ell = \kappa \, y \, D$$

Here, D is the Prandtl-Van Driest damping factor which is used to drive the eddy viscosity to zero as ℓ approaches zero, $\kappa = 0.4$ is von Karman's constant, and $|\omega|$ is given by

$$|\omega| = |u_y - v_x|$$

The inner layer is assumed to exist up to the point where the inner and outer values of eddy viscosity are equal. In the outer layer, the Baldwin-Lomax model uses a locally constant eddy viscosity formula similar to that in the Cebeci-Smith model. However, the former model circumvents the difficulty associated with having to define the edge of the developing boundary layer.

5. TWO-DIMENSIONAL NAVIER-STOKES RESULTS

We have demonstrated in section 3 that weak blade-vortex interactions (i.e., those with a vortex miss distance on the order of 0.25 C or larger) can be efficiently modeled using the unsteady full potential formulation. However, there are situations where the clearance between the vortex trajectory and the rotor disk is very small (on the order of 0.1 C or less) leading, quite often, to head-on collisions between the vortex and the airfoil. To model such close encounters and the interaction between the vortex and the developing boundary layer over the airfoil's surface requires two- and three-dimensional Navier-Stokes-based formulations.

In the present work, close BVI interactions, and close BVI-flap interactions are studied using the method developed by Sankar and Tang [20]. In the past, close BVI interactions were difficult to study using Eulerian, vortex capturing algorithms due to excessive smearing of the vortex by numerical viscosity. As we mentioned earlier, Sankar and Tang overcame this problem by applying the numerical smoothing operations only to the difference between the computed velocity field and the velocity field associated with the passing vortex.

Figures (19,20) illustrate respectively the predicted instantaneous vorticity and streamline contours for a strong BVI case. Here, the airfoil is the NACA 0012 section. The freestream Mach number and Reynolds number are 0.8 and 3.6 million respectively. It is clear from Fig. (19) that the structure of the vortex, manifested in its core size, is captured without excessive diffusion. Figure (21) depicts the predicted variations of lift coefficient as a function of vortex position, using the vortex-capturing Navier-Stokes method and, an approximate "Euler" analysis which utilized the velocity transpiration approach of section 2.2 to model the vortex-induced effects. With the exception of the slightly different minimum lift levels, the overall viscous and inviscid lift variations are quite similar. This is expected here since the vortex miss distance considered, $y_0/C = -0.26$, does not allow for the direct interaction between the vortex and the developing boundary layer on the airfoil.

To investigate the influence of the trailing edge flap on the airfoil-vortex interactions, the vortex capturing Navier-Stokes method was modified to handle the user-prescribed trailing edge flap motions. Similar to the two-dimensional full potential formulation, the user prescribes the flap schedule as a table of flap deflection angles as a function of non-dimensional time. A linear interpolation of the flap deflection angles was performed in time to determine the instantaneous flap deflection angle and hence the flap surface grid velocities. A subcritical case for the NACA 0012 airfoil, at a freestream Mach number of 0.2 with a clockwise sense of rotation, vortex strength equal to 0.2, zero angle of attack, and vortex miss distance of 0.1 was chosen to exercise the BVI-flap interaction code. Figure (22) depicts the trailing edge flap schedule utilized in the analysis. Note that the maximum flap deflection of 15 degrees occurs when the vortex is in the vicinity of the airfoil's leading edge where the lift drops very rapidly to a minimum. On the other hand, when the vortex is near the airfoil's trailing edge, the flap is deflected by -15 degrees to counter act the anticipated rise in the lift coefficient which is caused by the changes in the vortex-induced velocity field. In Fig. (23) we depict the predicted sectional drag and moment coefficients,

30

as a function of streamwise vortex position, for the baseline NACA 0012 airfoil and for the flapped NACA 0012 airfoil during the interactions with the vortex. In Fig. (24) we illustrate the predicted vorticity and streamline contours for four streamwise vortex positions namely, x_v/C = -2.0, 0.0, 1.0, and 2.0. It is clear that the BVI-flap analysis captures the vortex structure, the effects resulting from the motion of the flap, and the interaction of the boundary layer over the airfoil/flap with the vortex. Note also that recirculation regions are created in the vicinity of the flap when the flap is near the positions of maximum and minimum deflections.

6. THREE-DIMENSIONAL FULL POTENTIAL FORMULATION

As mentioned earlier, the numerical simulations of three-dimensional BVI were performed using the RFS2.BVI code (a modified version of the unsteady three-dimensional, full potential, rotor flow solver, RFS2, developed by Sankar and Prichard [39]). In this section, the equations governing the flow are briefly described.

The governing equation expressing conservation of mass for a three-dimensional, compressible, unsteady, inviscid flow is given by

$$(\rho)_t + (\rho \phi_x)_x + (\rho \phi_y)_y + (\rho \phi_z)_z = 0 \tag{38}$$

In Eq. (38), ϕ is the velocity potential function and ρ is the density. We assume that any shock waves present are weak and hence do not represent a source of vorticity in the flow. By combining the energy equation, viz.,

$$a^2 = 1 - 0.5 (\gamma - 1) [2\phi_t + \phi_x^2 + \phi_y^2 + \phi_z^2] \tag{39}$$

and the isentropic gas relationship for a calorically perfect gas, i.e.,

$$\rho = (a^2)^{1/(\gamma-1)} \tag{40}$$

we obtain an expression for the density as a function of the velocity potential function ϕ

$$\rho = [1 - 0.5 (\gamma - 1)(2\phi_t + \phi_x^2 + \phi_y^2 + \phi_z^2)]^{1/(\gamma-1)} \tag{41}$$

In Eqs. (38-41), the density ρ is normalized by the free stream density; the local speed of sound a, and the velocity components (first spatial derivatives of the potential function) by the free stream speed of sound; distances by the local blade chord length C; and time by the ratio between the chord to the free stream speed of sound. Using Eq. (41) to eliminate the

first term on the left hand side of Eq. (38), we obtain the familiar hyperbolic equation for the velocity potential

$$(\rho / a^2) [\phi_{tt} + \phi_x \phi_{xt} + \phi_y \phi_{yt} + \phi_z \phi_{zt}] = [(\rho \phi_x)_x +$$

$$(\rho \phi_y)_y + (\rho \phi_z)_z] \qquad (42)$$

To facilitate the application of surface boundary conditions and the treatment of arbitrary blade geometries, we consider a three-dimensional coordinate transformation of the form,

$$\begin{aligned}
\xi &= \xi(x, y, z, t) \\
\eta &= \eta(y, t) \\
\zeta &= \zeta(x, y, z, t) \\
\tau &= t
\end{aligned} \qquad (43)$$

where the ξ - direction is aligned with the blade chordwise direction x, the η - direction with the spanwise or radial direction y, and the ζ - direction roughly with the normal direction to the blade, z. In the present study, a three-dimensional rigid grid (attached to the blade in the rotating blade-fixed coordinate system) was constructed by the interpolation of two-dimensional near orthogonal sheared parabolic C-type grids generated at user selected blade radial stations, see Fig. (25). The two-dimensional grids were constructed using Jameson's [30] algebraic grid generation procedure built into the RFS2.BVI code. With ξ, η, ζ, τ as new independent variables, we rewrite Eq. (42) as

$$(\rho / J a^2) [\phi_{\tau\tau} + U \phi_{\xi\tau} + V \phi_{\eta\tau} + W \phi_{\zeta\tau}] = [(\rho U / J)_\xi +$$

$$(\rho V / J)_\eta + (\rho W / J)_\zeta] + S \qquad (44)$$

Here, J is the Jacobian of the coordinate transformation,

$$J = \eta_y (\xi_x \zeta_z - \xi_z \zeta_x) \qquad (45)$$

U, V, and W are the contravariant velocity components,

$$\begin{aligned}
U &= \phi_x \xi_x + \phi_y \xi_y + \phi_z \xi_z + \xi_t \\
V &= \phi_y \eta_y + \eta_t \\
W &= \phi_x \zeta_x + \phi_y \zeta_y + \phi_z \zeta_z + \zeta_t
\end{aligned} \qquad (46)$$

33

and S is a function which contains terms related to the grid motion, viz.,

$$S = (\rho / J a^2) [\phi_\xi (\xi_t)_\tau + \phi_\eta (\eta_t)_\tau + \phi_\zeta (\zeta_t)_\tau]$$

(47)

The metrics of the coordinate transformation are related to the physical plane coordinates (x,y,z) through the following relationship

$$\begin{bmatrix} \xi_x & \xi_y & \xi_z \\ \eta_x & \eta_y & \eta_z \\ \zeta_x & \zeta_y & \zeta_z \end{bmatrix} = \begin{bmatrix} x_\xi & x_\eta & x_\zeta \\ y_\xi & y_\eta & y_\zeta \\ z_\xi & z_\eta & z_\zeta \end{bmatrix}^{-1}$$

In Eqs. (46,47), the terms ξ_t, η_t, ζ_t reflect the motion of the grid which is associated with that of the blade. These quantities are thus functions of the physical plane grid velocities x_τ, y_τ, z_τ and may be expressed as

$$\xi_t = - (x_\tau \xi_x + y_\tau \xi_y + z_\tau \zeta_z)$$
$$\eta_t = - y_\tau \eta_y$$
$$\zeta_t = - (x_\tau \xi_x + y_\tau \xi_y + z_\tau \zeta_z)$$

To further simplify the analysis, grid motion effects were not taken into account in the full potential computations. However, these effects were accounted for in the helicopter/rotor trim code CAMRAD/JA [40] predictions of the vortex wake trajectories.

Similarly, Eq. (41) is recast in terms of the computational plane coordinates,

$$\rho = \{ 1 + 0.5 (\gamma - 1) [1 - 2 \phi_\tau - (U + \xi_t) \phi_\xi - (V + \eta_t) \phi_\eta - $$

$$(W + \zeta_t) \phi_\zeta]\}^{1 / (\gamma - 1)}$$

(48)

It is to be noted that if the function S appearing on the right hand side of Eq. (44) is neglected, then a non-conservative (only in time) form of the full potential equation is obtained. In the present study, due to the relatively low rotor advance ratios considered, shock waves, if present, are weak and hence the necessity to account for this function is absent. Moreover, in Refs. [17,39], it has been demonstrated that the incorporation of such a term only adds quantities which are on the order of the truncation error in time.

6.1. SOLUTION ALGORITHM

Equation (44) is discretized using standard central differences for the spatial flux-like terms appearing on the right hand side, and two-point upwind differences for the mixed time-space terms appearing on the left hand side. For convenience, the mesh spacing is set equal to unity in the box-like computational domain, see Fig. (25). Assuming that the velocity potential function ϕ and its temporal derivative are known at a time level n we proceed to evaluate the left hand side of Eq. (44) as follows:

1) The local speed of sound a, Jacobian J, and the density P, are evaluated at the time level n using Eqs. (39,45, and 48 respectively).

2) The contravariant velocities U,V, and W appearing on the left hand side are evaluated at the time level n using Eqs. (46). In this process, two-point central differences were used to evaluate the transformation metrics at the grid points and locations mid distance between the grid points.

3) The temporal derivatives are represented by two-point backward finite-difference operators.

In this respect, we can express Eq. (44) as follows,

$$(\rho/J\,a^2)^n\,[\,\bar{\delta}_\tau\bar{\delta}_\tau + U^n\bar{\delta}_\xi\bar{\delta}_\tau + V^n\bar{\delta}_\eta\bar{\delta}_\tau + W^n\bar{\delta}_\zeta\bar{\delta}_\tau\,]\,\phi =$$

$$[\,(\rho\,U/J)_\xi + (\rho\,V/J)_\eta + (\rho\,W/J)_\zeta\,] + S \qquad (49)$$

For example, at a typical grid node (i,j,k), we express the first term inside the square brackets of Eq. (49) as

$$\bar{\delta}_\tau\bar{\delta}_\tau\phi = (\phi^{n+1} - 2\phi^n + \phi^{n-1})/(\Delta t)^2$$

or

$$\bar{\delta}_\tau\bar{\delta}_\tau\phi = \frac{1}{\Delta t^2}[\,(\phi^{n+1} - \phi^n) - (\phi^n - \phi^{n-1})\,] = [\,\Delta\phi^{n+1} - \Delta\phi^n\,]/\Delta t^2$$

In the previous expression, $\Delta\phi$ represents the change in the solution in two consecutive time steps n and (n+1), or (n-1) and n. The mixed space-time derivatives appearing in Eq.

(49) are discretized using upwind-differencing for the spatial derivative, and two-point backward-differencing for the temporal derivative. For example, in evaluating the second, third, and fourth terms we have,

$$U^n \bar{\delta_\xi} \bar{\delta_\tau} \phi = (\Delta\phi (i,j,k) - \Delta\phi (i-1,j,k))^{n+1} / \Delta t \quad U^n (i-1/2,j,k) > 0$$

$$= (\Delta\phi (i+1,j,k) - \Delta\phi (i,j,k))^{n+1} / \Delta t \quad U^n (i+1/2,j,k) < 0 ,$$

$$V^n \bar{\delta_\eta} \bar{\delta_\tau} \phi = (\Delta\phi (i,j,k) - \Delta\phi (i,j-1,k))^{n+1} / \Delta t \quad V^n(i,j-1/2,k) > 0$$

$$= (\Delta\phi (i,j+1,k) - \Delta\phi (i,j,k))^{n+1} / \Delta t \quad V^n(i,j+1/2,k) < 0 ,$$

and

$$W^n \bar{\delta_\xi} \bar{\delta_\tau} \phi = (\Delta\phi (i,j,k) - \Delta\phi (i,j,k-1))^{n+1} / \Delta t \quad W^n(i,j,k-1/2) > 0$$

$$= (\Delta\phi (i,j,k+1) - \Delta\phi (i,j,k))^{n+1} / \Delta t \quad W^n(i,j,k+1/2) < 0$$

The flux-like terms appearing on the right hand side of Eq. (44) are evaluated using two-point central-difference formulas, i.e.,

$$[(\rho U / J)_{i,j,k}]_\xi = (\rho U / J)_{i+1/2,j,k} - (\rho U / J)_{i-1/2,j,k}$$

$$[(\rho V / J)_{i,j,k}]_\eta = (\rho V / J)_{i,j+1/2,k} - (\rho V / J)_{i,j-1/2,k}$$

$$[(\rho W / J)_{i,j,k}]_\zeta = (\rho W / J)_{i,j,k+1/2} - (\rho W / J)_{i,j,k-1/2}$$

To avoid having a large band width for the coefficient matrix for ϕ and maintain good stability characteristics, only some of the ϕ derivatives appearing in Eqs. (46) for U,V, and W are evaluated at the (n+1) time level. More precisely, when computing U, ϕ_ξ is evaluated implicitly at (n+1) while the other partial derivatives of ϕ (i.e. ϕ_η, ϕ_ζ) are evaluated at the n th time level, viz.,

36

$$U(i,j,k) = A^n(i,j,k)\, \phi_\xi^{n+1}(i,j,k) + B^n(i,j,k)\, \phi_\eta^n(i,j,k) + C^n(i,j,k)\, \phi_\zeta^n(i,j,k)$$

where

$$A^n(i,j,k) = (\xi_x^2 + \xi_y^2 + \xi_z^2)^n_{i,j,k}$$

$$B^n(i,j,k) = (\xi_y \eta_y)^n_{i,j,k}$$

$$C^n(i,j,k) = (\xi_x \zeta_x + \xi_y \zeta_y + \xi_z \zeta_z)^n_{i,j,k}$$

Similarly, when computing V and W, ϕ_η and ϕ_ζ are evaluated respectively at the (n+1) time level and the remainder of the derivatives at the n th time level, i.e.,

$$V(i,j,k) = D^n(i,j,k)\, \phi_\xi^n(i,j,k) + E^n(i,j,k)\, \phi_\eta^{n+1}(i,j,k) + F^n(i,j,k)\, \phi_\zeta^n(i,j,k)$$

$$W(i,j,k) = G^n(i,j,k)\, \phi_\xi^n(i,j,k) + H^n(i,j,k)\, \phi_\eta^n(i,j,k) + I^n(i,j,k)\, \phi_\zeta^{n+1}(i,j,k)$$

In the above expressions, the coefficients D(i,j,k) through I(i,j,k) are only functions of the coordinate transformation metrics evaluated at the n th time level at the grid node (i,j,k). The nodal values of ϕ at the (n+1) time level are then expressed as the sum of ϕ at the n th time level plus a correction $\Delta\phi$ at the (n+1) time level, i.e.,

$$\phi^{n+1}(i,j,k) = \phi^n(i,j,k) + \Delta\phi^{n+1}(i,j,k)$$

The density values were evaluated in the usual manner at mid grid point positions at the n th time level. Furthermore, to maintain numerical stability in regions of supersonic flow, the density values were biased in the direction of the flow using a formula suggested by Hafez and Lovell [41], viz.,

$$\bar{\rho} = \rho - \delta_\xi (\rho q)/q \qquad \text{for } M > 1$$

or

$$\bar{\rho}(i,j,k) = \rho(i,j,k) - [\,(\rho q)_{i,j,k} - (\rho q)_{i-1,j,k}\,]/q(i,j,k) \, ,$$

and

$$\bar{\rho}(i,j,k) = \rho(i,j,k) \qquad \text{for } M < 1$$

In the present solver, biasing of the density only along the chordwise ξ-direction has proved to be satisfactory.

When the left and right hand sides of Eq. (44) are discretized as discussed above, the following difference equation results,

$$a_{i,j,k}^{n} \, \Delta\phi_{i,j,k-1}^{n+1} + b_{i,j,k}^{n} \, \Delta\phi_{i,j-1,k}^{n+1} + c_{i,j,k}^{n} \Delta\phi_{i-1,j,k}^{n+1} + d_{i,j,k}^{n} \Delta\phi_{i,j,k}^{n+1} +$$

$$e_{i,j,k}^{n} \, \Delta\phi_{i+1,j,k}^{n+1} + f_{i,j,k}^{n} \, \Delta\phi_{i,j+1,k}^{n+1} + g_{i,j,k}^{n} \, \Delta\phi_{i,j,k+1}^{n+1} = R_{i,j,k}^{n} \qquad (50)$$

Here, the coefficients a, b, c, d, e, f, g and R are functions of the transformation metrics, the contravariant velocities, the local flow density ρ, the local speed of sound a, and the time step Δt. Application of Eq. (50) at grid nodes inside and on certain portions of the computational domain boundaries result in a sparse pentadiagonal matrix system which may be expressed as,

$$[M] \, [\Delta\phi]^{n+1} = [R]^{n} \qquad (51)$$

A lower-upper (LU) approximate factorization scheme, originally devised by Stone [42], was employed to facilitate the inversion of the matrix M. In Stone's strongly implicit procedure (SIP), the matrix M is expressed as the product of two sparse lower, [L], and upper [U], matrices each having four diagonals. Equation (51) can thus be expressed as,

$$[L] \, [U] \, [\Delta\phi]^{n+1} = [R^{n}] \qquad (52)$$

with the coefficients of the lower and upper matrices being recursively related to the coefficients of the matrix M, see Ref. [43]. The solutions to Eqs. (52) are then obtained using a two-step procedure where we first solve for a temporary solution vector T, i.e.,

$$[L] \, [T] = [R]^{n}$$

where

$$[U] \, [\Delta\phi]^{n+1} = [T] \qquad (53)$$

and then solve Eq. (53) for the correction in the potential function $\Delta\phi$. At this juncture, it is noteworthy to mention that the above factorization procedure is applicable to both quasi-steady as well as unsteady rotor flow field solutions. In the former case, the temporal derivatives of the potential function are set equal to zero and the SIP can be regarded as an iterative relaxation procedure. In the latter case, the SIP is regarded as a one-step non-iterative time-accurate marching procedure.

6.2. NUMERICAL BOUNDARY CONDITIONS

Referring to Fig. (25) we notice that the present formulation requires boundary conditions to be specified along the blade's surface, trailing edge vortex sheet (commonly referred to as near wake or branch cut), far-field boundaries located outboard of the rotor tip, outer boundary, downstream or outflow boundary beyond the blade's trailing edge, and the most inboard boundary of the computational region. For lifting conditions, the effects of the far wake (the portion of the wake which lies outside the bounds of the computational domain) must also be taken into account in the full potential solution. These boundary conditions are briefly described in the next paragraphs.

Far-Field Boundaries (outer, downstream, outboard):

Since air is considered to be at rest at a large distance from the blade, the velocity potential function ϕ was set to zero on all three boundaries. This condition also implies that the flow velocities in the planes containing these boundaries assume free stream values. For example, for the outboard boundary, the u and w velocity components were set to zero while the v component, approximately normal to this boundary, was allowed to assume nonzero values. Moreover, at the outer boundary, u and v were set to zero while w, again approximately normal to this boundary, was allowed to vary. The nonzero normal velocity components, in a sense, allowed waves to propagate through these boundaries. As a result, contamination of the computational domain solutions which may otherwise occur due to far field wave reflections, was avoided. At the downstream boundary, whenever the local flow was supersonic, a two-point extrapolation formula was used to compute the potential using the interior grid points solutions, i.e.,

$$\phi^{n+1}(i,j,2) = 2\phi^n(i-1,j,k=2) - \phi^n(i-2,j,k=2) \qquad i=IMAX, j=2,...JMAX$$

In the previous equation, IMAX and JMAX are the grid point indices for the last grid point(s) in the wrap-around direction, and the last spanwise computational station respectively. In the computational domain, all grid points lying on the surface of the blade have the index k=2. The grid level defined by k=1 represents fictitious grid points which lie inside the blade. These fictitious points are only used when enforcing the "slip" surface boundary condition.

Inboard Boundary:

This boundary was typically located at the 55% radial position where the velocity potential ϕ was solved for as part of the numerical solution using Eq. (50) subject to the following condition

$$(\rho \, V / J)_{j=2} = 0 \qquad \text{or equivalently} \qquad (\phi_\eta)_{j=2} = 0$$

Blade Surface:

On the solid surface, the inviscid "slip" boundary condition was enforced during the computations, viz.,

$$\mathbf{V} \cdot \mathbf{n} = 0 \tag{54}$$

where $\mathbf{n}$ is the outward unit vector normal to the surface, and $\mathbf{V}$ is the local flow velocity vector. Since the present grid is nearly orthogonal everywhere, Eq. (54) reduces to

$$W = 0$$

This is due to the fact that the normal vector $\mathbf{n}$ is approximately aligned with the computational ζ – direction.

To model blade-vortex interactions, Eq. (54) was modified to reflect the vortex-induced velocities at grid point locations lying on the surface of the blade, i.e.,

$$(\mathbf{V} + \mathbf{V_I}) \cdot \mathbf{n} = 0 \tag{55}$$

In Eq. (55), V_I is the vortex-induced total velocity computed using the Law of Biot-Savart,

$$dV_I = \frac{\Gamma(d\mathbf{l} \times \mathbf{r})}{4\Pi r^3}$$

(56)

Here, $d\mathbf{l}$ is the length of the vortex segment, $\mathbf{r}$ is the position vector from the center of the segment to an arbitrary point on the surface of the blade, and Γ is the strength of the vortex segment. The velocity distribution calculated using Eq. (56) is singular at the center of the vortex. However, in order to obtain physically realistic velocities whenever the blade is in close proximity to the BVI wake elements, a core region where the flow is rotational and viscous forces are important must be modeled. In the present study, Scully's [44] core model was utilized to correct Eq. (56).

An additional modification to Eq. (54) was also necessary to simulate the unsteady motion of the trailing edge flap using the velocity transpiration approach. Here, by simulating the unsteady motion of the flap through the surface boundary condition, we have again facilitated the unsteady three-dimensional computations by using a fixed, rather than a time-varying, grid. By considering an argument similar to that presented in section 2.2, one can show that the modified surface boundary condition for the blade can be written as

$$(V + V_I + V_F) \cdot n = 0$$

(57)

In Eq. (57), V_F is the flap-induced normal surface velocity computed only at the grid nodes lying on the upper and lower surfaces of the flap.

Trailing Edge Vortex Sheet:

This sheet was assumed to coincide with the grid surfaces emanating from the blade's trailing edge. Note that there are two computational nodes (one on either side of the cut) for each physical plane point. At these nodes, it was assumed that the jump in the potential between any two points across the cut is equal to the jump in the potential at the blade's trailing edge (i.e., equal to the bound circulation). On the plane surface outboard of the blade's tip, the jump in the potential function across the cut was set equal to zero.

41

Modeling of Far Wake Effects:

To complete the numerical boundary value problem for the physical flow we must also account for the blade tip vortices, the remainder of the wake system which lies outside the computational region, and any wake elements which might have passed out of, and returned into the computational region. As mentioned above, the near wake is taken into account in the potential solution through the jump in the velocity potential at the blade's trailing edge. The influence of the far wake as well as the re-entering wake elements on the other hand is modeled in the form of an azimuthal and spanwise variation of an induced flow (or equivalently an induced angle of attack) at the quarter chord line of the blade. These angles are provided through a separate computation using the free wake model in the comprehensive rotor trim code CAMRAD/JA [40]. Once the inflow angles are calculated at computational stations through spanwise and azimuthal interpolations, these angles are then converted into surface transpiration velocities which are implicitly represented in the velocity **V** appearing in Eqs. (54 and 57).

The simplified approach just described above for modeling the far wake influence on the flow is not applicable in modeling the influence of the tip vortices which are at close proximity to the blade's surface (BVI wake elements). This is primarily due to the large chordwise and spanwise variations in the vortex-induced velocities during close encounters between the blade and the tip vortices. In the present approach to simulate BVI, the vortex-induced velocities are computed using the Law of Biot-Savart in the potential model. As a result, caution must be practiced in the computation of the far wake inflow angles as they must only reflect the influence of all the far wake elements, minus the influence of the trailing vortex sheet, minus the influence of the selected BVI wake elements (and hence the terminology "partial inflow angles"),viz.,

$$
\left\{\begin{array}{c} \text{partial} \\ \text{inflow} \\ \text{angles} \end{array}\right\} = \left\{\begin{array}{c} \text{total wake} \\ \text{system} \\ \text{inflow angles} \end{array}\right\} - \left\{\begin{array}{c} \text{near wake} \\ \text{inflow} \\ \text{angles} \end{array}\right\} - \left\{\begin{array}{c} \text{BVI} \\ \text{inflow} \\ \text{angles} \end{array}\right\}
$$

(CAMRAD/JA)   (CAMRAD/JA)   (RFS2.BVI)   (RFS2.BVI)

This, of course, was carried out to avoid accounting twice for the influence of the near wake, and the selected BVI wake elements (once in CAMRAD/JA and once in the potential solver RFS2.BVI). In the next section, we describe in detail how the BVI wake elements were identified, how the influence of the trailing edge flap motion was taken into account in

42

CAMRAD/JA, and how the BVI vortex wake element information (i.e., strength and blade separation distances) was integrated into the time-accurate full potential computations.

7. ROTOR TRIM ANALYSIS

7.1. CAMRAD/JA Flapped Rotor Model

The CAMRAD/JA rotor trim code was modified to enable the simulation of a rotor employing a blade-mounted trailing edge integral flap. The flap was implemented in the code to allow for user-specified flap deflections at each blade azimuth. This approach permits arbitrary flap motions, or conventional cyclic and collective inputs, to be applied over any portion(s) of the rotor disk. The flap motions are independent of the primary control system which employs standard root pitch for rotor trim. The flap can be simply placed between any two desired radial stations along the blade and may have an arbitrary length within the constraints of the number of aerodynamic segments representative of the blade.

In this study, the OLS rotor was modeled as a rigid teetering rotor system (i.e., not accounting for blade elastic deflections). Flap motion effects were modeled through changes in the aerodynamic characteristics of the local airfoil section constituting the blade. Flap dynamic motions were also neglected. The changes to the blade mass properties due to the installation of the trailing edge flap and due to the flap control mechanism were also not taken into account.

Aerodynamically, the effects of the flap were simulated through the two-dimensional airfoil data tables which contain the lift, drag and moment coefficients for a flapped airfoil at a specified angle of attack, Mach number, and flap deflection angle. Here, it is assumed that the aerodynamic coefficients will, implicitly, reflect the influence of the length of the flap (or the flap chord). The aerodynamic characteristics for the flapped OLS airfoil section were obtained from those for a flapped NACA 23012 airfoil [45,46]. That is, for a given flap deflection, the incremental changes in the lift, drag and moment coefficients were determined by subtracting the values for the NACA 23012 airfoil (i.e., airfoil without the trailing edge flap) from those for the flapped section. For the NACA 23012 airfoil, the incremental loads and moments were obtained for a range of Mach numbers varying between 0.3 and 0.8, angles of attack varying in the range -30 - +30 degrees and flap deflections varying between -10 (i.e., flap up) and +10 (i.e., flap down) degrees. The lift, drag, and

moment increments were then expressed in equation form and programmed into the CAMRAD/JA aerodynamic routines. The lift and moment increments exhibited reasonably linear variation while drag increments were highly nonlinear. For flap angles exceeding the data range, the lift and moment values were extrapolated. However, because of extrapolation , the drag values were fixed at their values corresponding to the limits for the trailing edge flap deflection angles of +/-10 degrees. The aerodynamic characteristics for the flapped OLS rotor sections were then simulated in CAMRAD/JA by adding the load and moment increments for the NACA 23012 to the 2-dimensional OLS airfoil data at the section local Mach numbers and angles of attack determined through the trim process. The two-dimensional sectional values were then corrected for unsteady and yawed flow effects using the standard CAMRAD/JA model for these corrections. The sectional loads were also independently evaluated using the three-dimensional full potential formulation coupled with a two-dimensional integral boundary layer solution procedure for the nonlifting OLS model rotor (to exclude the effects of the rotor far wake).

The modified CAMRAD/JA rotor trim code, which employs Scully's [44] free-wake model, was applied to the case of the flapped rotor. For large trailing edge flap deflections, finite core vortices are more likely to form at the inboard and outboard extremities of the flap. If these vortices are formed, Scully's wake model must then be modified to account for their distortion since, in its present form, it assumes a prescribed inboard wake geometry. This would require the simulation of two additional trailing vortex lines which will be present only over a small portion of the azimuth during the deployment of the flap. Further, the influence of these vortices will have to be removed from the partial inflow supplied to the full potential model and a history of their trajectory determined. In this study, it was felt that the formation of these two trailing vortices was primarily dominated by viscous effects which are beyond the realm of the adopted full potential formulation. As a result, their influence was not taken into account. It is also noteworthy to mention that the lift changes, and hence the changes in the bound circulation, produced by the trailing edge flap are taken into account as part of the normal shed and trailed wake modeled by the CAMRAD/JA code.

When the flap is deployed to reduce the strength (i.e., circulation) of the vortex line which interacts with the advancing blade, the generating blade may encounter negative lift loading near the tips. Under these conditions, CAMRAD/JA has a dual peak wake model which captures the positive and negative bound circulation peak distributions. This model was applied, in a limited number of runs, to investigate its effect on the resulting BVI wake

44

geometry and strength. However, in the majority of our calculations, an outboard single peak model was used. The single peak model resulted in the correct sign of the tip vortices.

7.2. CAMRAD/JA Modifications for BVI Analysis

The CAMRAD/JA code was modified to compute the wake geometry, wake strength, and inflow angles for azimuthal increments of 10 degrees, rather than the standard 15 degrees, to achieve a somewhat higher resolution in the wake distortion which is crucial in the accurate prediction of BVI. This was accomplished by simply increasing the common block sizes within the wake routines. To assure converged geometry solutions, all wake geometries presented here were obtained using three wake distortion iterations .

CAMRAD/JA contains a built-in capability to interface with computational fluid dynamics (CFD) rotor codes through angle of attack coupling. In the RFS2.BVI CFD code, the far wake inflow effects are represented by an azimuthal and spanwise distribution of partial angles of attack. These angles are computed using CAMRAD/JA at the rotor trim condition. The azimuthal resolution of these values however (presently equal to 10 degrees) is limited by CAMRAD/JA's ability to compute a stable wake solution for smaller azimuthal increments (i.e., 5 degrees or less). The 10 degrees azimuthal resolution is far less than that needed to adequately capture the rapid and, sometimes impulsive, inflow variations encountered during BVI conditions. By coupling the RFS2.BVI CFD rotor code to the CAMRAD/JA rotor trim code this limitation was circumvented. More precisely, this is accomplished here by removing the influence of the tip vortex elements responsible for the dominant blade-vortex interactions (BVI) from the CAMRAD/JA far wake partial angles of attack and directly computing their influence in RFS2.BVI using the CAMRAD/JA predicted vortex strengths and trajectories. Thus, the BVI version of CAMRAD/JA provides a modified partial angle of attack file and a new file which contains both BVI tip vortex element geometry (trajectories) and strengths as a function of rotor azimuth position. This information is then utilized in RFS2.BVI to compute the local vortex-induced inflow velocity distributions on the surface of the blade using the Biot-Savart law with the assumption of a finite vortex core radius. To meet the one-quarter degree azimuthal resolution required in the RFS2.BVI flow computations, the CAMRAD/JA wake positions and strengths are interpolated from their corresponding values provided at azimuthal increments of 10 degrees.

7.3. BVI Element Identification and Tracking

During BVI conditions, certain tip vortex segments along a given vortex line (i.e., the tip vortex generated by a given blade) may result in the most severe flow conditions in terms of the blade's acoustic response. Seemingly, it would be necessary to consider only those elements in the CFD model. In the course of our investigations of BVI for the model OLS rotor, it was found that the local inflow effects were more accurately represented when multiple vortex lines (from one or more blades) were being modeled in RFS2.BVI. This is attributed to the fact that when using partial angles of attack, the local flow angle of attack is assumed to be constant over the entire chord length whereas this angle varies locally when the BVI vortices are incorporated in the CFD computations. Further, when relying on the use of partial angles of attack to model BVI, any vortices in the vicinity of the blade will also have a low azimuthal resolution dictated by the 10 degree azimuthal increments used in CAMRAD/JA. Thus accurate BVI representation can only be achieved when all vortex lines near the blade are treated as BVI elements and their effect modeled in the CFD analysis.

The task of selecting which BVI elements to be removed from the CAMRAD/JA solution can be easily managed by removing a portion of the vortex lines generated by the advancing blades between selected azimuth limits as indicated in Fig. (26). Here, three revolutions of wake from one blade of a five-bladed rotor are shown. The elements denoted as "BVI elements" will be convected downstream in time to interact with other blades as indicated by the elements in "row 2". Generally, for low speed descent flight conditions, the BVI elements must be extracted from two revolutions of wake for each blade. These elements must be "tracked" relative to a master blade as it traverses the advancing side from the 0 to the 180 degrees azimuth. In the case of the two-bladed OLS model rotor, a total of three vortex lines were tracked; one from the master blade and two from the opposite blade, see Fig. (27). Seven BVI segments were chosen along each vortex line between the 90 and 160 degrees azimuthal positions. This azimuthal range enabled the BVI line to include those elements which interact with the tip of the master blade. The vortex lines also extend inboard to account for the inboard critical interactions which occur in the 60-120 degrees azimuthal range. The effect of varying this range, or equivalently the number of vortex segments per vortex line, on the accuracy of the predictions will be shown in section 10.1.1. in our discussions of the blade surface pressure results.

For the OLS rotor at any given master blade azimuth position, the wake geometry is such that all BVI elements along any vortex line will have been generated. However, for a rotor

having more than two blades, there will always be some azimuthal positions where one blade ahead of the master blade will have generated only part of the BVI element range (as can be inferred from Fig. (27)). In this case, a BVI segment is dropped from the oldest vortex line as a new element is being added, thereby maintaining a constant number of the total vortex segments to be modeled.

In CAMRAD/JA, the wake geometry is computed with respect to a tip path plane which is oriented with respect to a coordinate system attached to the rotor hub. However, in the RFS2.BVI full potential solver, the blade is referenced to a non-rotating shaft coordinate system in which blade flapping is not allowed (all blade motions were taken into account in the partial angles of attack changes supplied by CAMRAD/JA). Therefore, for consistency in CAMRAD/JA, it is necessary to compute the wake geometry with respect to the coned master blade in CAMRAD/JA in order to obtain the proper blade/vortex wake separation distances. This coordinate transformation was included in the routine which generates the RFS2.BVI geometry file. The geometry file contains the transformed wake element endpoint locations for each BVI line at each master blade position between the 0 and 180 degrees azimuthal positions. The vortex strength (i.e., the blade bound circulation at the generation azimuth) at each element endpoint is also included. These values remain constant from one vortex line to another since CAMRAD/JA does not model the diffusion of the tip vortex as a function of its age.

It should be noted that partial inflow values covering the complete azimuth range (i.e., 0-360 degrees) were supplied to RFS2.BVI. Our current BVI computations only model those interactions which occur on the advancing side of the rotor disk. This approach however, does not imply that retreating blade vortex interactions are completely neglected since their influence is still inherently contained in the CAMRAD/JA-predicted retreating blade partial angles of attack. The temporal resolution of the retreating blade interactions will somewhat be quite low since it is directly dependent on the resolution of the wake calculations in CAMRAD/JA (presently set at 10 degree increments). As a result, it is expected that the overall contribution of these interactions to the noise levels will be underpredicted. In our BVI analyses it was felt that the advancing blade interactions were quite dominant due to the higher Mach numbers associated with the blade-vortex encounters.

8. ACOUSTIC PREDICTION MODEL

Most rotor acoustic prediction methods have been based on the formulation of Ffowcs Williams and Hawkings [47] (known as FW-H formulation). Among these methods, Farassat's solution to the FW-H equation, commonly referred to as formulation 1A [21], has been extensively used in the field of rotorcraft.

$$
4\pi p_T(\overline{x},t) = \int_{f=0} \left[\frac{\rho_\infty \dot{v}_n}{r(1-M_r)^2} \right]_{ret} dS + \int_{f=0} \left[\frac{\rho_\infty v_n(r\dot{M}_i\hat{r}_i + a_0 M_r - a_0 M^2)}{r^2(1-M_r)^3} \right]_{ret} dS
$$

$$
4\pi p_L(\overline{x},t) = \frac{1}{a_0} \int_{f=0} \left[\frac{\hat{r}_i}{r(1-M_r)^2} \right]_{ret} dS + \int_{f=0} \left[\frac{\ell_r - \ell_i M_i}{r^2(1-M_r)^2} \right]_{ret} dS +
$$

$$
\frac{1}{a_0} \int_{f=0} \left[\frac{\ell_r(r\dot{M}_i\hat{r}_i + a_0 M_r - a_0 M^2)}{r^2(1-M_r)^3} \right]_{ret} dS
\tag{58}
$$

Farassat's formulation 1A, shown above, is currently computer coded in a program designated "WOPWOP". The program was originally developed at NASA Langley Research Center. Reference [48] contains a detailed derivation and description of the acoustic formulation as well as an extensive discussion of the numerical solution procedure employed in the code. In relation to BVI noise analysis, the WOPWOP program has been coupled with the RFS2.BVI rotor flow solver via the computed blade surface pressures which are used as input to the acoustic analyses. In our studies, to allow for the trailing edge flap motion effects, the designated variable "CAMBER" in WOPWOP was used to simulate the instantaneous flap deflection for a given schedule. To accurately mimic the flap motions simulated in the CAMRAD/JA and RFS2.BVI codes, the airfoil sections constituting the flapped portion of the rotor blade were allowed to deform as a function of time (or

equivalently azimuth). The necessary modifications to WOPWOP were the insertion of the "SRFNRM" subroutine inside the retarded time integration for the noise sources. As a result, the two variables "CMBR" and "CMBRP" which are directly influenced by the deployment of the flap are now functions of the retarded time integration. It is important to note here that the "SRFNRM" routine is used to compute the noise source position vector, in the blade-fixed frame of reference, on the upper and lower surfaces of the blade. It is also used to compute the normal and tangential vectors of the potential source in the same frame of reference.

In order to minimize the errors associated with the numerical integrations performed in a retarded time frame, the BVI noise analyses were conducted with the airloads extracted from the full potential solution every one degree of rotor azimuthal travel. The significance of using high resolution airloads in the analyses using WOPWOP was recently demonstrated by Visintainer, Burley, Marcolini, and Liu [49].

9. SOLUTION PROCEDURE

In this section, we outline how the CAMRAD/JA-predicted far-wake partial inflow angles, BVI vortex strengths and trajectories are incorporated into the full potential calculations to predict the blade airloads for the user-specified trailing edge flap schedules. Our final objective, of course, is to utilize the predicted aerodynamics loads in an acoustic analysis to predict the acoustic signature of the rotor and how it is impacted by the trailing edge flap motion.

1.   Using the far wake partial inflow angles of attack, a quasi-steady solution is first computed at the 0 degree azimuth.

2.   Having obtained a quasi-steady solution, the unsteady calculation is then initiated at the 0 degree azimuth position. Knowledge of the instantaneous relative positions of the identified BVI vortex elements with respect to the blade's surface allows the use of the Biot-Savart law to compute the vortex-induced velocities at grid point locations lying on the surface of the blade. This is repeated "m x n" times for an "m" number of vortex interactions, and "n" vortex segments on each interacting vortex element.

3. The sum of the normal components of the vortex-induced velocities are computed at the surface grid nodes and the surface slip (or condition of no flow penetration) boundary condition is modified in the potential flow model.

4. If trailing edge flap effects are to be simulated we proceed as follows: by knowing the instantaneous flap deflection angle and the deflection rate we compute the flap-induced velocities at all grid nodes lying on the surface of the flap. More precisely, for a given rotor azimuth, the flap deflection is found using simple interpolation from the a priori known user-specified flap schedule. The deflection rate is computed by finding the temporal gradient from the discrete input flap deflections.

5. The surface boundary condition is again modified if flap effects are to be correctly simulated in the three-dimensional full potential model.

6. The unsteady potential flow solution is then found using Stone's [42] strongly implicit procedure (SIP) discussed earlier.

7. The rotor is advanced to the next azimuth position.

8. Interpolation is then carried out among the CAMRAD/JA-predicted vortex trajectories, and vortex strengths to determine the new instantaneous positions and strengths of the various vortex segments with respect to the blade's surface which is assumed to lie in the rotor shaft plane. If trailing edge flap motion effects are being simulated, then the instantaneous deflection angles and deflection rates are also found.

9. If the final rotor azimuth position is not reached (chosen to be 180 degrees), steps 3 through 7 are again repeated.

10. The computational blade surface pressures are then utilized as input to the WOPWOP program to predict the acoustic waveforms and spectra for a rectangular grid of observer locations located below the rotor disk (the observer positions are representative of the far/near acoustic fields).

Figure (28) depicts a flow chart of the three coupled analysis methodologies required in the computation of rotor BVI noise. Note that steps 4 and 5 are bypassed if the unsteady motion of the trailing edge flap is not to be simulated.

10. THREE-DIMENSIONAL FULL POTENTIAL RESULTS

We have demonstrated in section 2 that the leading edge flap can be used to effectively alleviate the aerodynamics of supercritical-type interactions. For a helicopter rotor blade in descent flight, this condition is seldom met (most of the interactions which occur are subcritical). Under certain conditions, though the undisturbed flow over the blade is subcritical, blade-vortex encounters result in small local supercritical flow regions. This is also true for conditions where the flap is deployed in an originally subcritical flow. In any event, due to the small size of these regions, and to the small range of azimuthal angles in which these flows exist, one can assume that the flowfield is dominated by subcritical flow. Under these conditions, the trailing edge flap is considered to be a more effective device for altering the aerodynamic, and hence the acoustic, characteristics of the blade. Our three-dimensional numerical simulations were therefore conducted assuming that the rotor blade has only a trailing edge flap.

The numerical results presented in this section were obtained using a computational grid having 121 nodes in the wrap-around direction (91 nodes on the airfoil section), 24 radial stations (18 stations on the blade surface) extending 20% radius beyond the rotor tip, and 12 nodes in the normal direction. The body-conforming C-type mesh extended 3.5 chords ahead of the blade's leading edge, 6.3 chords beyond the blade's trailing edge, and had a maximum extent of 7.5 chords above the blade surfaces at the downstream outflow boundary. The trailing edge flap with a chord length of 0.25 C, extended between the 0.784 and 0.967 nondimensional blade radial stations (i.e., flap span = 18.3 % of the rotor tip radius). The flap radial position along the blade was selected based on the experimental wind tunnel data of Refs. [50,51] for the baseline model OLS rotor blade (i.e., without the trailing edge flap). More precisely, the radial position was selected to maximize the impact of the motion of the flap on the dominant BVI appearing in the experimental data near certain blade radial and azimuthal positions. The details of the selection process are given in section 10.1 below.

The solution procedure outlined in section 9 was applied to study the effects of the unsteady motion of the trailing edge flap on the aerodynamics and acoustics of: a) a 1/7th scale two-bladed model OLS rotor [50,51] and, b) a generic four-bladed model rotor. The results of these studies are presented in sections 10.1. and 10.2. respectively.

10.1. AERODYNAMICS OF 3-D BLADE-VORTEX INTERACTIONS

To alleviate the aerodynamics, and hence the acoustics of self-generated BVI, our strategy was to systematically address the effects of the trailing edge flap motion on the overall blade-vortex separation distances and on the strength of the vortex wake. For two-dimensional flow, as has been demonstrated in section 3.2, the problem was straightforward since the vortex path was dictated by the local flow velocities satisfying the full potential equation. The vortex strength was kept constant since no attempts were made to model the viscous diffusion mechanisms. In three-dimensional flow, the vortex elements are not convected in time using the full potential solution but rather, are convected using Scully's free wake model [44] in the lifting-line CAMRAD/JA solution. This time-dependent convection is only emulated in the RFS2.BVI solver through the use of interpolated values of the vortex wake position from those values predicted using CAMRAD/JA at azimuthal increments of 10 degrees. As a result, to investigate the effects of the trailing edge flap motion on the rotor wake, it was first necessary to perform this simulation in CAMRAD/JA, obtain the vortex wake trajectories and strengths, and then use the RFS2.BVI code to predict the unsteady aerodynamics associated with the motion of the trailing edge flap.

10.1.1. Baseline problem (2-bladed rotor)

To gain confidence in the accuracy of the BVI prediction procedure, it was necessary to first validate the RFS2.BVI flow solver. This was accomplished here using the experimental wind tunnel data of Refs. [50,51] for the two-bladed model OLS rotor. The OLS rotor is a one-seventh scale model of a modified Bell AH-1 Cobra rotor. The model was tested in the DNW (Deutch-Netherlands wind tunnel) wind tunnel to simulate full scale flight conditions in which strong blade vortex interaction noise was recorded while simultaneously obtaining blade surface pressure data.

In an earlier study of self-generated BVI [52], the rotor trim code CAMRAD [53] was utilized to compute the vortex wake trajectories and the far-wake inflow effects. This information was then utilized in the RFS2.BVI full potential solver which in turn provided the blade surface pressure data for the acoustic analyses using the WOPWOP code. The predicted surface pressures and the acoustic results for three cases representative of low speed descent flight were then validated using the aerodynamic and acoustic test data of Refs. [50,51]. In this study, an upgraded version of the CAMRAD code, designated "CAMRAD/JA"

[40], is employed for all rotor trim calculations. The CAMRAD/JA code includes a new second-order lifting-line formulation for predicting the airloads and provides an option for a dual circulation peak wake model. The second-order lifting line option allows the use of a more physically realistic tip vortex core radius which, in this study, was fixed at 20 percent of the blade chord for both the inflow and wake distortion calculations. This core radius was also consistent with the vortex core radii used in our earlier [18,52] and present full potential computations using the RFS2.BVI code. Apart from these two additional features, the OLS rotor dynamic and aerodynamic representations are unchanged from those in the original CAMRAD model.

In the validation study, the lifting one-seventh scale AH1-OLS rectangular model rotor was allowed to interact with elements of its own generated wake. The experimental wind tunnel conditions simulated low speed descent flight at the rate of 300 ft/min with an advance ratio (Mu) of 0.1477, a tip Mach number (Mtip) of 0.666, and a tip path plane (TPP) angle of 1.5 degrees aft. In the tests, the rotor was trimmed to zero-out the first flapping harmonic with respect to the rotor shaft while setting the collective pitch to produce the required rotor thrust (C_t/σ = 0.077). Figure (29) depicts comparisons between the RFS2.BVI-predicted and the measured differential pressures, in KPa, at a point located near the blade's leading edge (x/C=0.03). Here, three blade-vortex encounters (resulting from the wake vortex elements labeled I, II, and III in Fig. (27)) were identified and modeled using the solution procedure described in section 9. As seen, the interactions are characterized by the rapid rise and drop of the leading edge pressures (or differential pressures) as the BVI wake elements pass by the blade's leading edge. Referring to Fig. (29), one can easily conclude that the second BVI, resulting from the encounter with the vortex designated II in Fig. (27) is the most dominant among the three interactions being modeled. This, of course, is due to the very strong and rapid temporal variations of the measured and predicted leading edge differential pressures near the 78 degrees azimuth. On the average, the CAMRAD/JA-predicted time-dependent trajectory for vortex II indicated that it was closer (in vertical height) to the blade during its entire forward sweep (0-180 degrees) as compared to the two vortices designated I and III.

Numerical studies addressing the effects of the number of vortex wake segments per interaction vortex element on the accuracy of the predicted pressures have indicated that more accurate results, specifically in the vicinity of the blade tip, are obtained with the use of as many as 7 segments. Figures (29-31) illustrate comparisons between the predicted and measured differential pressures at five blade radial stations when using 7, 5 (used in

the studies of Ref. [52]), and 4 segments per wake element respectively . Note that the use of 4 or 5 segments/vortex element result in good correlation with the experimental data at the 0.756 and 0.808 radial positions up to the 90 degrees azimuth. By comparison, the use of 7 vortex segments results in the overprediction of the pressures up to an azimuth of 60 degrees. However, the peak drop in the differential pressures near the 76 degrees azimuth is well predicted. Near the 0.868, 0.91 radial stations, it is clearly seen that the use of 7 vortex segments result in a better correlation with the experimental data up to the 90 degrees azimuth.

Very near the tip, i.e., at RBAR = 0.979, it is evident that good correlation with the data is only achieved through the use of 7 segments/wake element, Fig. (29). This level of accuracy is crucial in the accurate prediction of BVI noise. In Fig. (30), the strength of the second interaction near the 76 degrees azimuth is underpredicted, and the strength of the third interaction near the 90 degrees azimuth is severely underpredicted. On the other hand, in Fig. (31), the predicted results indicate that there is little, or no, evidence of any strong interactions. Based on these results, it was decided that all BVI simulations (with and without the presence of the trailing edge flap) were to be conducted using 7 vortex segments/vortex element.

10.1.2. Effects of the trailing edge flap (2-bladed rotor)

When computing the rotor trim conditions with the trailing edge flaps deployed, we have allowed for variations in the rotor tip path plane angles while constraining the rotor forces (i.e., lift, propulsive/drag, side forces). This strategy allowed us to maintain vehicle descent rates which are identical to that of the baseline rotor (i.e., 300 ft/min.) for all the trailing edge flap schedules considered.

Limited deployment of the trailing edge flap during blade-vortex encounters:

The severity of the interactions resulting from the close encounters between the rotor blade and its vortex-wake depend on several factors which include; the average local blade loading during the encounter, the strength of the vortex-wake elements (i.e., their circulation), the average blade-vortex separation distance, and the orientation of the vortex-wake element relative to the blade. To address the two core issues of altering either the vortex strength, or the blade-vortex separation distances, or both, two approaches were

54

considered. In the first approach, it was felt that in order to alter the separation distances one only need know where the dominant BVI occur on the rotor disk (i.e., radial position, rotor azimuth). Once located, the trailing edge flap can then be deployed in a narrow azimuthal region encompassing the BVI azimuth in question. The flap position, of course, must also encompass the radial position, or positions, of the dominant BVI. The specific flap motion schedule, or time-dependent motion, would then influence the aerodynamic characteristics of the blade and the overall blade-vortex separation distances. Unfortunately, as will be seen, the sole use of this approach, especially for small flap deflections, was ineffective. In the second approach, we targeted the strength of particular vortex elements which eventually resulted in the dominant BVI as the rotor traversed certain azimuth positions. Our aim here was to use the trailing edge flap as a device to reduce the strength (i.e., weaken) of those elements at the particular azimuthal positions where they were being generated. Again, though significant changes in the strengths of the vortex wake elements were obtained, small changes in the overall blade-vortex separation distances were noticed. It was then quite obvious that perhaps the best approach to the problem was one where the flap played a dual role of both altering the blade-vortex separation distances as well as the strength of the vortex wake elements. This requirement, to a large extent, dictated the general form of what was considered as being an "effective" trailing edge flap schedule. The reader is however cautioned from interpreting "effective" as being "optimum" since no effort was expended to optimize any of the trailing edge flap schedules.

For the two-bladed model OLS rotor we have demonstrated that the most dominant BVI is the one which occurs as the blade traverses the azimuthal range bounded by the 65 and 85 degrees azimuth positions, see Fig. (29). Note that this strong interaction persists at the five radial stations shown. To alleviate this interaction, or equivalently reduce the temporal differential pressure gradients, using a blade-mounted trailing edge flap, we assumed two flap schedules of the form given in Fig. (32). Here, the peak deflections were intentionally specified to occur at the 75 degrees rotor azimuth position. According to the figure, the flap is deployed when the rotor is 15 degrees ahead of the 75 degree azimuth and retracted back to the neutral position (i.e., undeflected position) when the rotor reaches the 90 degree azimuth. The total duration for the deployment of the flap is therefore equivalent to the time required by the rotor blade to traverse 30 degrees of azimuth.

Figure (33) depicts comparisons between the RFS2.BVI-predicted differential pressures at x/C = 0.03 (i.e., near the blade's leading edge) for five radial stations as a

function of rotor azimuth and the trailing edge flap schedules of Fig. (32). For contrast, the predicted results for the baseline model rotor (i.e., without the trailing edge flap) are also shown. Note that the flap schedules are being identified by the maximum (or minimum) deflection angle of the flap. It is noteworthy to mention that only the radial stations corresponding to RBAR = 0.808, 0.869, and 0.914 fall within the flapped section of the rotor. The first station at RBAR = 0.756 is physically located at a distance equal to 3% Rtip (or 0.275 C) from the inboard flap juncture. The last station at RBAR = 0.979 is located at a distance equal to 1% Rtip (or 0.092 C) from the outboard flap juncture. From Fig. (33) it is seen that the deployment of the trailing edge flap results in a small increase (for the +8 degrees schedule), or decrease (for the -8 degrees schedule), in the magnitude of the differential pressures. These pressure changes reflect the small variations in the far wake inflow angles and the blade-vortex separation distances which are associated with the trailing edge flap motion as predicted by the CAMRAD/JA trim code. It is also evident that no changes in the temporal gradients of the differential pressures have taken place as a consequence of the unsteady motion of the trailing edge flap. This is clearly demonstrated in Fig. (34) where the temporal gradients of the upper and lower surface pressure coefficients are plotted as a function of rotor azimuth. The plots represent the fluctuations in the surface pressures near the blade's leading edge (x/C = 0.03) at the 0.86 nondimensional radial station. In Fig. (35) we illustrate comparisons between the predicted differential pressures at the flap hinge point (x/C = 0.75) as a function of rotor azimuth using the trailing edge flap schedules of Fig. (32). Again, notice that the maximum variations are obtained between the 60 and 90 degrees azimuthal positions where the trailing edge flap is being deployed. The magnitude of these changes, by comparison to those occuring near the blade's leading edge, are slightly higher. That is, for the given trailing edge flap schedule, the disturbances which occur in the vicinity of the flap hinge point are slightly larger than those felt by points near the blade's leading edge.

Figures (36,37) illustrate respectively the predicted variations in the sectional lift and moment coefficients as a function of rotor azimuth and the trailing edge flap schedules of Fig. (32). In Fig. (36), it is interesting to note that for the +8 degrees flap schedule, the sectional lift decreases (relative to the baseline rotor values) prior to the 60 degrees azimuth and as the rotor approaches the 90 degrees azimuth. For this schedule, one also expects the sectional lift to increase between the 60 degree and 90 degree azimuthal positions by virtue of the flap-down type motion. This behavior of the predicted sectional lift forces is a manifestation of the CAMRAD/JA rotor trim calculation where the rotor thrust has been maintained at a constant value corresponding to that of the baseline rotor.

More precisely, to maintain the thrust at a constant level, it was necessary in the trim calculation to reduce the lift forces on some portions of the rotor disk in order to compensate for the increase in the lift forces at a different location of the rotor disk (i.e., between the 60 and 90 degrees azimuthal positions). This behavior is further explained by the reductions (from the baseline values) in the magnitudes of the partial inflow angles of attack, predicted by the CAMRAD/JA trim code and utilized by the RFS2.BVI flow solver, at azimuth positions less than 60 degrees and as the rotor approaches the the 90 degrees azimuth. It is to be noted that an opposite behavior to that just described is obtained when considering the -8 degrees flap schedule. Here, in order to maintain the flapped rotor thrust at the baseline thrust value, the CAMRAD/JA trim code had to compensate for the anticipated reduction in lift forces due to the flap-up type motion by increasing the lift forces just ahead of the 60 degrees azimuth and as the rotor approached the 90 degrees azimuth.

Larger flap deflections were then investigated (peak deflections of +/-10, +/-20 degrees) while fixing the duration of deployment at 30 degrees of rotor azimuthal travel. The flap schedules utilized in these predictions were obtained by simply multiplying the +8 degree flap schedule shown in Fig. (32) by factors of +/-1.25 or +/-2.5 to yield peak deflections of +/-10 and +/- 20 degrees respectively. Figure (38) illustrates the CAMRAD/JA-predicted lift distributions as a function of blade radial position and blade azimuth for the +10 and -10 trailing edge flap schedules. In Fig. (39) we illustrate the effects of the trailing edge flap on the strength, or equivalently the circulation, of the BVI tip vortex elements. The variation of vortex strength along each BVI line is represented here as a function of each element's point of generation azimuth. Elements generated near the 90-120 degrees azimuth will generally convect downstream to interact with the tip of the following blade. On the other hand, vortex elements which are generated at later azimuths will tend to interact with the more inboard stations along the advancing blade, see Fig. (40a).

Note that for the -20 degree flap schedule, noticeable reductions in the circulation are obtained for those elements lying in the tip region. Figure (40) illustrates planform (40a) and sideview plots (40b,c) of the tip vortex position relative to the advancing blade. Figures (40b,c) depict the view one would see when looking radially inward from the 90 degree azimuth position. The effects of flap amplitude (i.e., +/-8, +/-20 degrees) on the CAMRAD/JA-predicted blade-vortex separation distances for each of the three vortex lines of Fig. (40a) are shown in Figs. (40b) and (40c) respectively. In this figure, the blade is

represented by a solid horizontal line which extends between the 0 and the 0.4 x/R values. Moreover, no blade coning is shown here since the vertical wake positions are given with respect to the rotating coordinates fixed at the center of rotation and aligned with the blade. As seen, elements from vortex line III lie above the plane containing the blade while those of vortex Line II pass below the blade. For those elements near the blade tip on Line II, negative flap inputs tend to move the vortex away from the blade while the opposite is true for the positive flap deflections. Thus, negative flap deflections appear to be most effective in reducing the vortex strength, and to a lesser extent, in increasing the blade-vortex separation distances. Note that in the CAMRAD/JA results presented, the flap was not activated in the azimuth regions where the BVI wake elements were generated. Consequently, changes in their strength and trajectories, from those corresponding to the baseline problem, must have occured as a result of rotor trim adjustments. The reduced vortex strengths is confirmed here by the small changes in the lift distributions at the 120 degrees azimuth, see Fig. (38).

The influence of flap amplitude on the rotor tip path plane angle and power requirements are illustrated respectively in Figs. (41,42). As seen in Fig. (41), the flap effectively functions as a cyclic control input causing the rotor to be tilted forward as larger negative (i.e., flap up) flap deflection angles are used. However, in order to maintain the baseline rotor forces, the collective pitch was increased and, as expected, the increased drag resulting from the deployment of the flap and the higher blade pitch angles contributed to the noticeable increase in the power required by the rotor, Fig. (42). The irregularity seen in the power curve slope for deflections less than -10 degrees reflects the limit of the two-dimensional airfoil drag data used in CAMRAD/JA.

Figure (43) depicts comparisons between the RFS2.BVI-predicted chordwise surface pressure coefficients, as a function of rotor azimuth, for the baseline and flapped (+20 degrees flap schedule) model rotors. Note that the area enclosed by the C_p - x/C curves for the flapped rotor reflect a reduction in the sectional lift values at the 45, 60, 90, and 105 degrees azimuthal positions. This reduction, as explained earlier, is necessary to compensate for the noticed increase in the sectional lift value at the 75 degree azimuth. In Fig. (44) we illustrate similar comparisons for a trailing edge flap schedule where the flap was deflected to a maximum angle of -20 degrees. For this case, the flap schedule was simply obtained by multiplying the -8 degree flap schedule of Fig. (32) by a factor of 2.5. It should be noted that by simply multiplying any of the flap schedules of Fig. (32) by a constant, the amplitudes as well as the deflection rates are also changed. In order to

maintain a constant flap deflection rate when considering larger flap deflection angles (e.g., -20 degrees up), it is clear that the deployment of the flap must take place over a larger azimuthal interval (i.e., 75 degrees of azimuth vs 30 degrees of azimuth for the -8 degrees flap up schedule).

Numerical experiments were also conducted to investigate the effects of flap deployment rate, for a given maximum deflection angle, on the temporal differential pressure gradients near the blade's leading edge. Figure (45) depicts two impulsive trailing edge flap schedules used in these experiments. As seen, for both schedules, the flap was deployed at the 74 degree azimuth, reached a peak amplitude of +8 or -8 degrees at the 75 degree azimuth, and was then retracted to the neutral position at the 76 degree azimuth. In Fig. (46) we illustrate comparisons between the predicted differential pressures, in KPa, as a function of rotor azimuth and the trailing edge flap schedules of Fig. (45) at x/C = 0.03. The predicted results for the baseline rotor are also shown. As seen, aside from the small changes in the differential pressures, the trailing edge flap had little or no impact on the temporal pressure gradients. At the hinge point location, Fig. (47) illustrates the formation of a positive pressure spike for the -8 degree impulsive flap schedule and a negative pressure spike for the +8 degree impulsive flap schedule near the 75 degree azimuth position. The slight overshoot in the predicted pressures near the 76 degree azimuth are a consequence of the unsteady effects associated with the retraction of the flap back to the neutral position. In Figs. (48,49) we illustrate the variations in the predicted sectional lift and moment coefficients for the baseline rotor configuration and for the flapped rotor configurations utilizing the impulsive trailing edge flap schedules of Fig. (45). As seen, the flapped rotor results are again characterized by the spikes in the lift and moment distributions at the 75 degree azimuth. The rapid increase followed by the rapid decrease in the lift values reflect the movement of the flap from the neutral position to the position of maximum positive deflection (i.e., +8 degrees) and then back to the neutral position. Similar, but opposite variations in the sectional lift forces occur for the -8 degrees flap schedule. The results obtained with the use of the impulsive trailing edge flap schedules are not encouraging especially when our prime goal is to alleviate the aerodynamics associated with the blade-vortex encounters. Clearly, through the use of these schedules, we have introduced impulsive variations in the blade aerodynamic loads which will undoubtedly give rise to vibration and noise levels. The results depicted in Figs. (46-49) are therefore provided for illustrative purposes only.

Deployment of the flap to reduce the vortex strength and to increase the blade-vortex separation distances:

Trailing Edge Flap Schedules A, B, And C

Prompted by the favorable reductions in the tip vortex strength with the use of the -20 degrees flap schedule, we decided to extend the duration of flap deployment into the second quadrant of the rotor disk. For convenience, the -20 degrees flap schedule will be referred to as schedule A in the remainder of this report. By extending the duration of flap deployment, our goal was to further reduce the strength of the dominant BVI tip vortex (i.e., vortex II in Fig. (27)), at the azimuth position where it was being generated. Figure (50) illustrates a comparison between schedule A and two additional schedules designated B and C. For schedule B, the flap deployment duration has been extended to reflect the time required by the rotor to travel between the 40 and 140 degrees azimuthal positions (i.e., 100 degrees of azimuthal travel). In schedule C, we reduced the duration of flap deployment in the first quadrant while at the same time maintained the deployment duration for schedule B in the second quadrant. Schedule C therefore represents one of our attempts to primarily control the strength of the tip vortex elements while minimizing the attendant increases in the rotor power requirements (proportional to the maximum flap amplitude and the duration of flap deployment). For schedules A, B, and C, the peak deflections are equal to -20 degrees. These peaks occur at the 75 degrees, 75 degrees, and 100 degrees azimuthal positions respectively.

Figure (51) illustrates comparisons between the CAMRAD/JA-predicted blade bound circulation distributions as a function of rotor azimuth and radial position for the trailing edge flap schedules B and C. Also shown in the figure are the predicted values for the baseline OLS model rotor. For the baseline rotor, the rapid azimuthal variations in the magnitude of the bound circulation reflect the severity of the blade-vortex encounters. The strongest advancing blade BVI events generally occured between the 70 degree and the 120 degree azimuthal positions (this range shifts slightly with radial position along the blade). For the flapped rotor cases considered, the variations in the bound circulation reflect both the effects of the flap as well as the blade-vortex encounters. The predicted variations for schedules B and C indicate the effectiveness of the flap in reducing the bound circulation strength in the blade tip region for azimuth positions where the BVI tip vortex elements are generated (in the 90 to 130 degrees azimuth range). For schedule B, the severity of the BVI between the 70 and 120 degrees azimuthal positions have been reduced. Schedule C results,

however, reveal that a "new" and a quite strong interaction has been created near the 50 degrees azimuth position where no interactions have existed for the baseline rotor. The appearance of this interaction, as will be shown later, is attributed to the decrease in the average miss distance for vortex line I as compared to the average miss distance for the baseline rotor. For the baseline rotor, the rapid azimuthal variations in the magnitude of the bound circulation reflect the severity of the blade-vortex encounters (e.g., at RBAR = 0.805 in the range 80-100 degrees of azimuth and, at RBAR = 0.895 in the range 70-90 degrees of azimuth). The effectiveness of the trailing edge flap as a device to alleviate the severity of these interactions through reductions in the magnitude of the bound circulation and their azimuthal rates of variations, is clearly demonstrated with the use of the trailing edge flap schedules B and C. Minor problems do however arise, albeit minor ones. Note that the use of schedule C results in the creation of "new" impulsive variations in the bound circulation near the 55 and 65 azimuth positions at all stations outboard of the 0.805 radial station. These rapid variations, as will be shown, are attributed to the decrease (relative to the baseline values) in the vortex line I overall blade-vortex separation distances.

Wake geometry plots illustrating the horizontal and vertical positions of vortex lines I, II, III of Fig. (27) with respect to the blade are given in Fig. (52a-c) as a function of blade azimuth for the trailing edge flap schedules B and C. In the figures, the vortex spatial coordinates are expressed in units of blade chord length C. Radial distances (y/C) are measured from the center of rotation, streamwise (x/C) and vertical (z/C) distances are measured relative to the quarter chord line which represents the blade in the lifting-line solutions. Also shown in the figures are the variations in the strength of the tip vortex lines (i.e., their circulation) as a function of the spanwise position. Figure (51) indicates that schedule B does not lower the bound circulation in the tip area enough to effectively reduce the tip vortex strength at azimuth locations where the BVI elements are generated. Thus, schedule C was implemented giving the results depicted by the dot-dash lines. The BVI element strengths are now considerably reduced as indicated by the low bound circulation values extending well beyond 90-degrees azimuth at all tip radial stations. An examination of Fig. (52) reveals that the flap has a strong influence on the BVI wake geometry and trajectory (recall the two-dimensional full potential results of section 3.2) in the vicinity of the blade. Surprisingly, this applies equally to the inplane as well as to the transverse wake positions. Most notably, the upwash created by the negative tip lift causes the BVI elements to be drawn up into and above the blade in the tip area. Thus, the wake trajectories are not solely dependent on the tip path plane angle, but also on the variations in the bound vortex strength which indirectly alters the wake distortion pattern, particularly in the

"rollup" regions near the disk lateral edges. Figures (52a,b) indicate that with schedule C, vortex line I lies in the rotor plane causing approximately 20 percent of the blade tip to slice through the vortex core in the 50-60 degrees azimuth range. Since vortex line I is nearly parallel to the blade at this position, it results in a strong and highly impulsive BVI which is obviously more severe than that resulting from vortex line I for the baseline problem. The BVI element strength for schedule C is also seen to be equal to, or greater than, the baseline values for those elements that will interact with the tip. This is also true for schedule B. However, in this case, the vortex miss distance is large enough to reduce its overall induced influence.

The vortex trajectories resulting during the interaction between the blade and the vortex line II are depicted in Figs. (52c,d,f). For the baseline configuration, the blade tip passes above vortex II. When schedule B is applied, the flap upwash causes the vortex to locally rise above the tip, see Fig. (52c), apparently allowing the blade to slice through the vortex line somewhere between the 60 and 70 degrees azimuthal positions. The remainder of vortex line II lies below the rotor, Fig. (52f). For schedule C, the upwash has had a longer time to develop causing vortex line II to lie well above the blade tip. Here, elements that first pass the tip also have significantly lower circulation (Fig. (52c,d). However, as vortex line II sweeps more inboard with increasing azimuth, Fig. (52f), the interaction becomes stronger as the miss distance decreases and the blade bound circulation increases above the baseline levels. The blade will eventually intersect and slice through vortex line II at some point beyond the 80-degrees azimuth and inboard of the 0.80 radial position, Fig. (52f). Figures (52e,g,h) illustrate the blade in the vicinity of vortex line III (i.e., last vortex line traversed by the blade). As seen, the upwash created by the flap has not had sufficient time to greatly impact the vortex geometry before encountering the blade. By comparison, schedule B results in the smallest miss distances while schedule C exhibits the largest values. Note that with schedules B and C, the vortex strength is significantly lower than that for the baseline rotor. In fact, our analyses show vortex element circulations with opposite signs to that of the baseline rotor.

Figure (53) depicts the RFS2.BVI-predicted differential pressures, in KPa, near the leading edge of the blade (i.e., $x/C = 0.03$) as a function of blade azimuth, radial position, and the trailing edge flap schedules B and C. For schedule C, the figure clearly illustrates the formation of a more "dominant" BVI between the 30 and 60 degrees azimuthal positions. As explained earlier, this dominant BVI results from the enhancement, rather than the alleviation, of the first BVI resulting from vortex I. The results also indicate that schedule C

is quite effective in alleviating the second and third interactions resulting from the vortex lines II and III. At this juncture, it is important to mention that for schedules B and C, it is quite difficult at this stage to quantify the impact of the temporal leading edge pressure variations on the acoustics of the BVI. While the use of schedule C alleviated the second and third interactions, it enhanced the first interaction. Schedule B on the other hand results in more uniform variations (despite being small) in the temporal gradients for all radial stations. The acoustic results for schedules B and C are given in section 10.2.2 of this report.

In light of the results presented above for schedules B and C, it was felt that a more effective schedule would be one which encompasses both schedules A and B. Schedule BC, shown in Fig. (54), was obtained by considering a curve which envelopes schedules B and C. As seen, the total duration of flap deployment is equivalent to that required by the rotor to traverse 100 degrees of azimuth. Note that the deployment durations in the first and second quadrants are equal. In this respect, our primary goal was to equally influence the blade-vortex separation distances as well as the strength of the vortex wake. Note also that unlike any of the schedules previously discussed, schedule BC is characterized by an azimuthal range (35 degrees) where the flap is deployed and then held fixed for a certain duration. This feature of schedule BC, as will be shown later, proved to have a significant impact on the aerodynamics and acoustics of BVI.

Figure (55) illustrates comparisons between the RFS2.BVI-predicted differential pressures, in KPa, near the blade's leading edge (x/C = 0.03) as a function of blade azimuth, radial station, and the trailing edge flap schedules B and BC. The predicted results for the baseline OLS rotor are also shown. As seen, near the tip of the blade (RBAR = 0.914, 0.9798), schedule BC alleviates the temporal pressure gradients resulting from the interactions with vortex lines II and III. For the inboard stations at RBAR = 0.8081, 0.8687, schedule BC tends to enhance the interaction resulting from vortex line I. At RBAR = 0.7566, the use of schedule BC results in the strengthening of the interactions resulting from vortex lines II.and III.

Prompted by these results, and in particular the alleviation of all BVI in the blade tip region, we attempted an alternate schedule, designated BC1 (see Fig. (54)), which is a variant of schedule BC. Here, the total duration of flap deployment was held fixed while increasing the amplitude of the flap deflections and the deflection rates. For schedule BC1, the flap was deflected upwards with a maximum angle of 25 degrees while again maintaining

this angle over 35 degrees of rotor azimuthal travel. Figure (56) depicts comparisons between the RFS2.BVI-predicted differential pressures, in KPa, as a function of blade azimuth, radial position, and the flap schedules BC and BC1. As seen, the effect of schedule BC1 was to reduce the temporal pressure gradients associated with the interactions resulting from vortex lines I and II. However, the interaction resulting from vortex line III at RBAR = 0.8687 was further enhanced.

Having addressed the effects of flap amplitude and rates of deployment on the temporal differential pressure gradients, and searching for means to alleviate it, it was decided that perhaps one need extend the duration of flap deployment into the second quadrant of the rotor disk to further reduce the strength of the vortex wake. An alternative option would be one where we extend the duration of flap deployment into the first quadrant to affect the blade-vortex separation distances. Of course, a third and a more effective option would be one where the duration of flap deployment is extended in both the first and second quadrants, hence simultaneously affecting the blade-vortex separation distances and the strength of the vortex wake.

Trailing Edge Flap Schedules D And E:

The trailing edge flap schedules D and E are depicted in Fig. (57). As seen, schedule D is basically identical to schedule BC with the exception of extending, in azimuth, the duration of the constant flap deflection of -20 degrees by an additional 10 degrees. The distribution of the bound circulation in the blade tip area resulting from the use of schedule D is given in Fig. (58). The associated CAMRAD/JA-predicted BVI geometry and vortex-wake strengths are illustrated in Fig. (59a-h). A quick comparison between the results of Fig. (58) and those of Fig. (51) reveal that schedule D effectively eliminates the strong first quadrant BVI created through the use of schedule C. The extended duration of flap deployment into the second quadrant has resulted in lowering the circulation of the BVI elements generated closer to the front of the disk. Consequently, the BVI occuring at stations further inboard of the advancing blade tip will be less severe. An additional benefit of schedule D appears to be in the slightly reduced negative circulation (or lift) peak compared to that generally found with schedules B and C. For schedule D, the geometry of vortex line I, Figs. (59a,b), is significantly altered, hence reducing the blade tip area impacted by the presence of the vortex. Although vortex line I lies much closer to the tip (as compared to its predicted positions with the use of schedule B or for the baseline rotor), its strength has also been significantly lowered. The overall result is a weaker encounter which, as will be seen,

64

alleviates the baseline rotor BVI noise levels. The BVI geometries of the remaining two vortex lines II and III are similar to those found with schedule C. Generally, the blade-vortex separation distances resulting from the use of schedule D are slightly smaller, and the radial locations where the blade slices through the vortex lines occur further outboard on the blade than have been observed with the use of schedule C. For schedule D, the overriding factor affecting the degree of severity of the BVI interactions appears to be the low circulation strength of the BVI elements.

Figure (60) illustrates comparisons between the RFS2.BVI-predicted differential pressures, in KPa, near the blade's leading edge as a function of blade azimuth, radial station and the trailing edge flap schedules BC and D. As seen, the use of schedule D has completely alleviated the three interactions resulting from vortex lines I, II, and III in the tip region of the blade (i.e., at RBAR = 0.9141, 0.9798). For the inboard radial stations, significant changes in the temporal pressure gradients and reductions in the peak-to-peak values of the differential pressures for the three interactions were achieved.

As indicated earlier, there is a power penalty associated with the use of the trailing edge flap. This penalty depends on the flap amplitude and deployment duration. The expected increase in power is a result of the flap profile drag, the drag associated with the flap induced lift and to the increased nonuniformity in the spanwise lift distribution. Recall that in all the numerical simulations, a constant speed of descent equal to that of the baseline rotor was maintained. For schedule D, the power has increased by 57 percent (over that required by the baseline rotor in descent flight) while the tip path plane has been rotated forward by 1.7 degrees. Due to this large power penalty associated with schedule D, an attempt was made to determine if a reduction of the maximum flap deflection to -15 degrees, while maintaining the schedule D deployment duration, would be beneficial. For the modified schedule, performance predictions indicated a 24.1 percent penalty in power which is substantially lower than the 56.7 percent penalty for the original schedule D. Figures (61) illustrates the effect of the modified flap schedule on the radial circulation distributions. The CAMRAD/JA-predicted circulation distributions for the baseline rotor and for schedule D are also shown. Although the BVI element geometry is not shown, it is evident that by reducing the peak flap amplitude to -15 degrees, several BVI are encountered. These encounters seriously degrade the otherwise smooth lift distributions gains achieved by the original schedule D.

Although schedule D does not exhibit strong BVI characteristics, it was felt that further extension of the flap deployment duration into the second quadrant may alleviate the aerodynamics, and hence the acoustics associated with the blade-vortex encounters. Figure (62) depicts the CAMRAD/JA-predicted bound circulation distributions for schedule E, a second variant of schedule D. Schedule E was derived from schedule D by maintaining the -20 degree flap deflection angle through an additional 10 degrees of azimuth. As seen, the results show no significant deterioration in the smooth lift variations exhibited by schedule D. For schedule E, the power penalty is 57.7 percent which, surprisingly, is higher than the power penalty for schedule D by less than one percent. The RFS2.BVI-predicted differential pressures, as a function of blade azimuth, radial position, and the trailing edge flap schedule E are given in Fig. (63). For contrast, the predicted results for the baseline model rotor and for the trailing edge flap schedule D are also given. Figure (63) illustrates that the use of schedule E has completely alleviated the BVI resulting from the vortex lines I, II, and III at four radial stations namely, RBAR = 0.8081, 0.8687, 0.9141, and 0.9798. At RBAR = 0.7568, the interactions are by far much weaker than those for the baseline rotor.

The results of our study have shown that negative flap deflections are required to reduce the strength of the advancing blade BVI encounters. Consequently, the spanwise circulation distributions must reflect a positive inboard peak and a negative more outboard peak. These two peaks can be modeled in the CAMRAD/JA code through the selection of the "dual peak" circulation option. All previous results were performed using the single outboard peak model which identifies the negative peak. The single peak model will give the correct tip vortex sign and strength, but will not properly model the inboard sheet when a dual peak is present. The dual peak model corrects this shortcoming. The dual peak model was employed with schedule D to assess its impact on the predicted circulation distributions. Figure (64) depicts comparisons between the CAMRAD/JA-predicted bound circulation distributions using the single and dual peak circulation models. As seen, the dual peak results do not significantly differ from the single peak results in the regions where strong BVI are normally encountered.

The effectiveness of the trailing edge flap as a device to alleviate BVI is best illustrated with a plot of the temporal leading edge pressure gradients. In Fig. (65) comparisons are made between the predicted pressure gradients at x/C = 0.03 for the baseline rotor and for the flapped rotor utilizing schedule E. As seen, the deployment of the trailing edge flap has completely eliminated the impulsive pressure gradients which are indicative, to a large extent, of the associated impulsive BVI noise levels. Near the 90 degrees azimuth, note that

66

not only has the deployment of the flap reduced the pressure gradients, but it has also reversed the signs of the gradients.

10.1.3. Baseline problem (4-bladed rotor)

Thus far, all results presented delineated the effectiveness of the trailing edge flap as a device to alleviate the BVI associated with the two-bladed OLS model rotor. The available aerodynamics and acoustics wind tunnel data served us well in the process of validating our aerodynamic and acoustic predictive tools. Today however, driven by efficiency and noise considerations, rotorcraft manufacturers build multi-bladed rotor systems (three-, four-, five-bladed) which inherently add more tip vortex lines into the flow field, thus complicating the BVI analysis. The two-bladed model results may therefore not be entirely representative of the more practical multi-bladed rotor systems and their BVI problems. To address the similarities between the BVI problems of two-bladed and multi-bladed rotor systems and to assess the usefulness of the trailing edge flap in alleviating the aerodynamics and acoustics of BVI, a study was conducted using a generic four-bladed model rotor. The model, originally proposed for a proof-of-concept wind tunnel test, is fully-articulated, has a 13-foot diameter, a constant 6.5-inch chord, a solidity of 0.1061, and -9 degrees of linear twist. To maintain uniformity in the CAMRAD/JA analyses, the number of blade segments and the flap locations were identical to those used in the CAMRAD/JA OLS model. The airfoil constituting the rotor is the HH-10 (12% thick) which is representative of advanced airfoils in current use. The wake model parameters, with the exception of one, remained unchanged from those utilized in the OLS CAMRAD/JA model. Here, the tip vortex core radius was increased to 50 percent chord, rather than 20% chord, as recommended in the CAMRAD/JA manual for predicting the airloads of model scale rotors. The larger core radius was not utilized in the simulations for the OLS model rotor in order to compare the results of the present calculations to some of our earlier results which were based on a vortex core radius of 0.20 C. Descending flight BVI conditions were simulated at 0.15 advance ratio (hover tip speed = 700 fps, tip Mach number = 0.627) with a 2-degree aft tip path plane angle. A high gross weight configuration was chosen (C_t = 0.00823) to guarantee the existence of severe BVI conditions.

Figure (66) illustrates a planform view of the CAMRAD/JA-predicted tip vortex trajectories for the four-bladed model rotor. The figure indicates the possibility of nine blade-vortex encounters with the vortex lines labeled 1 through 9. In the CAMRAD/JA

calculations, we have considered all 9 vortex lines. For the BVI calculations, all vortex lines generated between the 90 and 160 degrees azimuthal positions were considered. For vortex lines 1 and 9, special treatment was necessary. More precisely, as a new tip vortex segment was added to vortex line 9 between the 90 and 160 degrees azimuthal positions, the oldest (in age) BVI wake segment along vortex line 1 was discarded. Its effect however was taken into account through the far-wake inflow angles of attack. This process, requiring a significant amount of bookkeeping, was necessary in order to maintain a constant number of BVI vortex wake segments during the CAMRAD/JA and RFS2.BVI calculations.

10.1.4. Effects of the trailing edge flap (4-bladed rotor)

Prompted by the success achieved with the use of the trailing edge flap schedule D on the two-bladed OLS model rotor, we attempted to use the same schedule for the four-bladed rotor configuration. Here, however, the schedule will be designated 4A to avoid any confusion which may result from the mix-up between the trailing edge flap schedules for the two- and for the four-bladed model rotors. Figures (67) illustrate the CAMRAD/JA-predicted distributions of blade bound circulation for the baseline rotor configuration (i.e., without the flap) and for the flapped rotor configuration utilizing the trailing edge flap schedule 4A. Due to the numerous blade-vortex encounters, the results indicate that as one interaction is being alleviated, other interactions are being enhanced. Recall that schedule D was quite effective in alleviating the BVI for the two-bladed OLS model rotor. Its use, however, for the four-bladed model rotor, by comparison, proved to be moderately effective. More careful tailoring of the flap schedule was therefore necessary. An alternate trailing edge flap schedule, designated 4B, was then utilized in our calculations, see Fig. (68). In schedule 4B, the duration of flap deployment was expanded in both the first and second quadrants of the rotor disk. The maximum deflection of-20 degrees was held fixed. The CAMRAD/JA-predicted bound circulation distributions for schedule 4B are also shown in Figs. (67). As seen, these distributions do not indicate a clear advantage over the use of schedule 4A. Nonetheless, some of the rapid circulation variations near the 120 degrees azimuth at RBAR = 0.865 and 0.895 have been alleviated with the use of schedule 4B.

Table 1 depicts the rotor trim conditions for the baseline rotor and for the flapped rotors utilizing schedules 4A and 4B. Note that although the maximum flap deflections are equal for this rotor and for the two-bladed OLS model rotor, trim and power changes for the four-bladed rotor seem to be less affected by the flap. The lower power levels associated

Table 1. Trim conditions for the baseline four-bladed rotor and for the flapped rotor configurations utilizing schedules 4A and 4B

Schedule	TPP (Degs.)	Delta HP (%)
baseline	-2.0	0.0
4A	-1.63	16.1
4B	-1.64	17.2

with the four-bladed rotor are attributed to the fact that the flap is deployed on one blade at a time (i.e., say through individual blade control) as the blade traverses through the predetermined azimuth range for flap deployment. Moreover, for the two-bladed rotor, the increase in drag due to flap deployment represents an increase by 50% for all the blades, whereas for the four-bladed rotor, the increase in drag represents 25% for all the blades.

Figure (69) depicts comparisons between the RFS2.BVI-predicted differential pressures, in KPa, as a function of blade azimuth and radial position for the trailing edge flap schedules of Fig. (68). The predicted results for the baseline rotor are also shown. The figure clearly indicates the effectiveness of schedule 4B in alleviating the dominant interactions, especially the one which takes place between the 60 and 90 degrees azimuthal positions. Since the temporal pressure gradients associated with the results for trailing edge flap schedule 4B are quite smaller than those associated with schedule 4A, it is expected that the overall noise levels be lower for schedule 4B as compared with those for schedule 4A. Note that schedule 4B results in the enhancement of an interaction (absent in the baseline BVI problem) which occurs between the 30 and 60 degrees azimuthal positions. This is exemplified in Fig. (70) which illustrates the variations of the temporal pressure gradients at $x/C = 0.03$ for the baseline and for the flapped rotor configurations. It is conjectured here that perhaps a segmented flap can alleviate this problem through trailing edge deflections that are not necessary constant along the span of the flap. As a result, smaller deflections can be used where possible enhancements of existing weak interactions are anticipated, and larger deflections can be used to alleviate the more dominant interactions.

10.2. ACOUSTICS OF 3-D BLADE-VORTEX INTERACTIONS

After thorough examination of the predicted noise data (in spectra form), it was decided to limit the effective BVI noise frequency range to only 600 Hz (8th sound harmonic) through 6000 Hz (80th sound harmonic). Thus eliminating from our integration procedure the predicted noise information below the 8th sound harmonic (600 HZ), which is normally dominated by the rotor steady loading noise and by the thickness noise for inplane observer locations. The predicted BVI noise sound pressure levels within the 600 Hz and 6000 Hz were integrated to produce a single number, designated BVISPL, which is a measure of the BVI noise intensity. The influence of the flap on the low frequencies of BVI noise were investigated by performing the spectral analysis of the acoustic waveforms for only those

70

observer positions which have been identified in the region(s) significantly affected by the deployment of the flap.

Figure (71) is a schematic illustrating the microphone array used in the BVI noise reduction studies. The array extended four rotor radii in the cross flow direction, seven and a half rotor radii in the streamwise direction and was located at a distance equal to one rotor radius below the rotor plane. These dimensions yield a large range of directivity angles between the observer (a total of 144 observer positions) and the BVI noise source. Since our primary objective was to predict the perturbations in BVI noise for the no flap and flapped rotor configurations, the normalization of the predicted BVI noise data to a reference propagation distance to avoid the spherical spreading at each observer location was not performed. This normalization is normally required to assure that the noise source is in both the acoustic and geometric far-field location. It is noteworthy to mention that there is no clear, or even commonly accepted, definition of the acoustic geometric far-field, particularly for a complex source such as rotor BVI noise. Typically, a distance of one wave length has been claimed for the acoustic far-field and a distance of three to four times the dimension of the source is assigned to geometrical far-field [54].

Contour plots of the predicted BVISPL values at the observer locations depicted in the Fig. (71) are presented for the baseline (OLS two-bladed model rotor, generic four-bladed model rotor) and for the flapped rotor configurations utilizing the various trailing edge flap schedules.

To better represent and understand the impact of the trailing edge flap on the BVI acoustic results, three contour plots for each case are given. The first plot represents the BVISPL noise contours for the baseline rotor. The second plot represents the BVISPL noise contours for the flapped rotor. In the third plot, we present the differences in the predicted BVISPL, in dB, resulting from subtracting the BVISPL for the baseline rotor from the corresponding values for the flapped rotor configuration.

10.2.1. OLS Two-Bladed Model Rotor

Figures (72a) and (72b) clearly show that not only has the maximum BVI noise lobe been reduced by 1 dB with application of the trailing edge flap schedule A (see Fig. (50)), but also its position has been altered noticeably from approximately the 0.6 radial position

to the rotor tip region on the advancing side. A better assessment of this schedule in reducing BVI noise can be made from the results presented in Fig. (72c). Apart from some isolated regions where the BVI noise values have been reduced by up to 3-4 dB, generally, the noise values remained unchanged or increased noticeably by up to 3-4 dB. Obviously, schedule A which was primarily implemented to affect the vortex miss distance, is only effective in altering the BVI noise radiation characteristics and its magnitude by an average of 0.5 dB.

In pursuit of further reductions in BVI noise levels, the duration of the flap deployment was extended to the second quadrant of the rotor plane, see schedule BC in Fig. (54). The corresponding predicted BVISPL noise values are shown in Fig. (73). As seen, with schedule BC, the maximum BVI noise lobe was reduced by 1.5 dB and its position was again displaced to the rotor tip region on the advancing side. In Fig. (73) we illustrate the influence of the trailing edge flap schedule BC on reducing the BVI noise levels. Note that, as compared to schedule A, noise reductions on the order of 6-7 dB were obtained in some regions while moderate increases in the BVI noise levels (1-2 dB) were obtained in small isolated areas.

In light of the results obtained for schedule B, it was apparent that further reductions in BVI noise are attainable with the extension of the trailing edge flap deployment duration into the second quadrant of the rotor disk (recall that this strategy targeted the strength of the tip vortex). To examine the effects of varying the vortex strength on the BVI noise radiation, schedule C of Fig. (50) was utilized. Here, the maximum flap deflection is being chosen to occur at the azimuthal angle at which the primary vortices are generated (based on the CAMRAD/JA analysis). A number of salient features which pertain to the maximum BVI lobe and its location are clearly illustrated in the Figs. (74a) and (74b). In comparison to the noise levels predicted for schedules A and B, we note that the general characteristics of the maximum BVI noise radiation remained virtually unchanged except for its lobe size which was reduced for schedule C, Fig. (74b). Furthermore, the BVI noise radiation values were slightly increased on the advancing side by 2 dB and were significantly reduced by 5-6 dB on the retreating side of the rotor. Contrary to general belief, our acoustic results show that the reduction in the vortex strength has more influence on reducing the BVI noise characteristics as compared to the influence of the vortex-wake average miss distance.

The acoustic results obtained for schedules A, B, and C of Fig. (50) provided us with additional insight to effectively reduce the BVI noise radiation. As discussed in section 10.1.2., by combining schedules B and C we arrived at schedule BC shown in Fig. (54).

Since schedules D and E of Fig. (57) are improved variants of schedule BC, we will only present the acoustics results for schedule E. Aerodynamically, we have demonstrated that schedule E, as compared to schedule D, yields lower temporal pressure gradients near the blade's leading edge., Fig. (63) As a result, it is expected that the noise levels associated with schedule E be lower than those associated with schedule D. Figure (75b) depicts the predicted noise results for schedule E. As seen, the impact of the trailing edge flap is profound. Here, we notice that the maximum BVI noise level has been reduced by 4 dB. It is also clear from Fig. (75c) that the noise levels have been reduced every where by average of 5 dB.

Figures (76) and (77) depict, respectively, the predicted waveforms for one blade passage (1/2 rotor revolution) for the baseline rotor and for the flapped rotor configuration utilizing the trailing edge flap schedule E. As expected, the noise signatures on the advancing side of the rotor were changed significantly. For certain observer positions (e.g., observer 52), the acoustic impulsive pulses were completely eliminated. For example, the PNLT (Perceive Noise Level) values for microphones 43, 52 in the boxed regions of Figs. (76,77) have been reduced by 4 PNdB. Since the PNLT metric is a measure of subjective annoyance, and its integrated values are directly related to the EPNL (Effective Perceived Noise Level), it is therefore expected that the rotor EPNL values will be reduced in a similar fashion to the PNLT values with the use of schedule E.

Figure (78) depicts the physical positions of microphones 43, 49, and 52 for which the spectral analyses were performed to determine the magnitude of the BVI noise reduction in SPL (Sound Pressure Level) metric as function of frequency. The corresponding spectra for these microphones are presented in Figs. (79-81) for 80 sound harmonics (75 Hz to 6000 Hz). As shown in these figures, the SPL values associated with the trailing edge flap schedule E are substantially lower than those for the baseline rotor with the exception of the 1st few harmonics (1-5 sound harmonics). It is noteworthy to mention that similar increases in the SPL values (up to 10 dB) within the low frequency range were observed with the use of Higher Harmonic Control (HHC) for BVI noise reduction.

10.2.2. Generic Four-Bladed Model Rotor

Figure (82) depicts the carpet plots of the BVISPL noise values predicted for the baseline and flapped rotor configuration utilizing the trailing edge flap schedule 4B of Fig.

(68). Also shown is the carpet plot for the 'Delta' SPLBVI {i.e., SPLBVI(with flap) - SPLBVI(no flap)}. Here, the extension of the carpet plot information has been limited to only 2.5 radii in the streamwise direction while preserving the extent of the crossflow to four rotor radii. As shown in Fig. (82a), two distinct maximum BVI noise lobes have been predicted for the baseline configuration with both lobes being on the advancing side of the rotor. This unique feature is typical for a four-bladed rotor in descent flight conditions. In addition, Fig. (82b) depicts a reduction of 2 to 3 db in the maximum BVI noise lobe with similar effects everywhere else in the BVI noise domain. Figure (82c), depicts a noticeable reduction in BVI noise levels, up to 9 dB, on the retreating side of the rotor. Carpet plots of the acoustic time histories for one blade passage (1/4 rev.) of the rotor are shown respectively in Figs. (83) and (84) for the baseline rotor and for the flapped rotor configuration utilizing the trailing edge flap schedule 4B. As seen, with the application of schedule 4B, the impulsive BVI characteristics of the acoustic waveforms depicted for the baseline rotor have been altered to a non-impulsive signature. Also, the PNLT values boxed in Fig. (84) reflect average BVI noise reductions on the order of 5 dB.

For completeness, selected observer locations for which the spectral analyses have been performed are schematically depicted in Fig. (85). The corresponding spectra associated with observers 17 and 52 are shown in Figs. (86) and (87) respectively. Note that with the application of schedule 4B, the SPL values were reduced for all the frequencies considered in the analyses (i.e., in the range 75 Hz - 6000 Hz). Moreover, there is no evidence of any significant increases in the SPL values within the low frequency range of the spectra (i.e., below 600 Hz).

11. SUMMARY 3-D AERODYNAMIC AND ACOUSTIC RESULTS

Table 2 summarizes the aerodynamic performance and acoustics results for all viable trailing edge flap schedules considered in this study. Shown in the table are the results obtained for the two-bladed model OLS rotor and those for a proposed generic four-bladed model rotor. Note that a fine balance must be maintained between the rotor power requirements and the dB noise reduction associated with a given schedule. The ramifications of the trailing edge flap on the overall performance of the rotor must be equally considered unless a higher priority is given to the acoustic characteristics of the rotor. The reader is reminded that increased power requirements are dictated solely by the trailing edge flap schedule and in particular the maximum deflection angle and the duration for which the flap

Table 2. Summary of the three-dimensional aerodynamics and acoustics results

Number of Blades	Schedule Designation	Max. Deflec-tion (Degs.)	TPP* (degrees)	Delta HP** (%)	Avg. BVI*** (Delta dB)
	Baseline	0	-1.5	0	0
	1	-10	-1.39	4	-
Two-bladed (OLS)	2	8	-1.55	0.7	0.5
	A	-20	-1.22	9.7	0.5
	BC	-20	-0.77	21.8	3
	C	-20	-1.05	17.4	1
	D	-20	0.2	56.7	3.4
	E	-20	0.12	57.7	5
Four-bladed (generic)	Baseline	0	-2	0	0
	4B	-20	-1.64	17.2	4.8

* TPP angles for all schedules provide same rate of descent as the baseline rotor

** Delta HP = [HP(flapped) - HP(baseline)]/HP(baseline)

*** Avg. BVI = Sum [SPLBVI(baseline)-SPLBVI(flapped)]/Number of microphones

is held fixed at this angle. It is conjectured here that reductions in the additional rotor power requirements can be obtained by considering flap schedules with smaller maximum deflections of a larger flap (i.e., with a 0.3 C flap chord rather than a 0.25 C flap chord). A spanwise segmented flap may also be equally effective since different segments of the flap can be deployed following different schedules to accommodate the anticipated blade-vortex encounters. The results summarized in table (3) dictate the need for the optimization of the trailing edge flap schedules for minimum power penalties and maximum BVI noise reductions.

Table 3 depicts the computer CPU time requirements for CAMRAD/JA, RFS2.BVI and the WOPWOP programs. Note that the CPU time requirements for RFS2.BVI also include the CPU time required to obtain the initial quasi-steady solution necessary for the unsteady calculations.

Table 3. Summary computer CPU time requirements

Code	Computer	CPU (2 blades)	CPU (4 blades)
CAMRAD/JA	VAX 3100	1500 secs	2400 secs
RFS2.BVI	CRAY2	420 secs	1335 secs
WOPWOP	CRAY2	3.6 hrs	7.2 hrs

12. CONCLUDING REMARKS

Numerical procedures, based on the unsteady two-dimensional full potential equation, the unsteady two-dimensional full Reynolds-averaged Navier-Stokes equations, and the unsteady three-dimensional full potential equation, have been developed for simulating the effects of leading (2-D full potential only) and trailing edge flaps on the aerodynamics of airfoil/blade-vortex interactions. The full potential-based procedures utilized the velocity "transpiration" approach for simulating vortex-induced effects as well as the local surface-induced effects which result from the unsteady motions of the control surfaces. For subcritical onset flows, our 2-D full potential results indicate that only trailing edge flaps need be used to significantly alter the aerodynamics of the baseline airfoil-vortex interactions. For supercritical onset flows, our results suggest the need for a leading edge flap to alter the flow in the vicinity of the airfoil's leading edge. Under these conditions, the trailing edge flap is rendered ineffective due to the presence of upper and lower surface regions of supercritical flow which tend to obstruct the upstream propagation of disturbances created near the airfoil's trailing edge. We have also demonstrated that care must be taken in the synchronization of the unsteady leading and trailing flap motions if the primary objective is the alleviation of the near impulsive load variations typical of airfoil-vortex interactions. The necessity of a Navier-Stokes-based formulation to accurately model the head-on collision between the vortex and the airfoil and provide insight into the unsteady drag variations during the encounter have been demonstrated.

The following conclusions are made based on the aerodynamic and the acoustic results of the three-dimensional study:

1. The trailing edge flap is an effective device which influences the trajectories of the tip vortex, the strength of the tip vortex, and the BVI noise levels.

2. Negative flap deflections appear to be most effective in reducing the vortex strength, and to a lesser extent, in increasing the blade-vortex separation distances.

3. Due to the numerous blade-vortex encounters on the advancing portion of the rotor disk, our results have indicated that as one interaction is being alleviated, other interactions are being enhanced.

C-2

4. The deployment of the trailing edge flap significantly changes the BVI noise signature and directivity.

5. We have demonstrated that average noise reductions on the order of 5 dB can be achieved with moderate power penalties which are on the order of 58% for a two-bladed rotor and 18% for a four-bladed rotor.

6. Contrary to general belief, our acoustic results show that the reduction in the vortex strength has more influence on reducing the BVI noise characteristics as compared to the influence of the vortex-wake average miss distance.

7. Further work need to be carried out to optimize the trailing edge flap schedule and flap parameters (i.e., flap chord, flap span) for maximum BVI noise reduction.

8. Blade-vortex interactions which occur on the retreating side of the rotor disk must be explicitly simulated (i.e., in a manner similar to that adopted for modeling the advancing blade interactions) to accurately represent their influence on the overall BVI noise levels and directivity.

9. The computer CPU time and memory requirements for our solution approach are minimal and, as such, provide the opportunity for a myriad of numerical experiments which can provide more insight into what constitutes an optimum trailing edge flap schedule.

13. REFERENCES

1. Kalkhoran, I., Wilson, D., and Seath, D., "An Experimental Investigation of the Parallel Vortex-Airfoil Interaction at Transonic Speeds,"AIAA Paper 89-1833, June 1989.

2. Seath, D. D., and Wilson, D. R., "Vortex-Airfoil Interaction Tests," AIAA Paper 86-0354, January 1986.

3. Seath, D. D., Kim, J. M., and Wilson, D. R., "An Investigation of the Parallel Blade-Vortex Interaction in a Low Speed Wind Tunnel," AIAA Journal of Aircraft, Vol. 26, No. 4, pp. 328-333, April 1989.

4. Poling, D. R., Wilder, M. C., and Telionis, D. P., "Two-Dimensional Interaction of Vortices with a Blade," AIAA Paper 88-0044, January 1988.

5. Jones, H. E., and Caradonna, F. X., "Full Potential Modeling of Blade-Vortex Interactions," Vertica, Vol. 12, No. 1/2, pp. 129-145, 1988.

6. Srinivasan, G. R., McCroskey, W. R., and Baeder, J. D., "Aerodynamics of Two-Dimensional Blade-Vortex Interactions," AIAA Journal, Vol. 24, No. 10, October 1986.

7. George, A. R., and Chang, S. B., "Flow Field and Acoustics of Two-Dimensional Transonic Blade-Vortex Interactions," AIAA Paper 84-2309, 1984.

8. Wu, J. C., Hsu, T. M., Tang, W., and Sankar, L. N., "Viscous Flow Results for the Vortex-Airfoil Interaction Problem," AIAA Paper 85-4053, October 1985.

9. George, A. R., and Lyrintzis, A. S., "Mid-Field and Far-Field Calculations of Blade-Vortex Interactions," AIAA Paper 86-1854, 1986.

10. Caradonna, F. X., Laub, G. H., and Tung, C., "An experimental Investigation of the parallel Blade-Vortex Interaction," Presented at the Tenth European Rotorcraft Forum, The Hague, Netherlands, August 28-31, 1984.

11. Kokkalis, A., and Galbraith, R. A. McD., "Results From The Glasgow University Blade-Vortex Interaction (B.V.I.) Facility," Presented at the Thirteenth European Rotorcraft Forum, Arles, France, September 8-11, 1987.

12. Caradonna, F. X., Lautenschlager, J. L., and Silva, M. J., "An Experimental Study of Rotor-Vortex Interactions," AIAA Paper No. 88-0045, 1988.

13. Wagner, W. J., "Comparative Measurements of the Unsteady Pressures and the Tip Vortex Parameters on Four Oscillating Wing Tip Models," Presented at the Tenth European Rotorcraft Forum, Paper No. 9, The Hague, The Netherlands, August 1984.

14. Desopper, A., Lafon, P., and Prieur, P. J., "Effect of An Anhedral Sweptback Tip on the Performance of a Helicopter Rotor," Presented at the Thirteenth European Rotorcraft Forum, Paper No. 2.4, Arles, France, September 1987.

15. Muller, R. H. G., "The Influence of Winglets On Rotor Aerodynamics," Presented at the Twelfth European Rotorcraft Forum, Paper No. 34, Garmisch-Parten Kirchen, Fedral Republic of Germany, September 1986.

16. Muller, R. H. G., "Winglets on Rotor Blades in Forward Flight - A Theoretical and Experimental Investigation," Presented at the Fourteenth European Rotorcraft Forum, Paper No. 10, Milano, Italy, September 1988.

17. Sankar, L. N., and Malone, J. B., "Unsteady Transonic Full Potential Solutions for Airfoils Encountering Vortices and Gusts," AIAA Paper 85-1710, 1985.

18. Hassan, A. A., and Charles, B. D., "Simulation of Realistic Rotor Blade-Vortex Interactions Using a Finite-Difference Technique," AIAA Paper 89-1847, June 1989.

19. Bharadvaj, B. K., "Computation of Steady and Unsteady Control Surface Loads in Transonic Flow," Presented at the AIAA 31st Structures, Structural Dynamics and Materials Conference, Long Beach, California, 1990.

20. Sankar, L. N., and Tang, W., "Numerical Solutions of Unsteady Viscous Flow Past Rotor Sections," AIAA Paper No. 85-0129, 1985.

21. Farassat, F., and Succi, G. P., "A Review of Noise Prediction Technology with Emphasis on Two Current Methods for Time Domain Calculations," Journal of Sound and Vibration, Vol. 71, No. 3, August 1980.

22. Kober, H., "Dictionary of Conformal Representations," Dover Publications Inc., 1957.

23. Beam, R. M., and Warming, R. F., "An Implicit Factored Scheme for the Compressible Navier-Stokes Equations," AIAA Journal, Vol. 16, No. 4, April 1976.

24. Hassan, A. A., Tung, C., and Sankar, L. N., "Euler Solutions For Self-Generated Rotor Blade-Vortex Interactions," AIAA paper 90-1588, 1990.

25. Lamb, H. : Hydrodynamics. Sixth Edition, Dover publications, New York, 1932.

26. Srinivasan, G. R., "Computations of Two-Dimensional Airfoil-Vortex Interactions," NASA CR-3885, May 1985.

27. Tijedman, H., "Investigations Of The Transonic Flow Around Oscillating Airfoils," NLR TR 77090U, NLR, The Netherlands, 1977.

28. Siddon, T. E, "Surface Dipole Strength by Cross-Correlation Method," Journal of the Acoustic Society of America, Vol. 53, No. 2, pp. 619-633, February 1973.

29. Ahmadi, A. R., "An Experimental Investigation of the Chopping of Helicopter Main Rotor Tip Vortices by the Tail Rotor. NASA CR-177338, 1984.

30. Jameson, A., "Iterative Solutions of Transonic Flow Over Airfoils and Wings Including Flows at Mach 1," Comm. Pure Appl. Math., Vol. 27, pp 283-309, 1974.

31. Wu, J-C, "A Study of Unsteady Turbulent Flow Past Airfoils," Ph. D. Dissertation, Georgia Institute of Technology, Atlanta, Georgia, August 1988.

32. Baldwin, B. S. and Lomax, H. "Thin Layer Approximation and Algebraic Model for Separated Turbulent Flows," AIAA Paper No. 78-257, 1978.

33. Pulliam, T. H. and Steger, J. L. "Recent Improvements in Efficiency, Accuracy, and Convergence for Implicit Approximate Factorization Algorithms," AIAA Paper No. 85-0360, January 1985.

34. Jameson, A., Schmidt, W. and Turkel, E. "Numerical Solutions of the Euler Equations by Finite-Volume Methods Using Runge-Kutta Time-Stepping Schemes," AIAA Paper No. 81-1259, 1981.

35. Hedstrom, G. W. "Nonreflecting Boundary Conditions for Nonlinear Hyperbolic Systems," Journal of Computational Physics, Vol. 30, pp. 222-237, 1979.

36. Tang, W., "Numerical Solutions of Unsteady Flow Past Rotor Sections," Ph. D. Dissertation, Georgia Institute of Technology, Atlanta, Georgia, September 1986.

37. Cebeci, T., and Smith, A.M.O. : Analysis of Turbulent Boundary Layers. Academic Press, 1974.

38. Schlichting, H., "Boundary Layer Theory," McGraw-Hill Book Company, New York, 1955.

39. Sankar, L. N., and Prichard, D., "Solution of Transonic Flow Past Rotor Blades Using the Conservative Full Potential Equation," AIAA Paper No. 85-5012, 1985.

40. Johnson, W., "A Comprehensive Analytical Model Of Rotorcraft Aerodynamics and Dynamics," Volume I: Theory Manual, Volume II: User's Manual, Johnson Aeronautics, Palo Alto, California 1988.

41. Hafez, M., and Lovell, D., "Entropy and Vorticity Corrections for Transonic flows," AIAA Paper No. 83-1926, 1983.

42. Stone, H. L., "Iterative Solution of Implicit Approximations of Multidimensional Partial Differential Equations," SIAM J. of Numerical Analysis, Vol. 5, No. 3, September 1968.

43. Sankar, L. N., Malone, J. B., and Tassa, Y., "An Implicit Conservative Algorithm for Steady and Unsteady Potential Flows," Proceedings of the AIAA 5th Computational Fluid Dynamics Conference, 1981.

44. Scully, M. P., "A Method of Computing Helicopter Vortex Wake Distortion," Massachusetts Institute of Technology, Aeroelastic and Structures Research Laboratory report ASRL TR-138-1, June 1967.

45. Lemnios, A. Z., and Smith, A. F., "An Analytical Evaluation of the Controllable Twist Rotor Performance and Dynamic Behavior," USAAMRDL TR 72-16, May 1972.

46. Lemnios, A.Z., and Howes, H. E., "Wind Tunnel Investigation of the Controllable Twist Rotor Performance and Dynamic Behavior," USAAMRDL TR 77-10, June 1977.

47. Ffowcs Williams, J. E., and Hawkings, D. L., "Sound Generated by Turbulence and Surfaces in Arbitrary Motion," Philos. Trans. Roy. London, Ser. A, vol. 264, no. 1151, May 8, 1969, pp. 321-342.

48. Brentner. K. S., "Prediction of Helicopter Rotor Discrete Frequency Noise," – A Computer Program Incorporating Realistic Blade Motions and Advanced Acoustic Formulation. NASA TM-87721, October 1986.

49. Visintainer, J. A., Burley, C. L., Marcolini, M. A., and Liu, S. R., "Acoustic Predictions Using Measured Pressures From A Model Rotor in the DNW," presented at the 47th Annual Forum of the American Helicopter Society, Phoenix, Arizona, May 1991.

50. Boxwell, D. A., Schmitz, F. H., Splettstoesser, W. R., and Schultz, K. J., "Model Helicopter Rotor High-Speed Impulsive Noise: Measured Acoustics and Blade Pressures," Presented at the Nineth European Rotorcraft Forum, Stresa, Italy, September 1983.

51. Schmitz, F. H., Boxwell, D. A., Splettstoesser, W. R., and Schultz, K. J., "Model Rotor High-Speed Impulsive Noise: Full-Scale Comparisons and Parametric Variations," Vertica, Vol. 8, No. 4, 1984.

52. Hassan, A. A., Tadghighi, H., and Charles, B. D., "Aerodynamics and Acoustics of Three-Dimensional Blade-Vortex Interactions," NASA CR-182026, July 1990.

53. Johnson, W., "A Comprehensive Analytical Model of Rotorcraft Aerodynamics and Dynamics. Part 1, Analysis and Development," NASA TM-81182, AVRADCOM TR-80-A-7 June 1980.

54. Paternson, A. R. M., "Handbook of Noise Measurement," Nineth Edition, GenRad Inc., 1980.
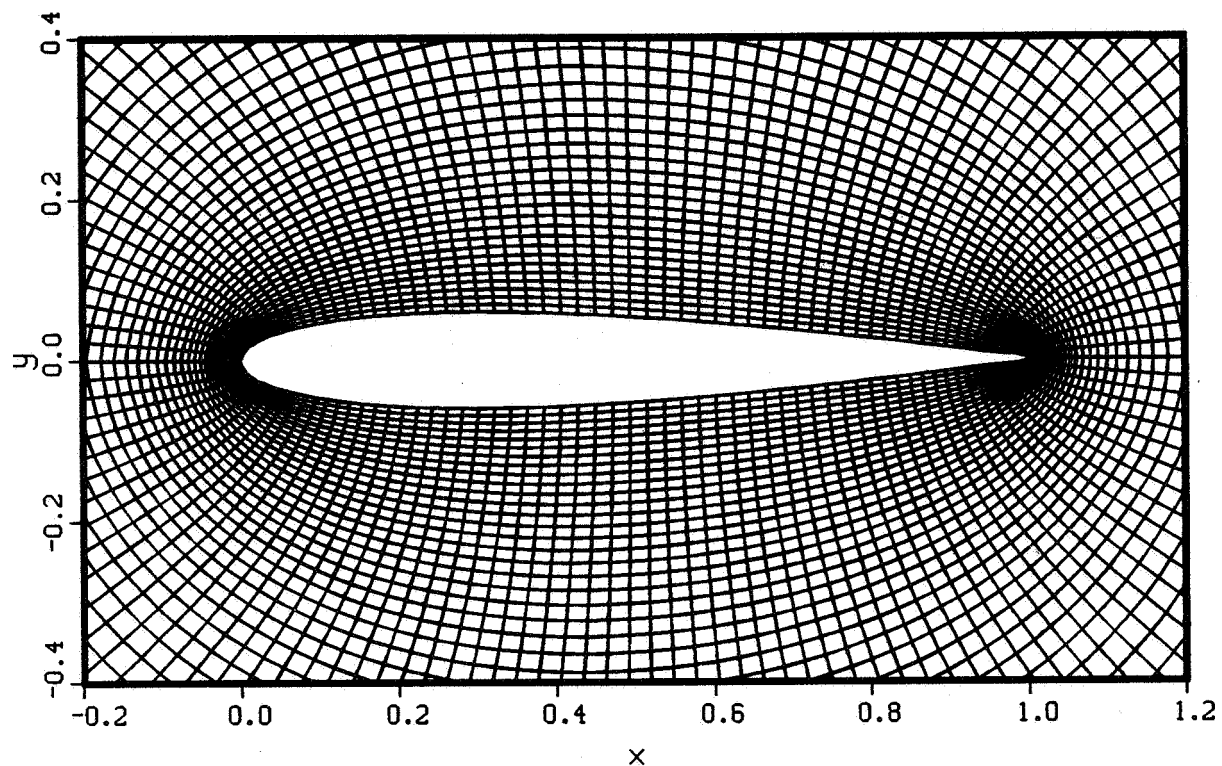
Fig. (1) Close-up view of the algebraically-generated computational O-type grid for the NACA 0012 airfoil (grid resolution : 141x51)
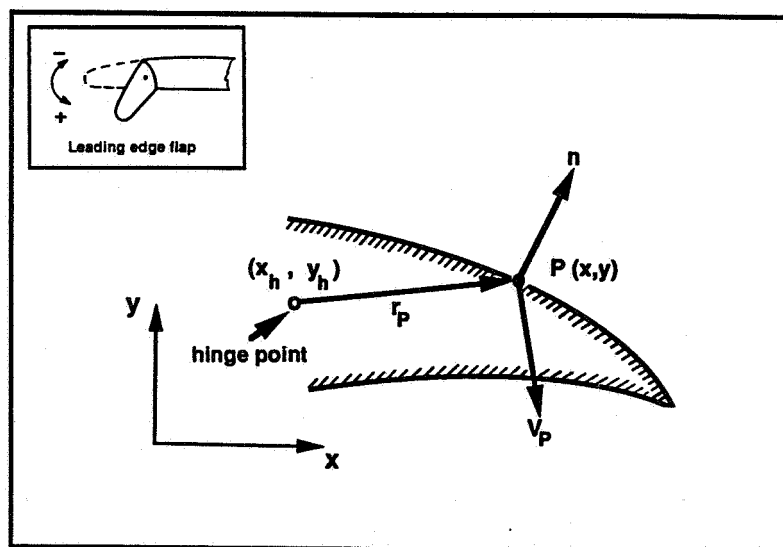
Fig. (2) Sketch illustrating the surface-induced velocities due to the unsteady motion of the trailing edge flap
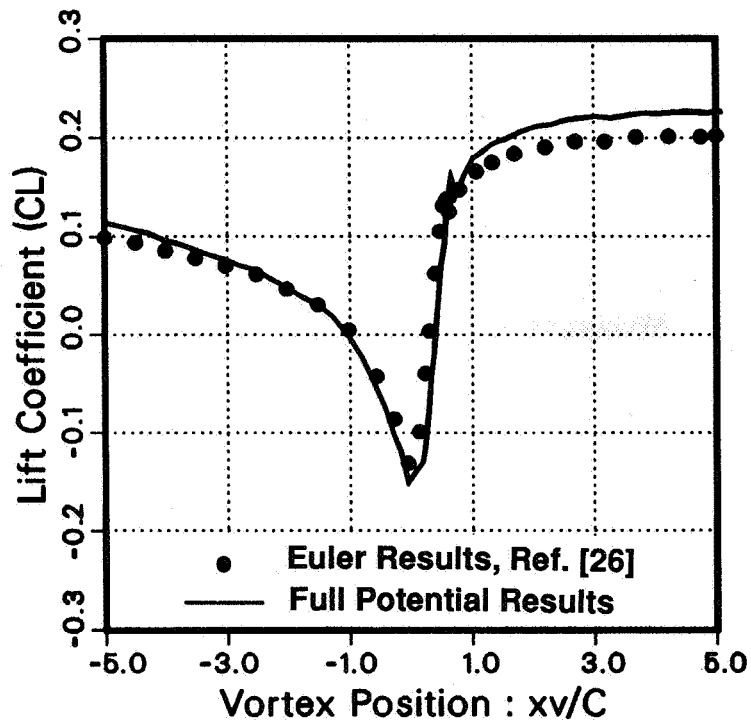
Fig. (3)   Predicted lift variations for the baseline airfoil-vortex interaction problem of Ref. [26] (Airfoil position: 0 < xv < 1, Minf = 0.8, Alpha = 0.5 degrees, rv/C = 0.05, Γ = 0.2 clockwise)
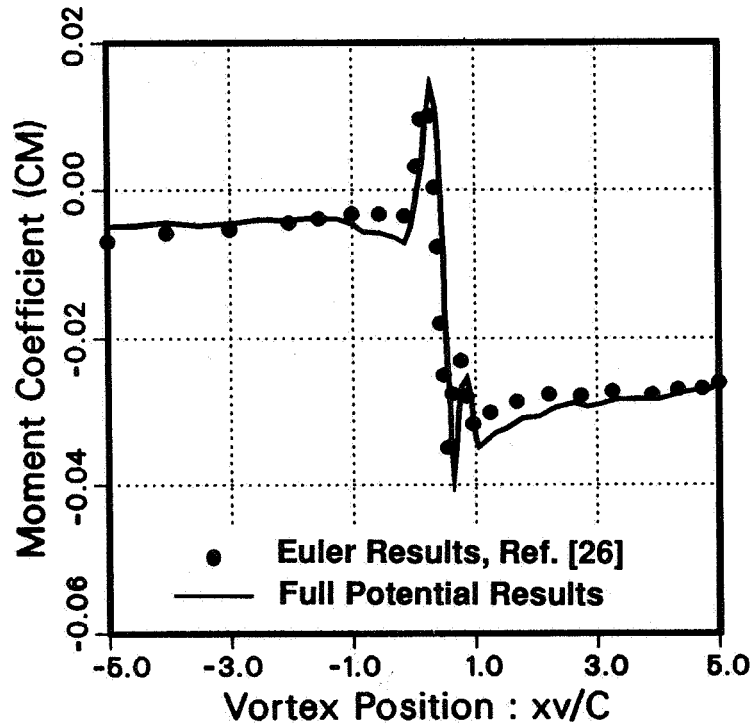
Fig. (4)   Predicted moment variations for the baseline airfoil-vortex interaction problem of Ref. [26] (Airfoil position: 0 < xv < 1, Minf = 0.8, Alpha = 0.5 degrees, rv/C = 0.05, Γ = 0.2 clockwise)
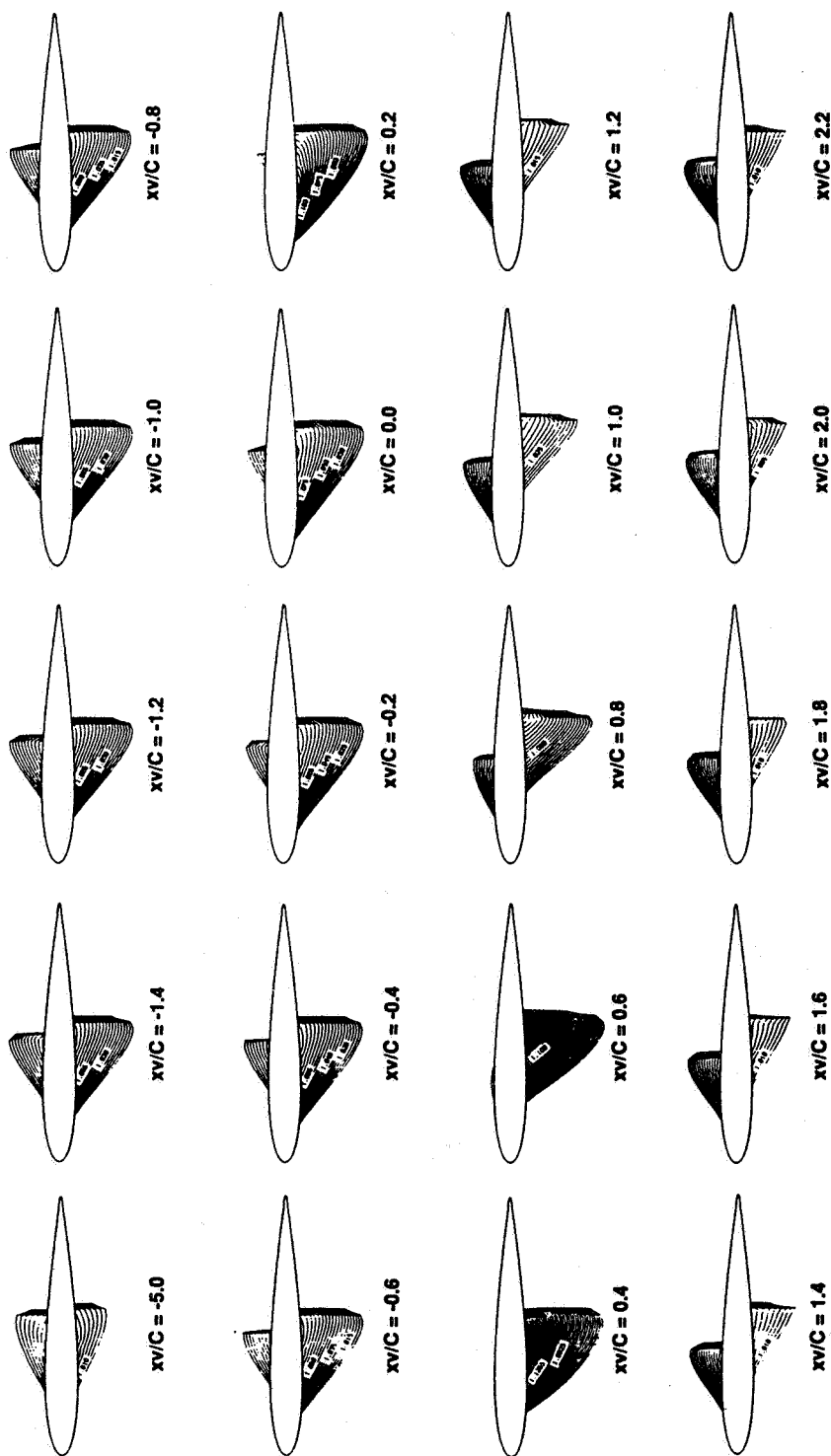
Fig. (5) Predicted supersonic flow regions on a NACA 0012 airfoil as a function of vortex position. The outer Mach contour represents the locus of the predicted sonic points (Minf = 0.8, Alpha = 0 degrees, r_v/C = 0.05, Γ = 0.2 clockwise, x_o/C = -6, y_o/C = -0.26)
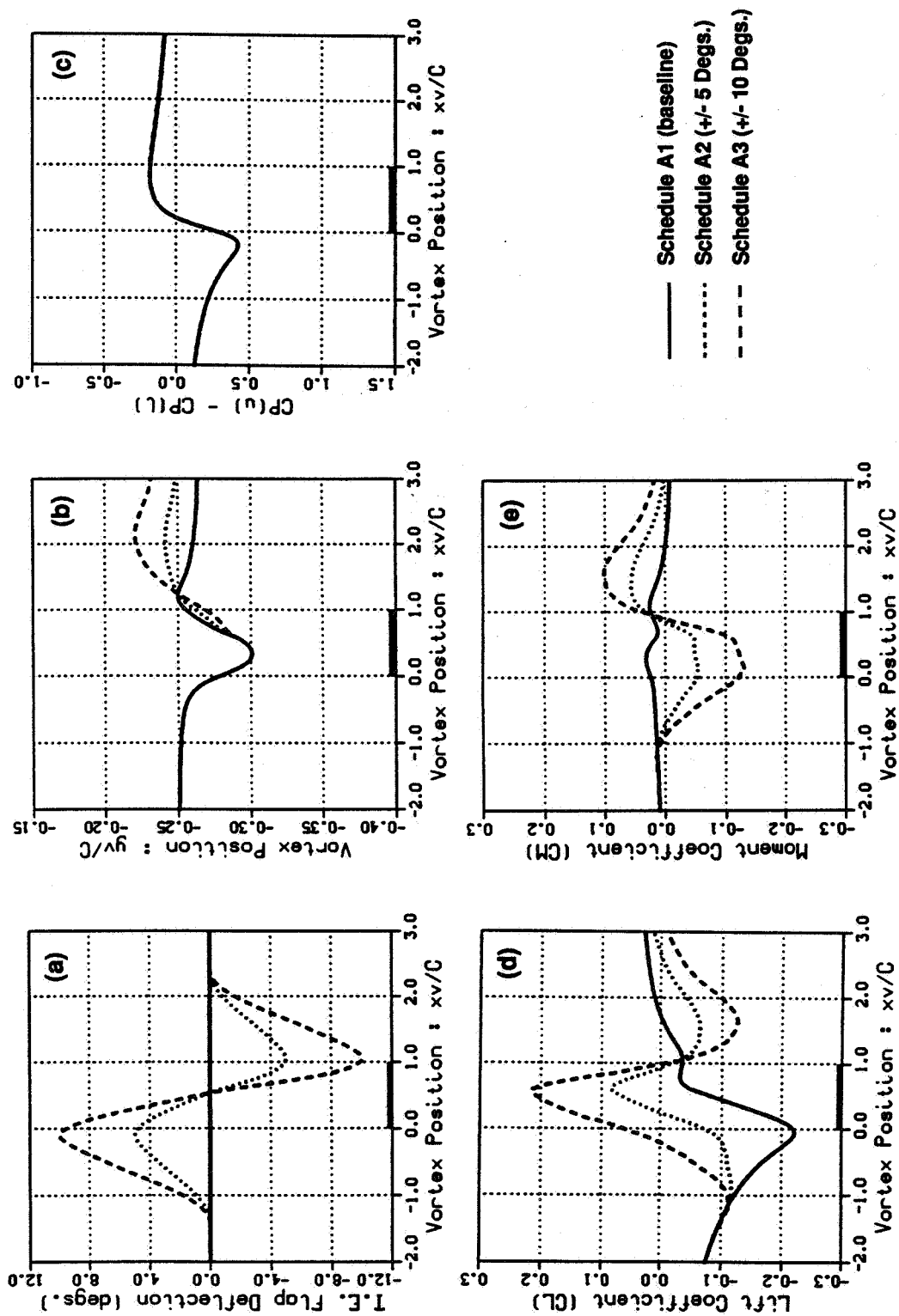
Fig. (6) Effect of various trailing edge flap schedules on the aerodynamic characteristics of the NACA 0012 airfoil during airfoil-vortex interactions (Minf = 0.8, Alpha = 0 degrees, rv/C = 0.05, Γ = 0.2 clockwise, xo/C = -10, yo/C = -0.25)

$$R_1 = 0.037 \ C$$
$$R_2 = 0.072 \ C$$
$$R_3 = 0.124 \ C$$
$$R_4 = 0.203 \ C$$
$$R_5 = 0.329 \ C$$
$$R_6 = 0.612 \ C$$
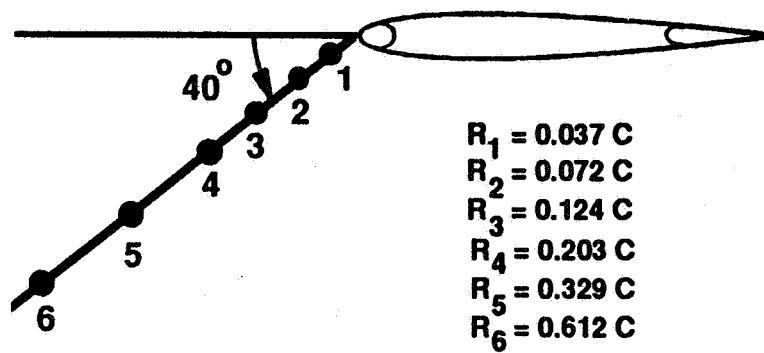
Fig. (7)   Sketch illustrating the selected six observer positions relative to the NACA 0012 airfoil
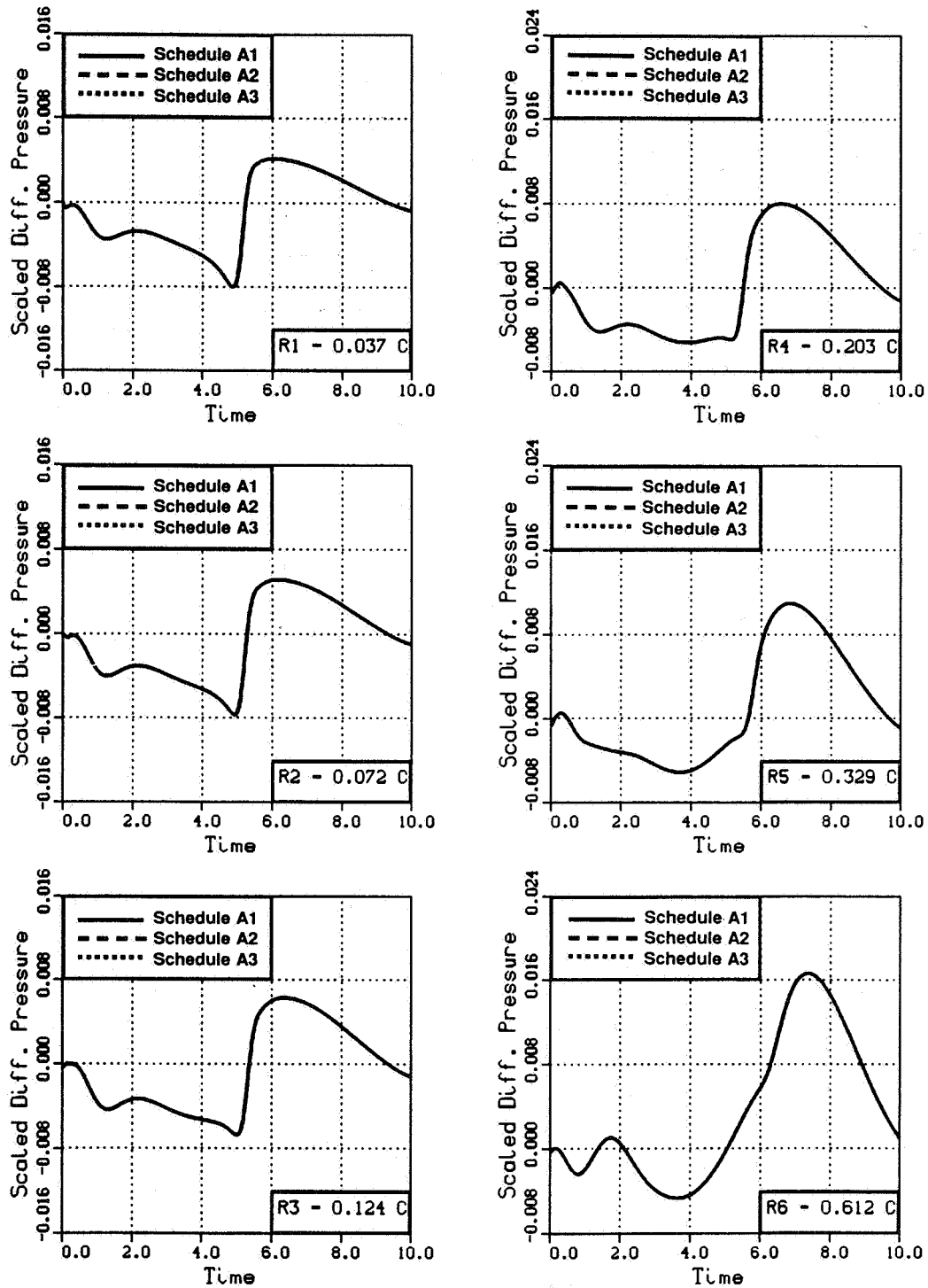
Fig. (8)   Predicted perturbation (or differential) pressures at the six observer locations of Fig. (7) as a function of trailing edge flap schedule (Minf = 0.8, Alpha = 0 degrees, rv/C = 0.05, Γ = 0.2 clockwise, xo/C = -10, yo/C = -0.25)
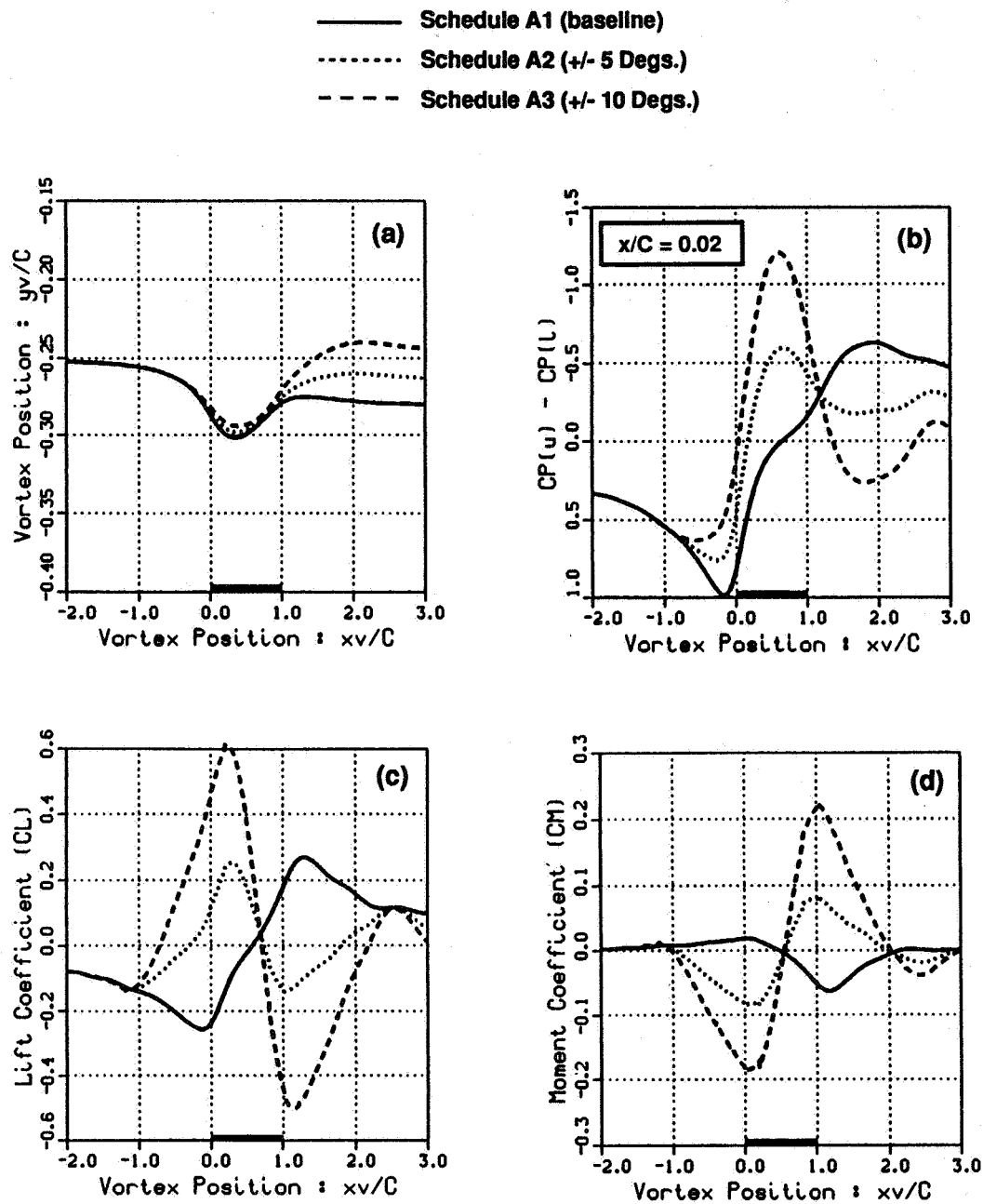
Fig. (9)   Effects of the three trailing edge flap schedules of Fig. (6a) on the aerodynamic characteristics of the NACA 0012 airfoil during airfoil-vortex interactions (Minf = 0.2, Alpha = 0 degrees, rv/C = 0.05, Γ = 0.2 clockwise, xo/C = -10, yo/C = -0.25)
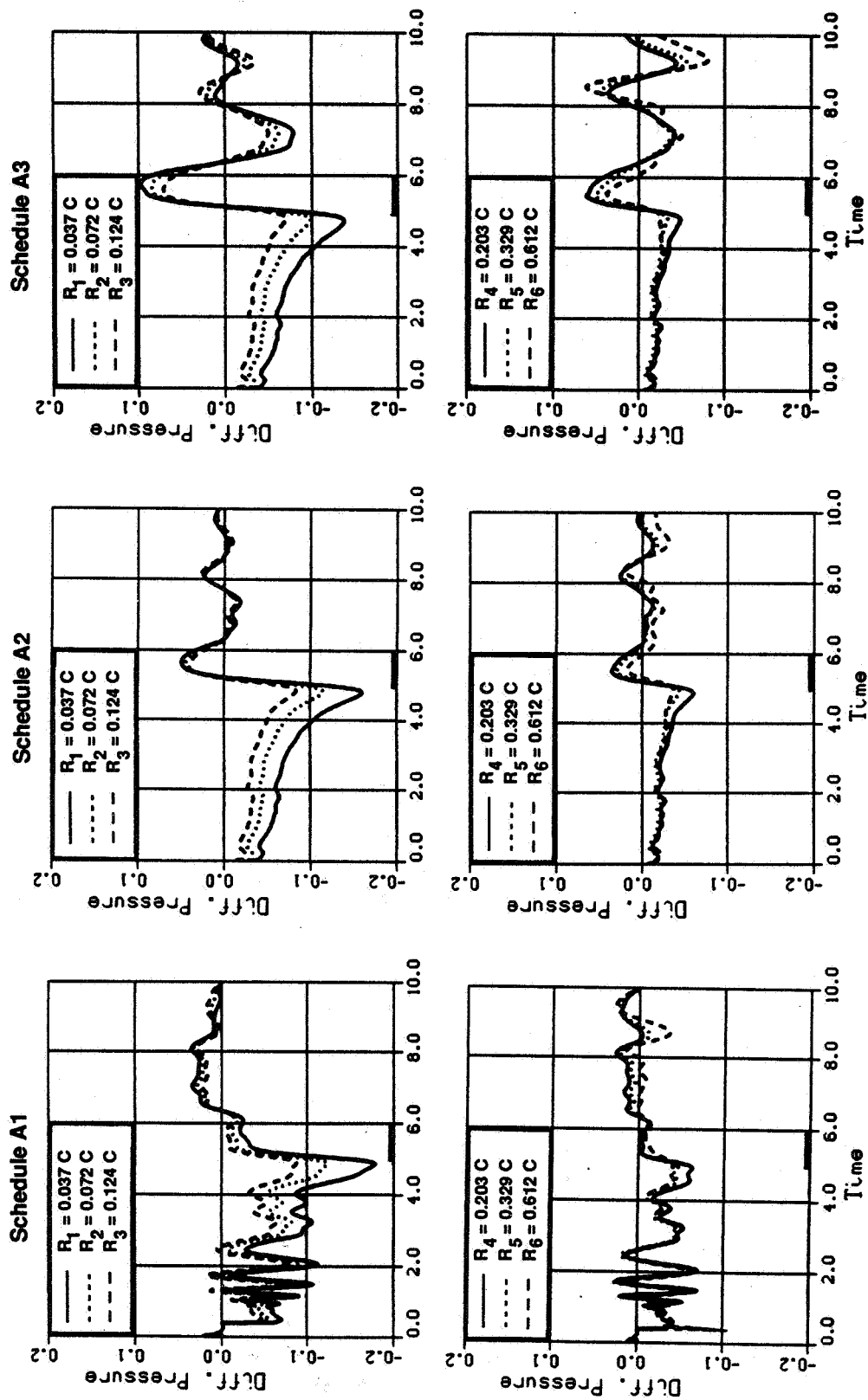
Fig. (10) Predicted perturbation (or differential) pressures at the six observer locations of Fig. (7) as a function of trailing edge flap schedule (Minf = 0.2, Alpha = 0 degrees, rv/C = 0.05, Γ = 0.2 clockwise, xo/C = -10, yo/C = -0.25)
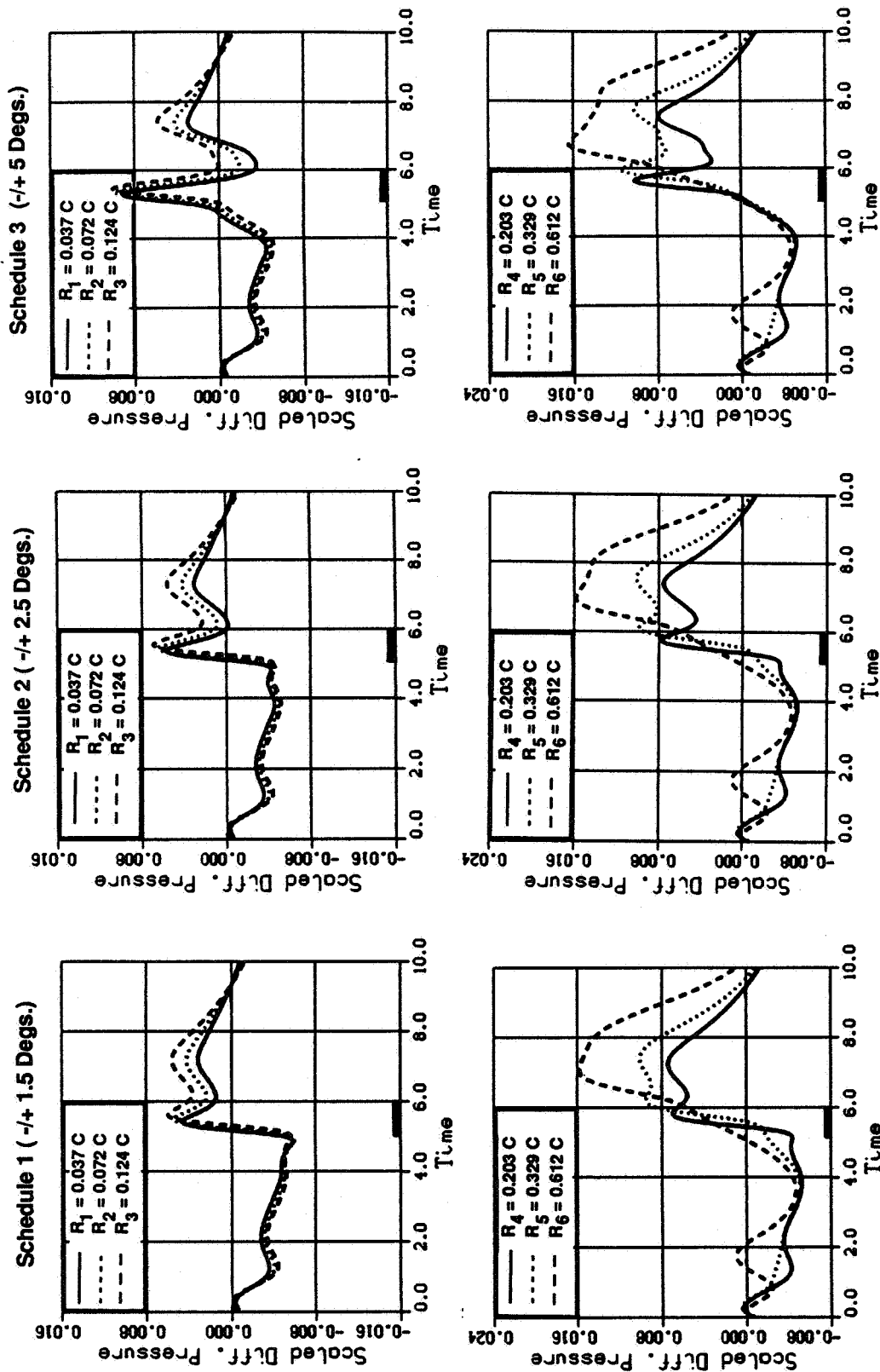
Fig. (11) Predicted perturbation (or differential) pressures at the six observer locations of Fig. (7) as a function of leading edge flap schedule (Minf = 0.8, Alpha = 0 degrees, rv/C = 0.05, Γ = 0.2 clockwise, xo/C = -10, yo/C = -0.25)
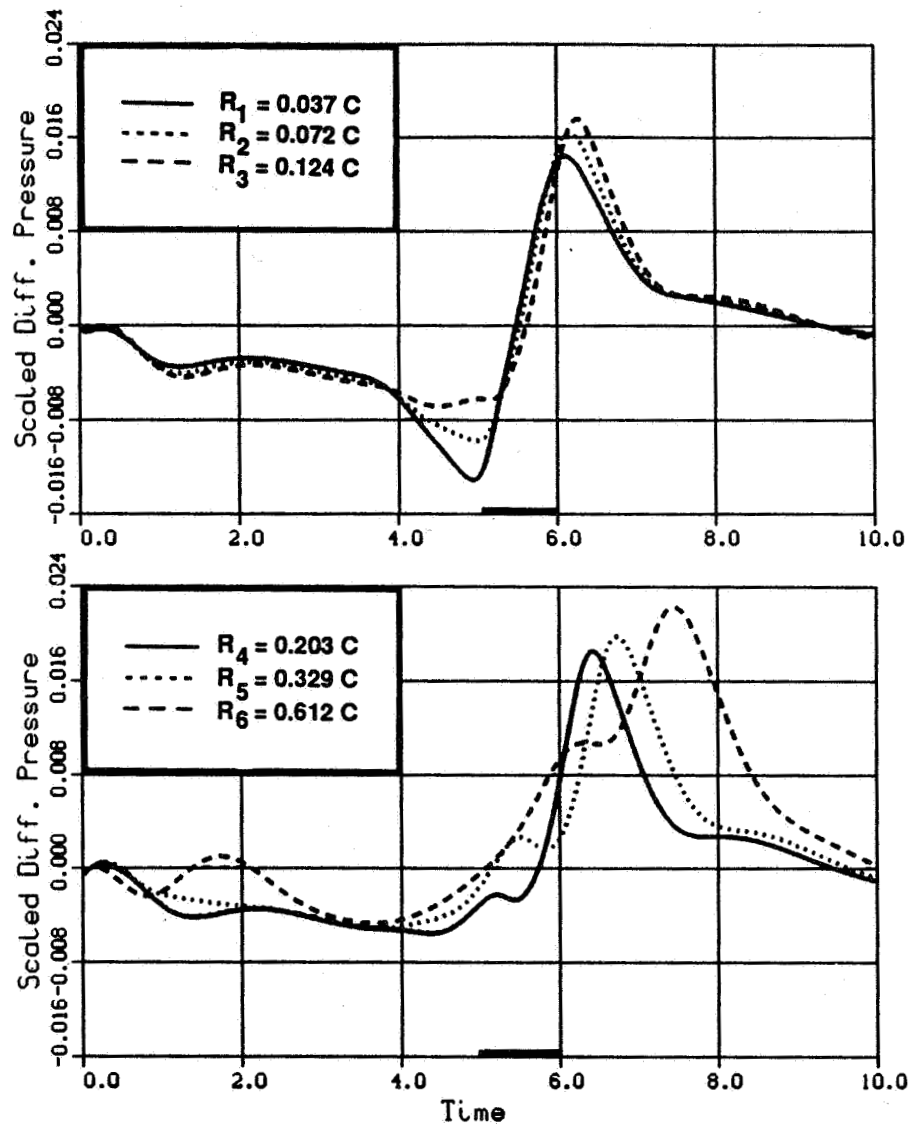
Fig. (12) Computed temporal perturbation pressures as a function of observer position (Minf = 0.8, Alpha = 0 degrees, leading edge flap schedule C: +/- 5 degrees)

93
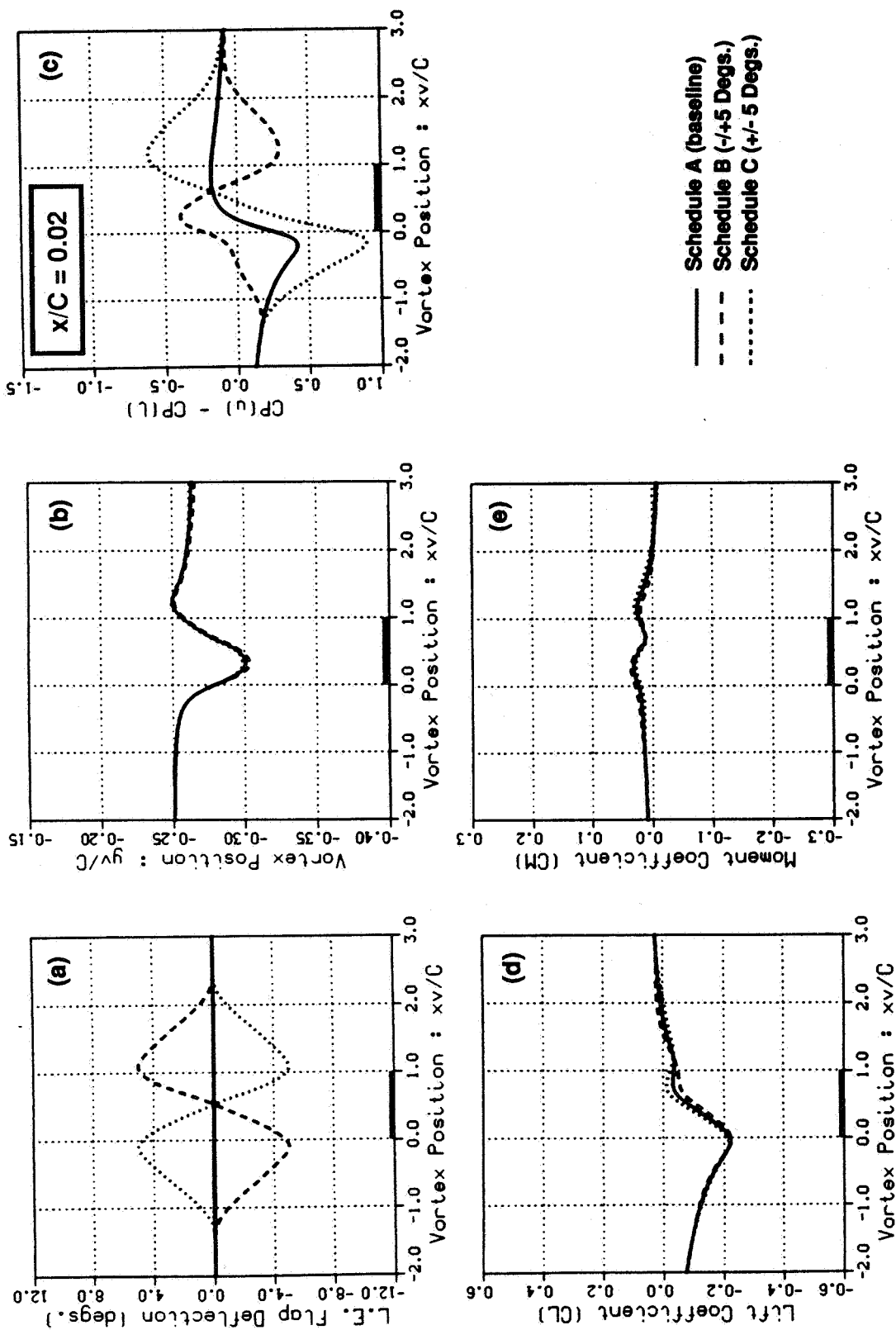
Fig. (13) Effects of three leading edge flap schedules on the aerodynamic characteristics of the NACA 0012 airfoil during airfoil-vortex interactions (Minf = 0.2, Alpha = 0 degrees, rv/C = 0.05, Γ = 0.2 clockwise, xo/C = -10, yo/C = -0.25)
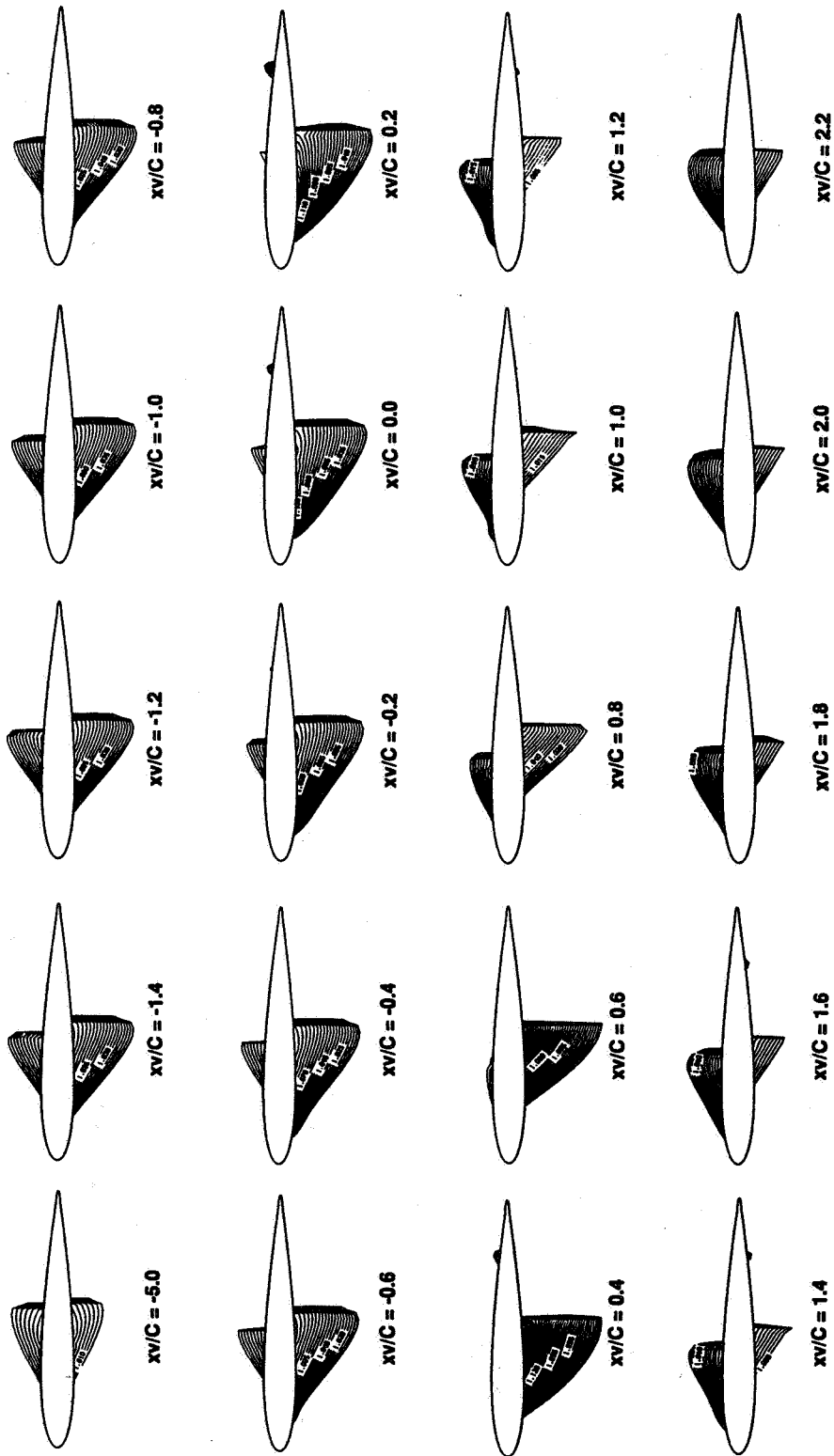
Fig. (14) Predicted supersonic flow regions on a NACA 0012 airfoil as a function of vortex position. The outer Mach contour represents the locus of the predicted sonic points (L.E. Schedule B, T.E. Schedule A3, Minf = 0.8, Alpha = 0 degrees, rv/C = 0.05, Γ = 0.2 clockwise, xo/C = -10, yo/C = -.25)
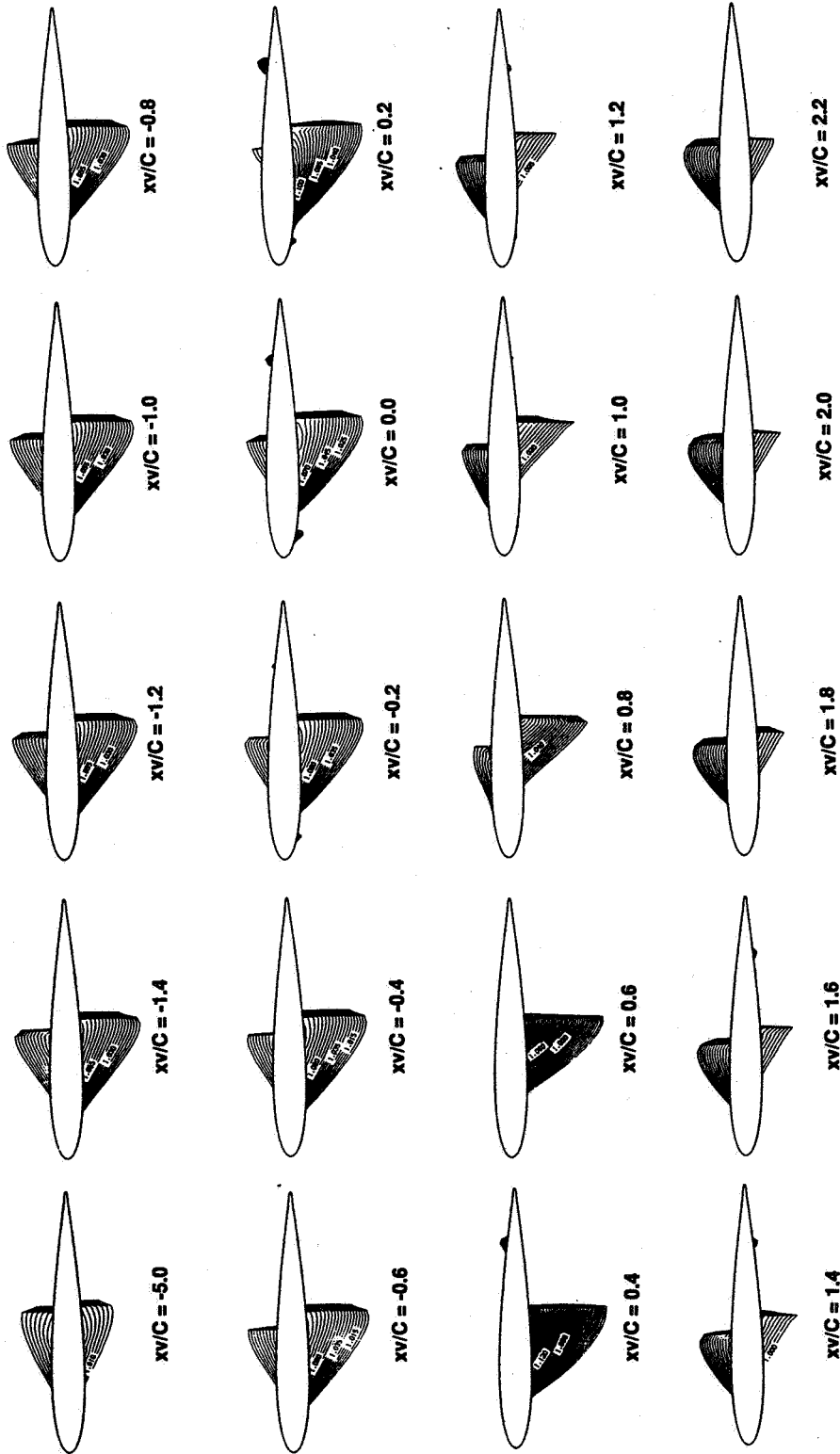
Fig. (15) Predicted supersonic flow regions on a NACA 0012 airfoil as a function of vortex position. The outer Mach contour represents the locus of the predicted sonic points (L.E. Schedule C, T.E. Schedule A3, Minf = 0.8, Alpha = 0 degrees, rv/C = 0.05, Γ = 0.2 clockwise, xo/C = -10, yo/C = -.25)
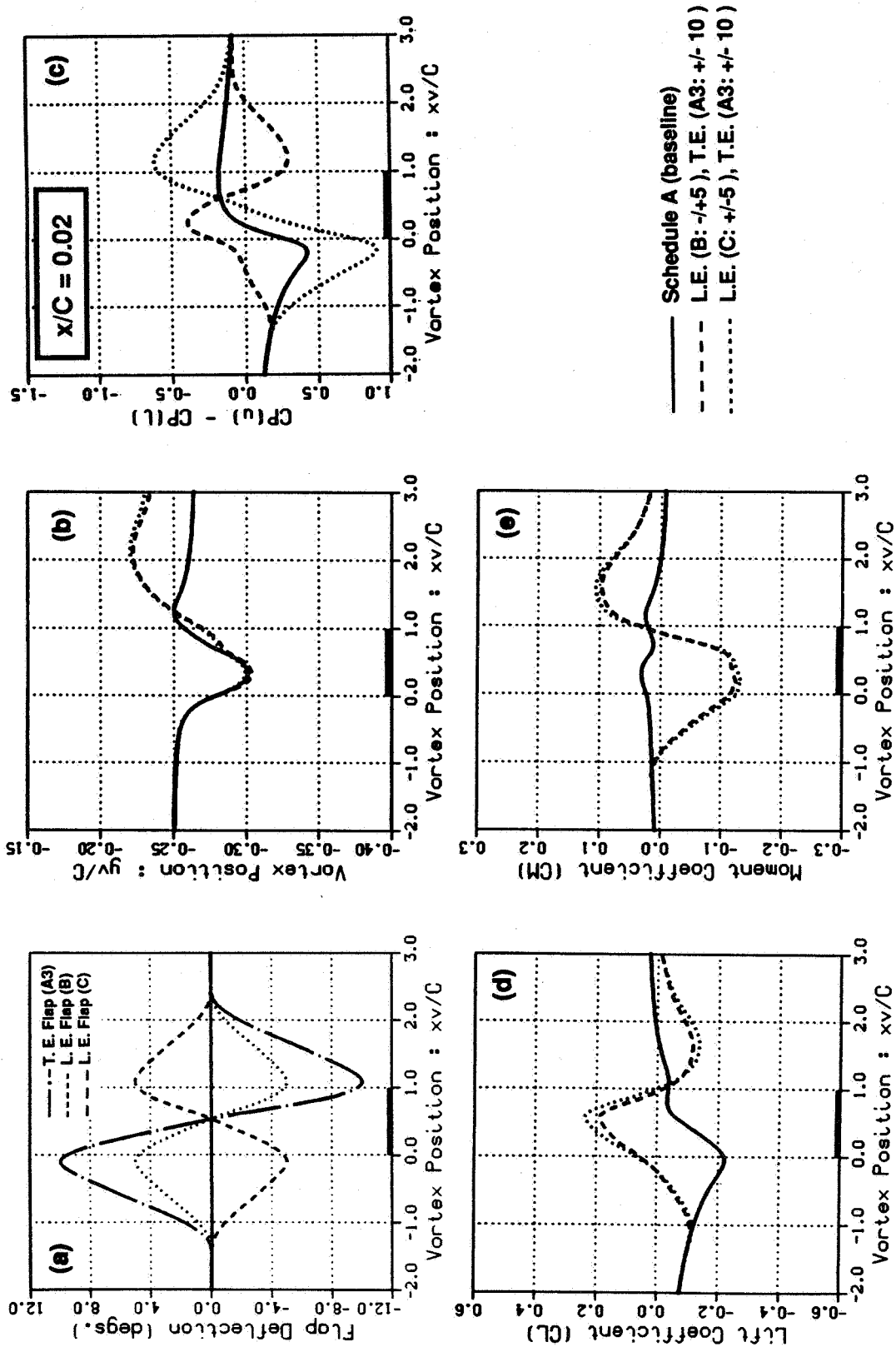
Fig. (16) Effects of leading and trailing edge flaps on the aerodynamic characteristics of the NACA 0012 airfoil during airfoil-vortex interactions (Minf = 0.8, Alpha = 0 degrees, rv/C = 0.05, Γ = 0.2 clockwise, xo/C = -10, yo/C = -.25)

97
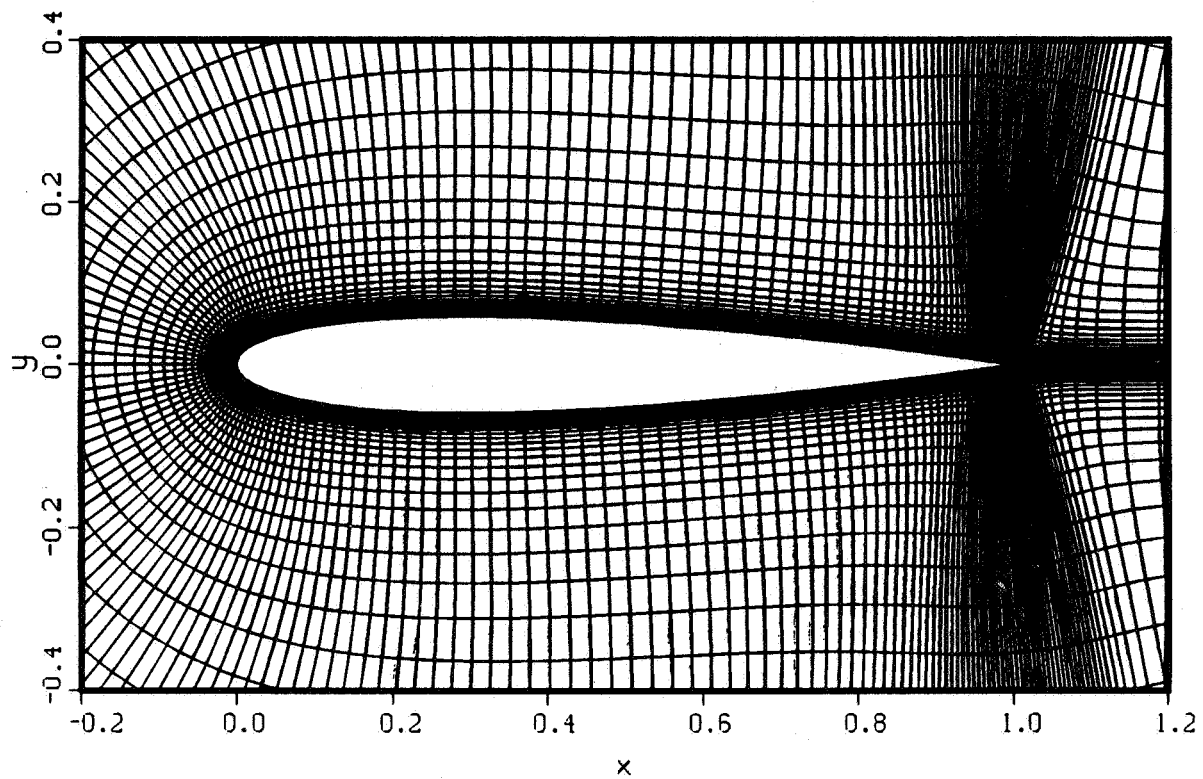
Fig. (17) Close-up view of an algebraically-generated C-type grid for the
NACA 0012 airfoil (grid resolution : 161x61)
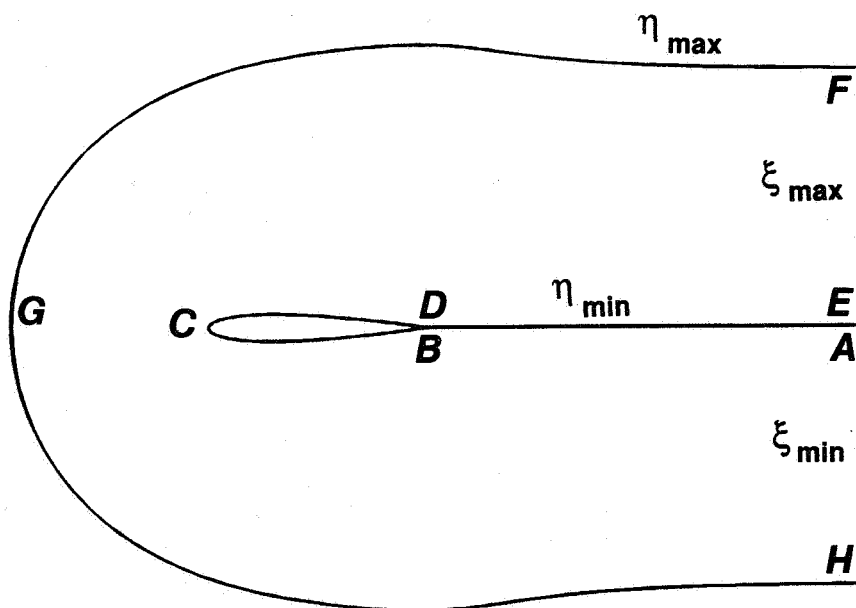
Fig. (18) Sketch depicting the extent of the computational region in the
physical x-y plane

xv/C = -0.2

xv/C = 0.2

xv/C = 0.6

xv/C = 1.0

xv/C = 1.4
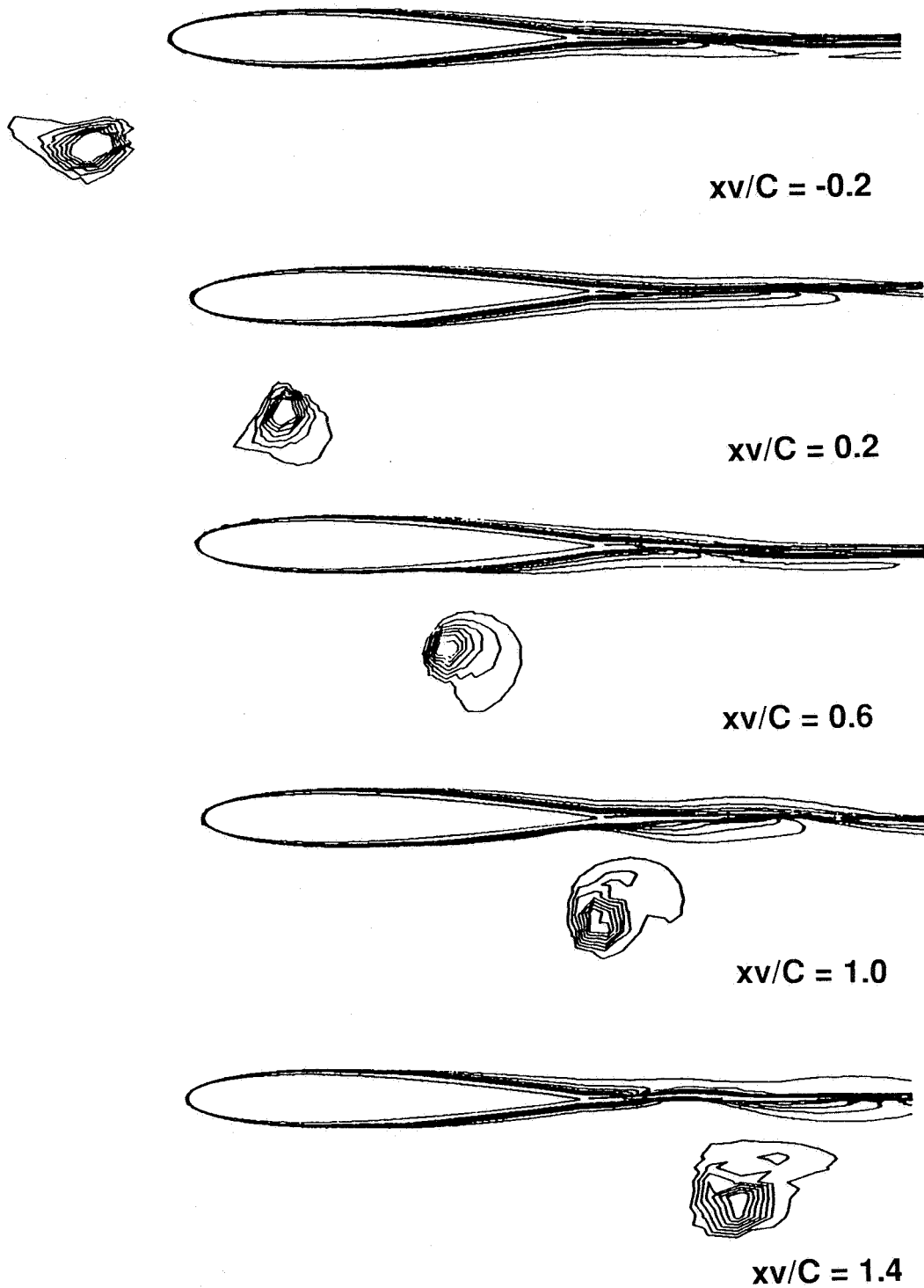
Fig. (19) Predicted vorticity contours for the supercritical interaction between the NACA 0012 airfoil and a vortex (Minf = 0.8, Alpha = 0.0 degrees, xo/C = -5.12, yo/C = -0.26, Re = 3.6 million)
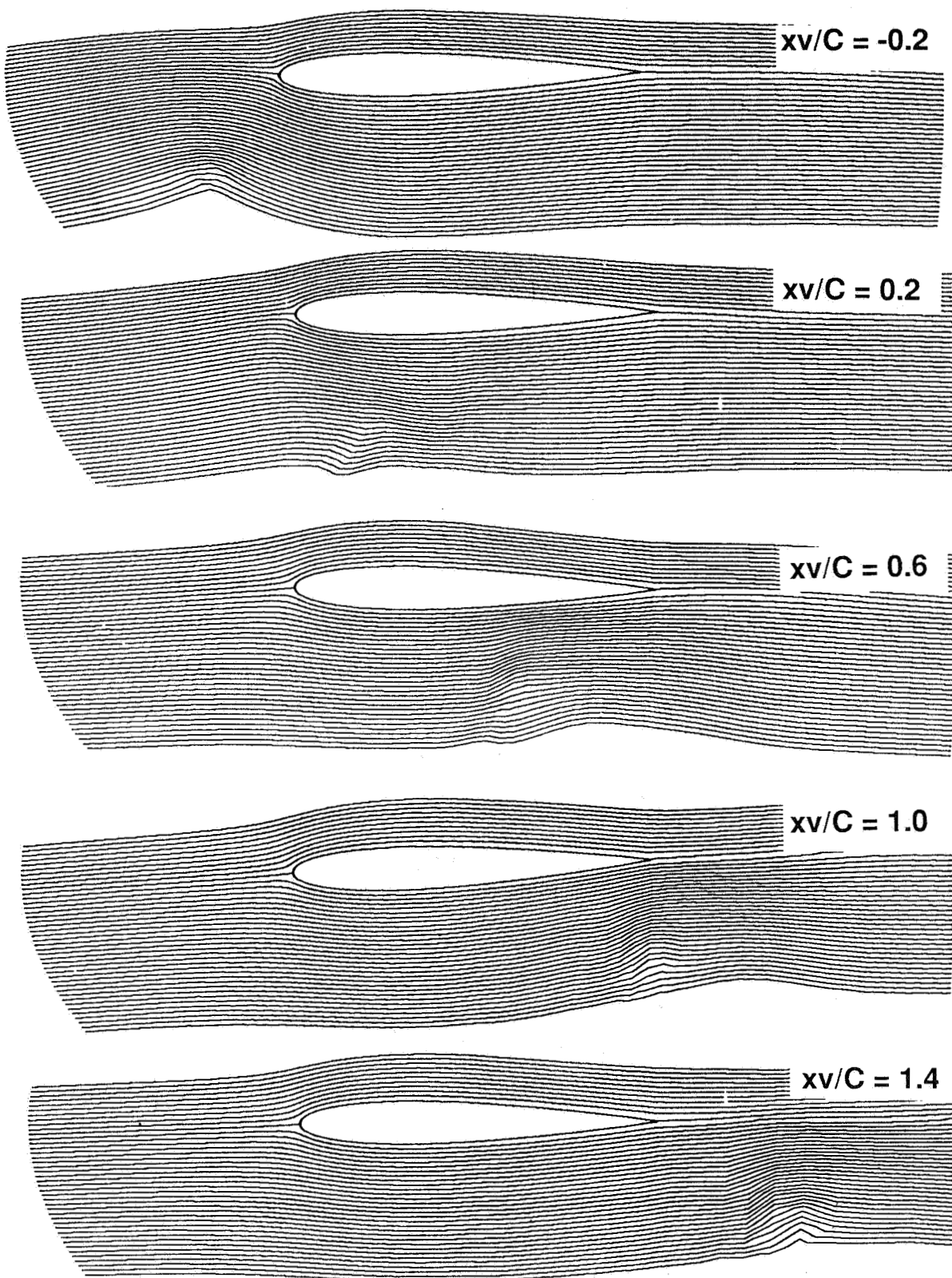
Fig. (20) Predicted streamline contours for the supercritical interaction between the NACA 0012 airfoil and a vortex (Minf = 0.8, Alpha = 0.0 degrees, xo/C = -5.12, yo/C = -0.26, Re = 3.6 million)
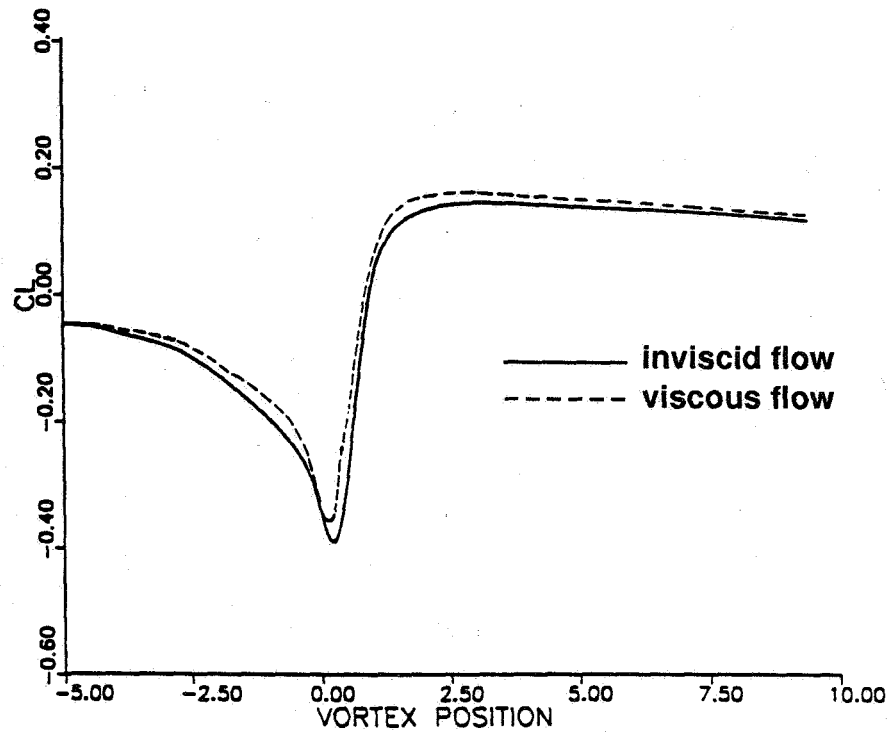
Fig. (21) Comparisons between the predicted unsteady lift coefficients using the Euler and the Navier-Stokes formulations (Minf = 0.8, Alpha = 0.0 degrees, xo/C = -5.12, yo/C = -0.26, Re = 3.6 million)
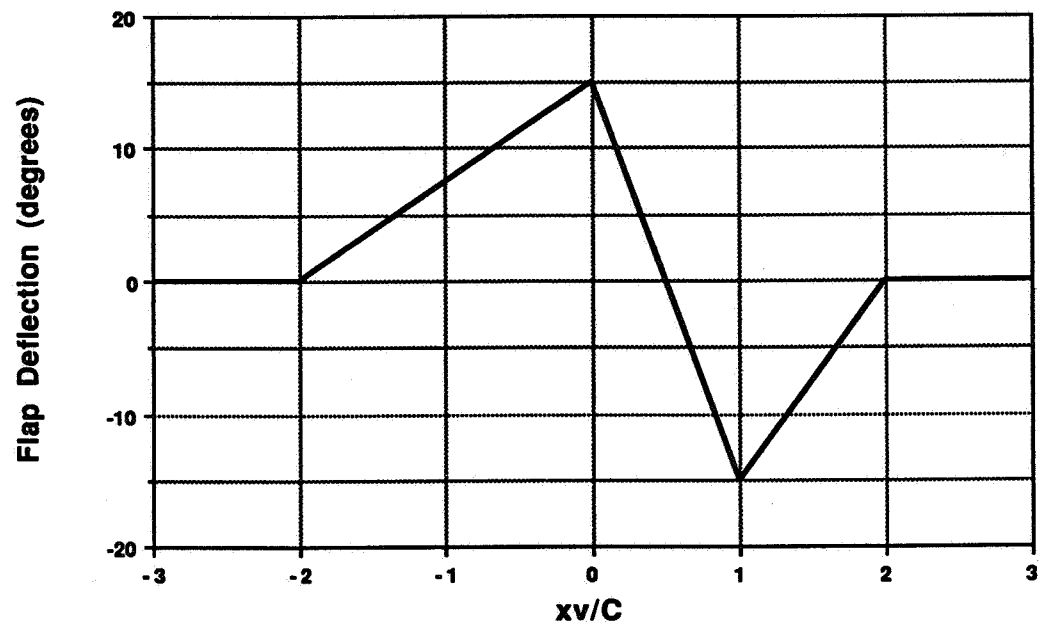
Fig. (22) Trailing edge flap schedule utilized in the Navier-Stokes simulations of airfoil-vortex-flap interactions
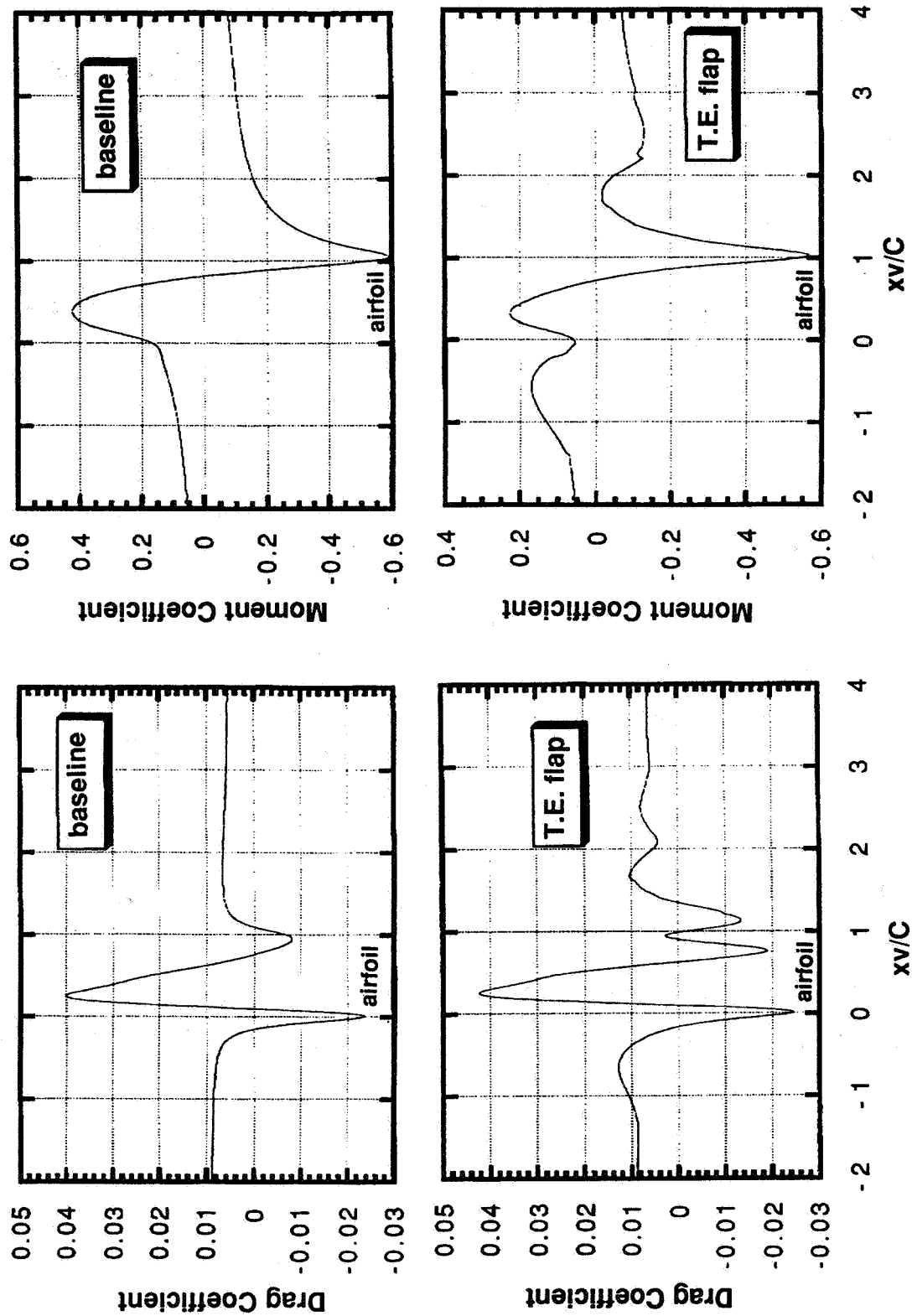
Fig. (23) Predicted unsteady sectional drag and moment coefficients for the NACA 0012 airfoil and for the flapped NACA 0012 airfoil during vortex interactions (Minf = 0.2, Alpha = 0.0 degrees, yo/C = - 0.10, Re = 3.6 million)

xv/C = -2.0

xv/C = 0.0

xv/C = 1.0

xv/C = 2.0

Stream Function   **Vorticity Contours**
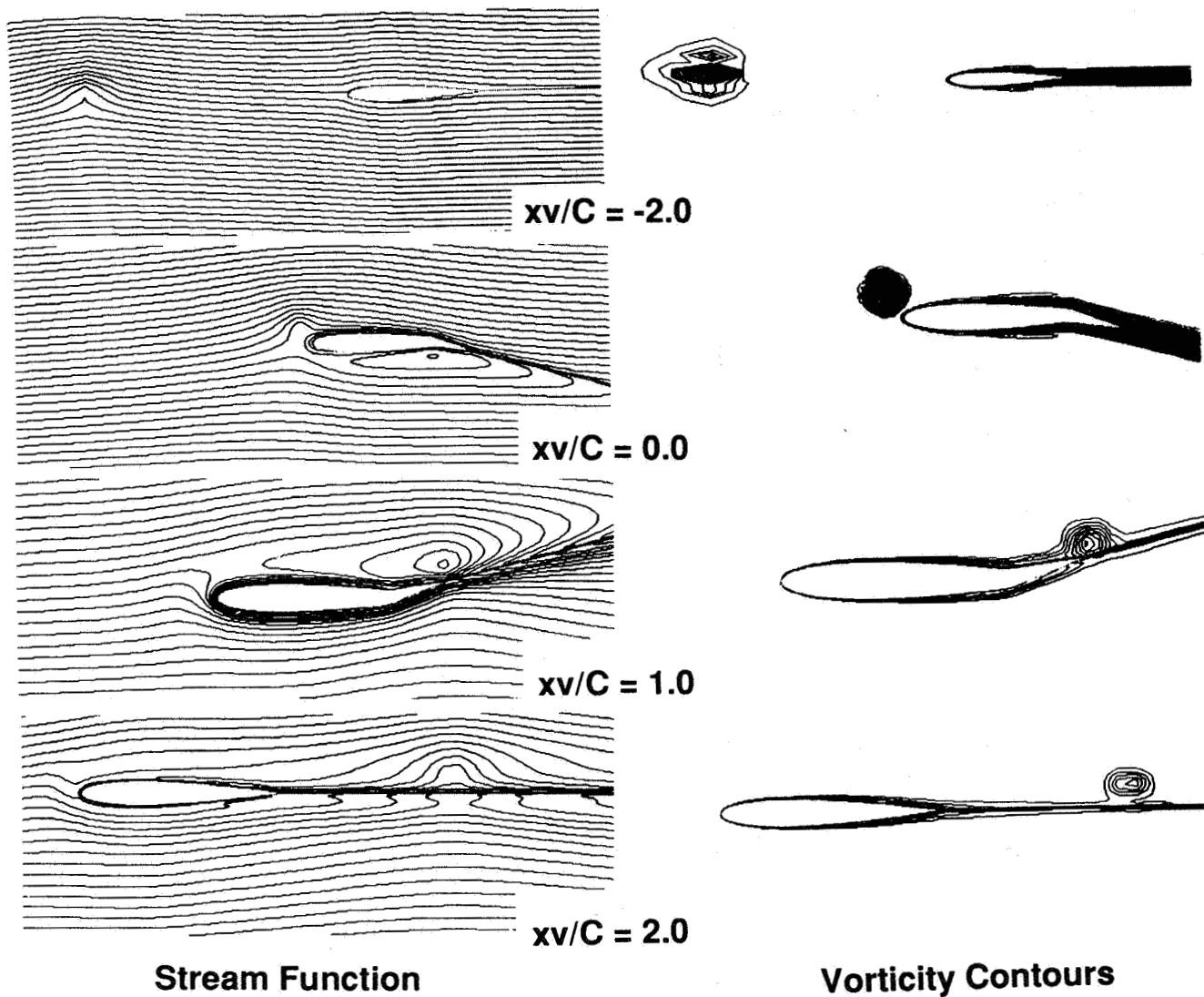
Fig. (24) Predicted vorticity and streamline contours for the subcritical interaction between the NACA 0012 airfoil and a vortex (Minf = 0.2, Alpha = 0.0 degrees, xo/C = -5.12, y0/C = 0.10, Re = 3.6 million)
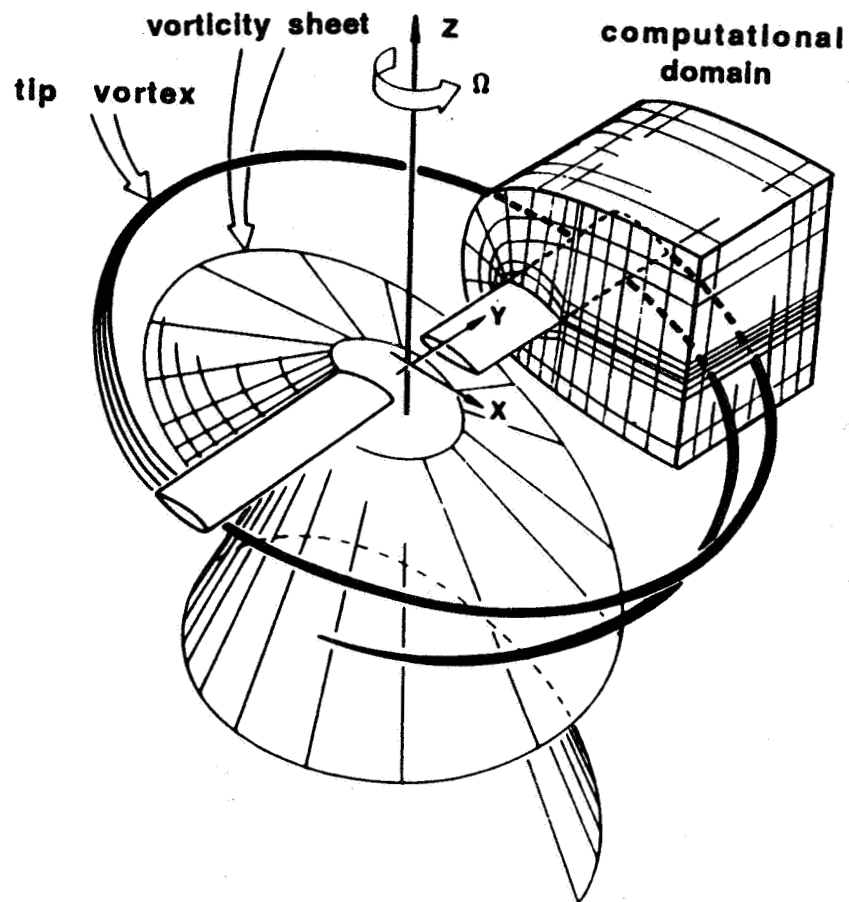
Fig. (25) Schematic of a rotor blade and its wake system
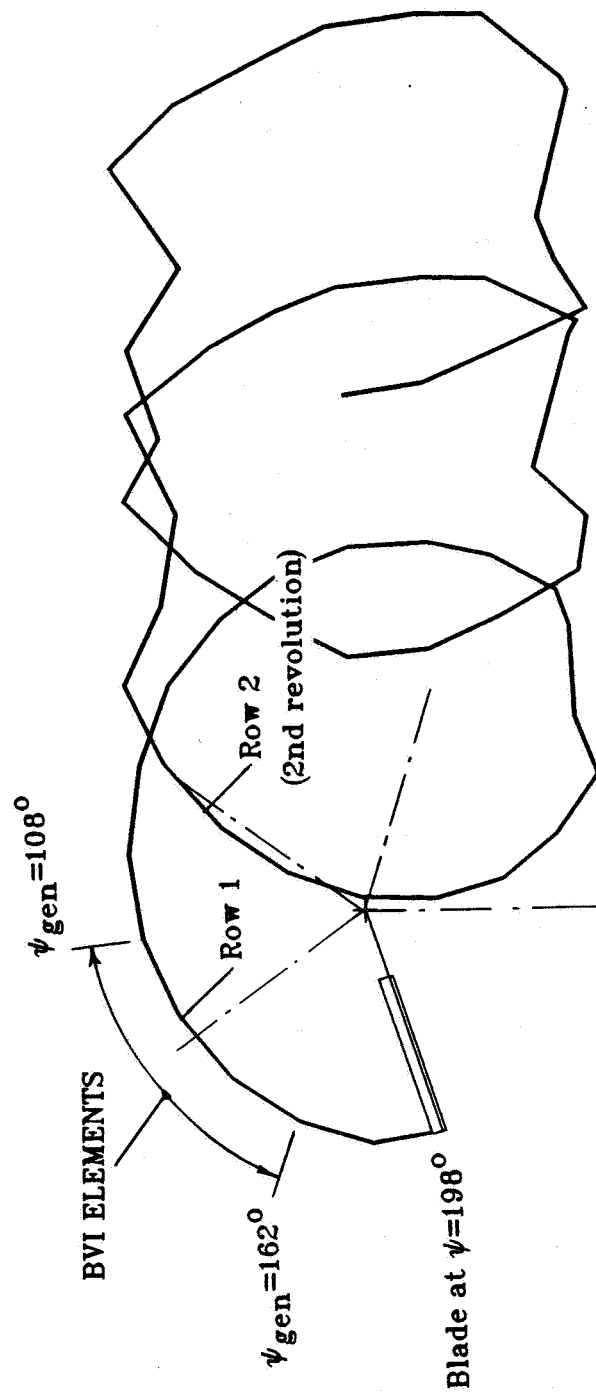
Fig. (26) Identification of vortex-wake elements for the BVI calculations

PSI = 0.0°

PSI = 30.0°

PSI = 40.0°

PSI = 60.0°

PSI = 70.0°

PSI = 90.0°
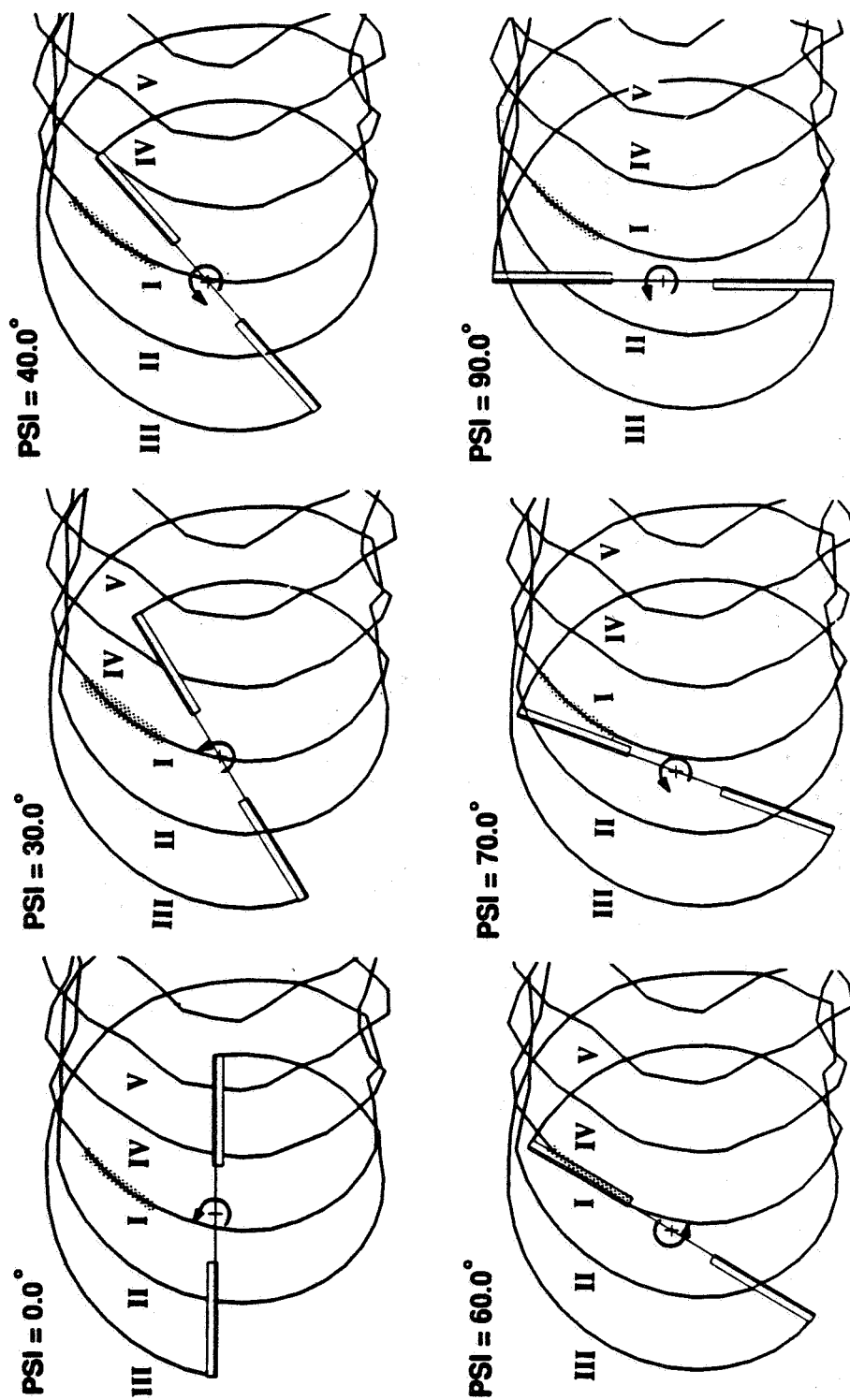
Fig. (27) Planform view of the CAMRAD/JA-predicted tip vortex trajectories for the two-bladed OLS model rotor (Mtip = 0.666, Mu = 0.147)

107
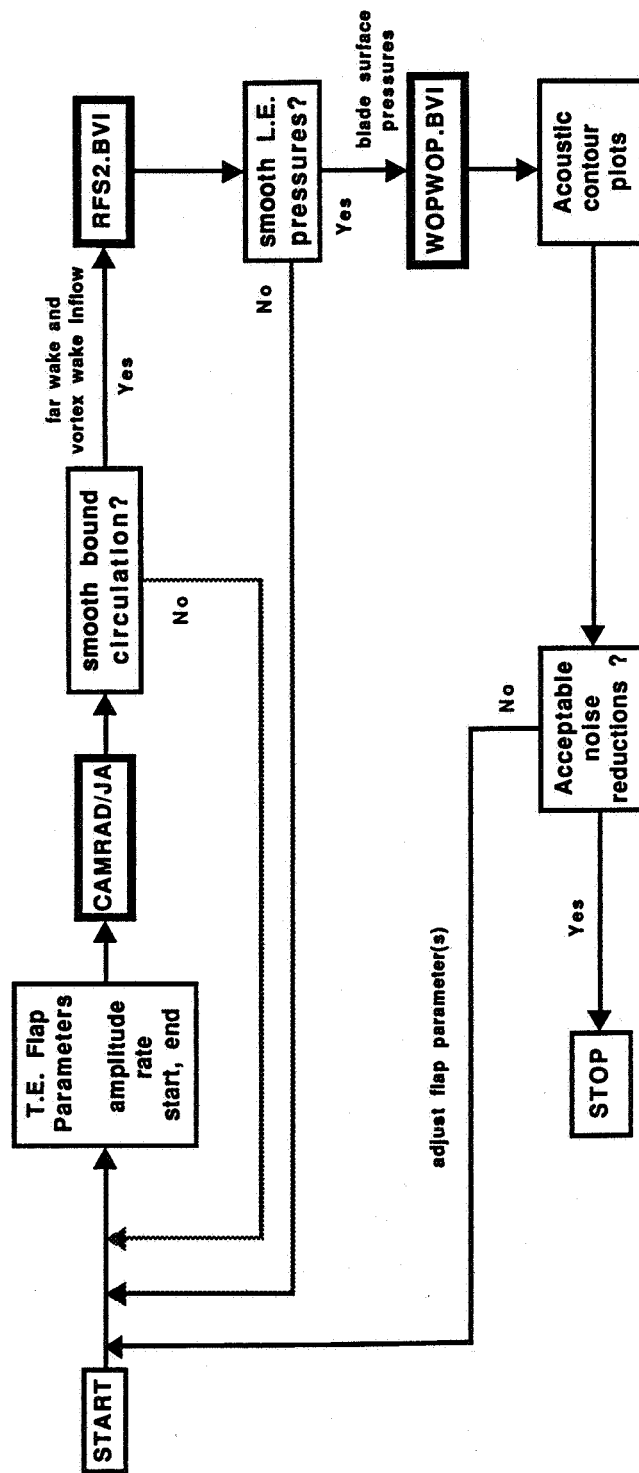
Fig. (28) Flow chart depicting the three coupled analysis methodologies for predicting rotor blade-vortex interactions
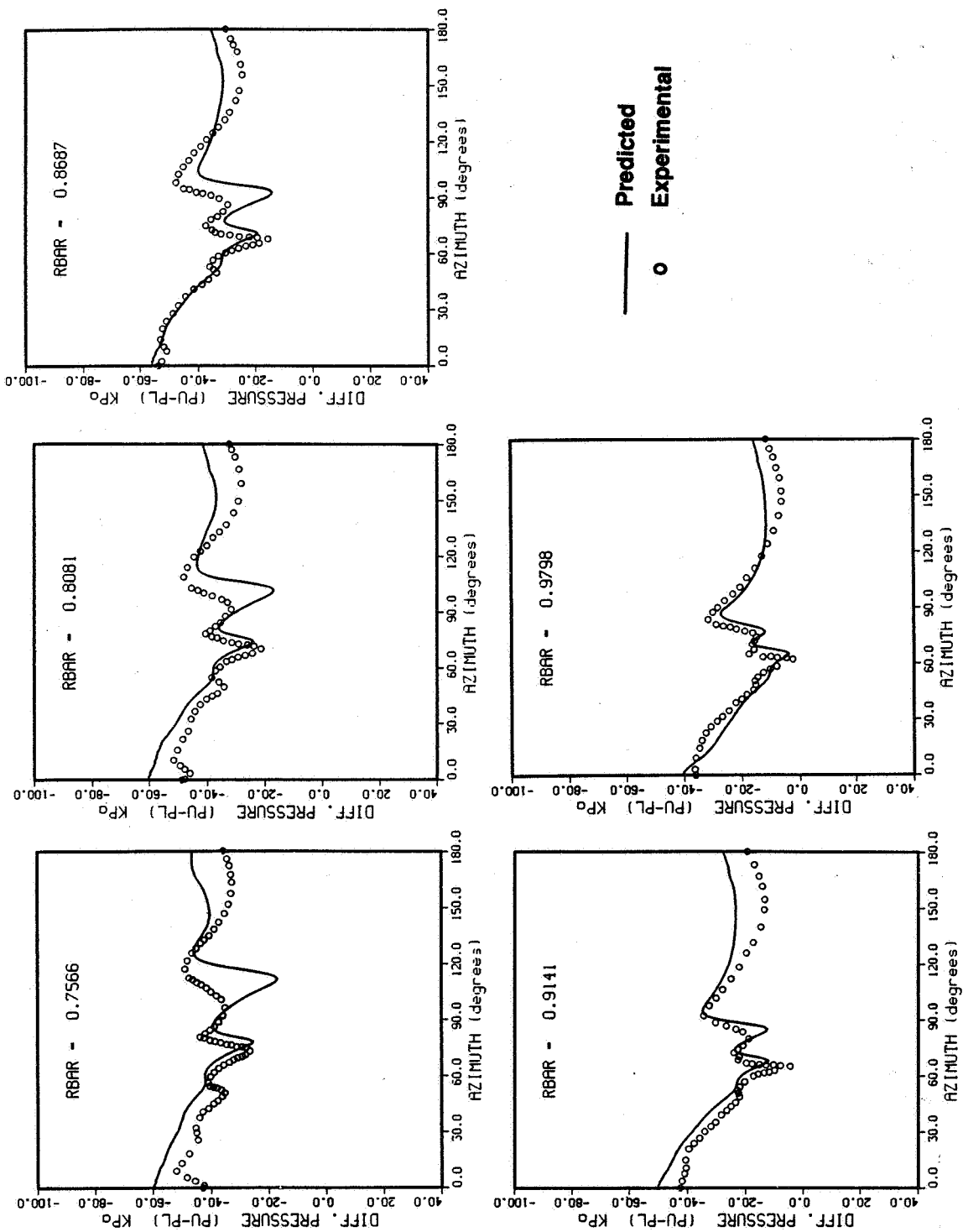
Fig. (29) Predicted and measured surface pressures for the model OLS rotor during self-generated blade-vortex interactions (3 vortex interactions, 7 vortex segments/vortex line, Mtip = 0.666, Mu = 0.147, x/C = 0.03, rv/C = 0.20, TPP = 1.5 degrees aft)
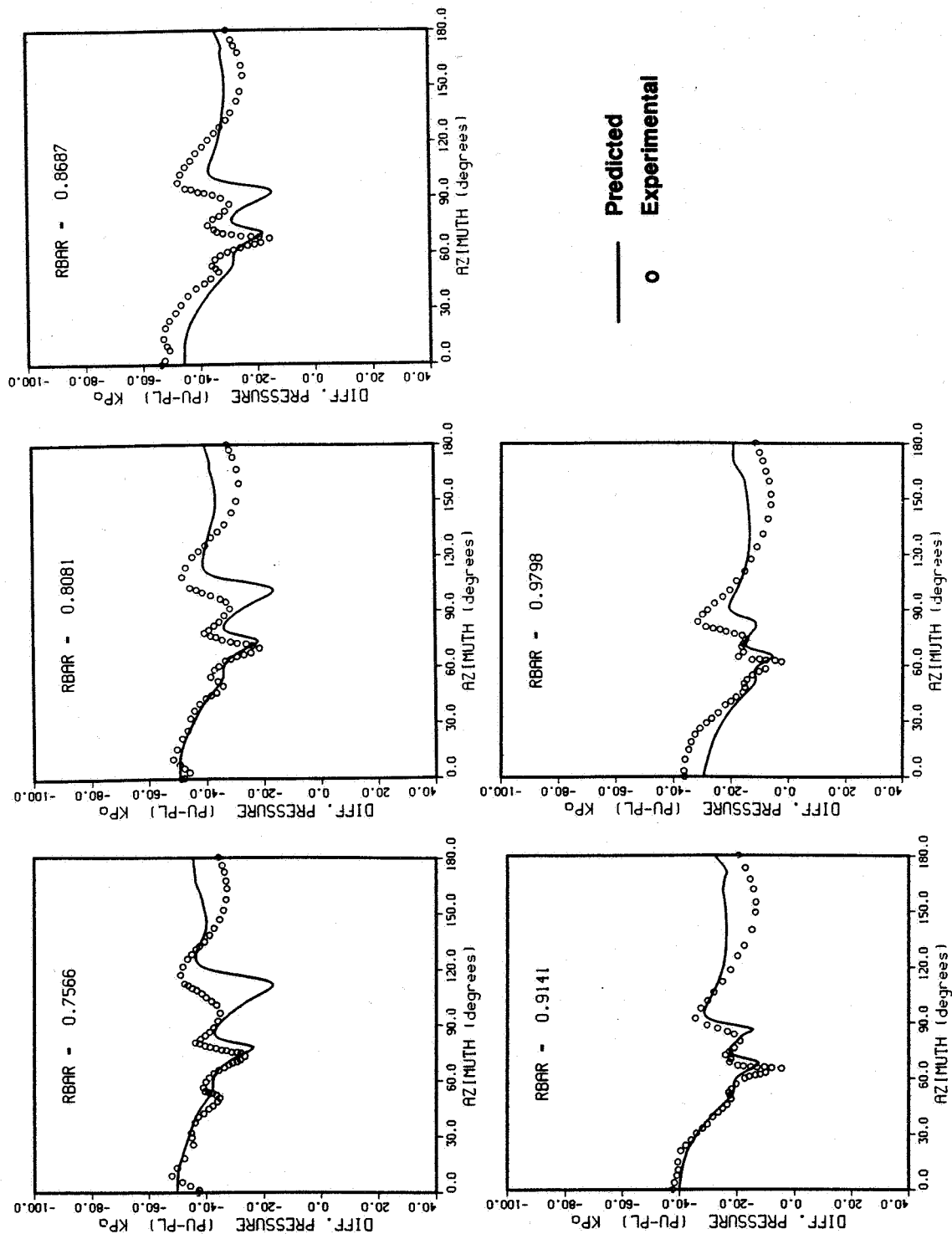
Fig. (30) Predicted and measured surface pressures for the model OLS rotor during self-generated blade-vortex interactions (3 vortex interactions, 5 vortex segments/vortex line, Mtip = 0.666, Mu = 0.147, x/C = 0.03, rv/C = 0.20, TPP = 1.5 degrees aft)
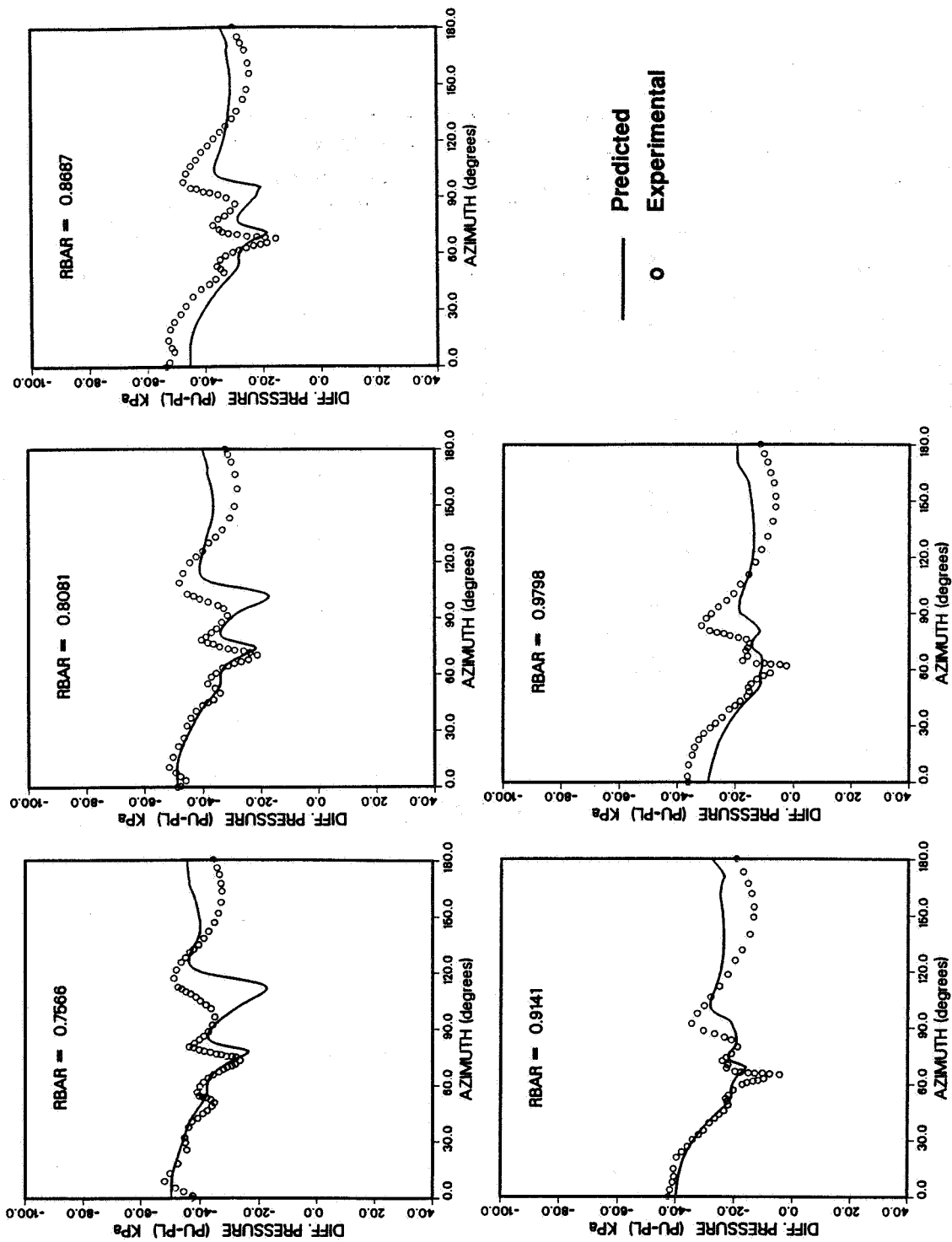
Fig. (31) Predicted and measured surface pressures for the model OLS rotor during self-generated blade-vortex interactions (3 vortex interactions, 4 vortex segments/vortex line, Mtip = 0.666, Mu = 0.147, x/C = 0.03, rv/C = 0.20, TPP = 1.5 degrees aft)

111
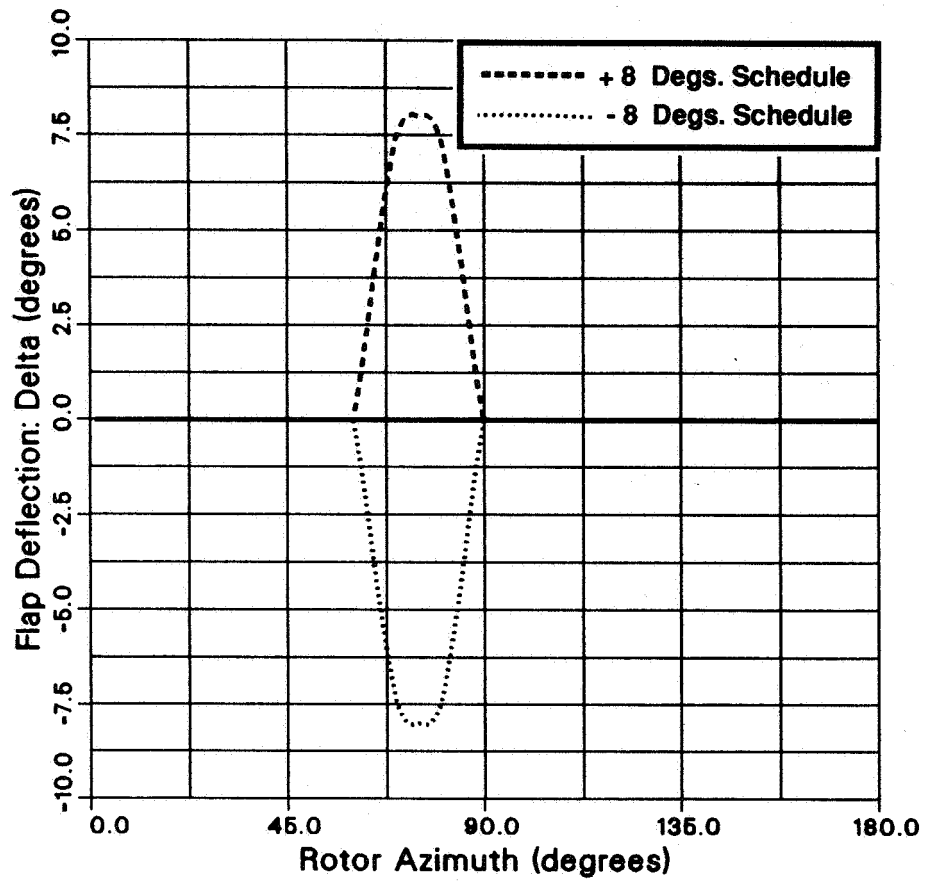
Fig. (32) Trailing edge flap deflection angles as a function of blade azimuth
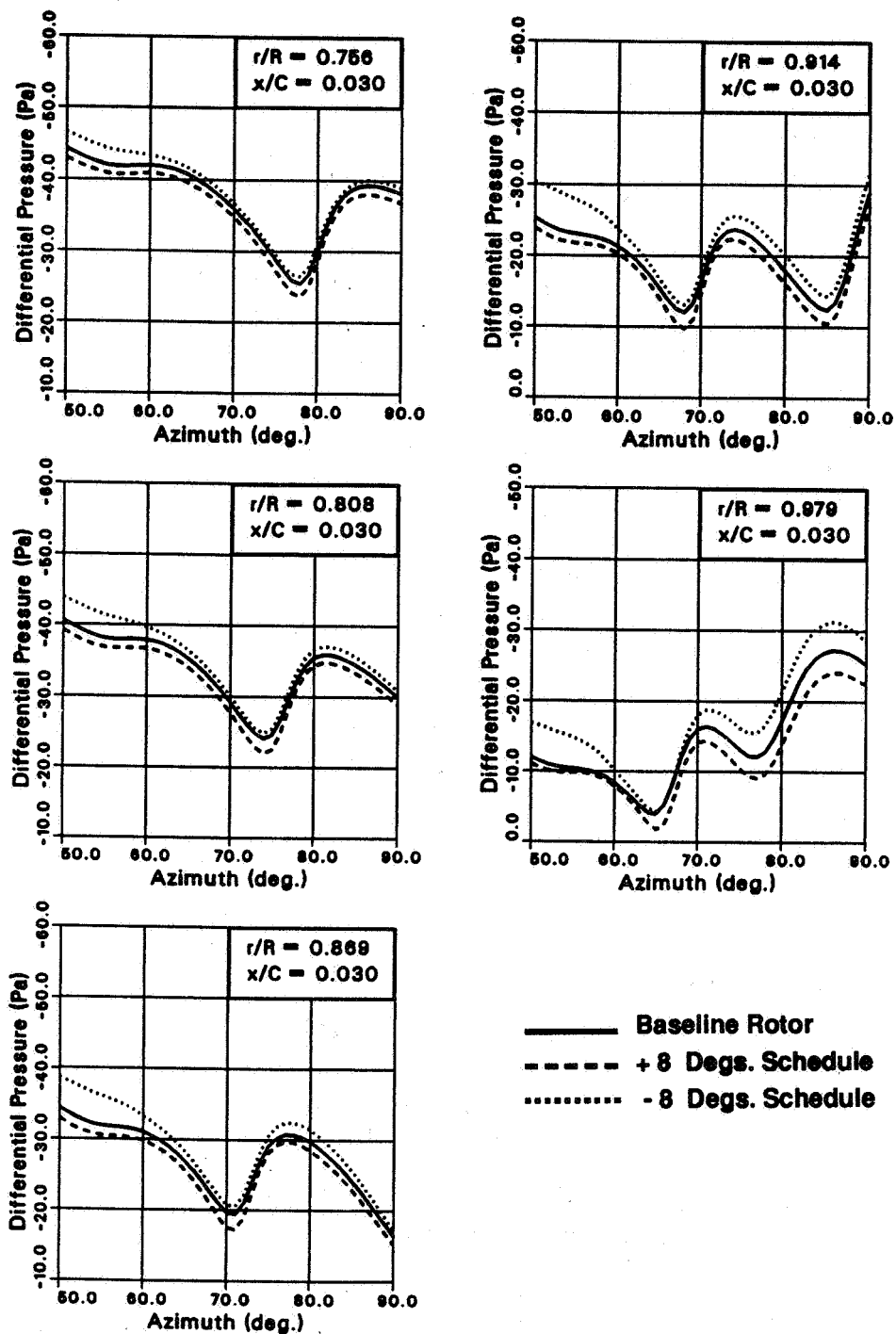
Fig. (33) Effects of the trailing edge flap on the RFS2.BVI-predicted differential pressures for the model OLS rotor during self-generated blade-vortex interactions (3 vortex interactions, Mtip = 0.666, Mu = 0.147, x/C = 0.03, rv/C = 0.20)
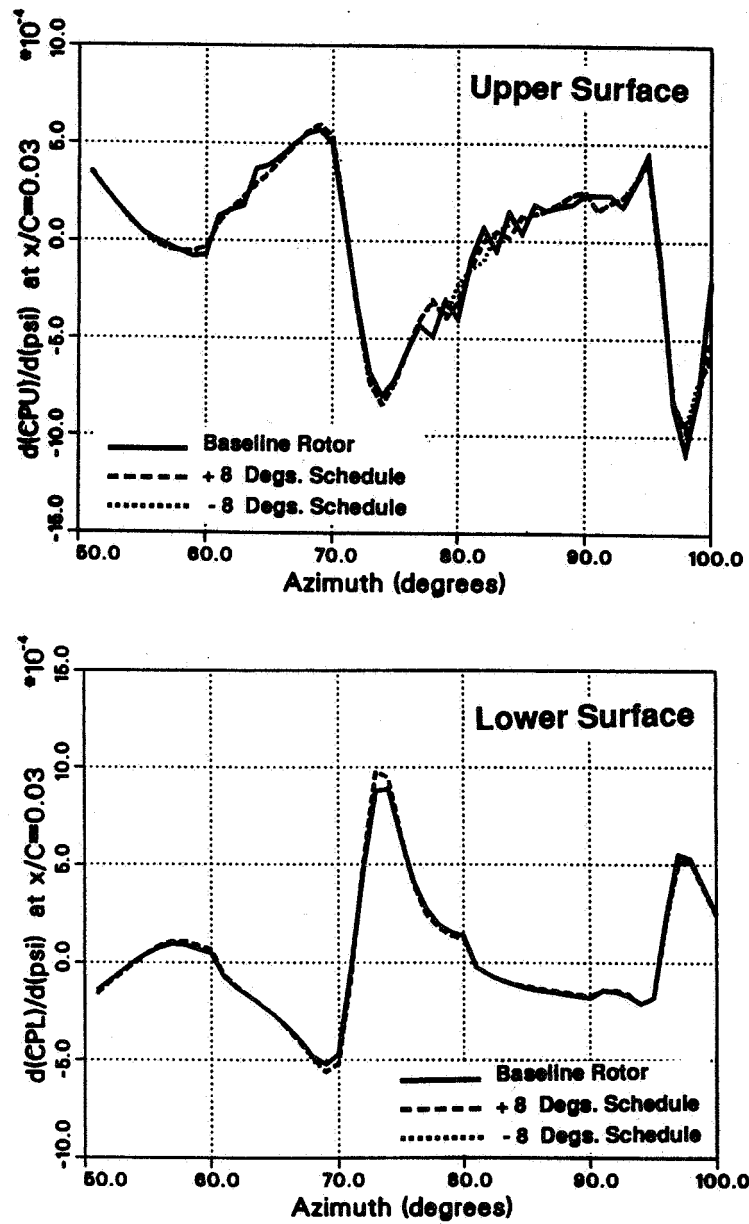
Fig. (34) RFS2.BVI-predicted upper "U" and lower "L" surface temporal pressure gradients as a function of blade azimuth (RBAR = 0.86)

114
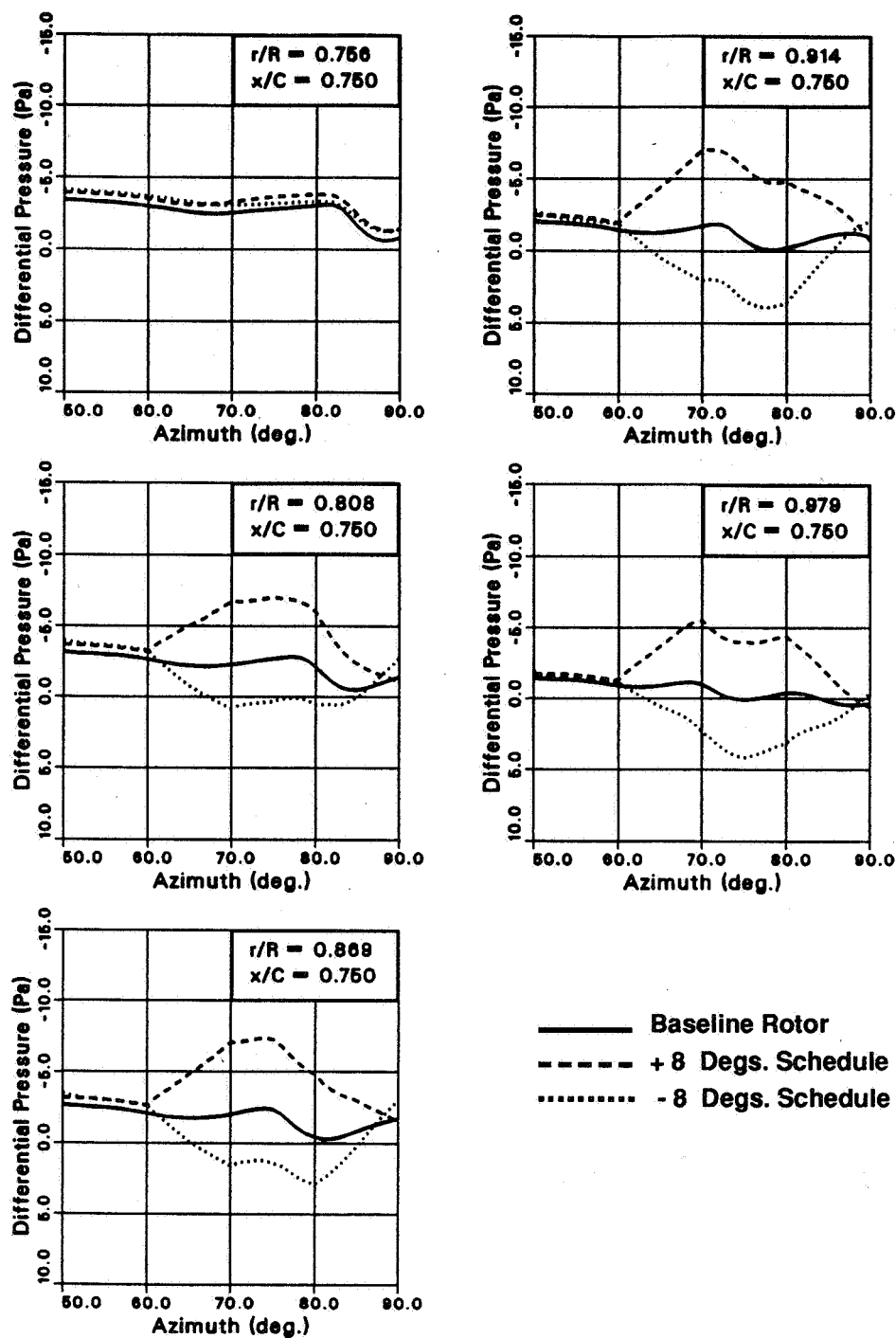
Fig. (35) Effects of the trailing edge flap on the RFS2.BVI-predicted differential pressures for the model OLS rotor during self-generated blade-vortex interactions (3 vortex interactions, Mtip = 0.666, Mu = 0.147, x/C = 0.75, rv/C = 0.20)
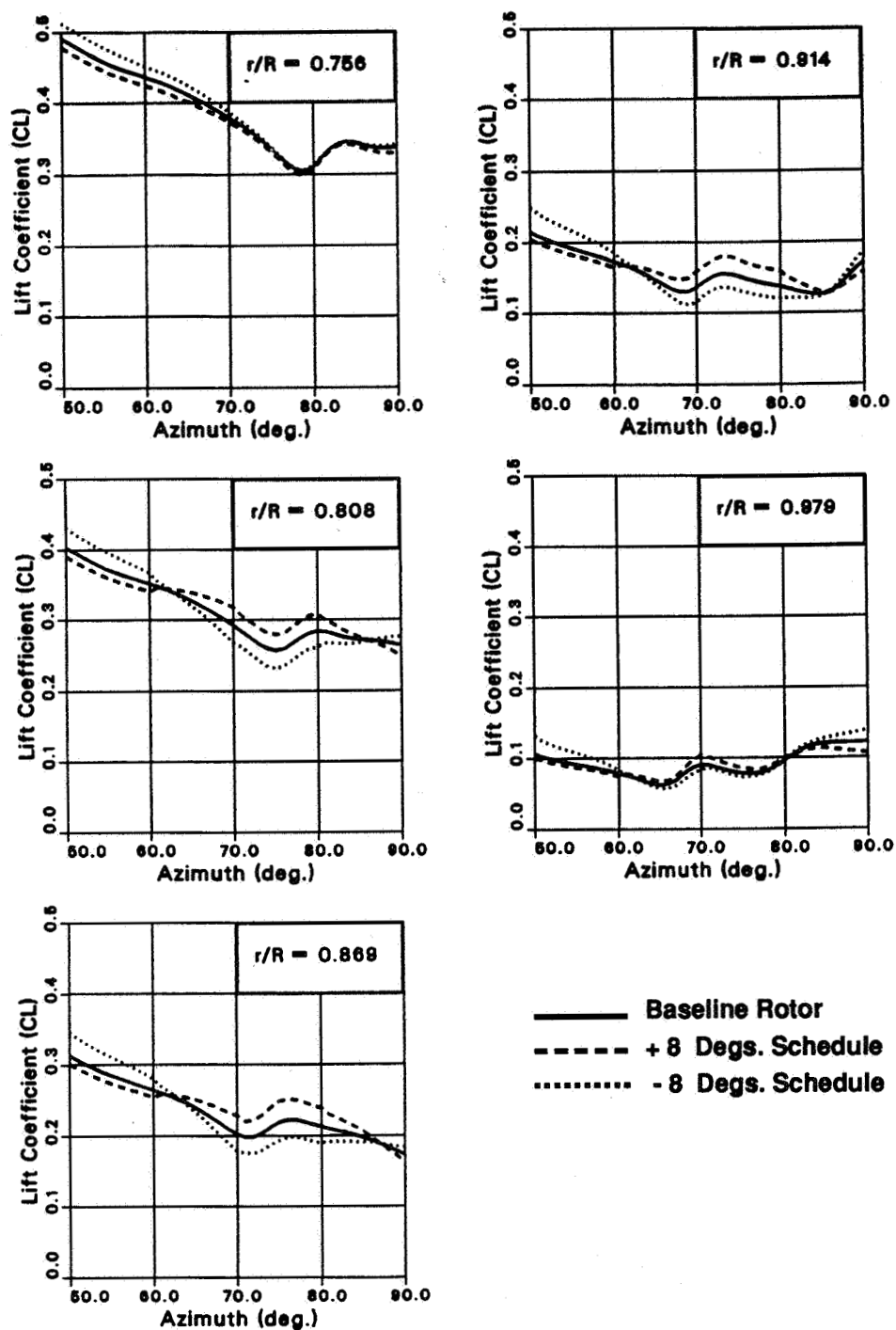
Fig. (36) Effects of the trailing edge flap on the predicted sectional lift forces for the model OLS rotor during self-generated blade-vortex interactions (3 vortex interactions, Mtip = 0.666, Mu = 0.147, rv/C = 0.20)
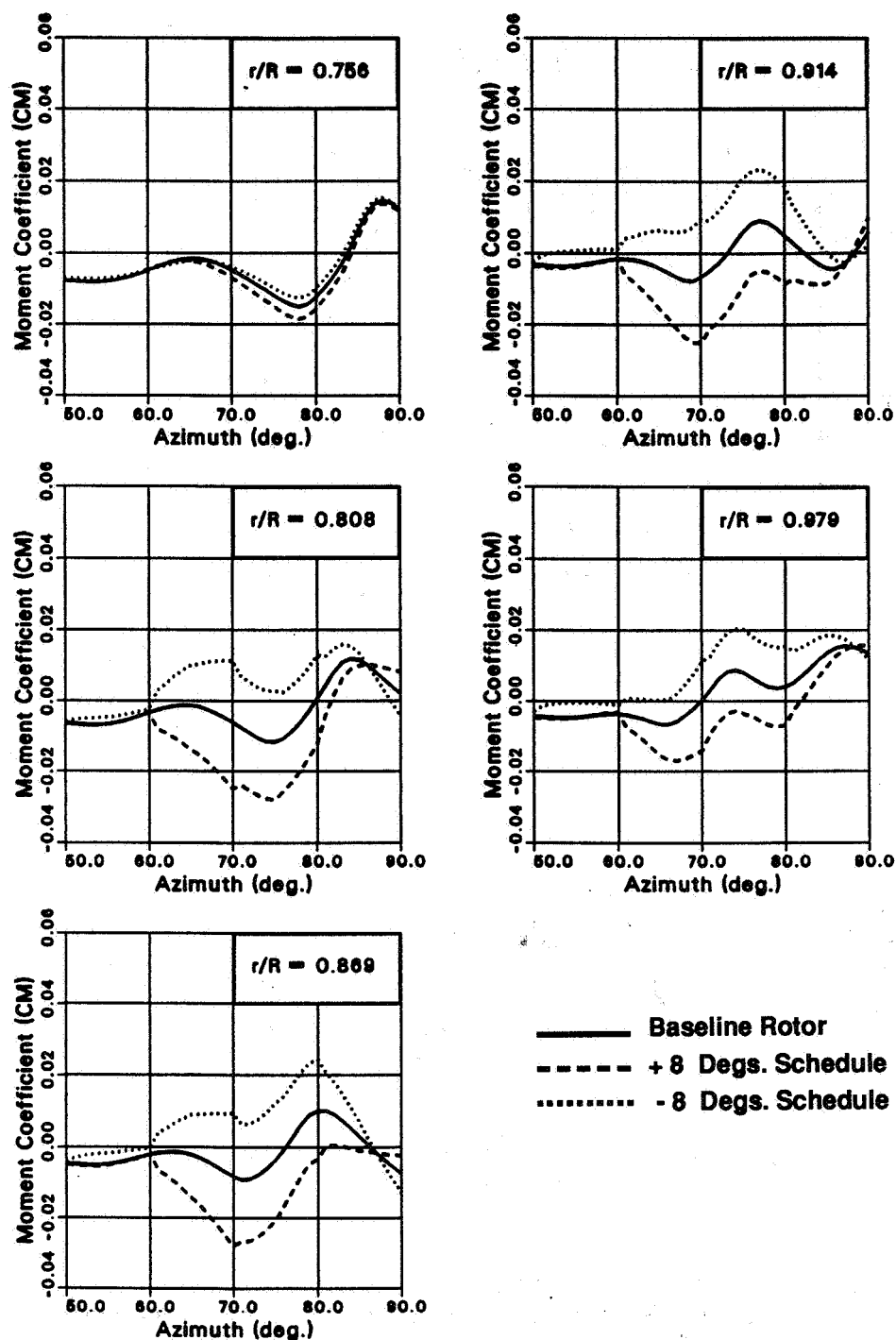
Fig. (37) Effects of the trailing edge flap on the predicted sectional moments for the model OLS rotor during self-generated blade-vortex interactions (3 vortex interactions, Mtip = 0.666, Mu = 0.147, rv/C = 0.20)
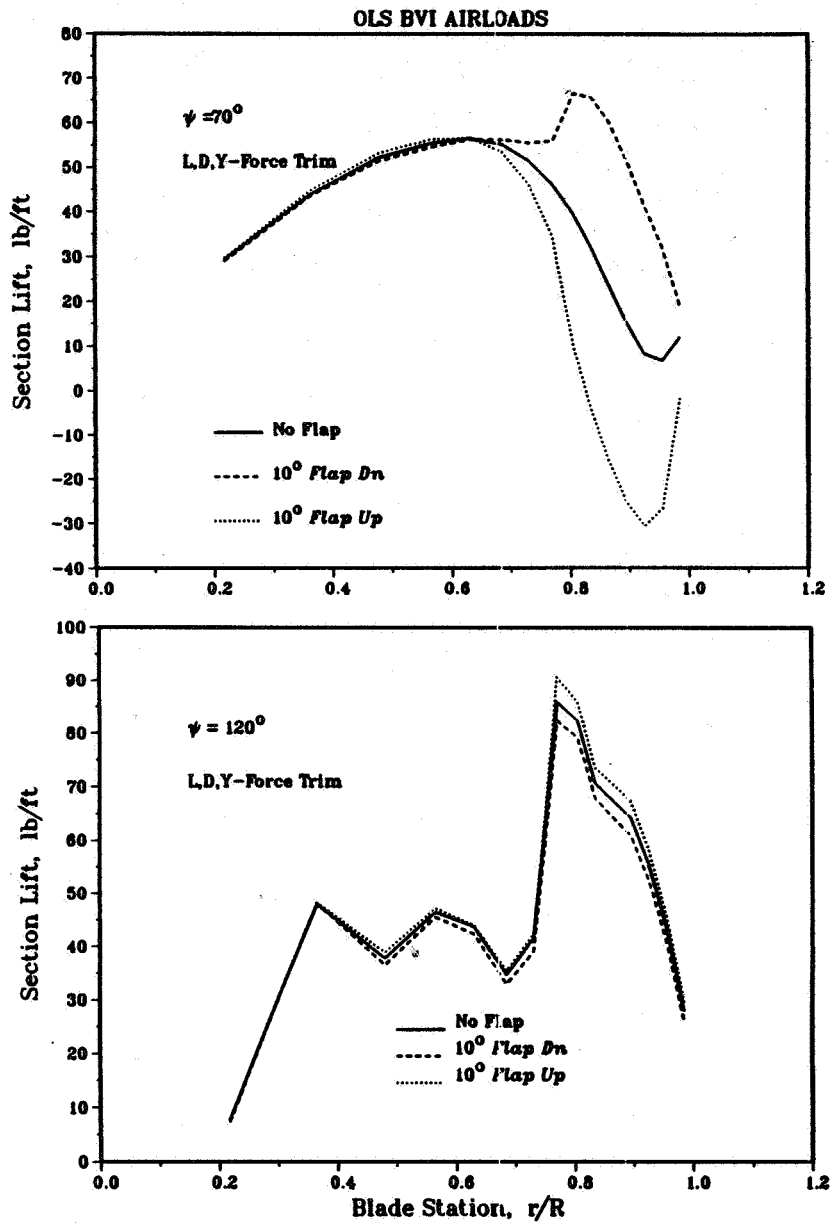
Fig. (38) Effects of the trailing edge flap on the CAMRAD/JA-predicted radial lift distributions for the OLS model rotor during blade-vortex interactions (Mtip = 0.666, Mu = 0.147, rv/C = 0.20)
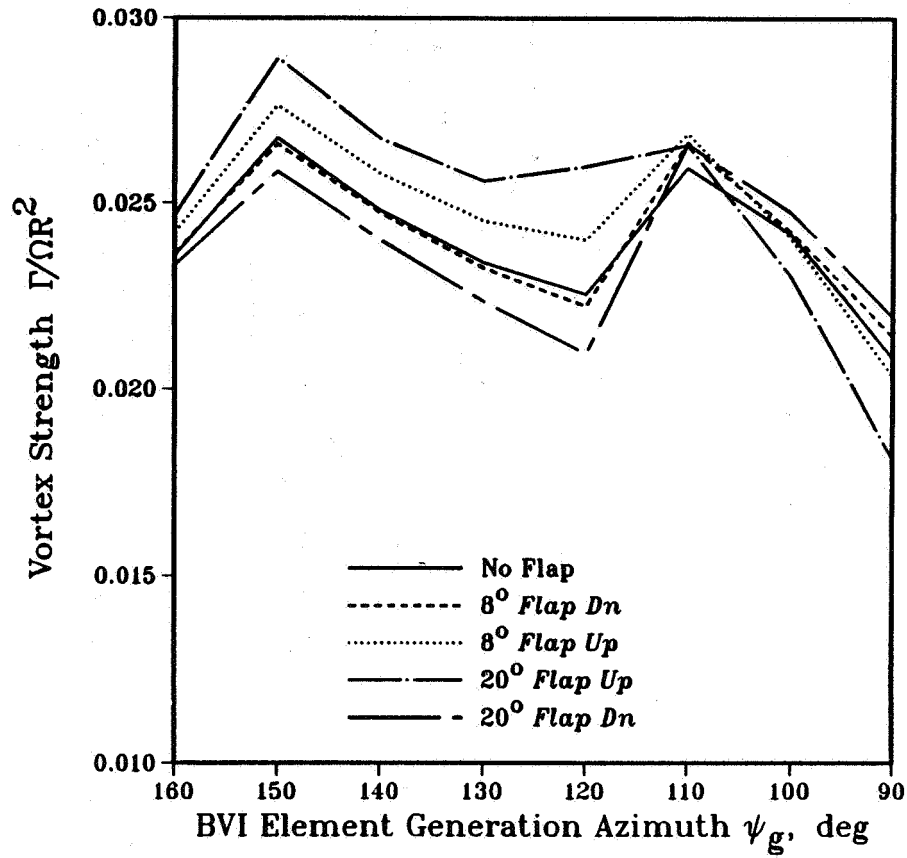
Fig. (39) Effects of the trailing edge flap on the CAMRAD/JA-predicted vortex strengths for the OLS model rotor during blade-vortex interactions (Mtip = 0.666, Mu = 0.147, rv/C = 0.20)
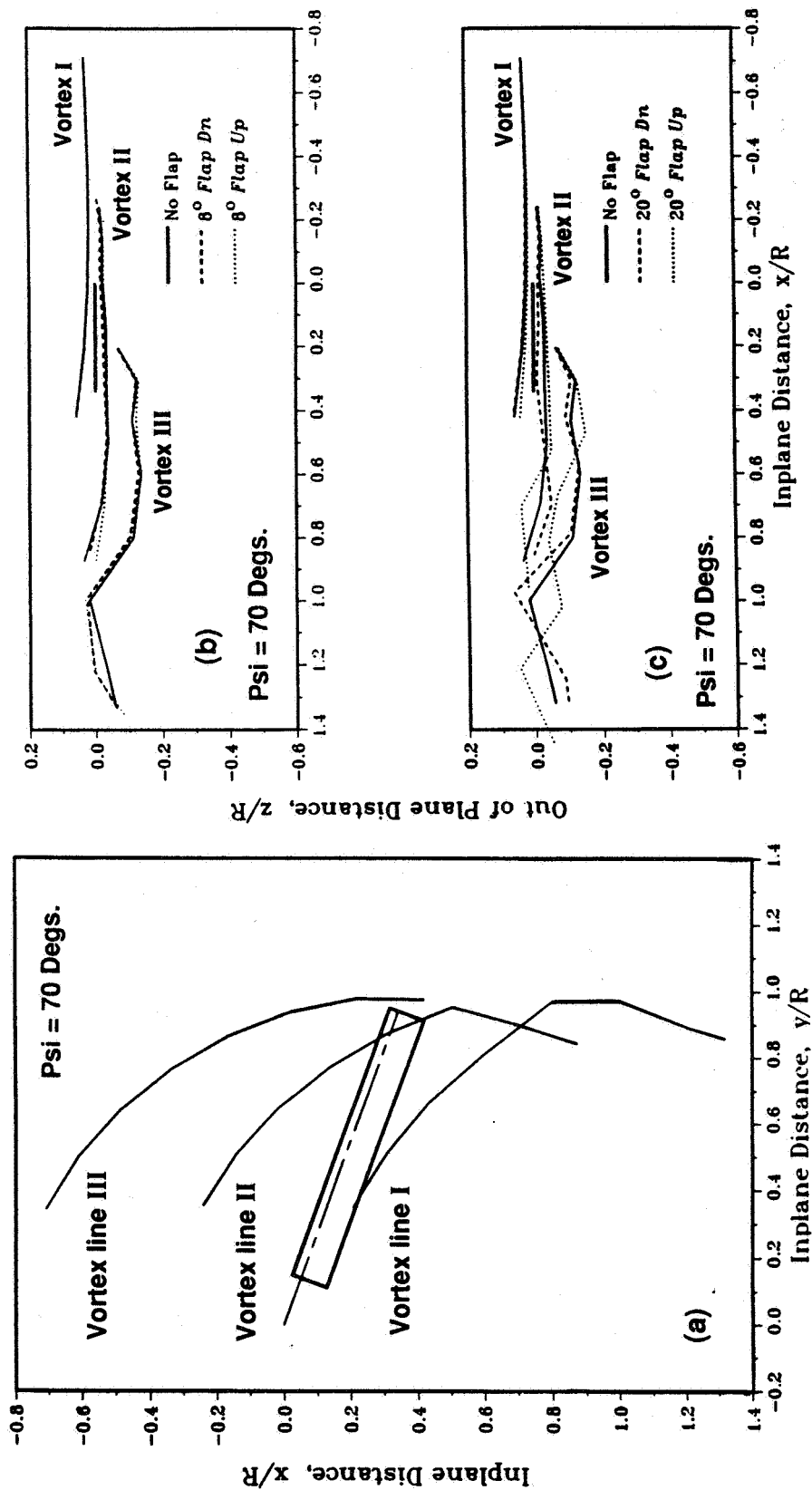
Fig. (40) Plan and side views of the CAMRAD/JA-predicted vortex-wake geometries for the OLS model rotor (three vortex interactions, Mtip = 0.666, Mu = 0.147)

120
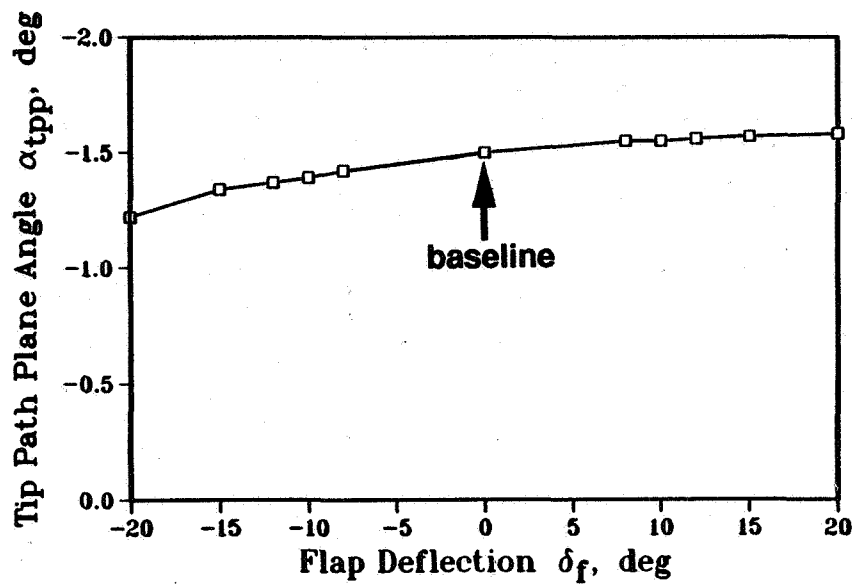
Fig. (41) Effects of the peak flap deflection on the CAMRAD/JA-predicted tip path plane angles for the OLS model rotor (total duration of flap deployment is held fixed at 30 degrees of rotor azimuthal travel)
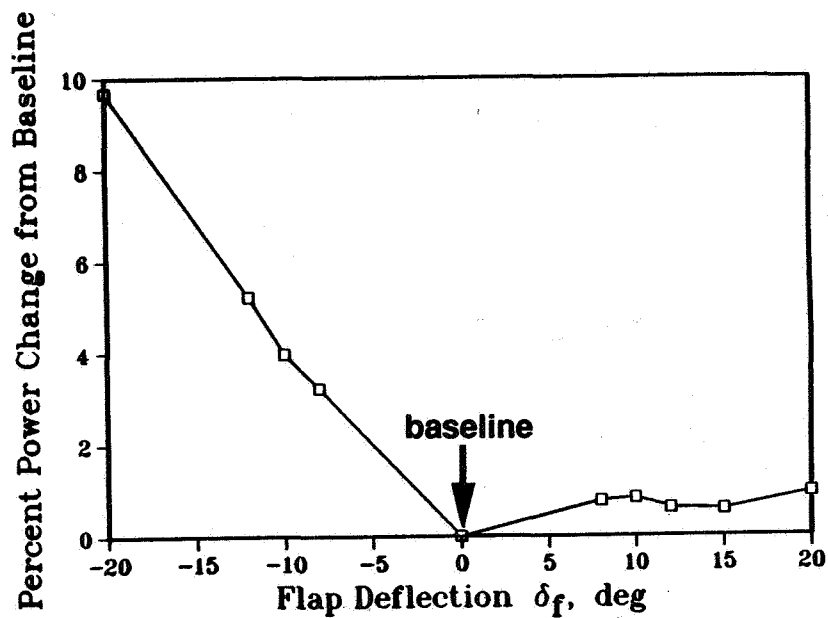
Fig. (42) Effects of the peak flap deflection on the CAMRAD/JA-predicted power requirements for the OLS model rotor (total duration of flap deployment is held fixed at 30 degrees of rotor azimuthal travel)
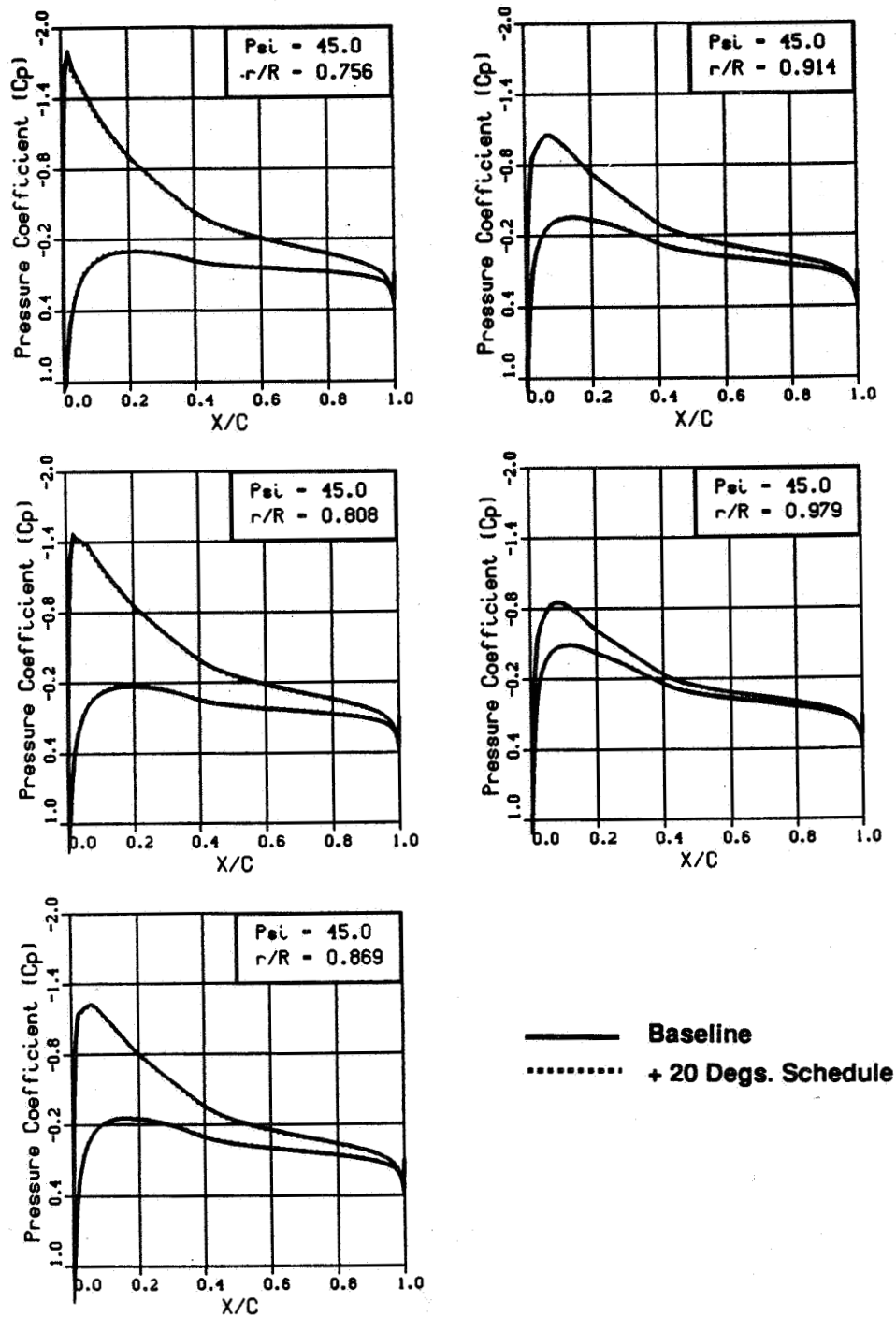
Fig. (43) Predicted surface pressures for the baseline and flapped model OLS rotors during self-generated blade-vortex interactions (3 vortex interactions, flap deployment duration = 30 degrees, trailing edge schedule +20 degrees, Mtip = 0.666, Mu = 0.147, rv/C = 0.20)
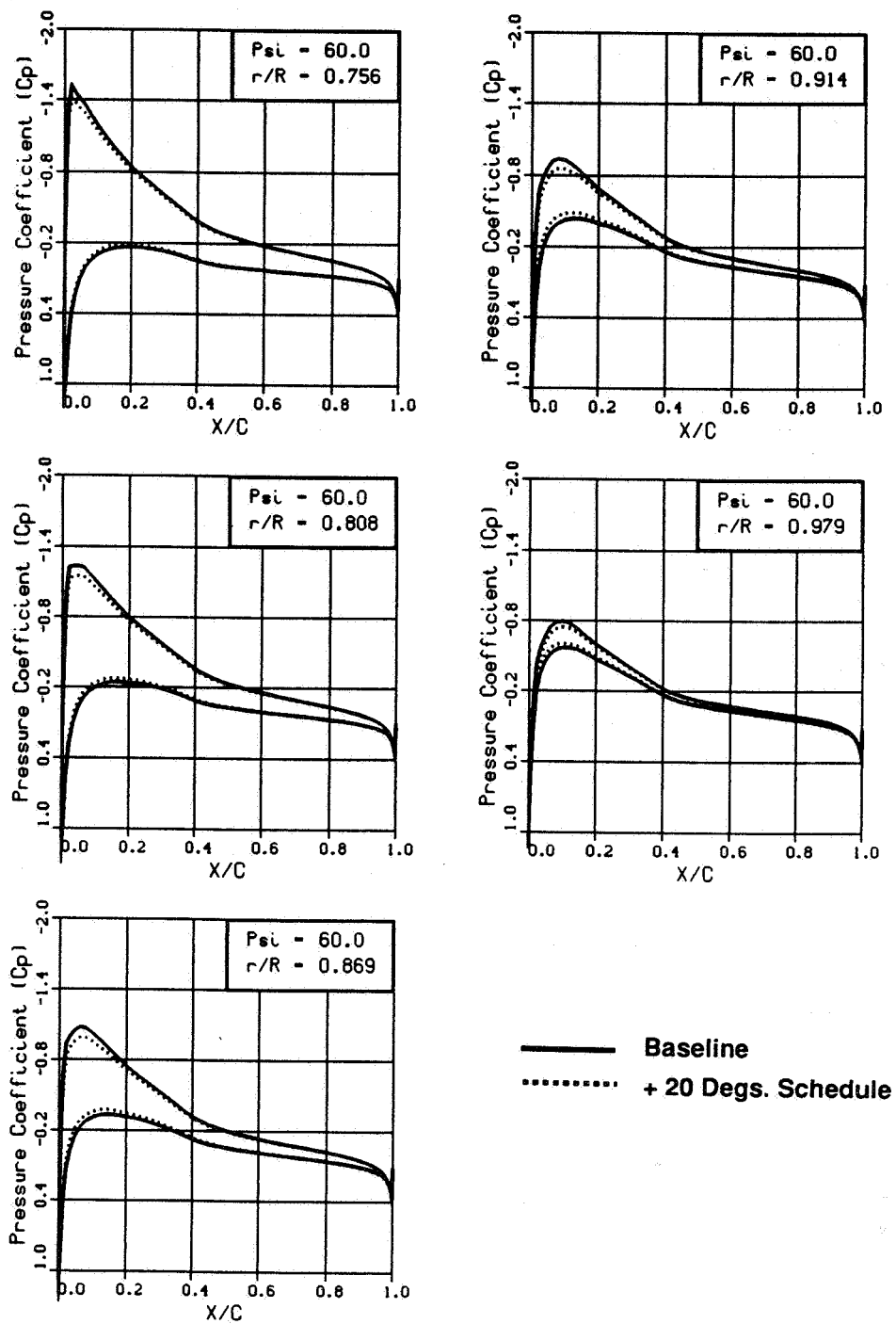
Fig. (43) continued
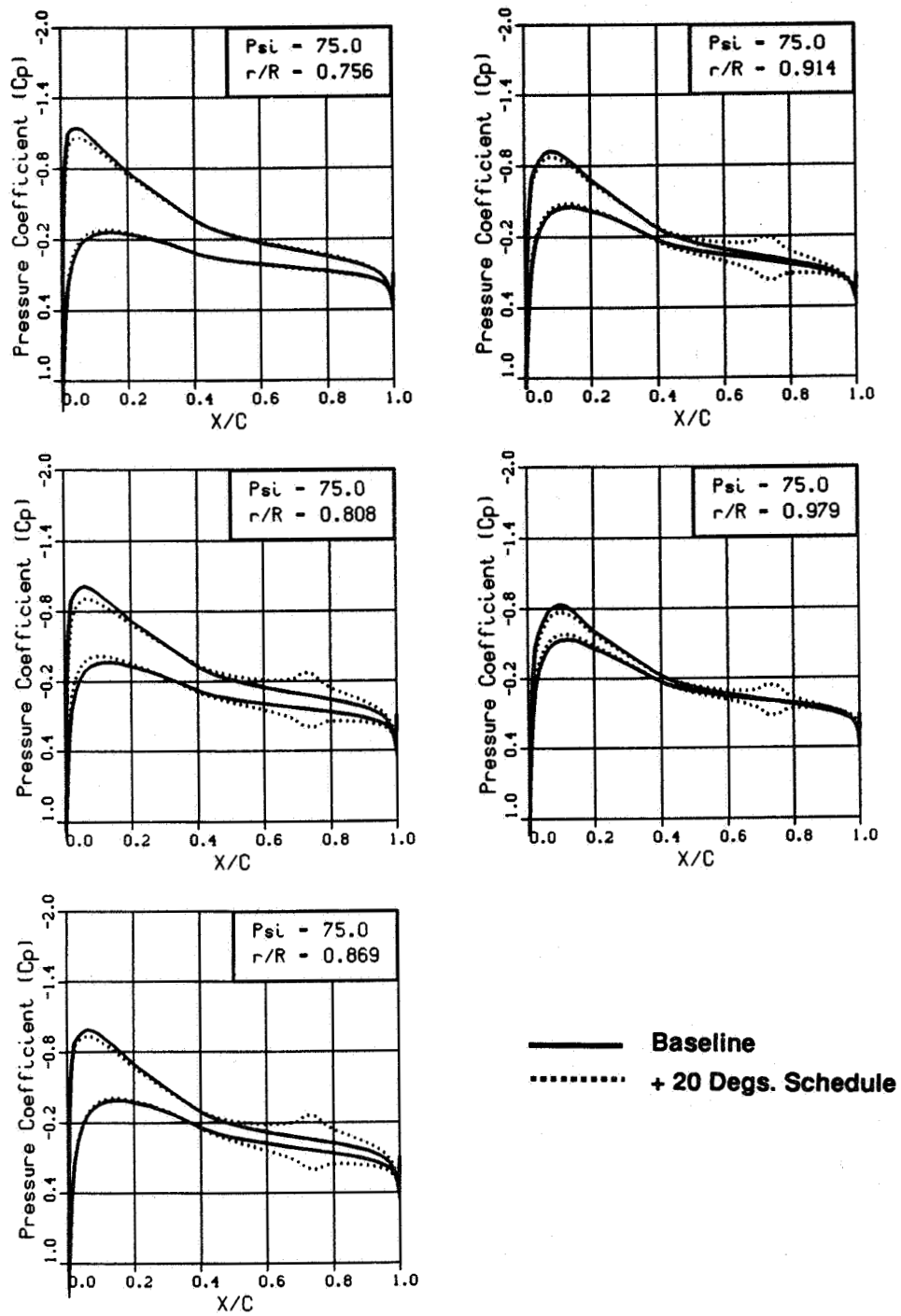
Fig. (43) continued
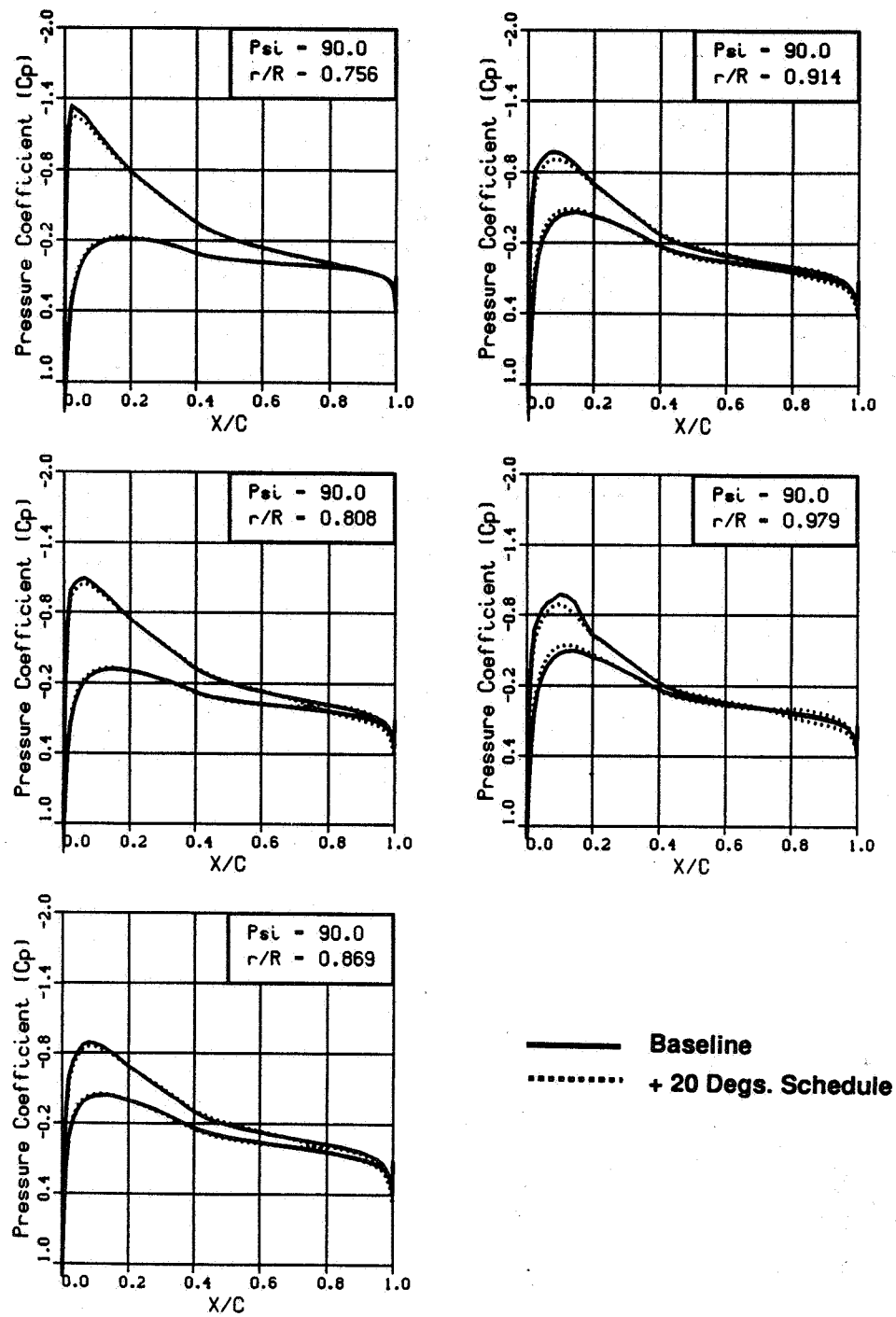
Fig. (43) continued
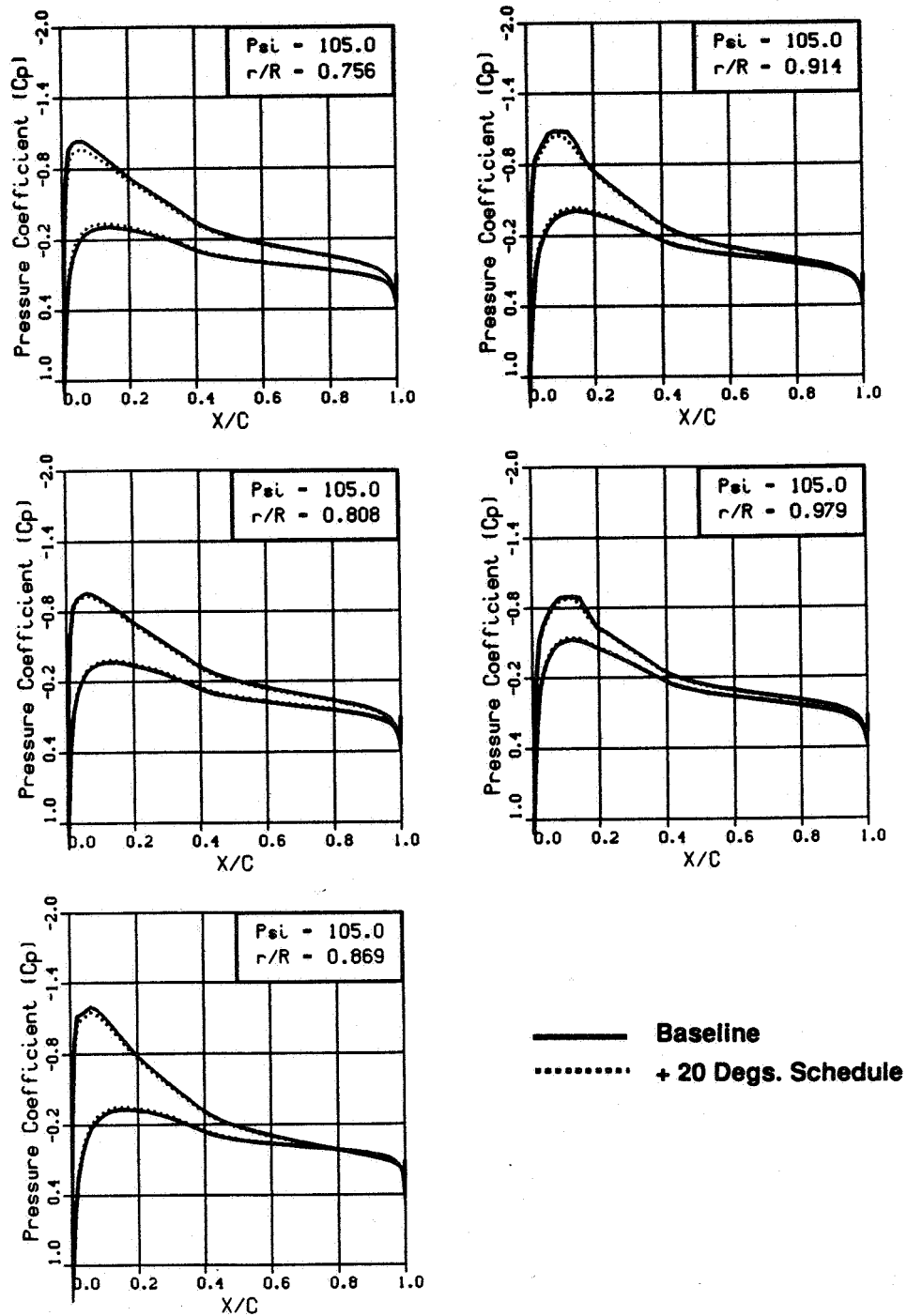
Fig. (43) concluded
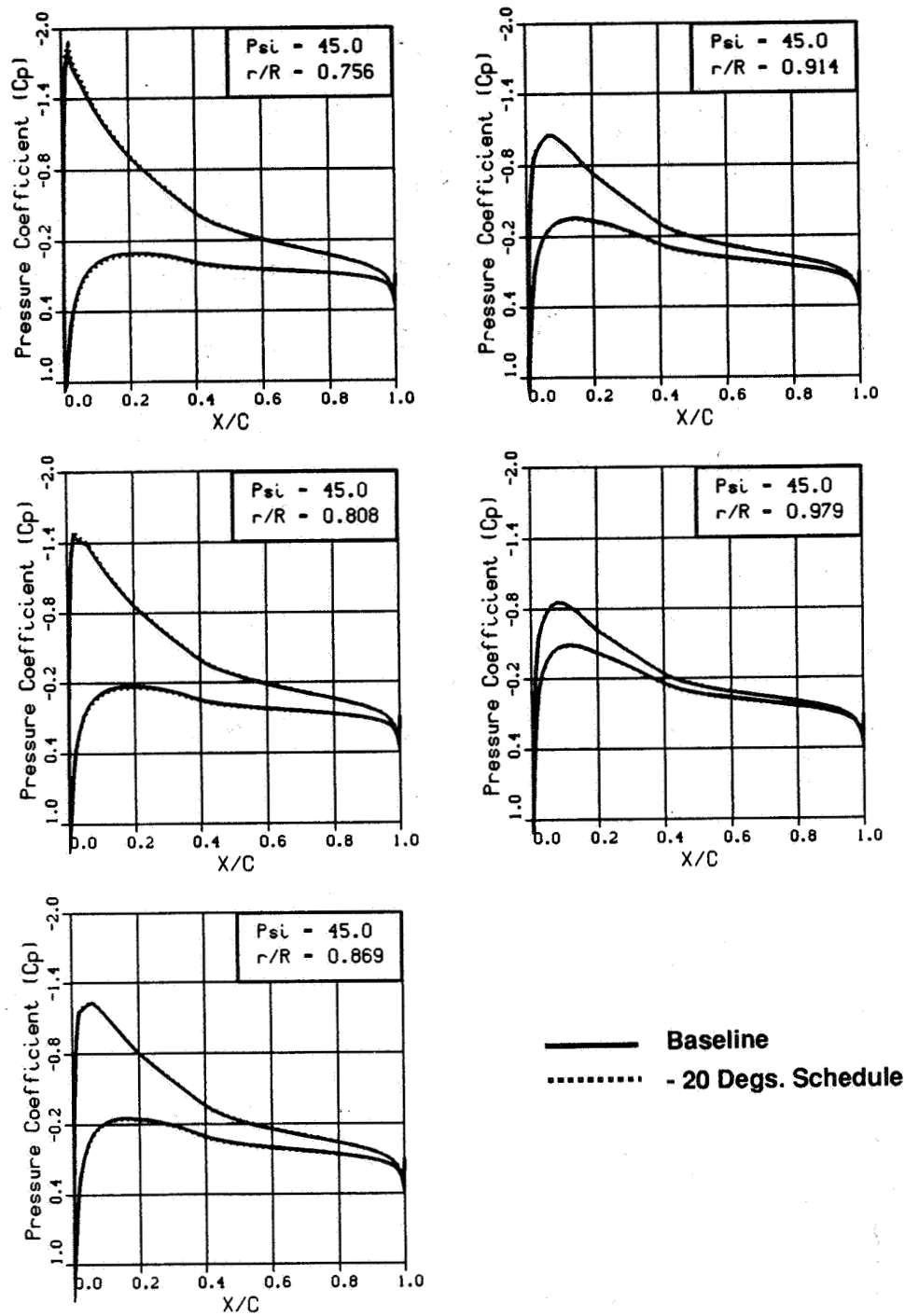
Fig. (44) Predicted surface pressures for the baseline and flapped model OLS rotors during self-generated blade-vortex interactions (3 vortex interactions, flap deployment duration = 30 degrees, trailing edge schedule -20 degrees, Mtip = 0.666, Mu = 0.147, rv/C = 0.20)

Fig. (44) continued

128
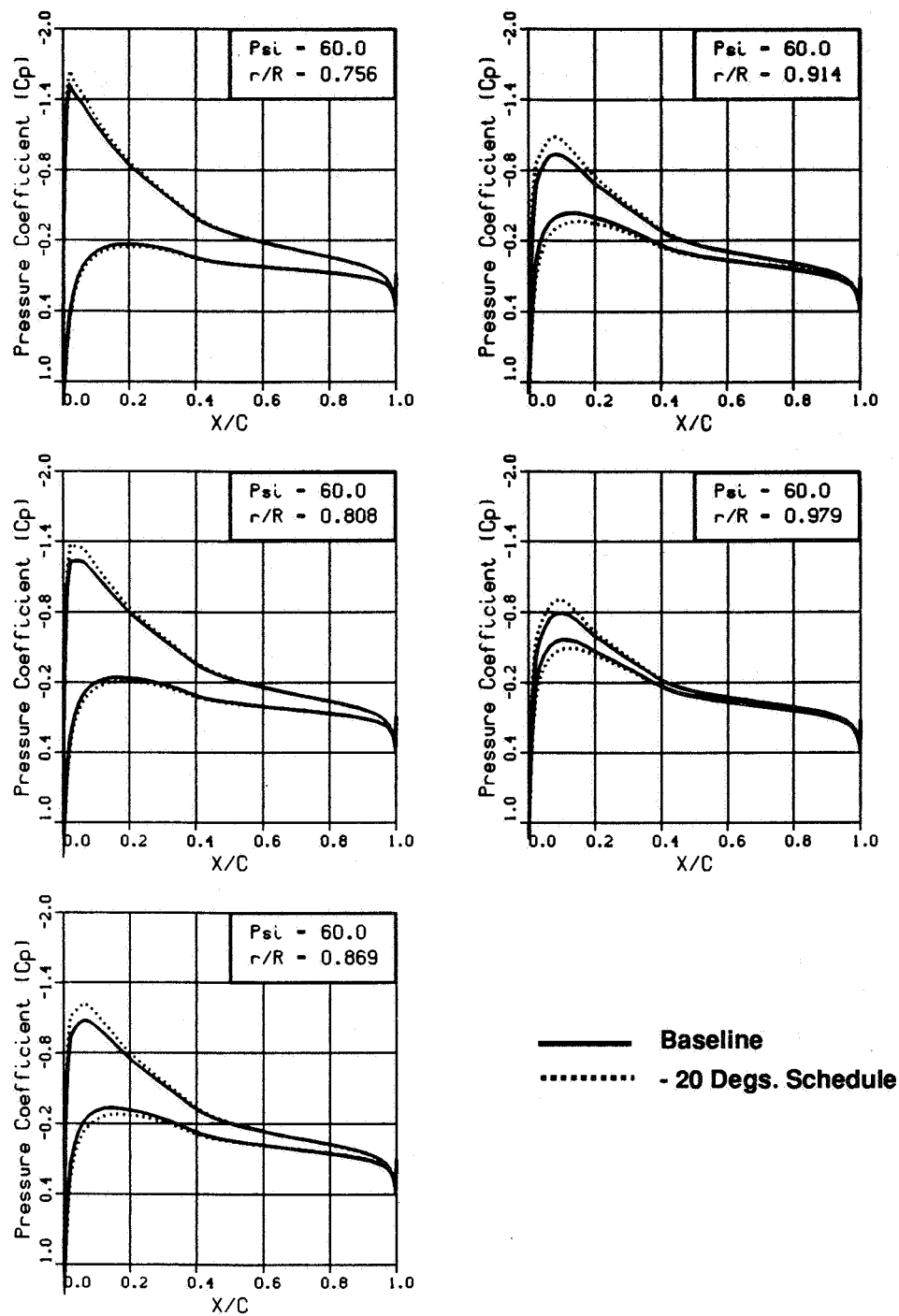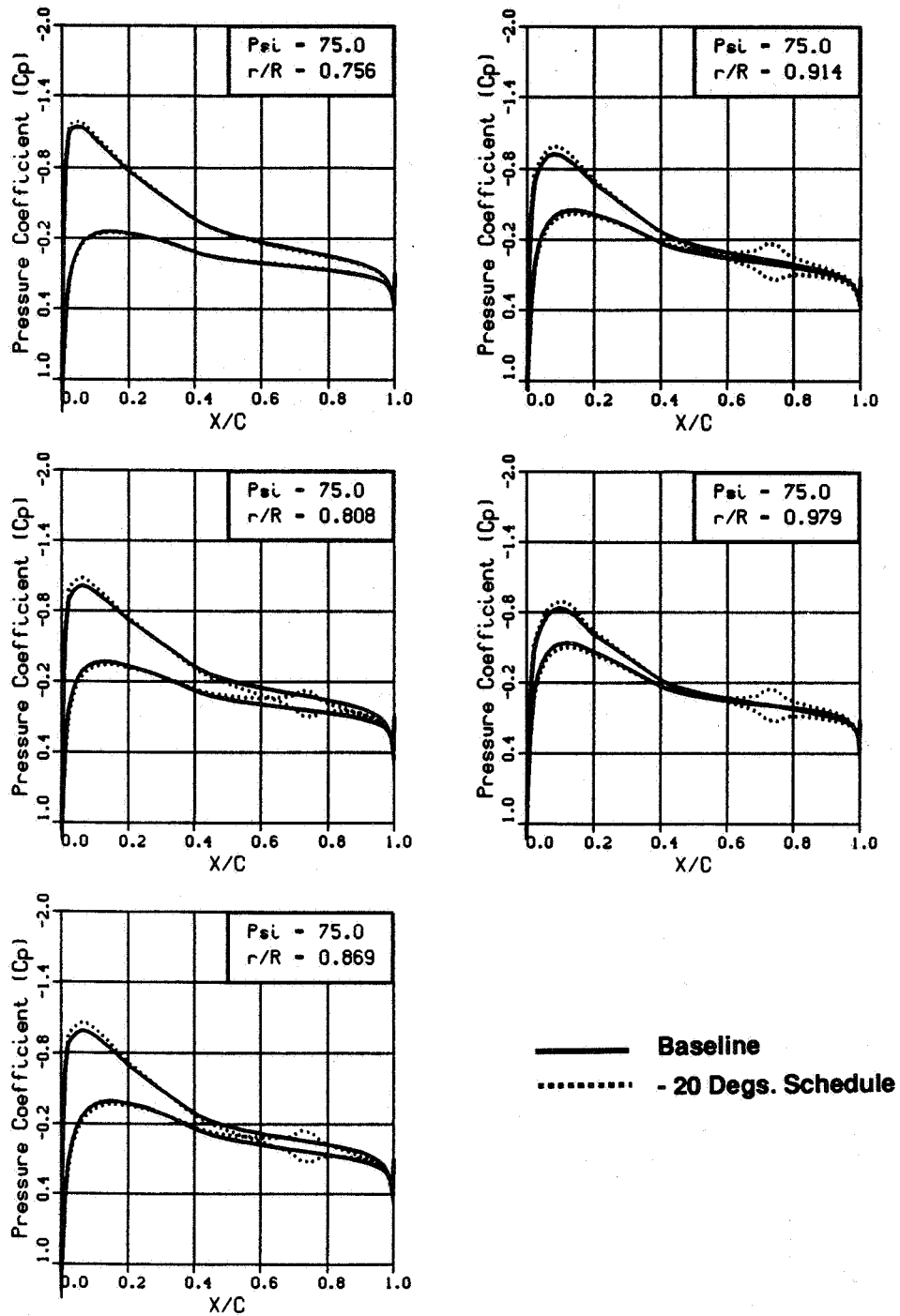
Fig. (44) continued
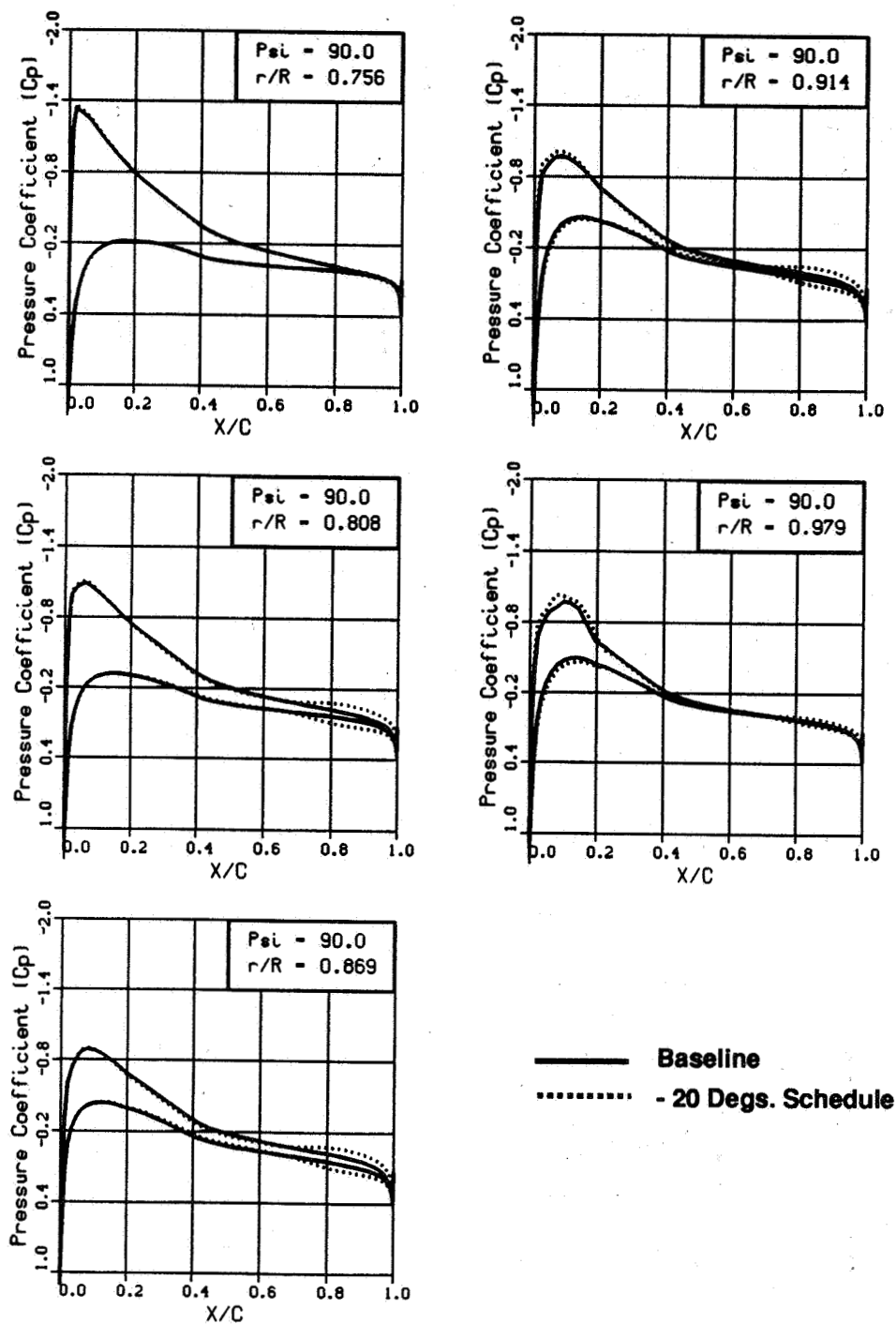
Fig. (44) continued
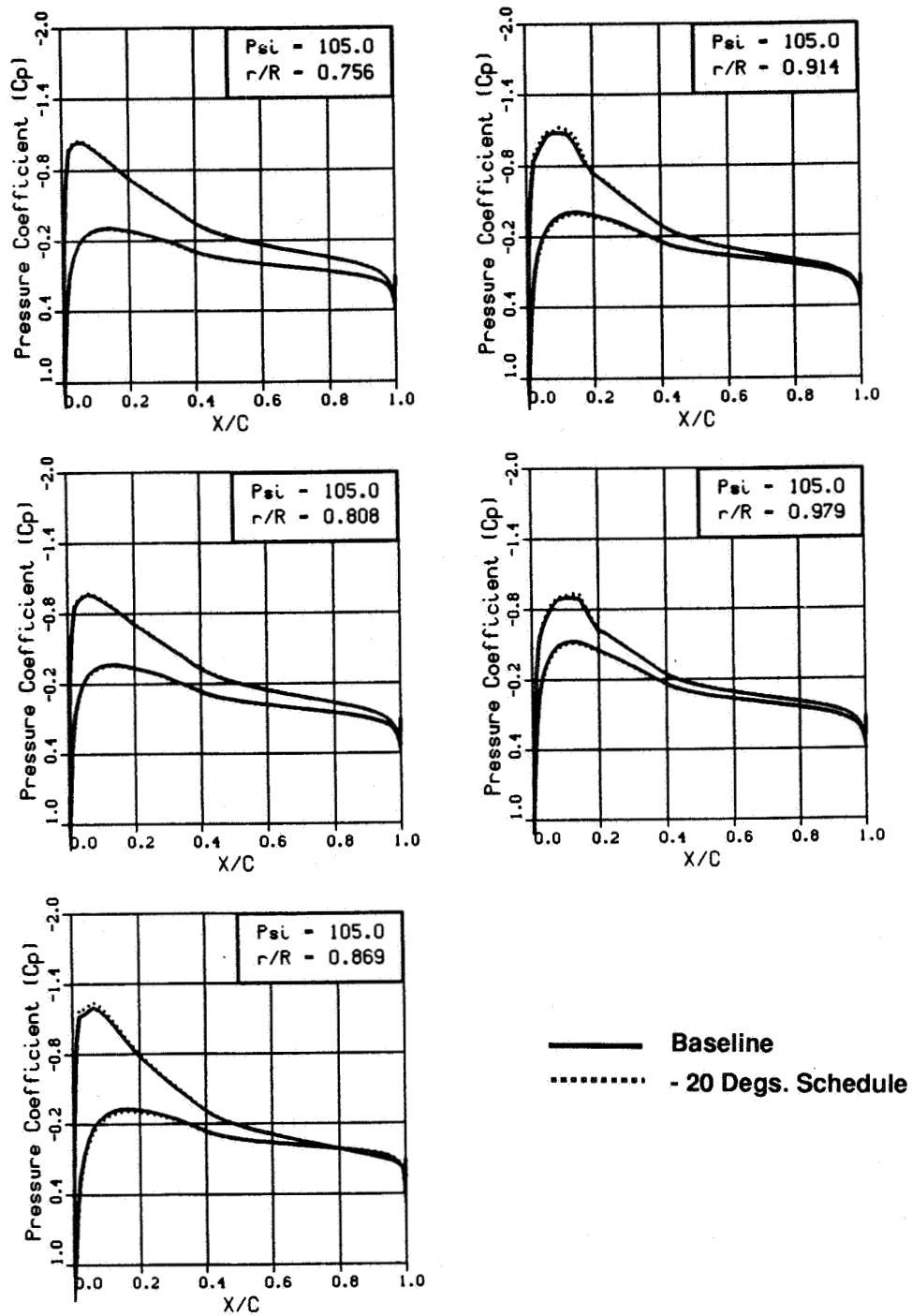
Fig. (44) concluded
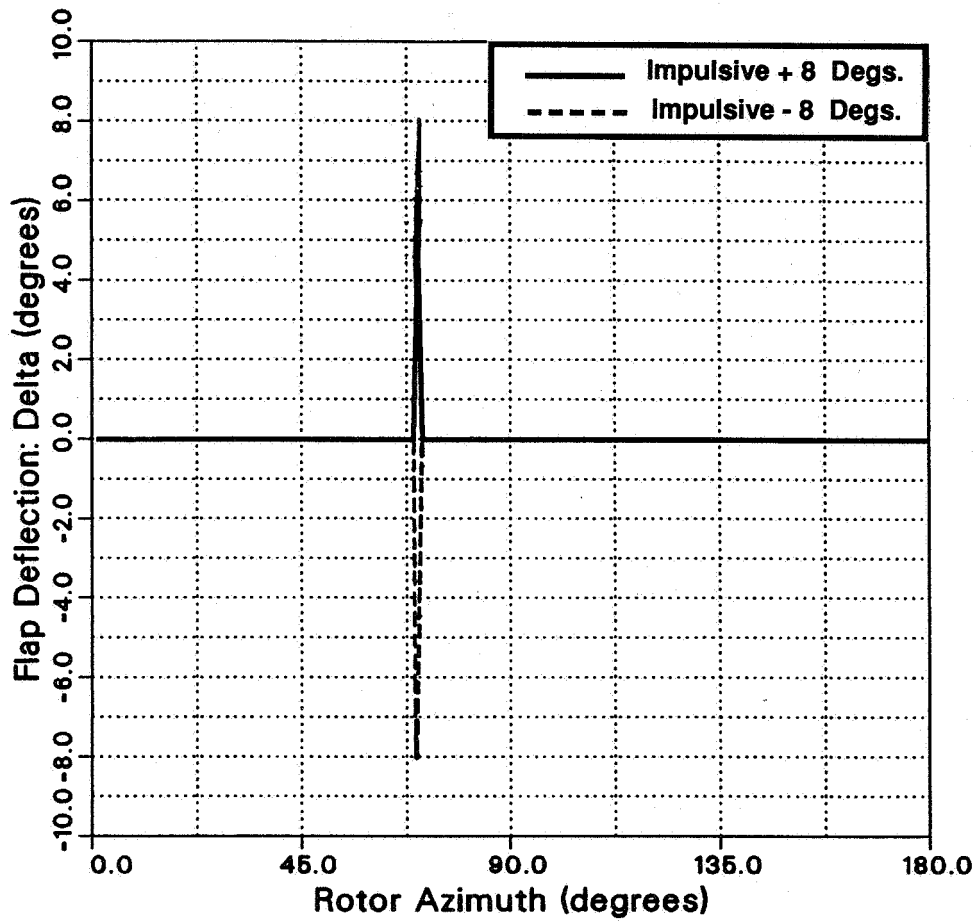
Fig. (45) Impulsive trailing edge flap schedules utilized in the numerical simulations
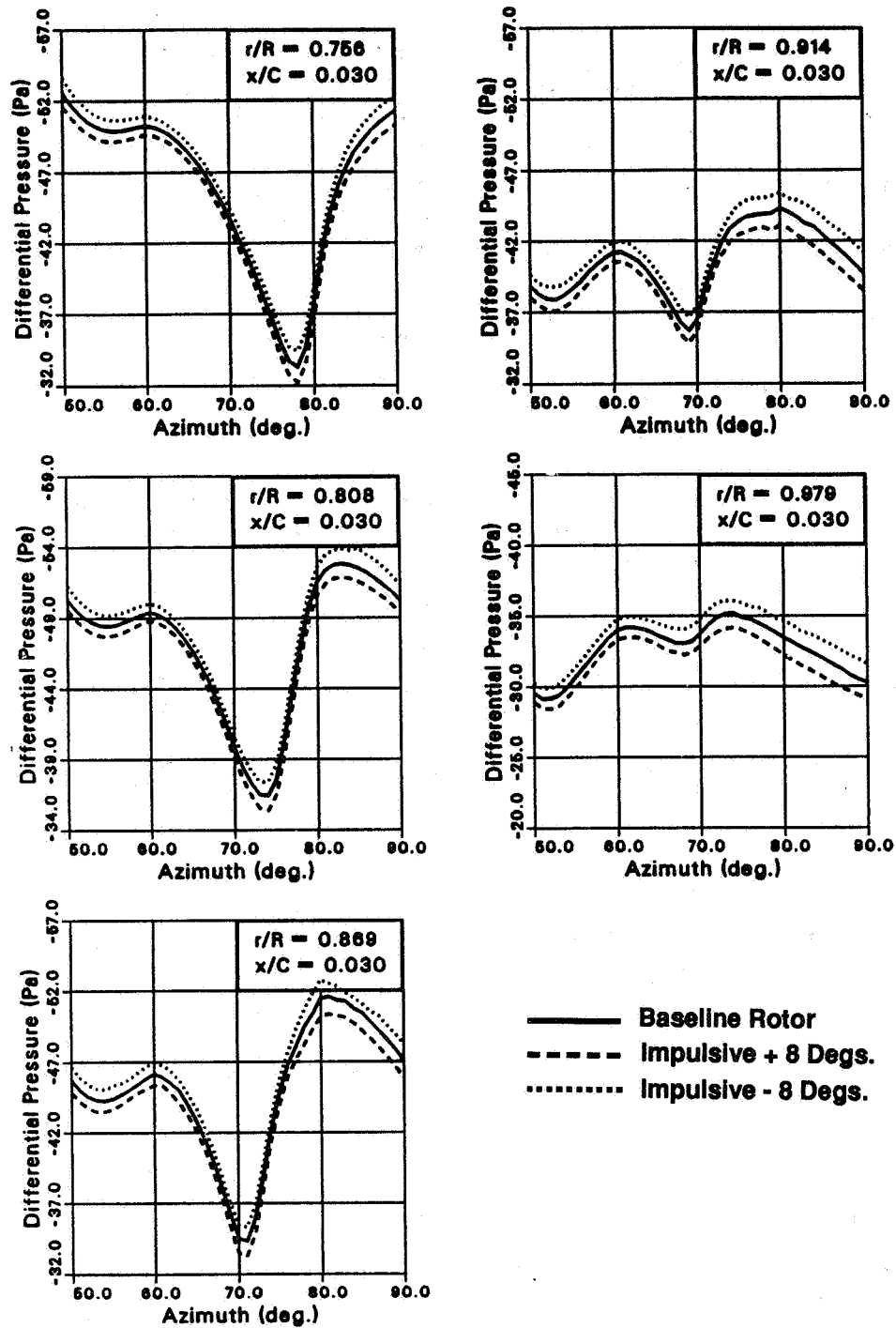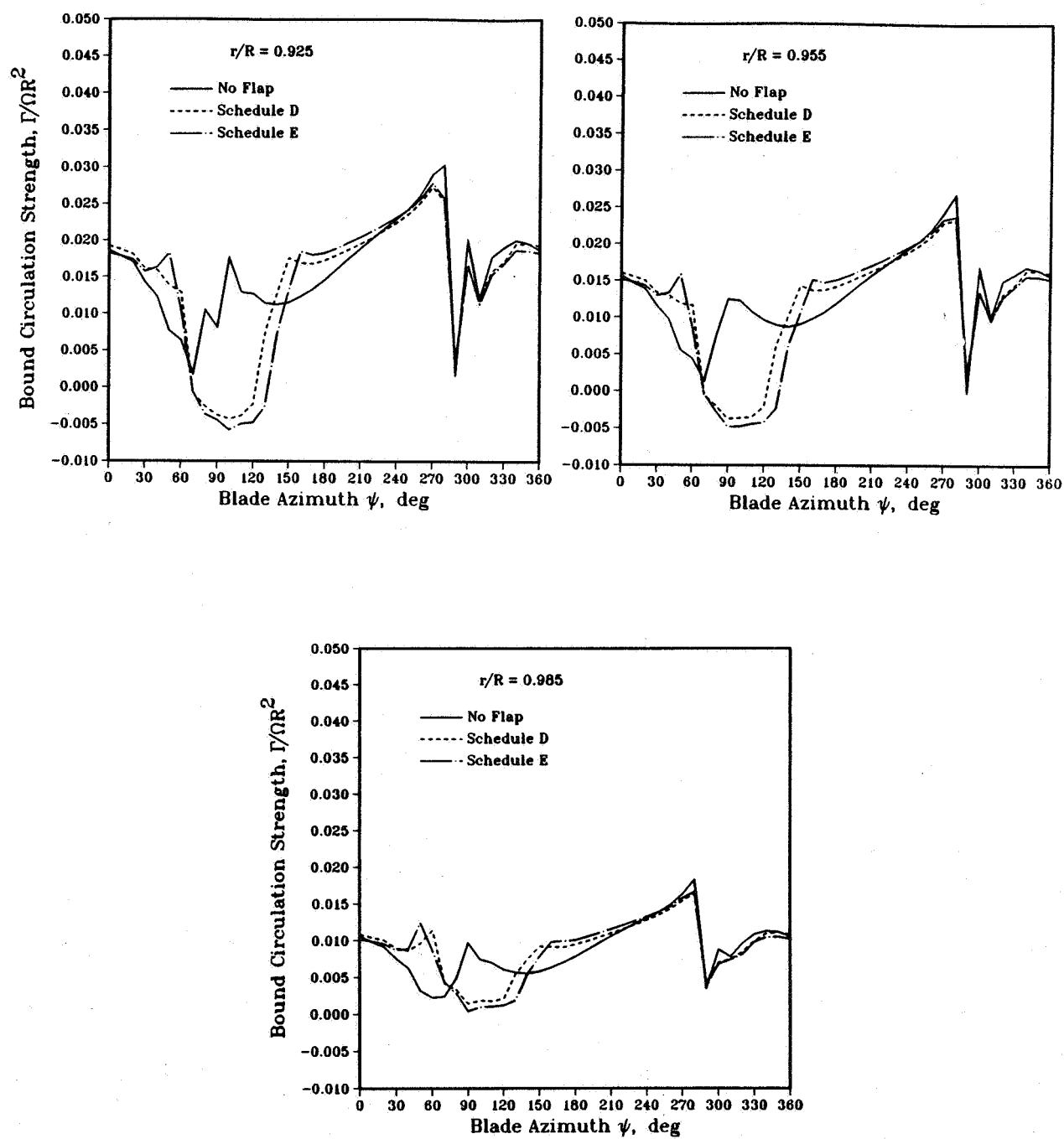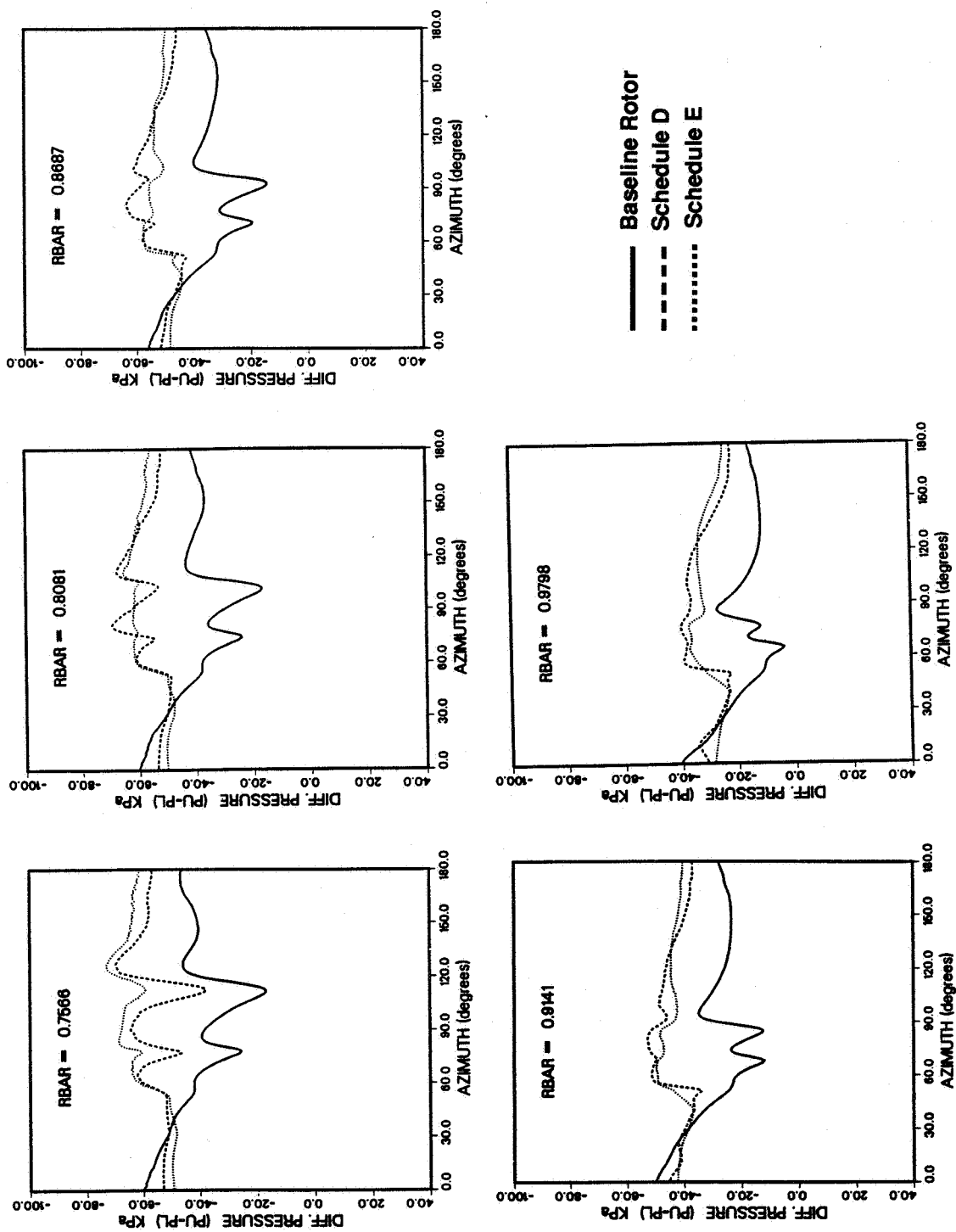
Fig. (46) Effects of the trailing edge flap on the RFS2.BVI-predicted differential pressures for the model OLS rotor during self-generated blade-vortex interactions (3 vortex interactions, Mtip = 0.666, Mu = 0.147, x/C = 0.03, rv/C = 0.20)
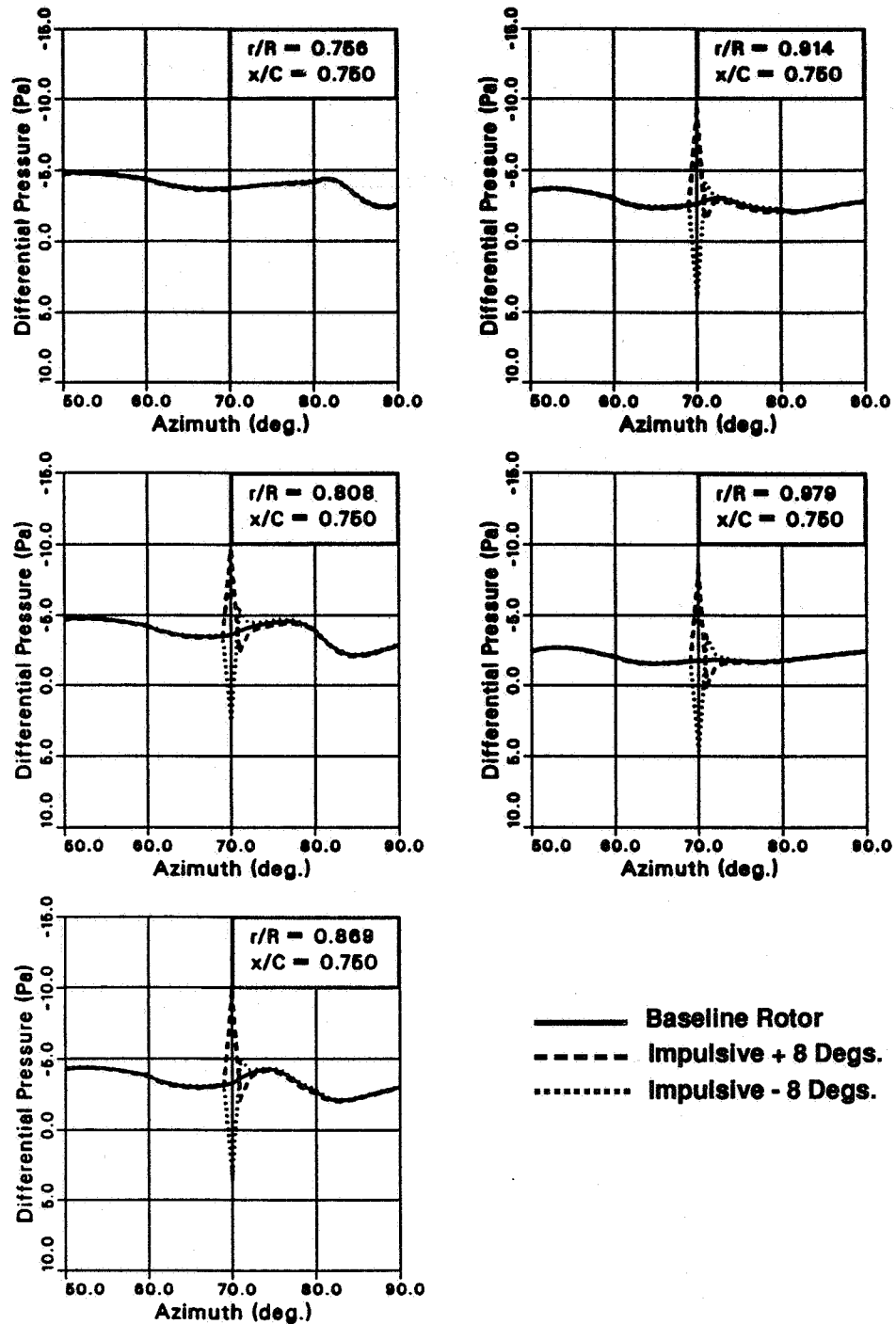
Fig. (47) Effects of the trailing edge flap on the RFS2.BVI-predicted differential pressures for the model OLS rotor during self-generated blade-vortex interactions (3 vortex interactions, Mtip = 0.666, Mu = 0.147, x/C = 0.75, rv/C = 0.20)
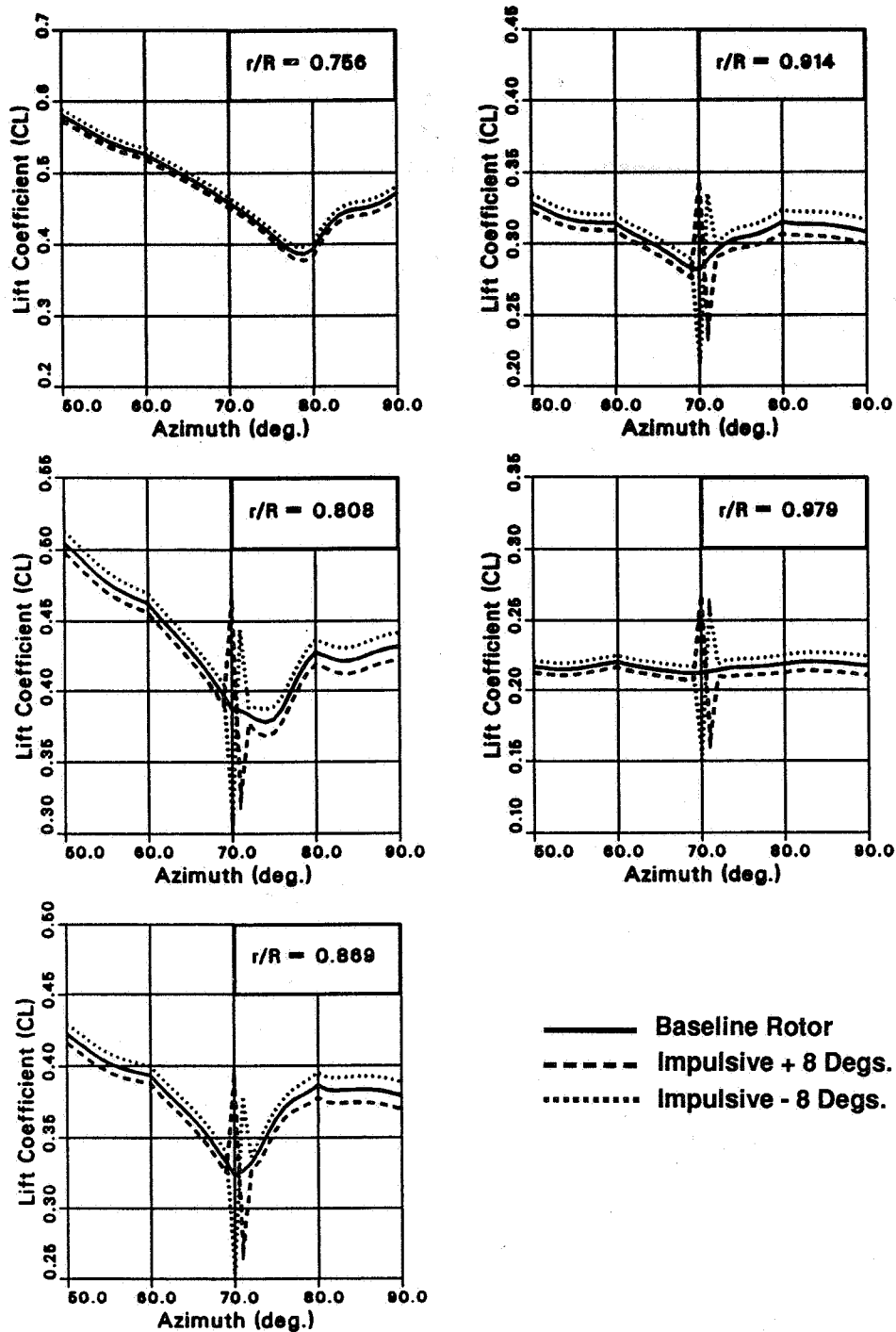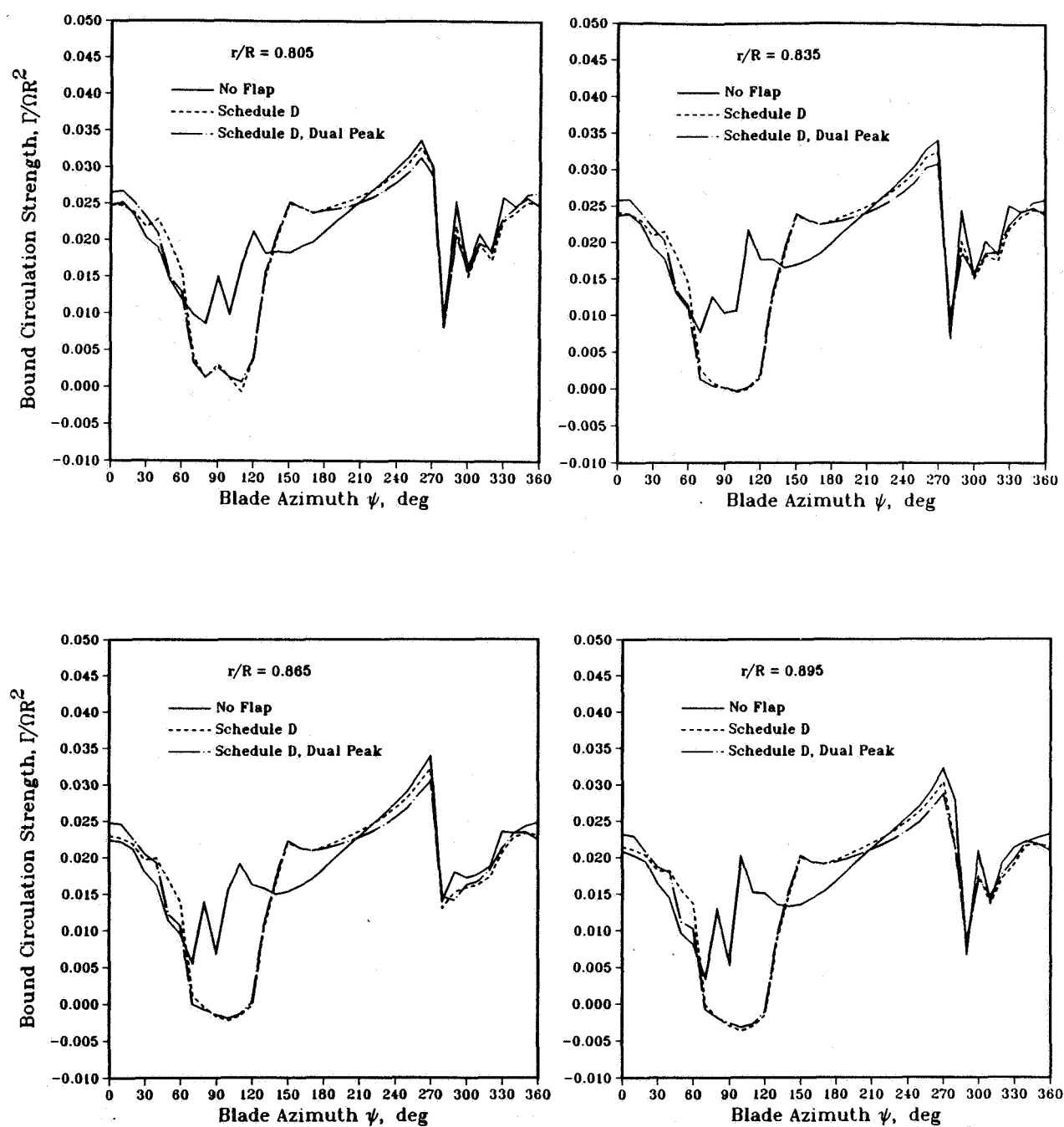
Fig. (48) Effects of the trailing edge flap on the predicted sectional lift forces for the model OLS rotor during self-generated blade-vortex interactions (3 vortex interactions, Mtip = 0.666, Mu = 0.147, rv/C = 0.20)
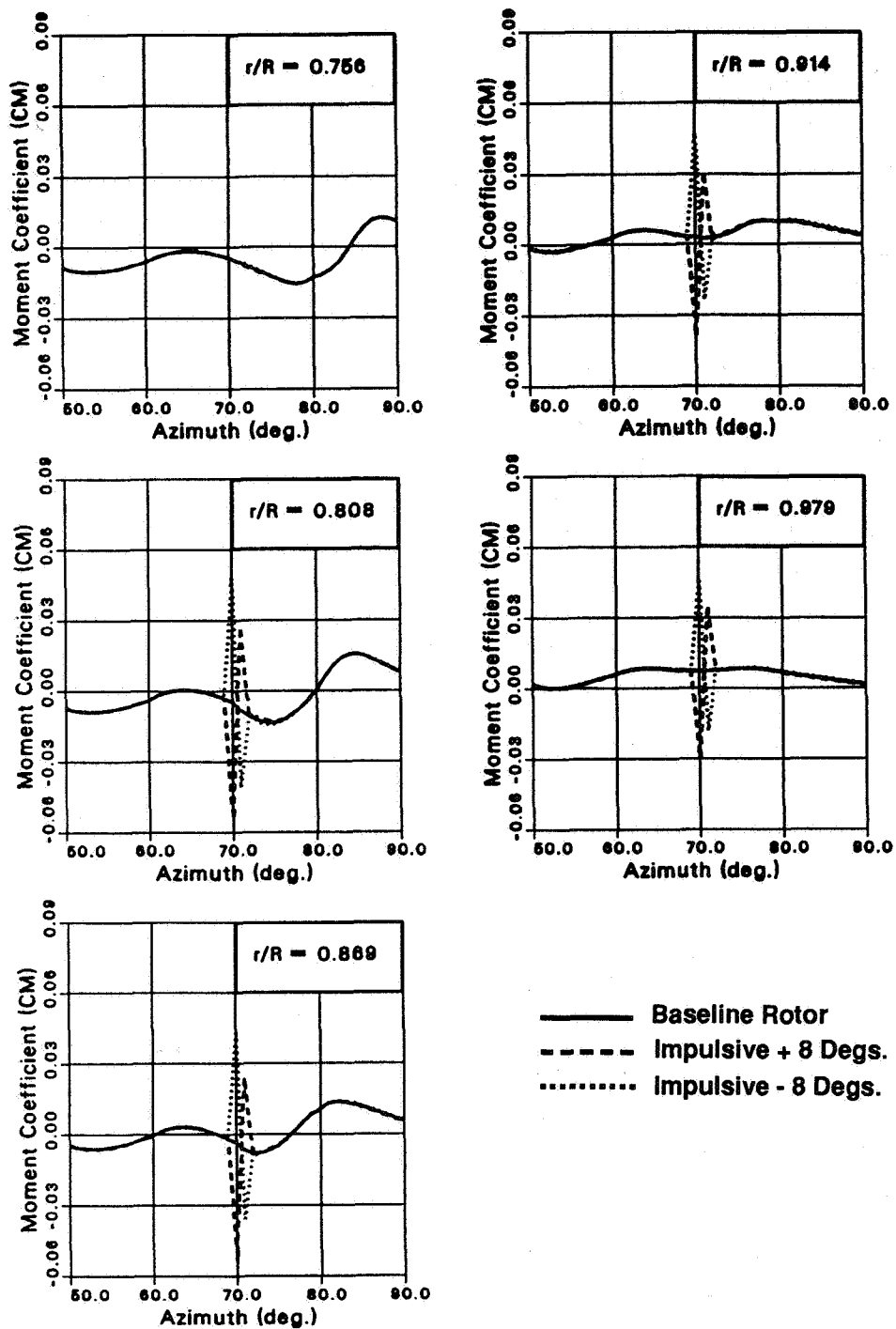
Fig. (49) Effects of the trailing edge flap on the predicted sectional moments for the model OLS rotor during self-generated blade-vortex interactions (3 vortex interactions, Mtip = 0.666, Mu = 0.147, rv/C = 0.20)

136
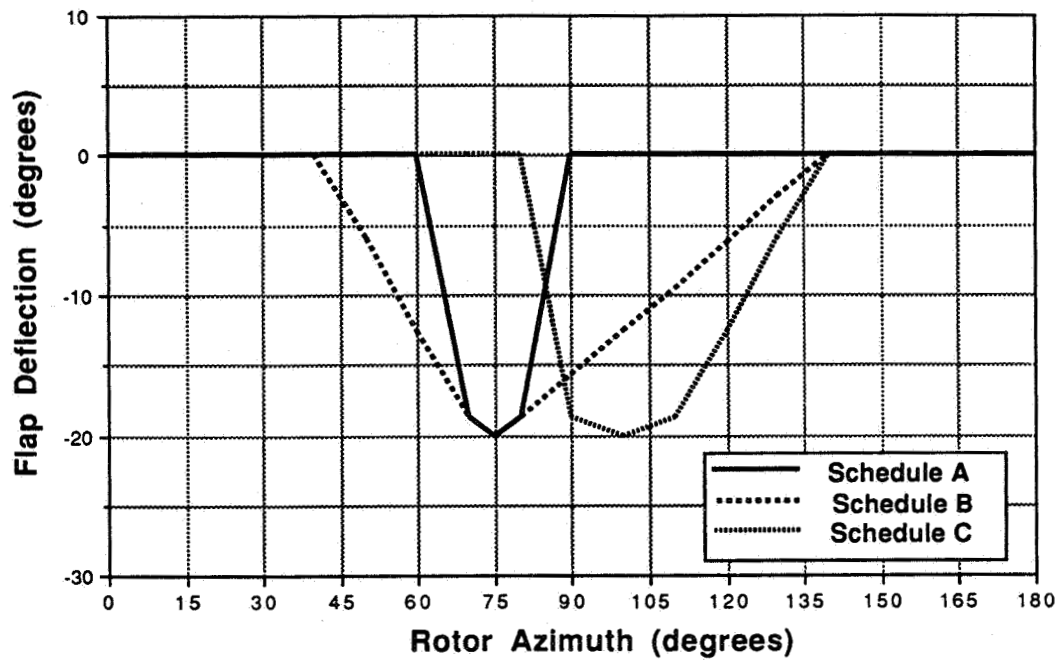
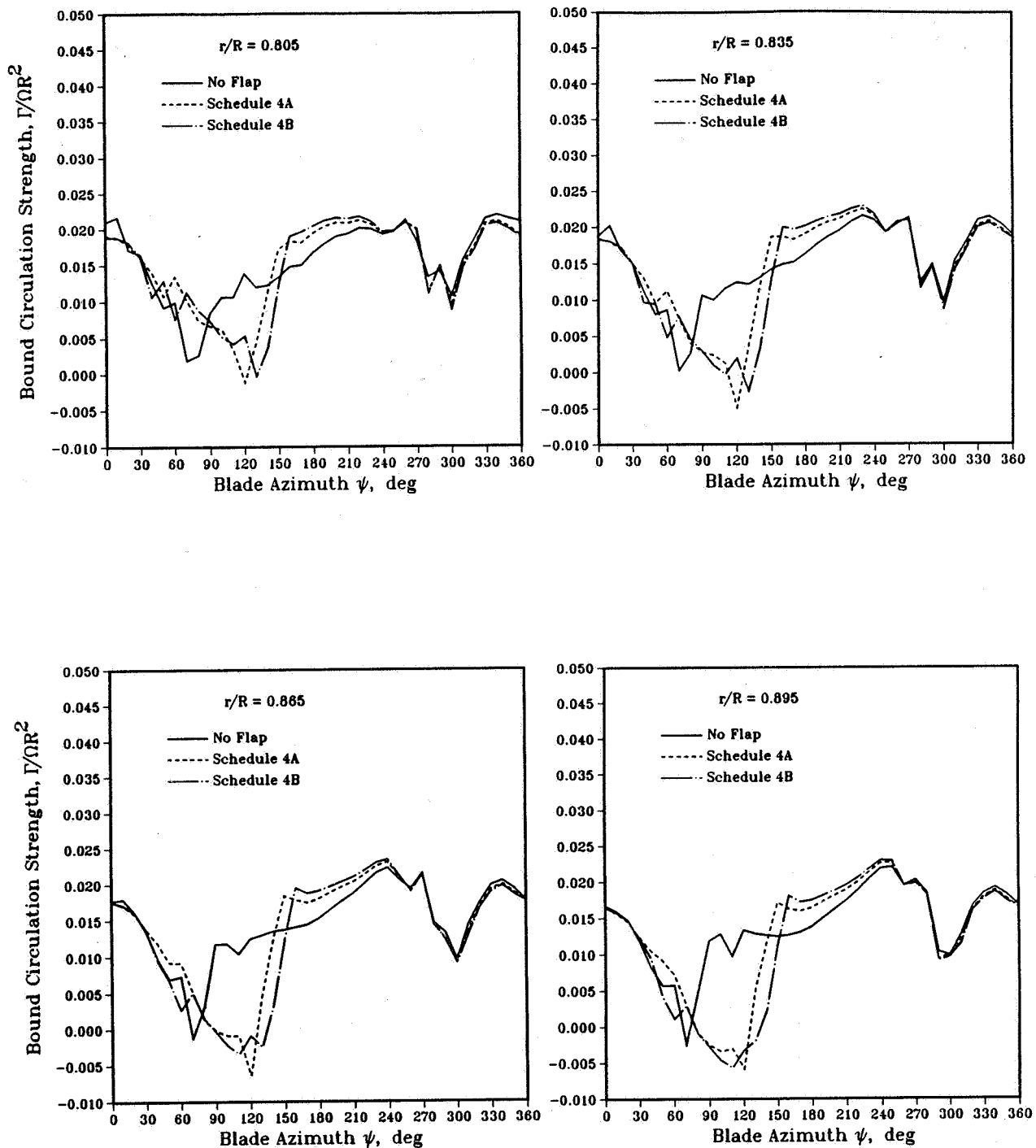Fig. (50) Variation of the trailing edge flap deflection angles as a function of blade azimuth for schedules A, B, and C
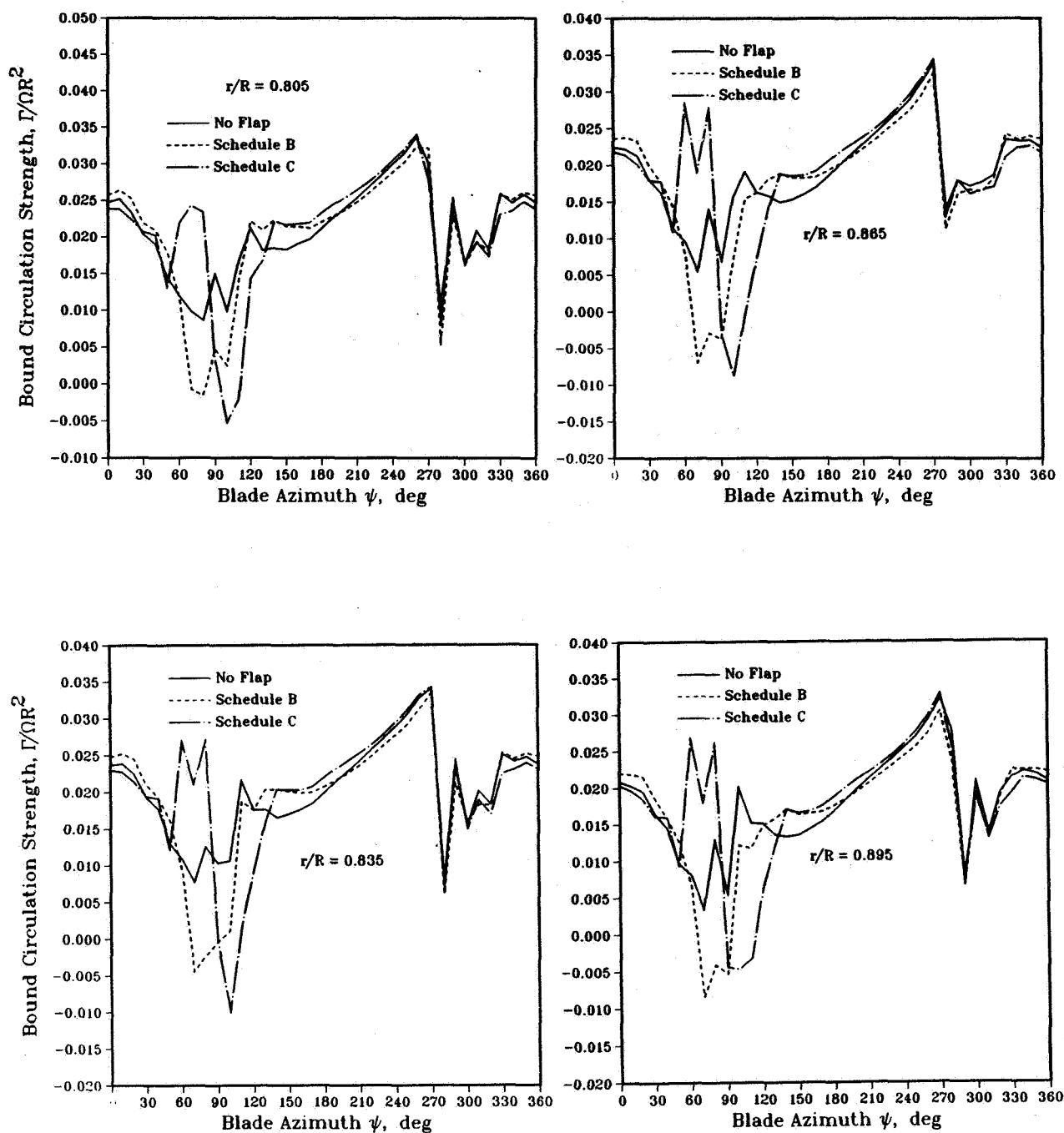
Fig. (51) Effects of the trailing edge flap on the CAMRAD/JA-predicted bound circulation distributions for the OLS model rotor during blade-vortex interactions (Mtip = 0.666, Mu = 0.147, rv/C = 0.20)

138
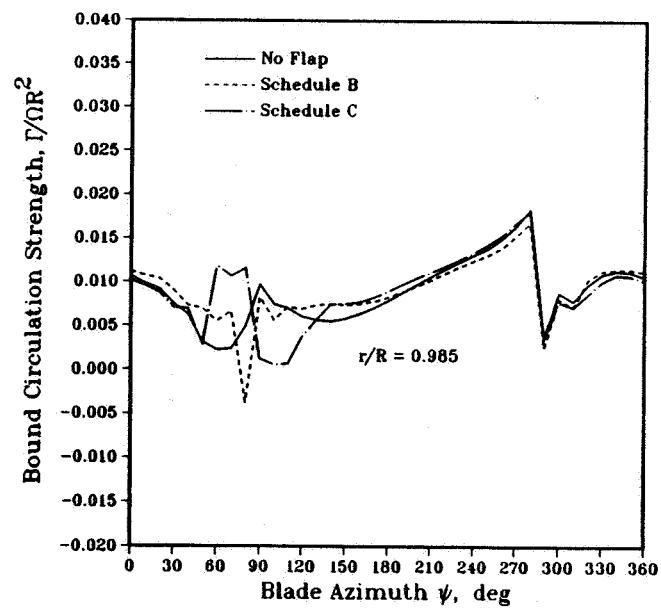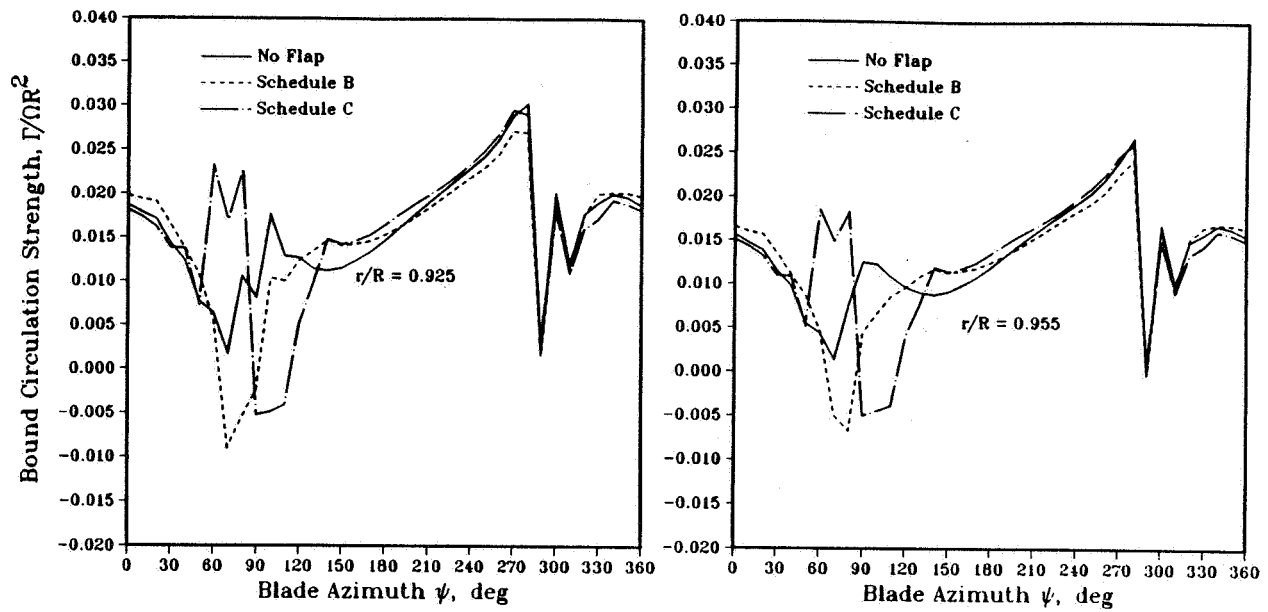
Fig. (51) concluded
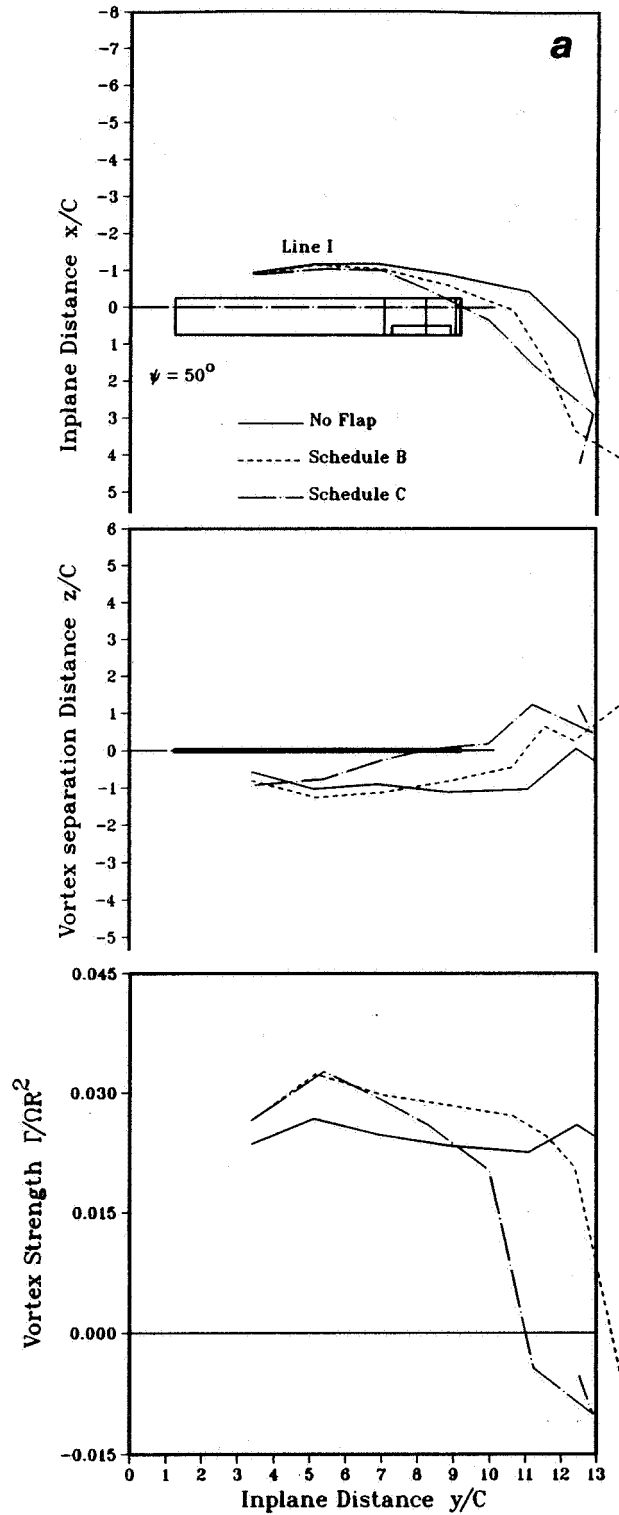
Fig. (52) Effects of the trailing edge flap on the CAMRAD/JA-predicted vortex wake geometry and strength for the OLS model rotor during blade-vortex interactions (Mtip = 0.666, Mu = 0.147, rv/C = 0.20)
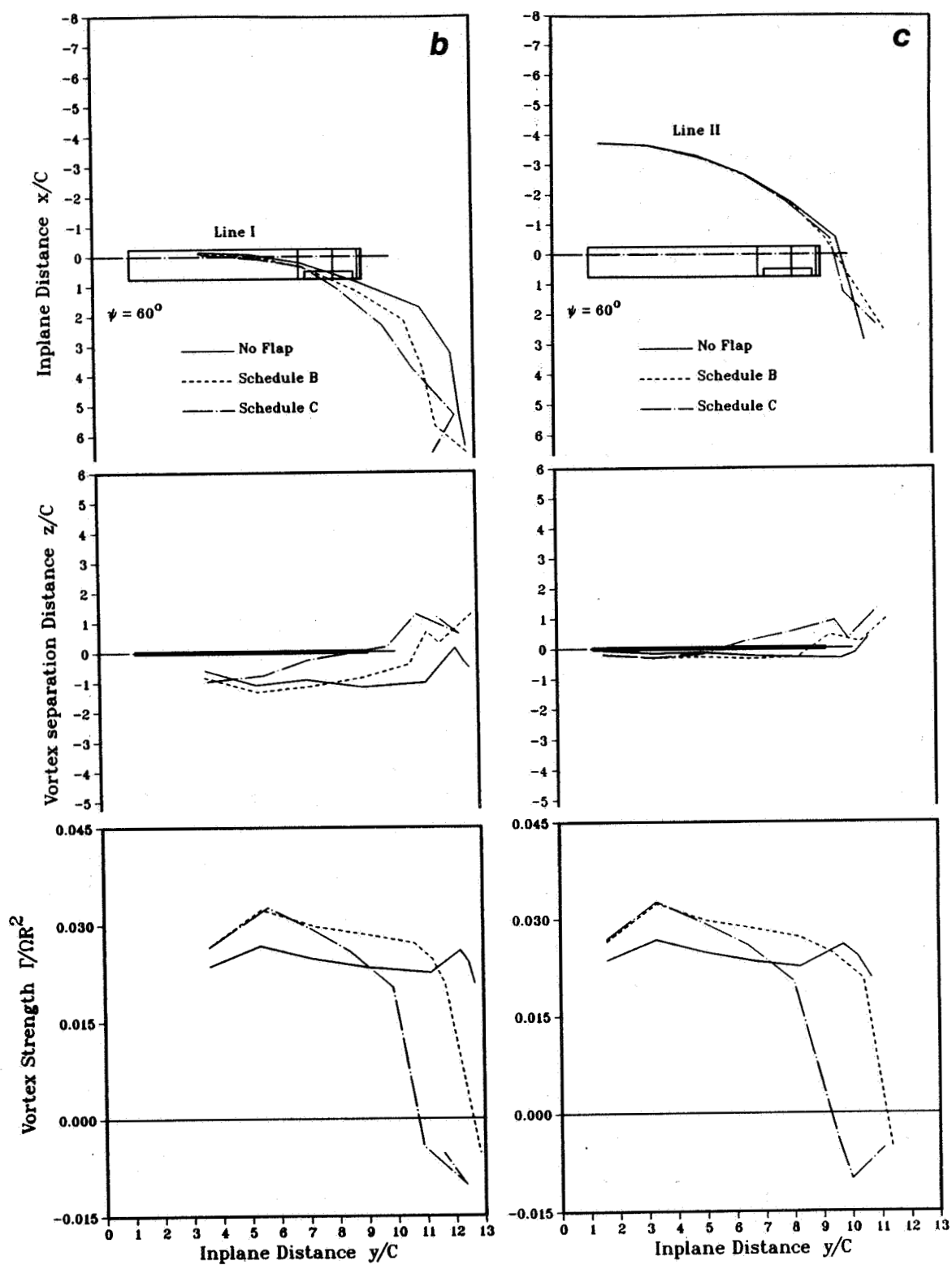
Fig. (52) continued
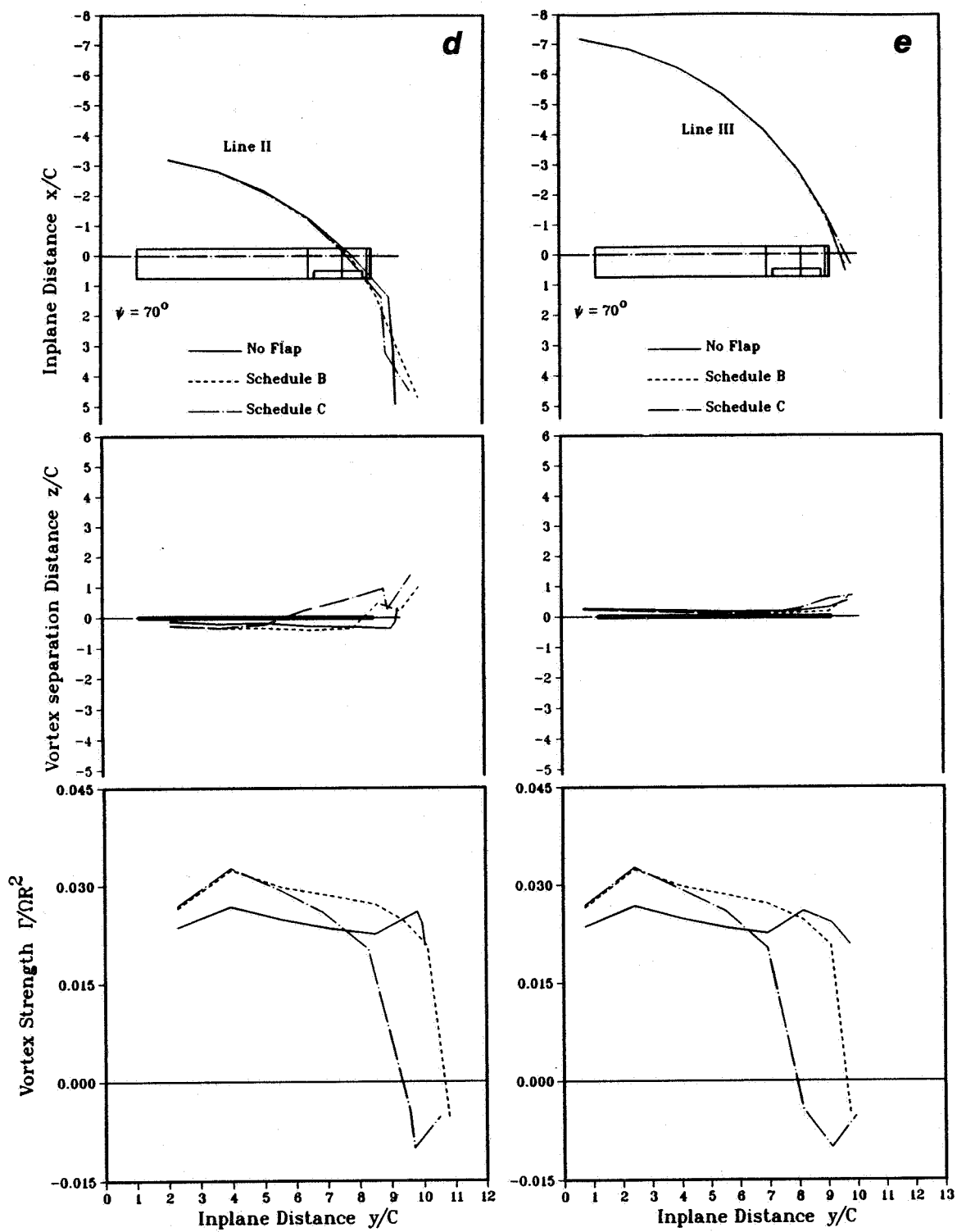
Fig. (52) continued
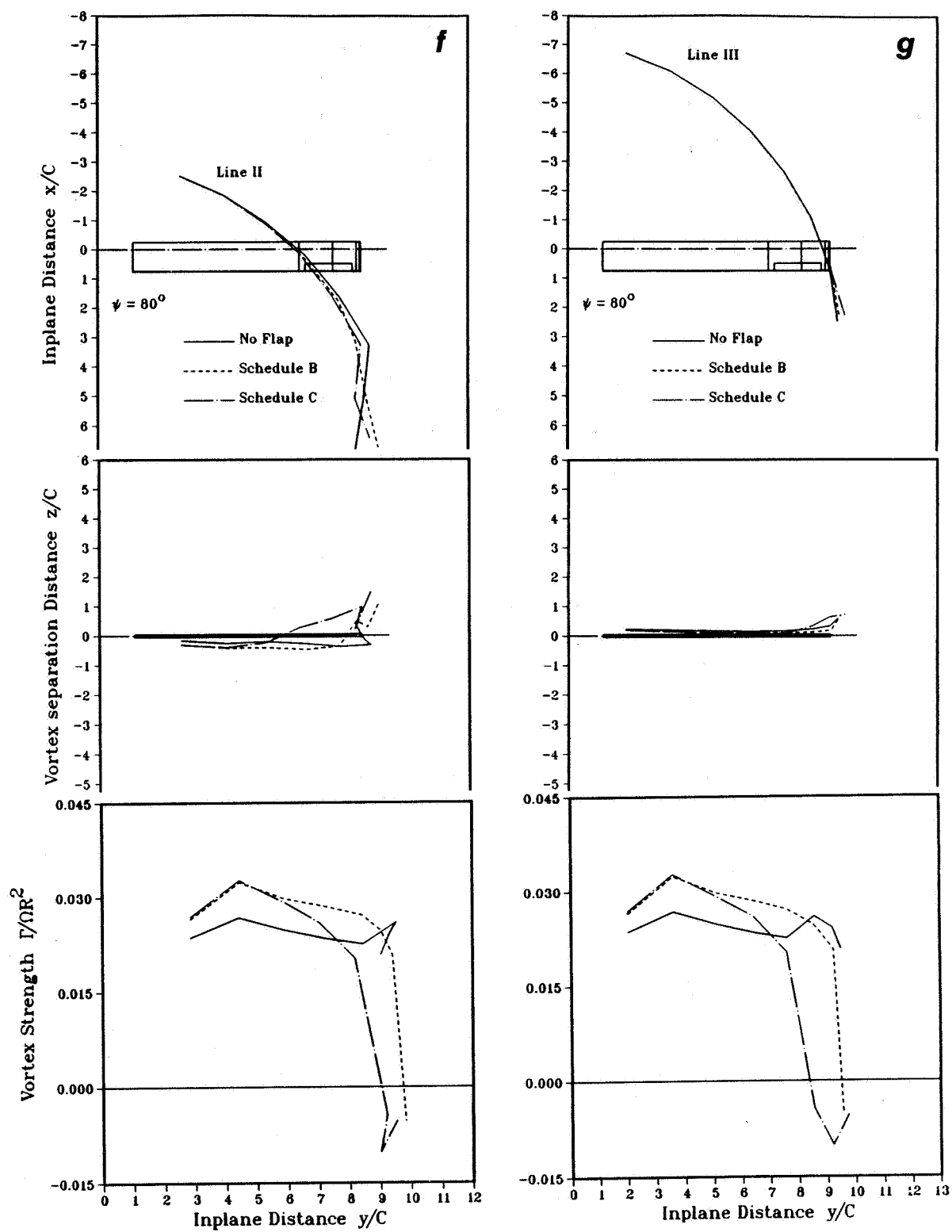
Fig. (52) continued
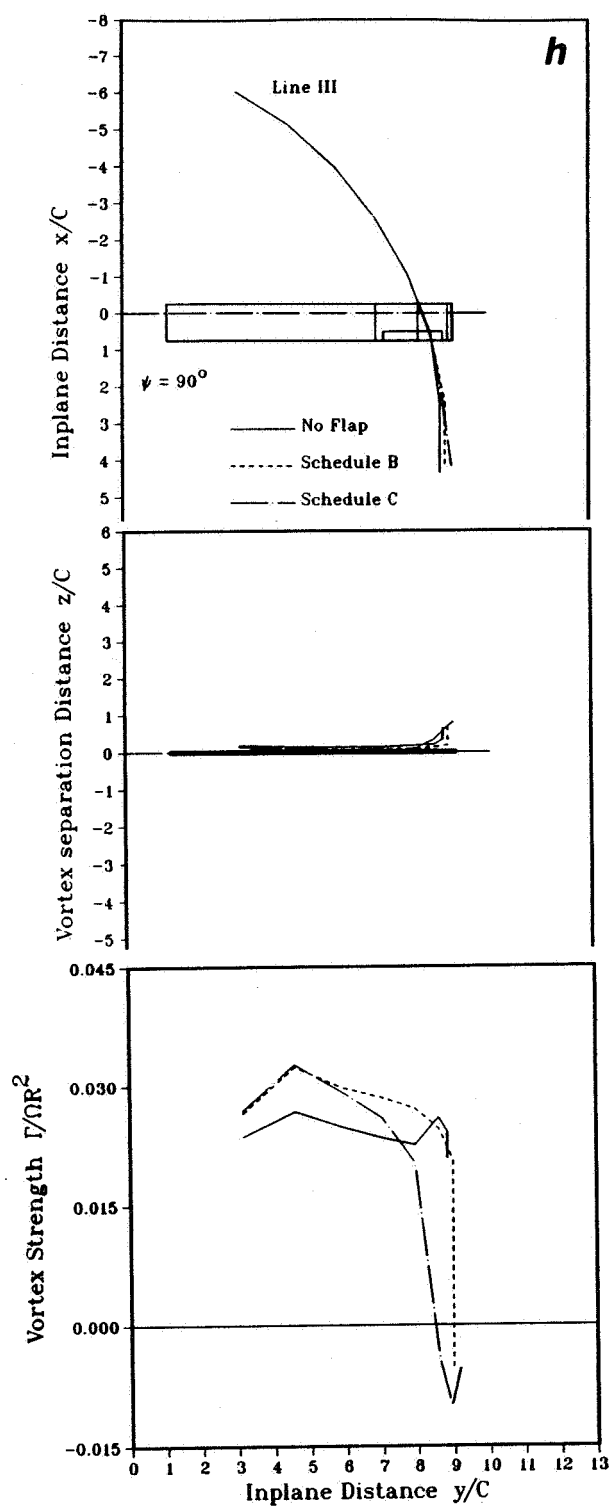
Fig. (52) concluded
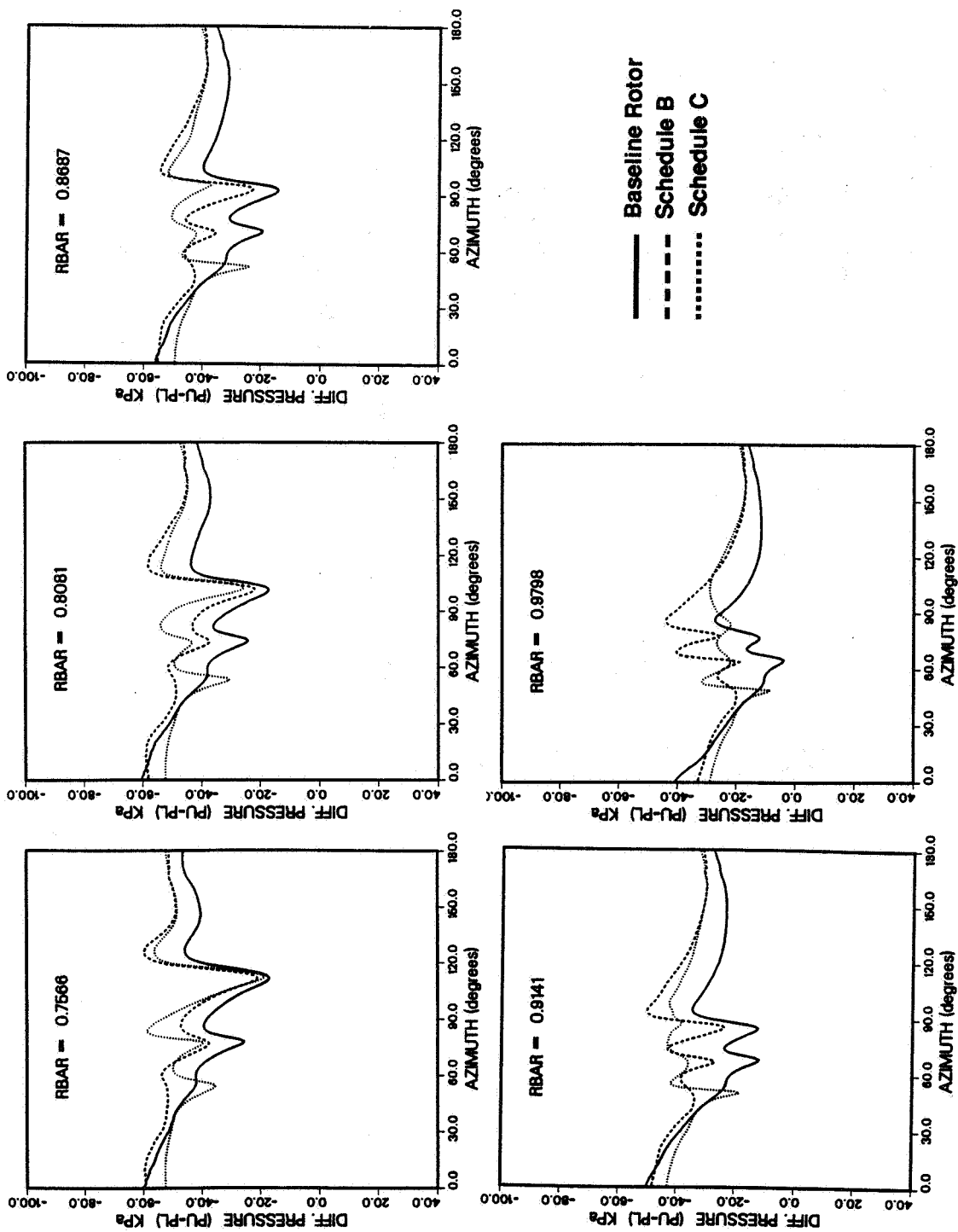
Fig. (53) Effects of the trailing edge flap on the RFS2.BVI-predicted differential pressures for the model OLS rotor during blade-vortex interactions (3 vortex interactions, Mtip = 0.666, Mu = 0.147, x/C = 0.03, rv/C = 0.20)
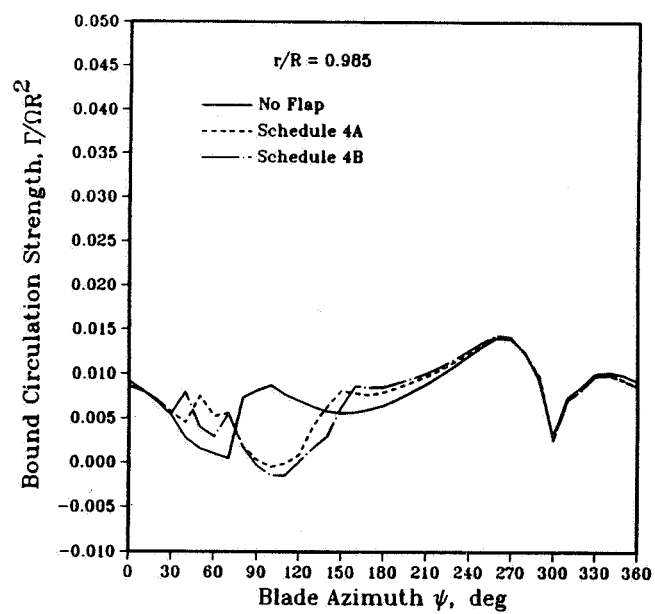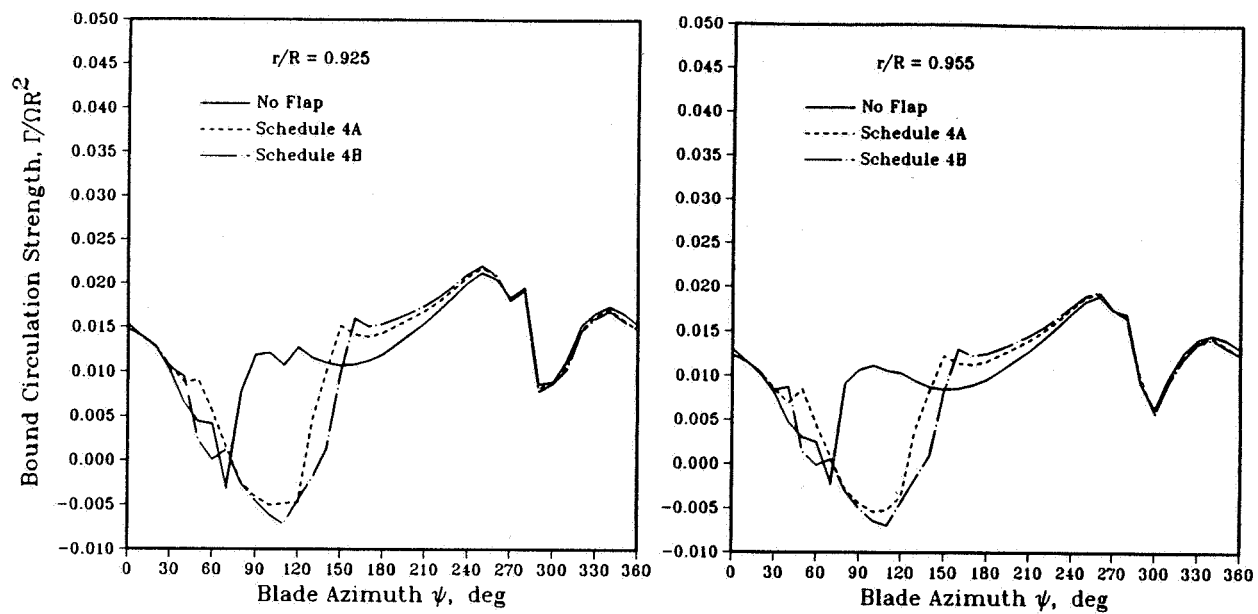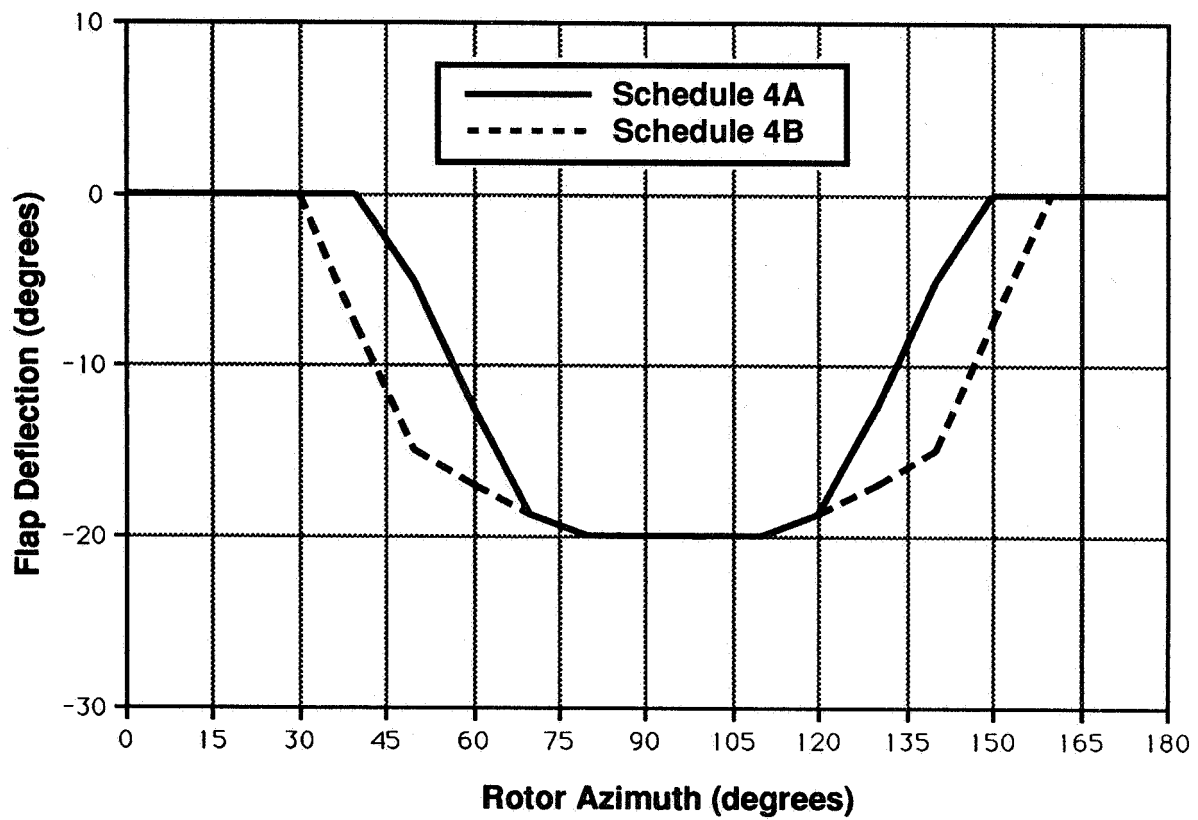
145
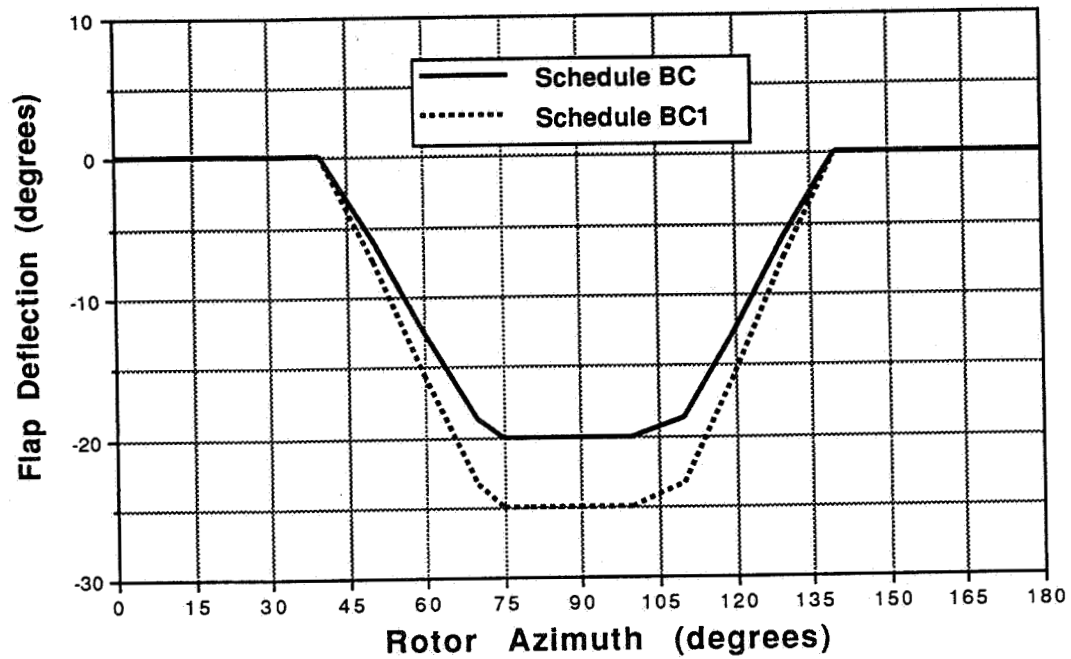
Fig. (54) Variation of the trailing edge flap deflection angle as a function of blade azimuth for schedules BC and BC1
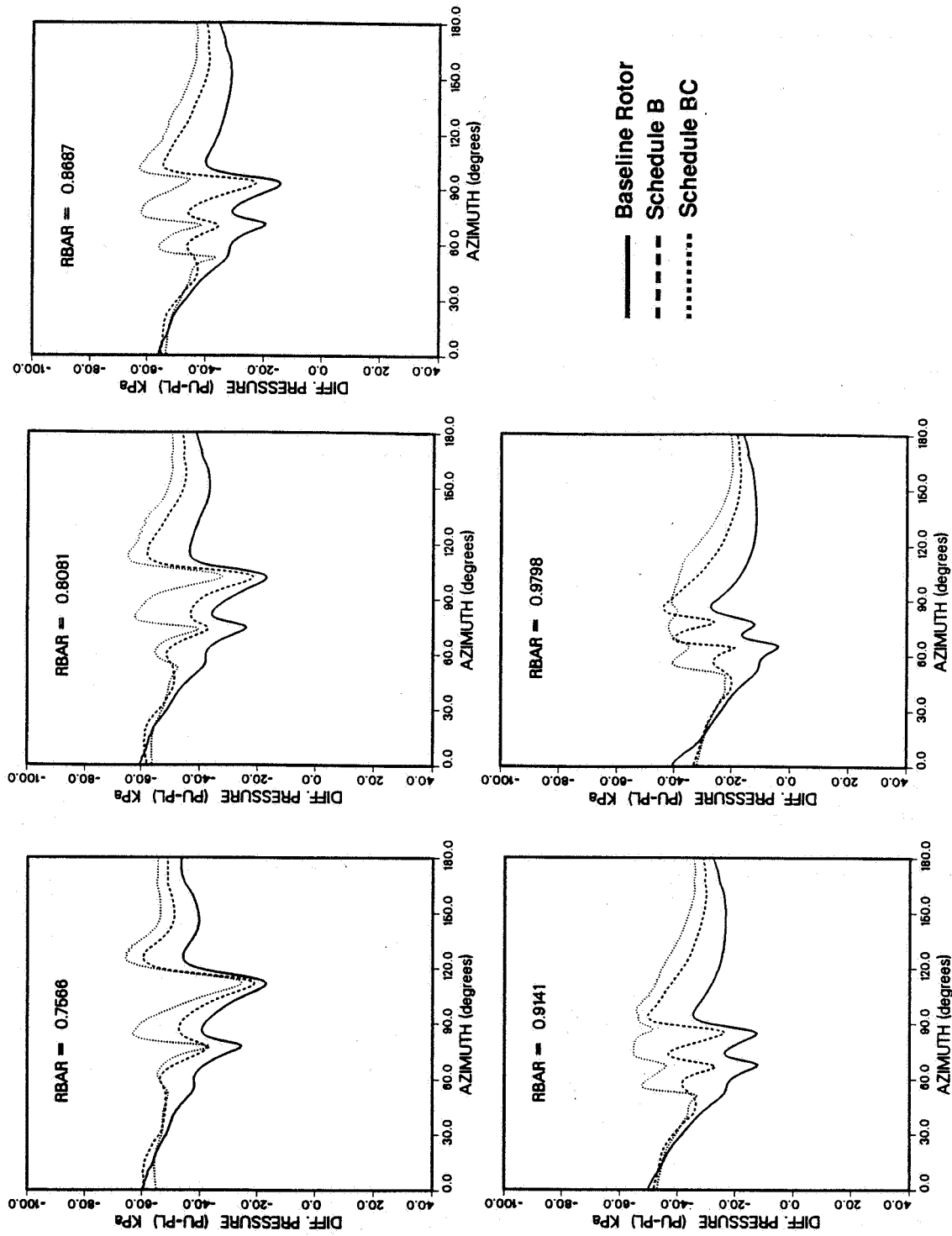
Fig. (55) Effects of the trailing edge flap on the RFS2.BVI-predicted differential pressures for the model OLS rotor during blade-vortex interactions (3 vortex interactions, Mtip = 0.666, Mu = 0.147, x/C = 0.03, rv/C = 0.20)
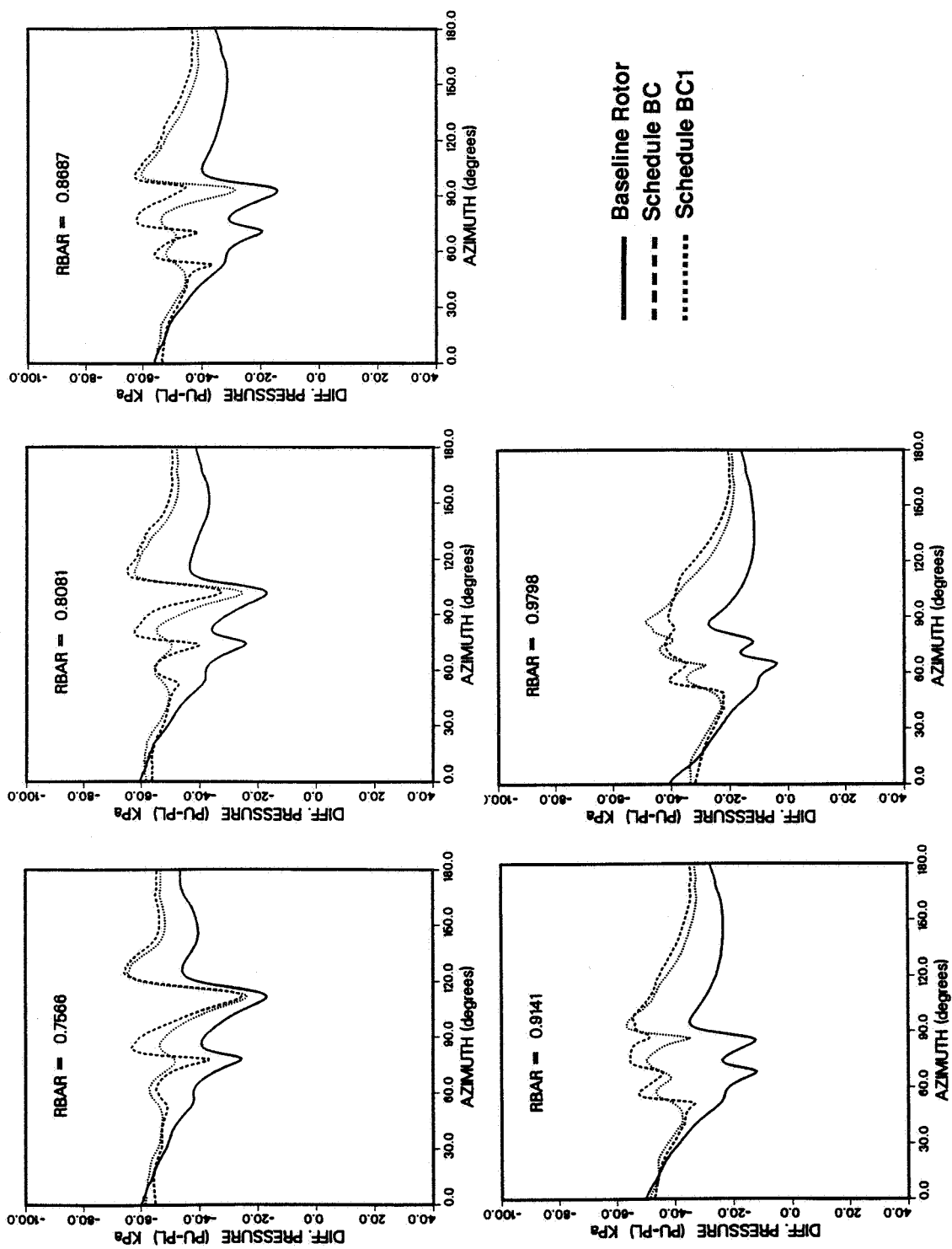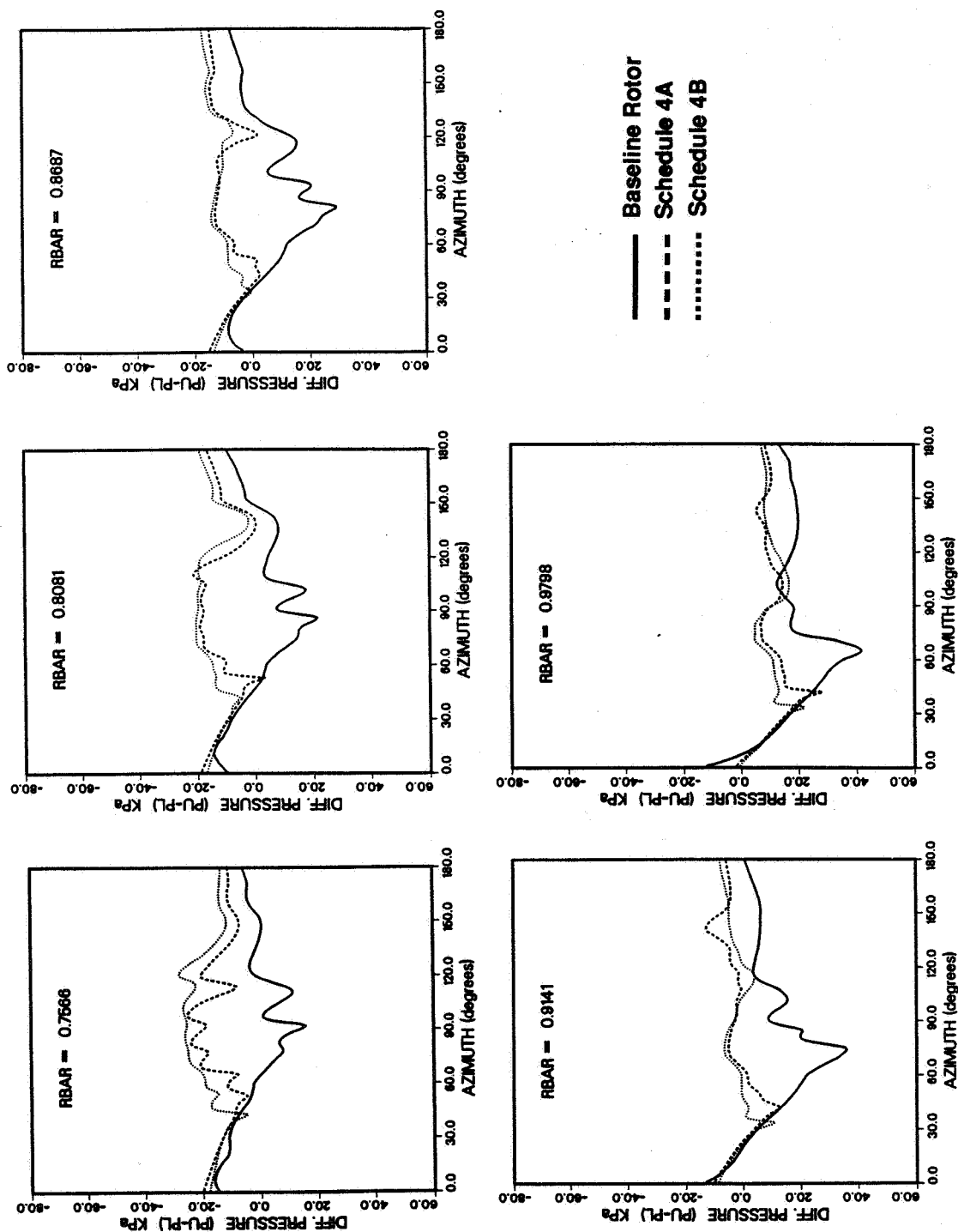
Fig. (56) Effects of the trailing edge flap on the RFS2.BVI-predicted differential pressures for the model OLS rotor during blade-vortex interactions (3 vortex interactions, Mtip = 0.666, Mu = 0.147, x/C = 0.03, rv/C = 0.20)
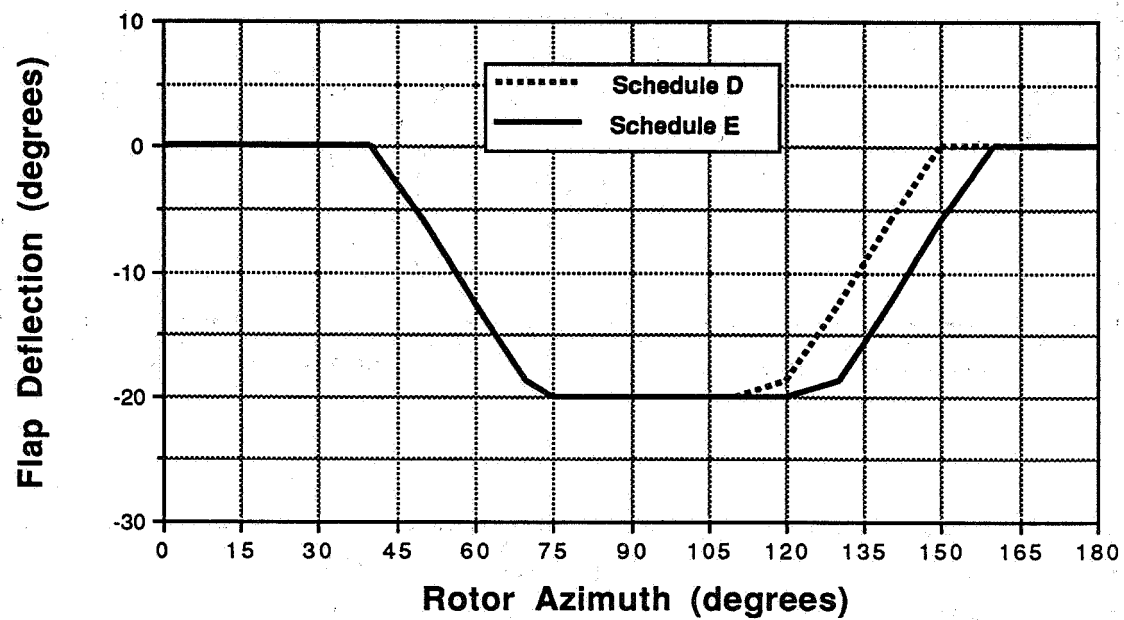
Fig. (57) Variation of the trailing edge flap deflection angles as a function of blade azimuth for schedules D and E
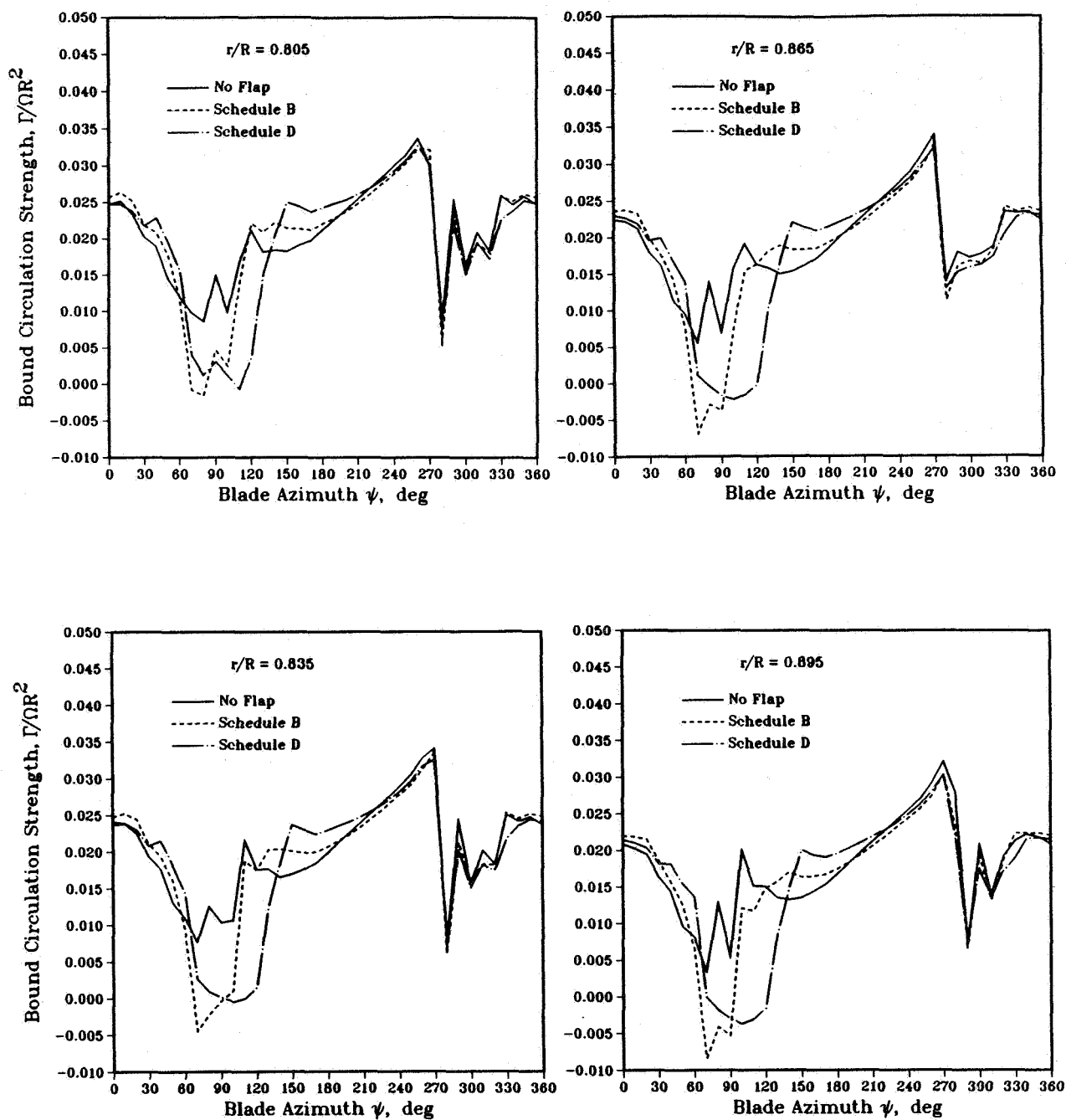
Fig. (58) Effects of the trailing edge flap on the CAMRAD/JA-predicted bound
circulation distributions for the OLS model rotor during blade-
vortex interactions (Mtip = 0.666, Mu = 0.147, rv/C = 0.20)
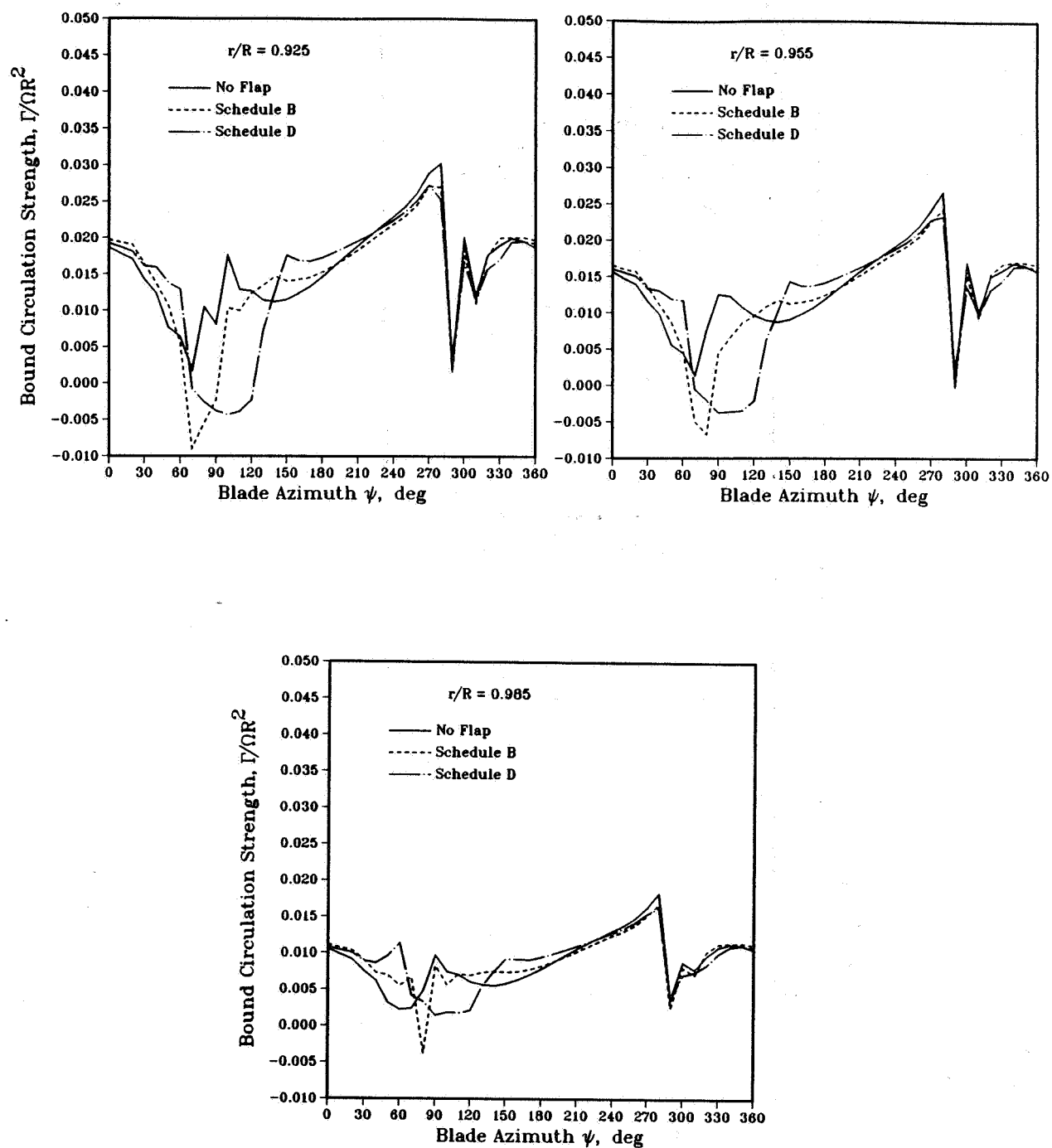
Fig. (58) concluded
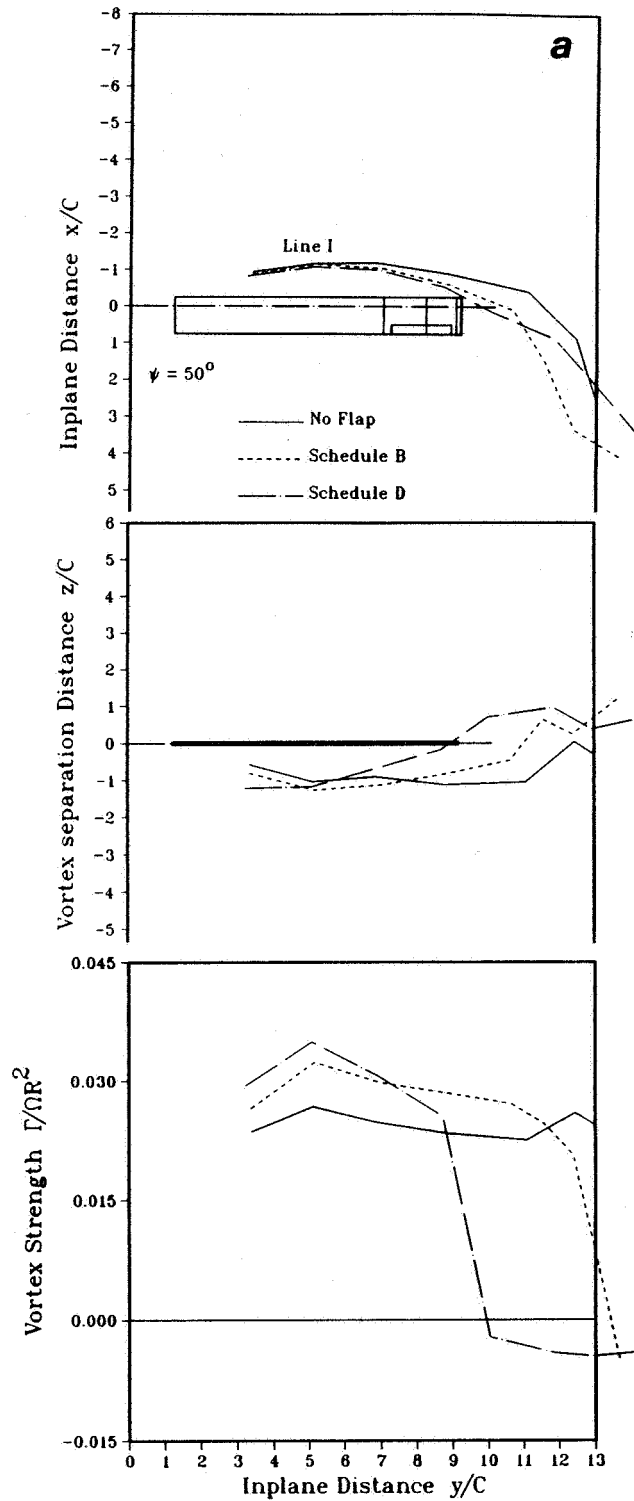
Fig. (59) Effects of the trailing edge flap on the CAMRAD/JA-predicted vortex wake geometry and strength for the OLS model rotor during blade-vortex interactions (Mtip = 0.666, Mu = 0.147, rv/C = 0.20)
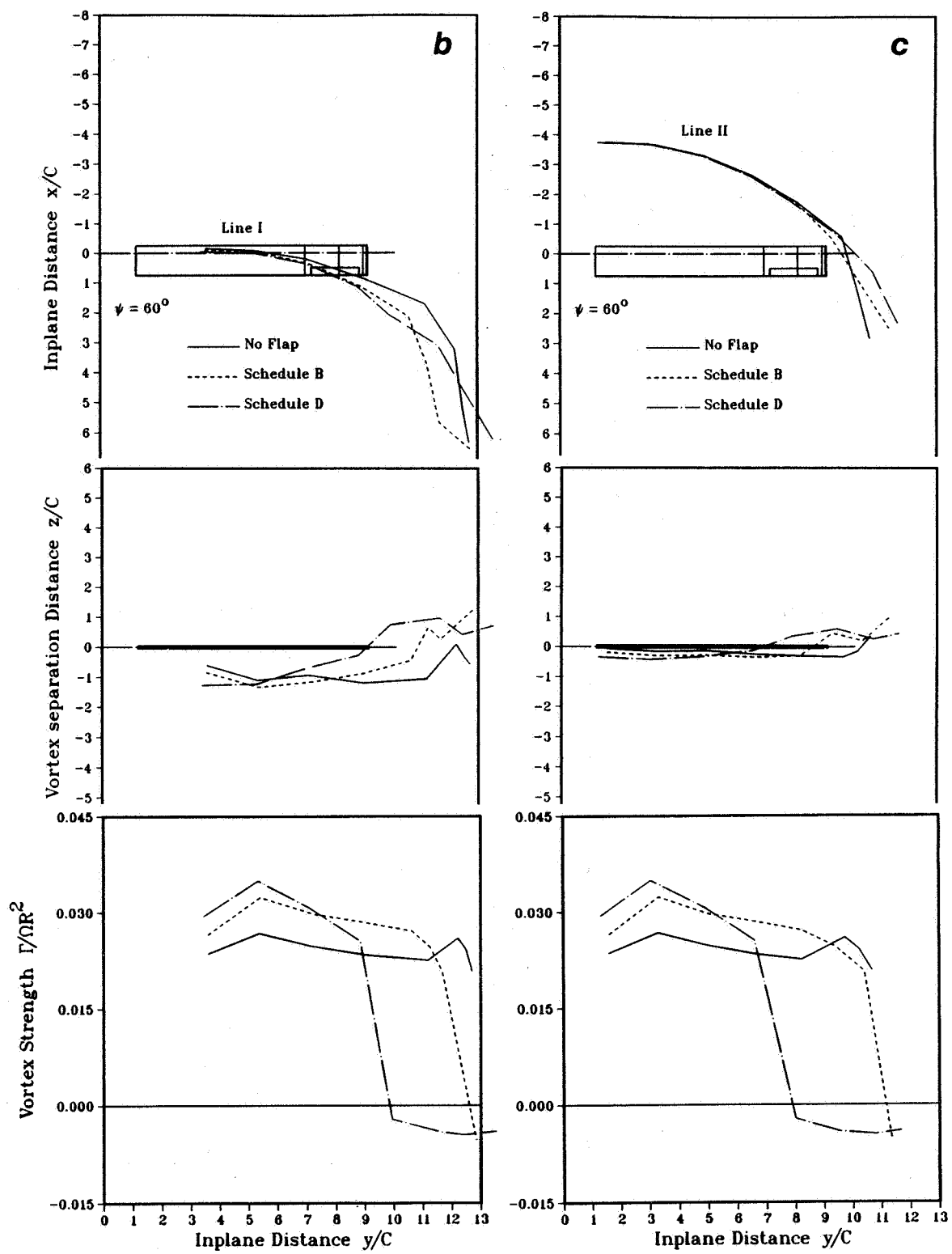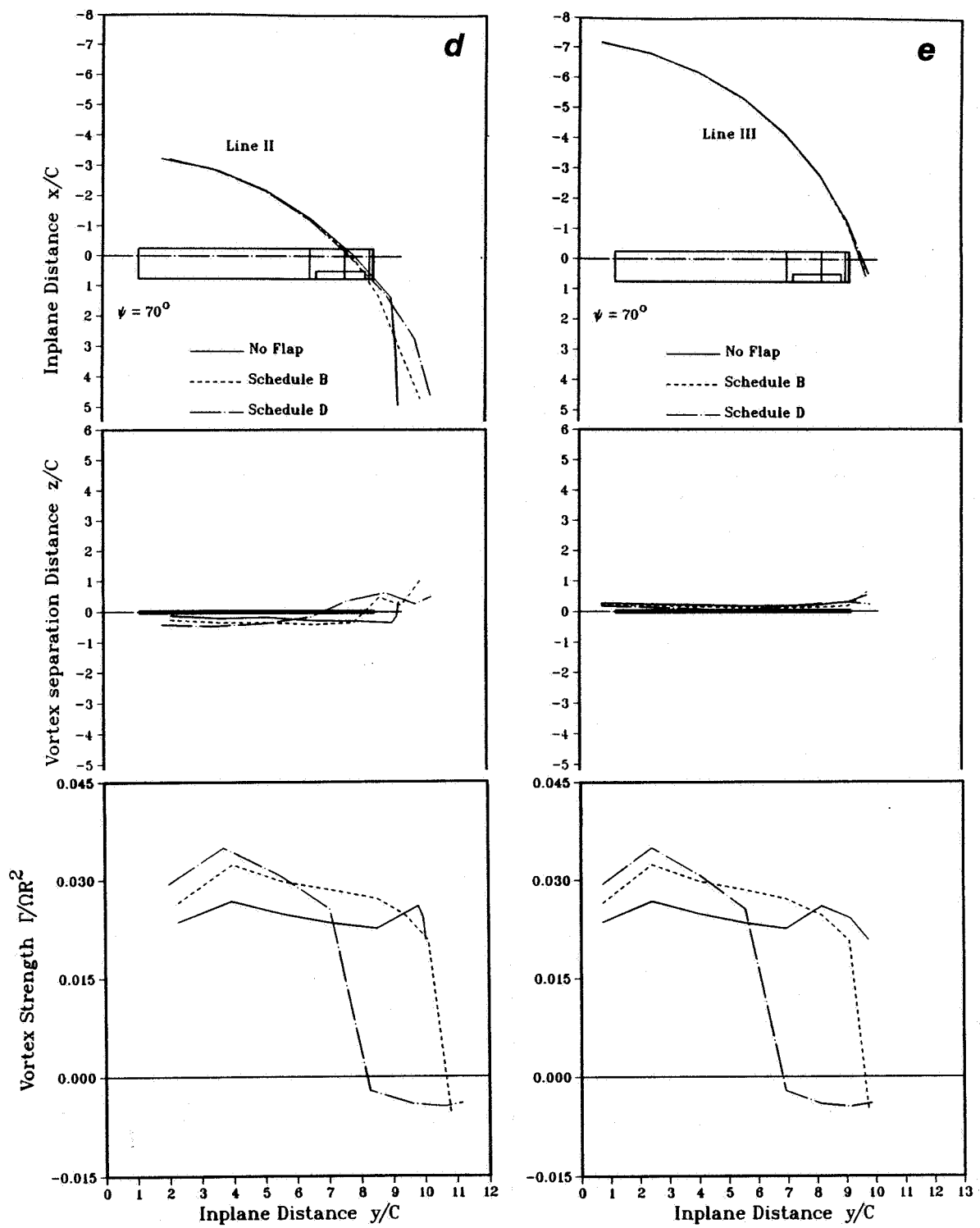
Fig. (59) continued

Fig. (59) continued

154
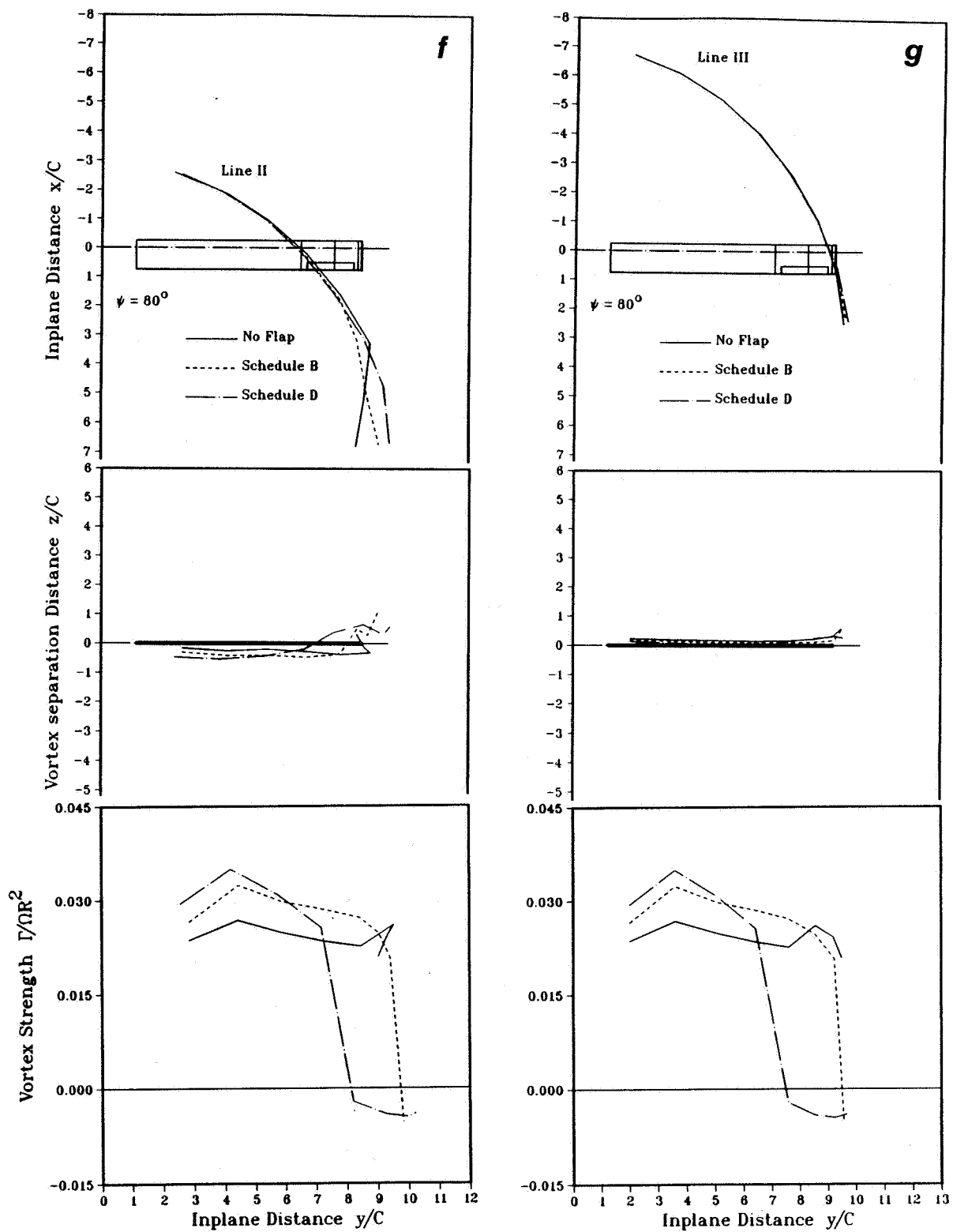
Fig. (59) continued
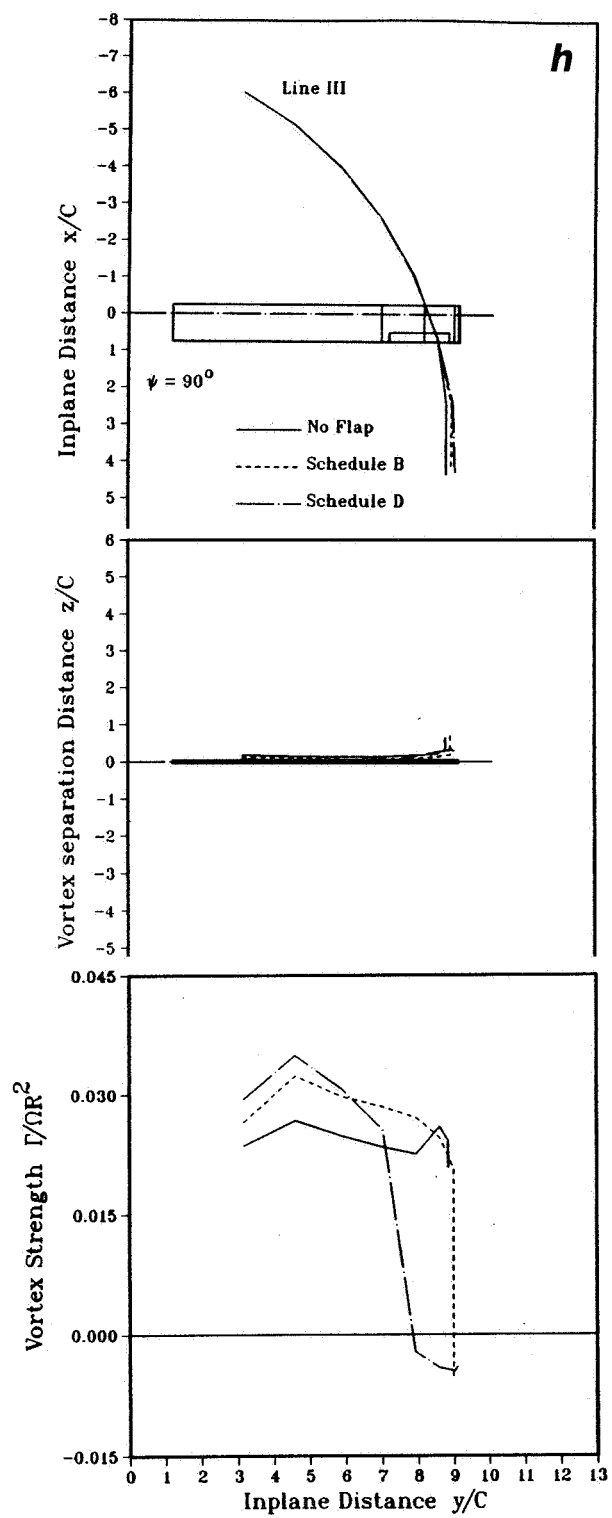
Fig. (59) concluded
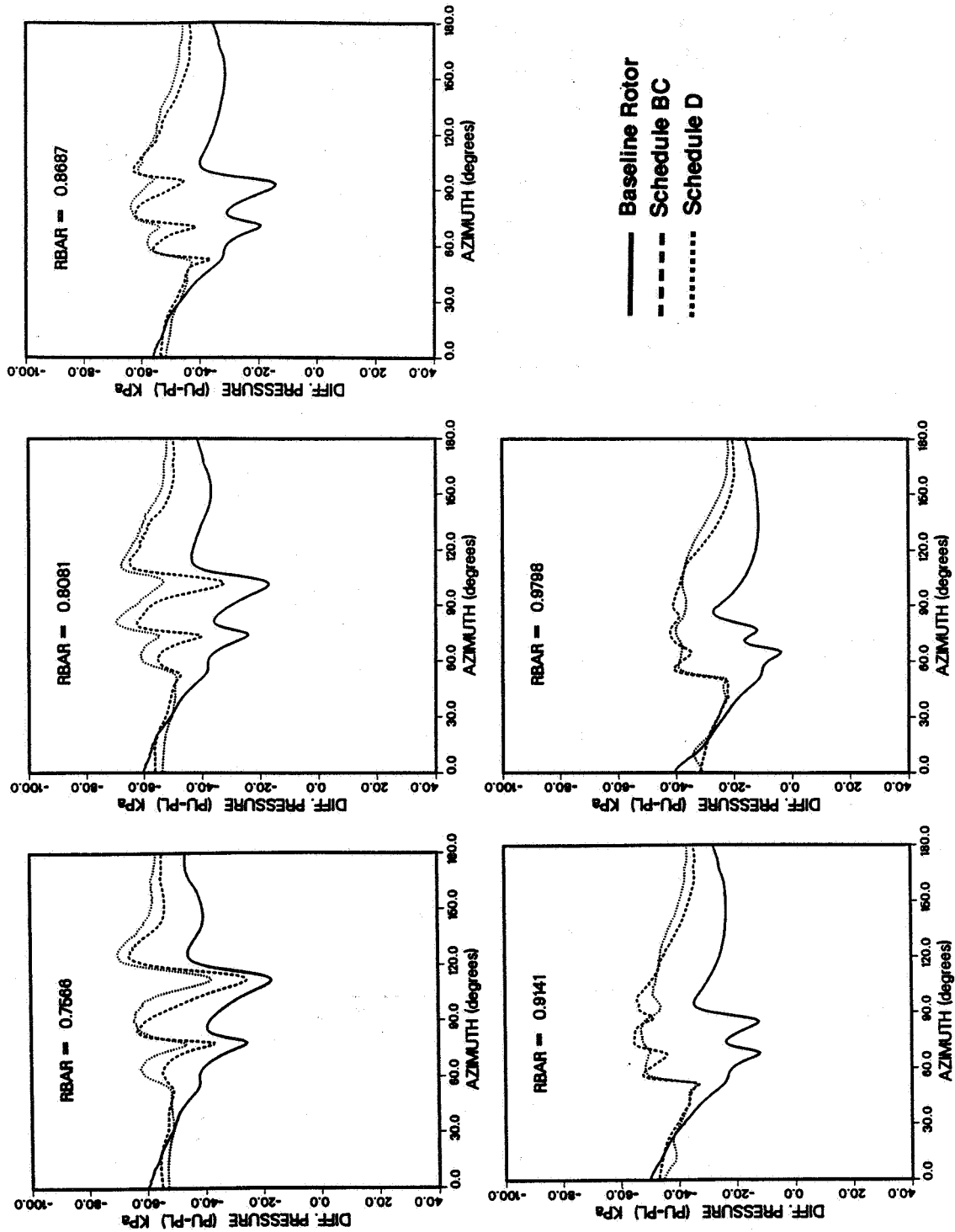
Fig. (60) Effects of the trailing edge flap on the RFS2.BVI-predicted differential pressures for the model OLS rotor during blade-vortex interactions (3 vortex interactions, Mtip = 0.666, Mu = 0.147, x/C = 0.03, rv/C = 0.20)
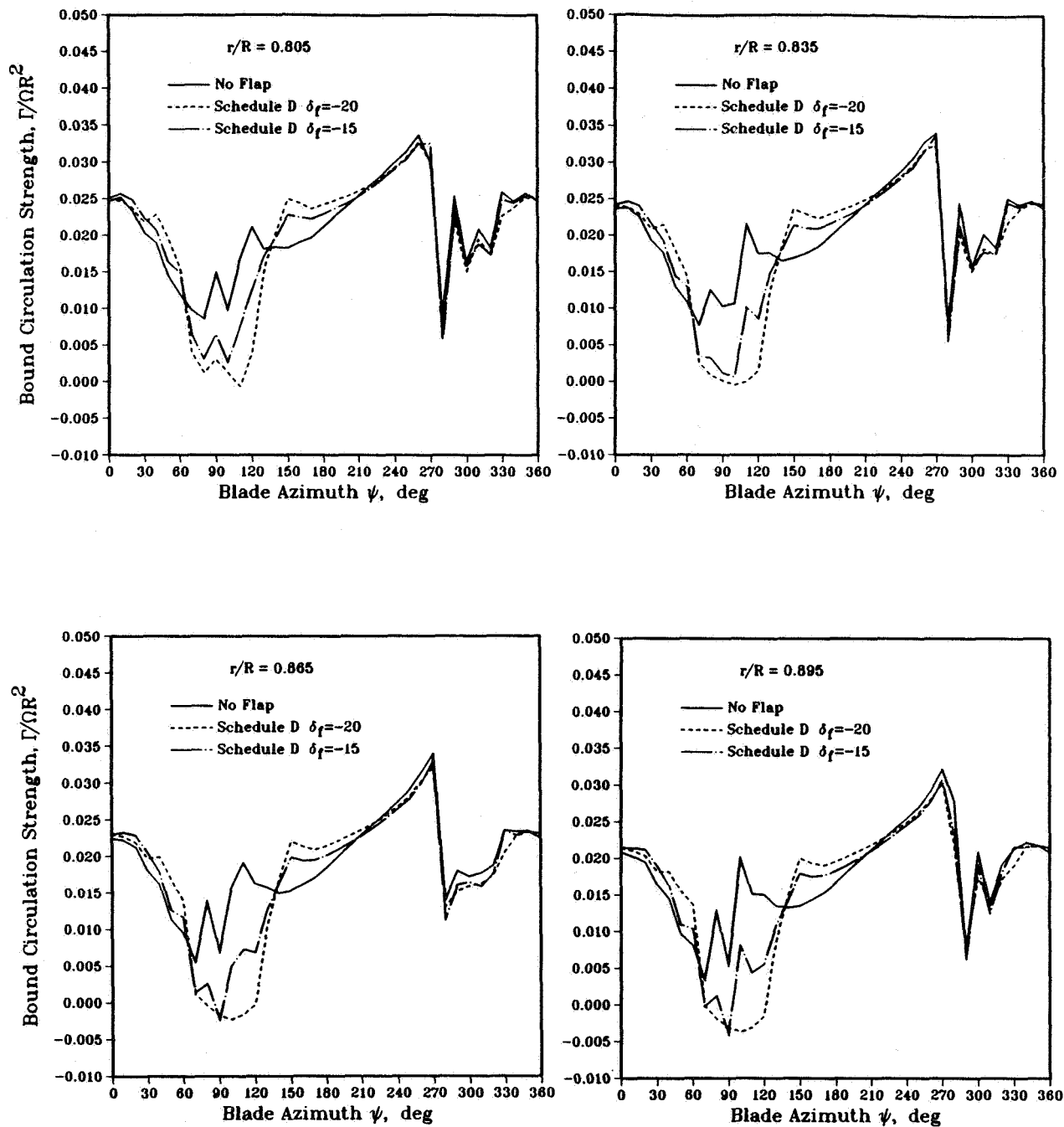
Fig. (61) Effects of the trailing edge flap on the CAMRAD/JA-predicted bound circulation distributions for the OLS model rotor during blade-vortex interactions (Mtip = 0.666, Mu = 0.147, rv/C = 0.20)
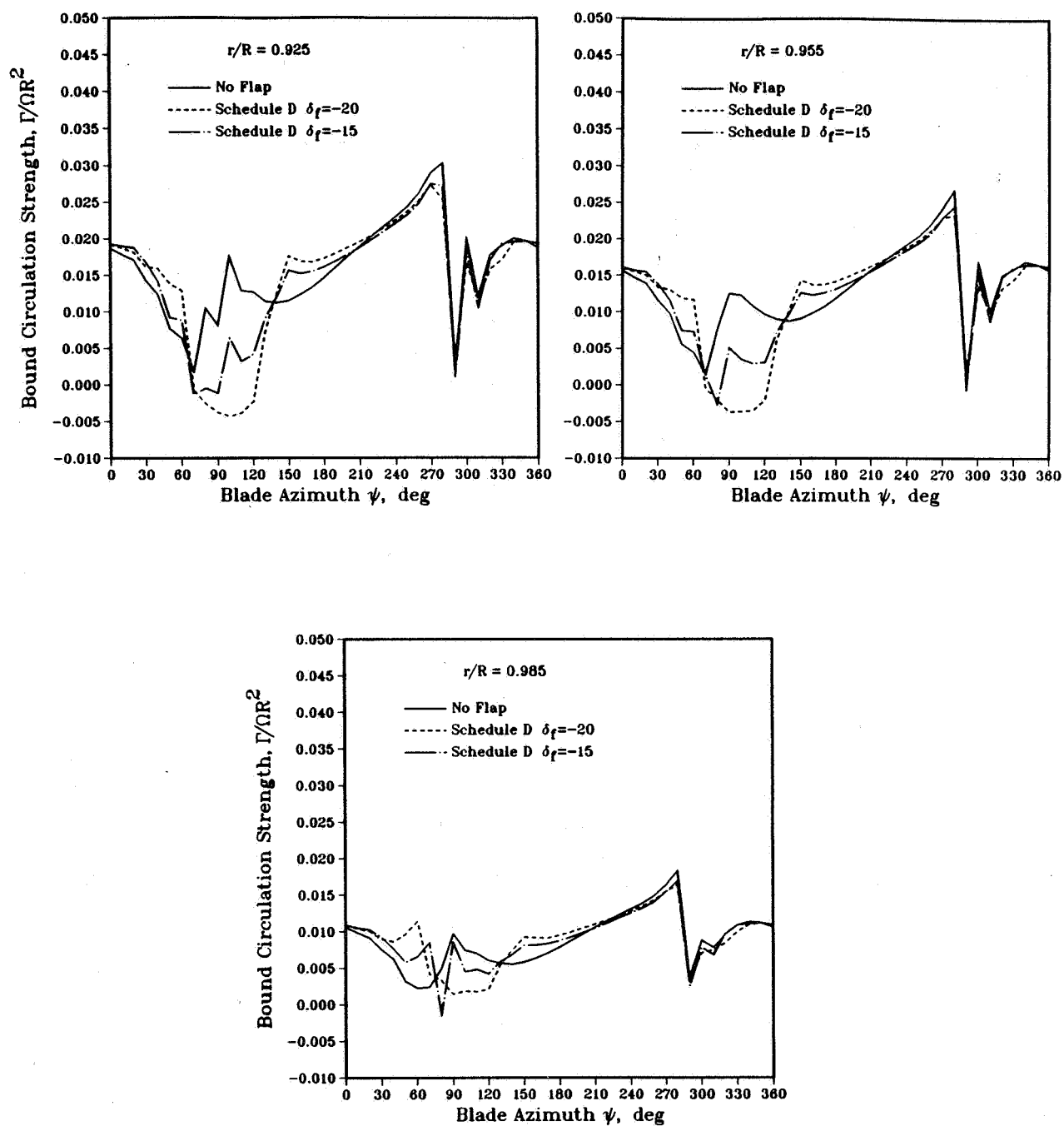
Fig. (61) concluded
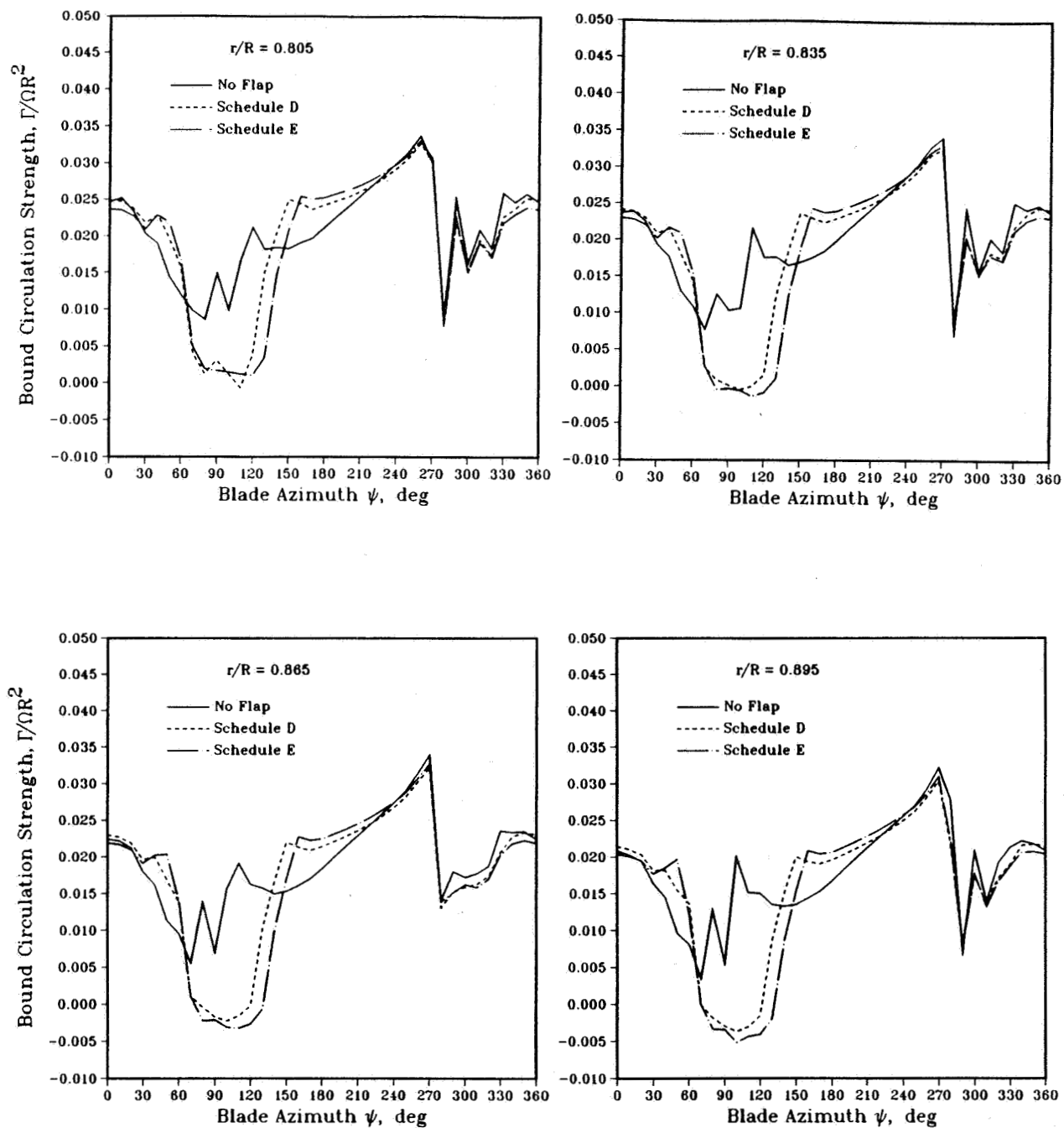
Fig. (62) Effects of the trailing edge flap on the CAMRAD/JA-predicted bound circulation distributions for the OLS model rotor during blade-vortex interactions (Mtip = 0.666, Mu = 0.147, rv/C = 0.20)

160

Fig. (62) concluded

Fig. (63) Effects of the trailing edge flap on the RFS2.BVI-predicted differential pressures for the model OLS rotor during blade-vortex interactions (3 vortex interactions, Mtip = 0.666, Mu = 0.147, x/C = 0.03, rv/C = 0.20)

162

Fig. (64) Comparisons between the CAMRAD/JA-predicted bound circulation distributions using the single and dual peak circulation options
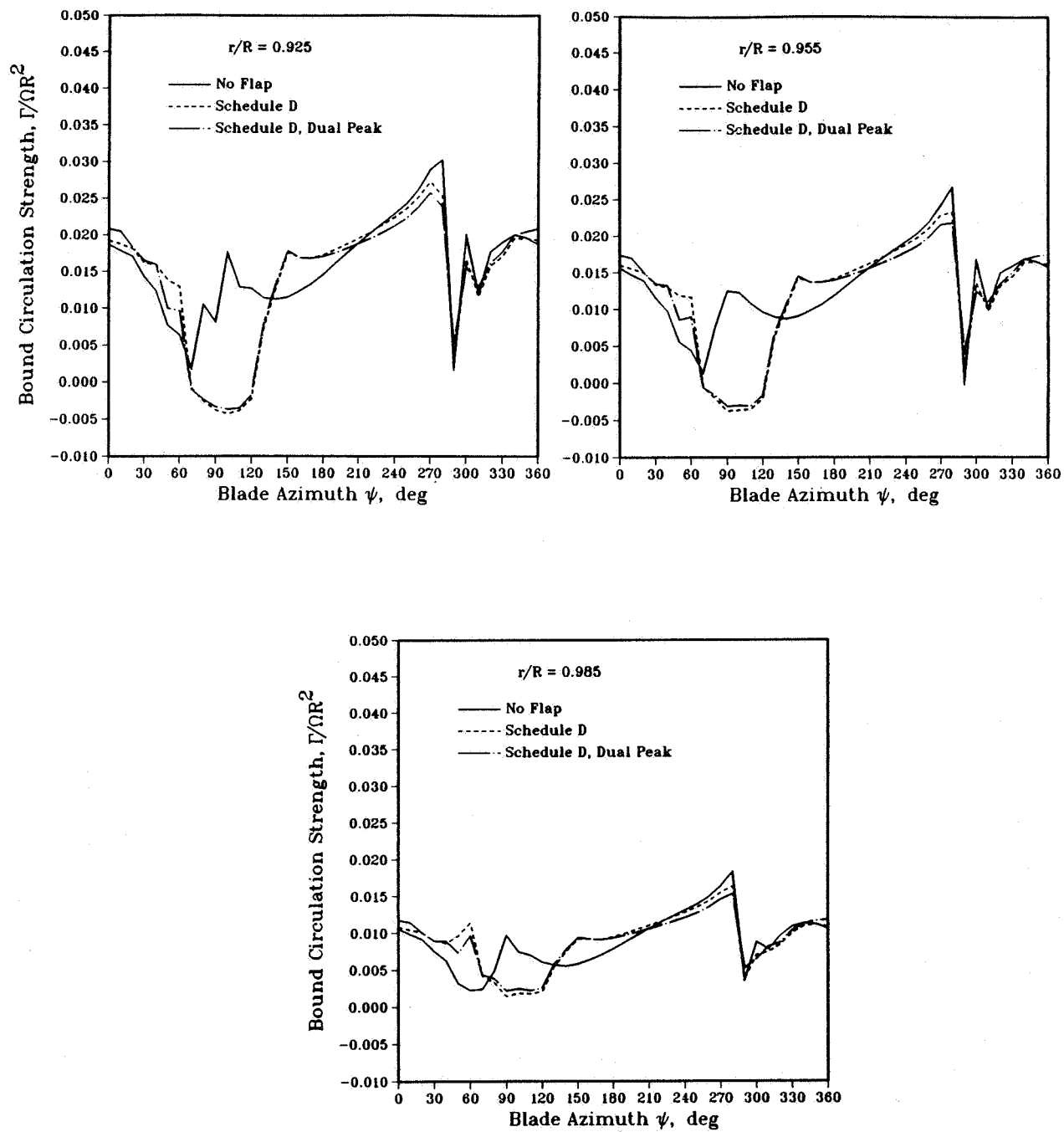
Fig. (64) concluded
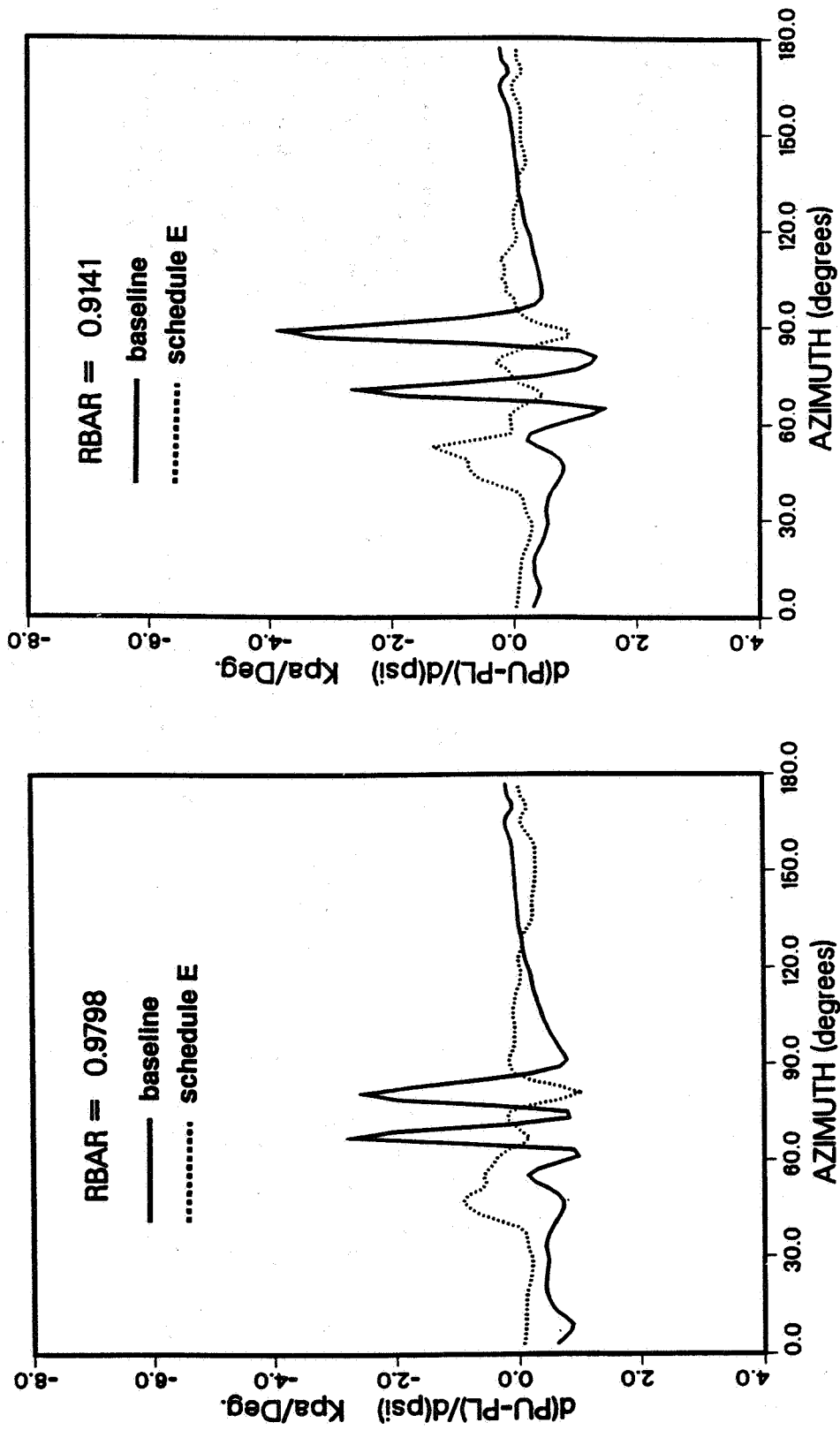
Fig. (65) Predicted temporal pressure gradients for the OLS rotor during blade-vortex interactions (3 vortex interactions, Mtip = 0.666, Mu = 0.147, rv/C = 0.20)
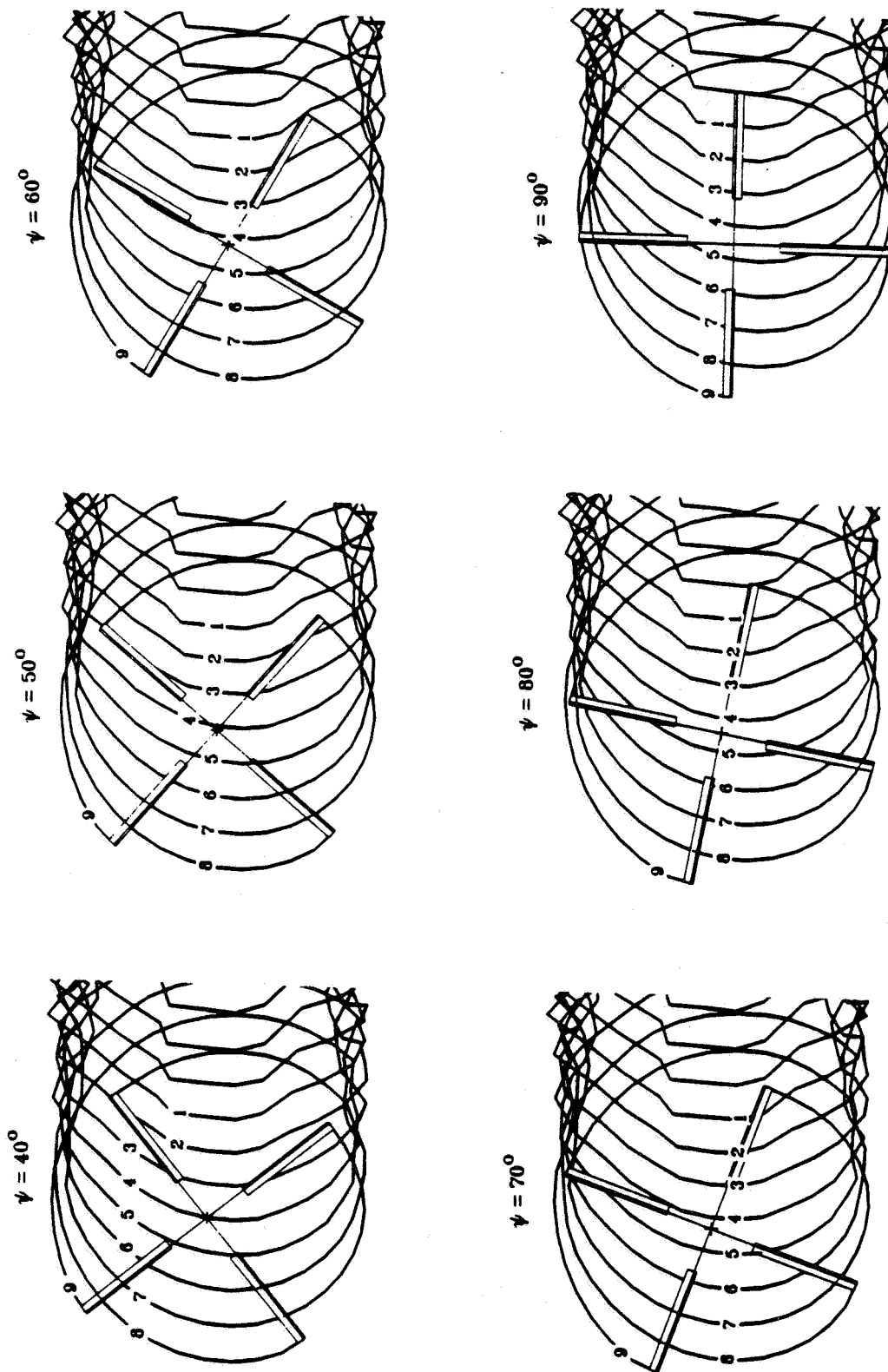
Fig. (66) Planform view of the CAMRAD/JA-predicted tip vortex trajectories for the generic four-bladed model rotor (Mtip = 0.627, Mu = 0.15, TPP = 2 degrees aft)

166

Fig. (67) Effects of the trailing edge flap on the CAMRAD/JA-predicted bound circulation distributions for the four-bladed model rotor during blade-vortex interactions (Mtip = 0.627, Mu = 0.15, rv/C = 0.20)

Fig. (67) concluded

Fig. (68) Variation of the trailing edge flap deflection angles as a function of blade azimuth for schedules 4A and 4B

Fig. (69) Effects of the trailing edge flap on the RFS2.BVI-predicted differential pressures for the four-bladed model rotor during blade-vortex interactions (9 vortex interactions, Mtip = 0.627, Mu = 0.15, x/C = 0.03, rv/C = 0.20)

170
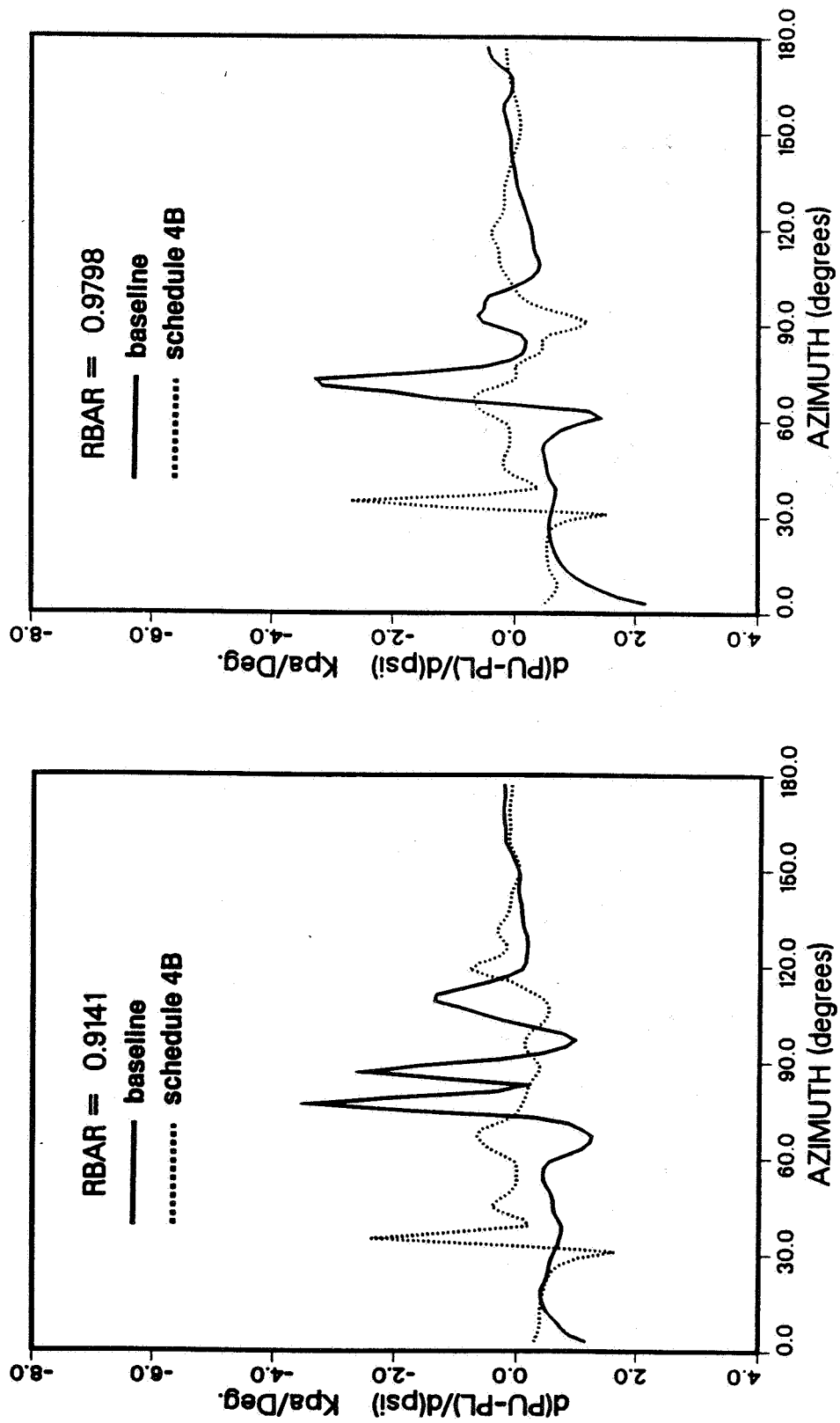
Fig. (70) Predicted temporal pressure gradients for the four-bladed model rotor during blade-vortex interactions (9 vortex interactions, Mtip = 0.627, Mu = 0.15, rv/C = 0.20)
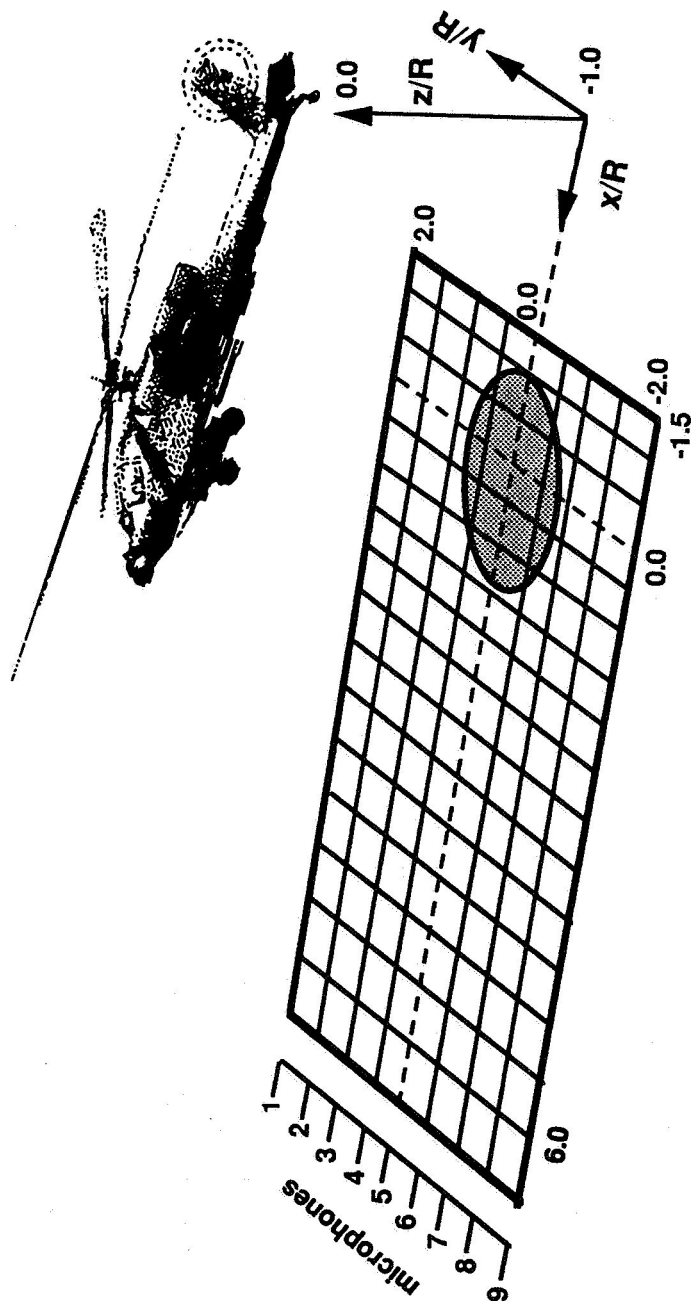
Fig. (71) Schematic depicting microphone array positions for the acoustic analyses (total number of microphones is 144)
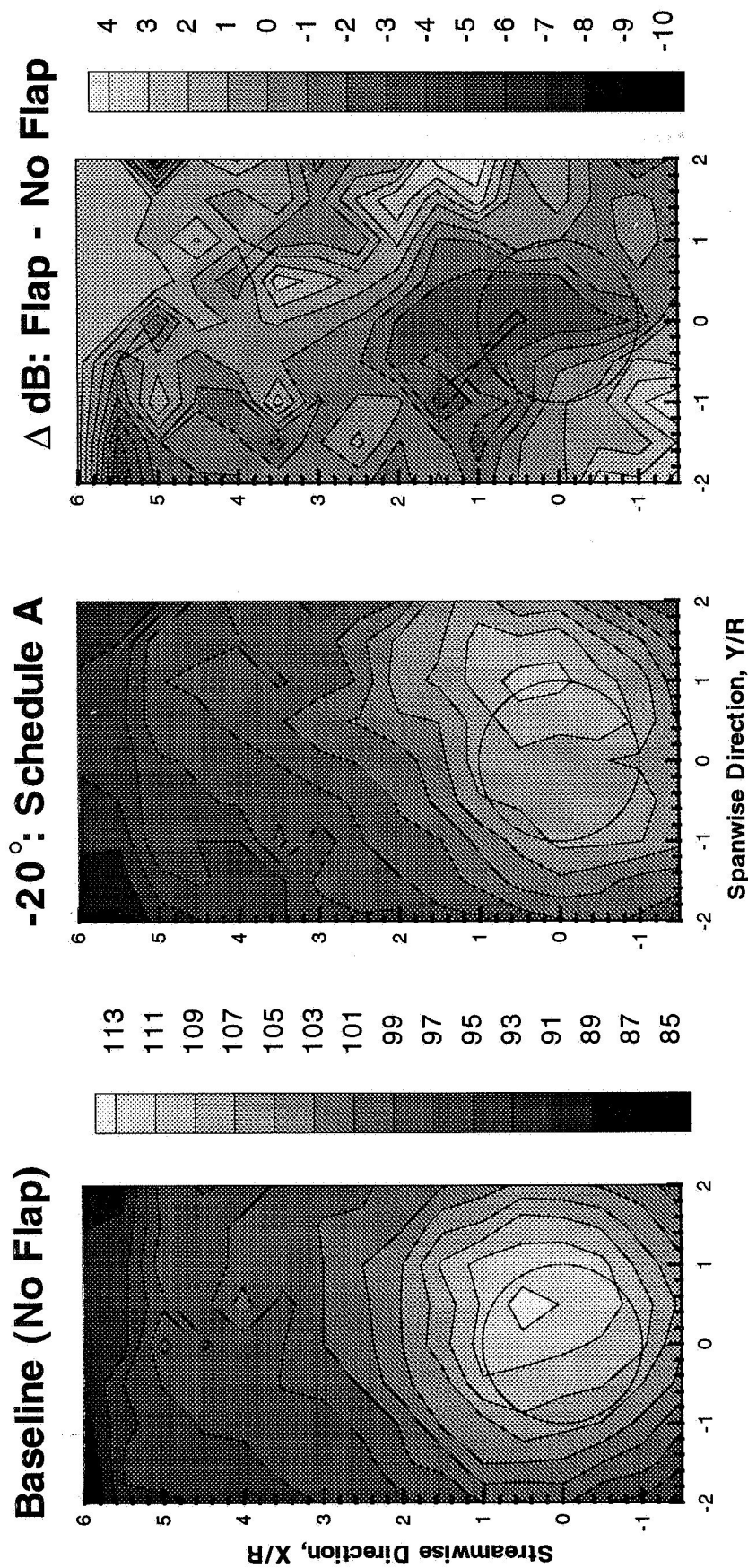
Fig. (72) Effects of the trailing edge flap on the predicted BVI directivity and noise levels for the OLS model rotor (Schedule A, Mtip = 0.666, Mu = 0.147)

173
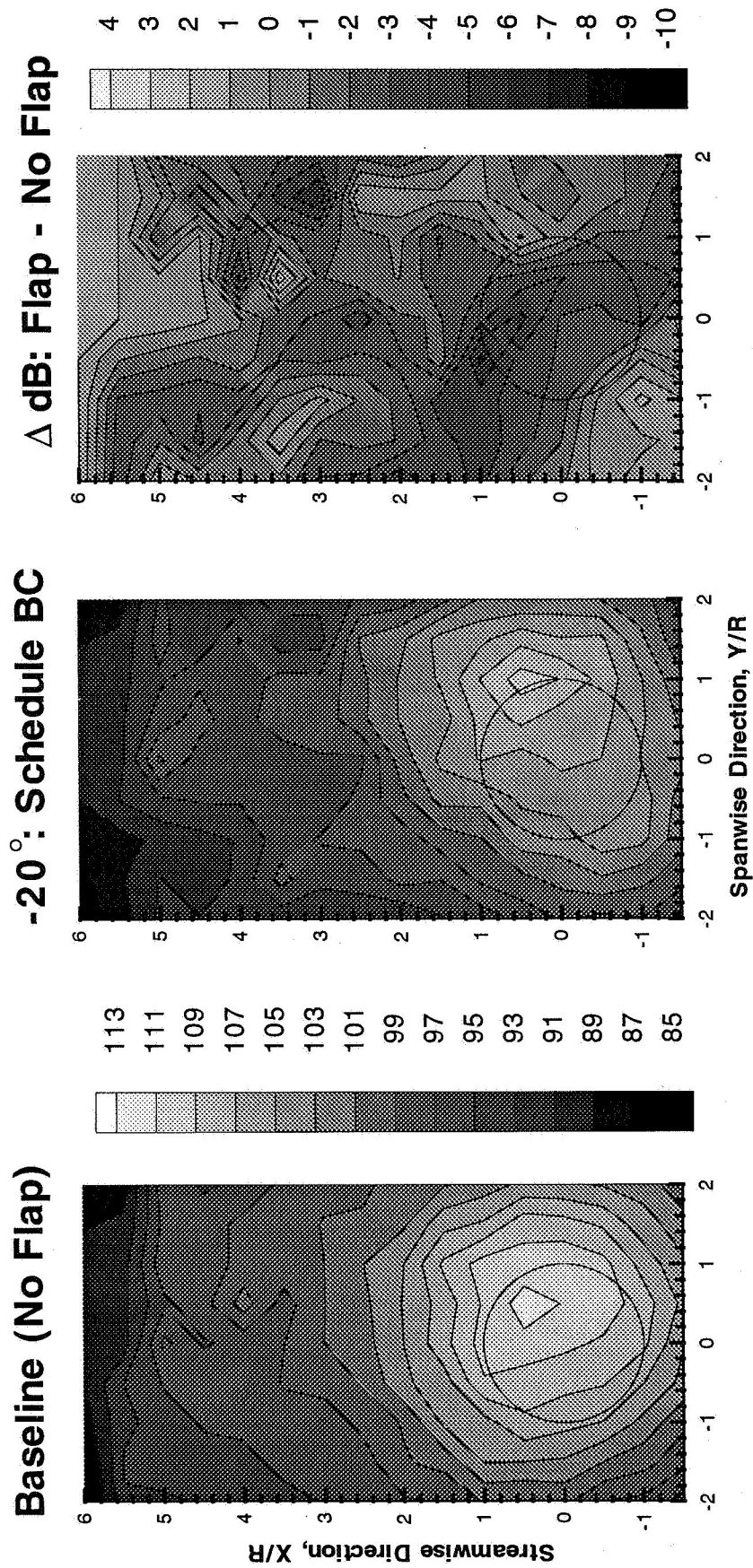
Fig. (73) Effects of the trailing edge flap on the predicted BVI directivity and noise levels for the OLS model rotor (Schedule BC, Mtip = 0.666, Mu = 0.147)

174
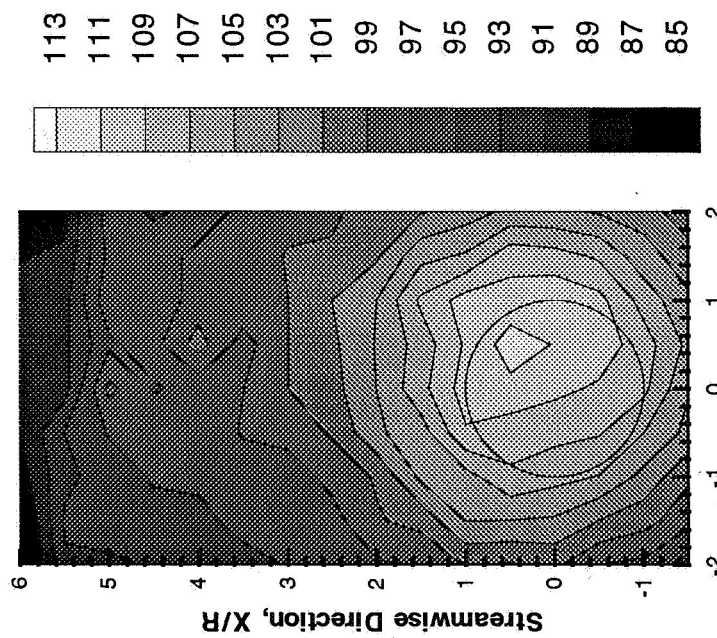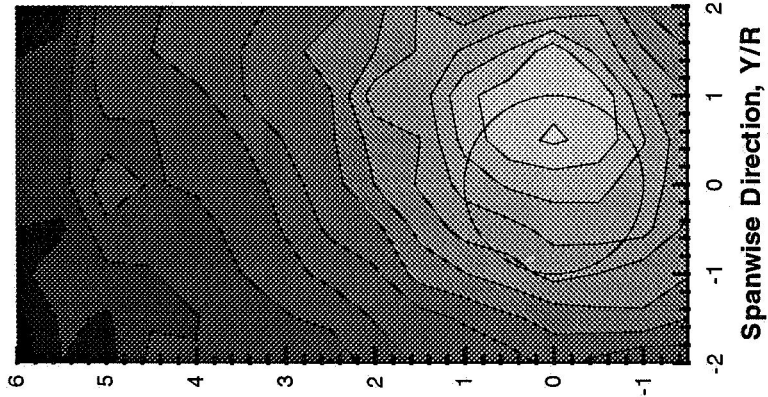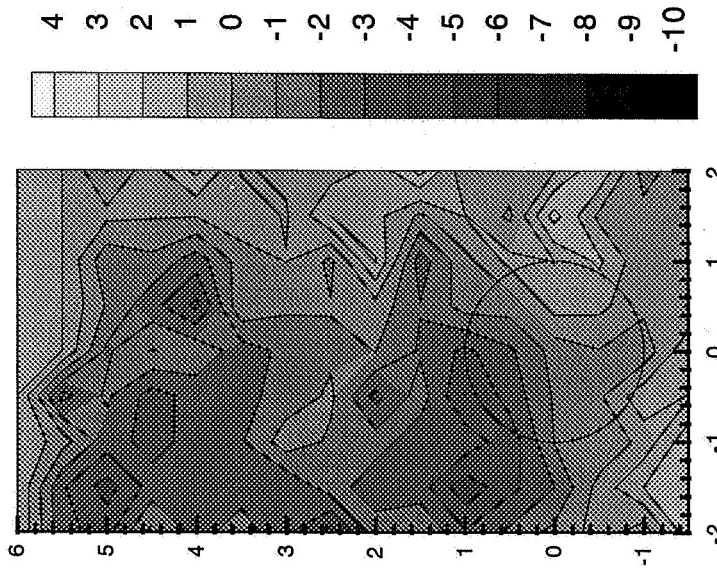
Fig. (74) Effects of the trailing edge flap on the prtegraledicted BVI directivity and noise levels for the OLS model rotor (Schedule C, Mtip = 0.666, Mu = 0.147)

C-3
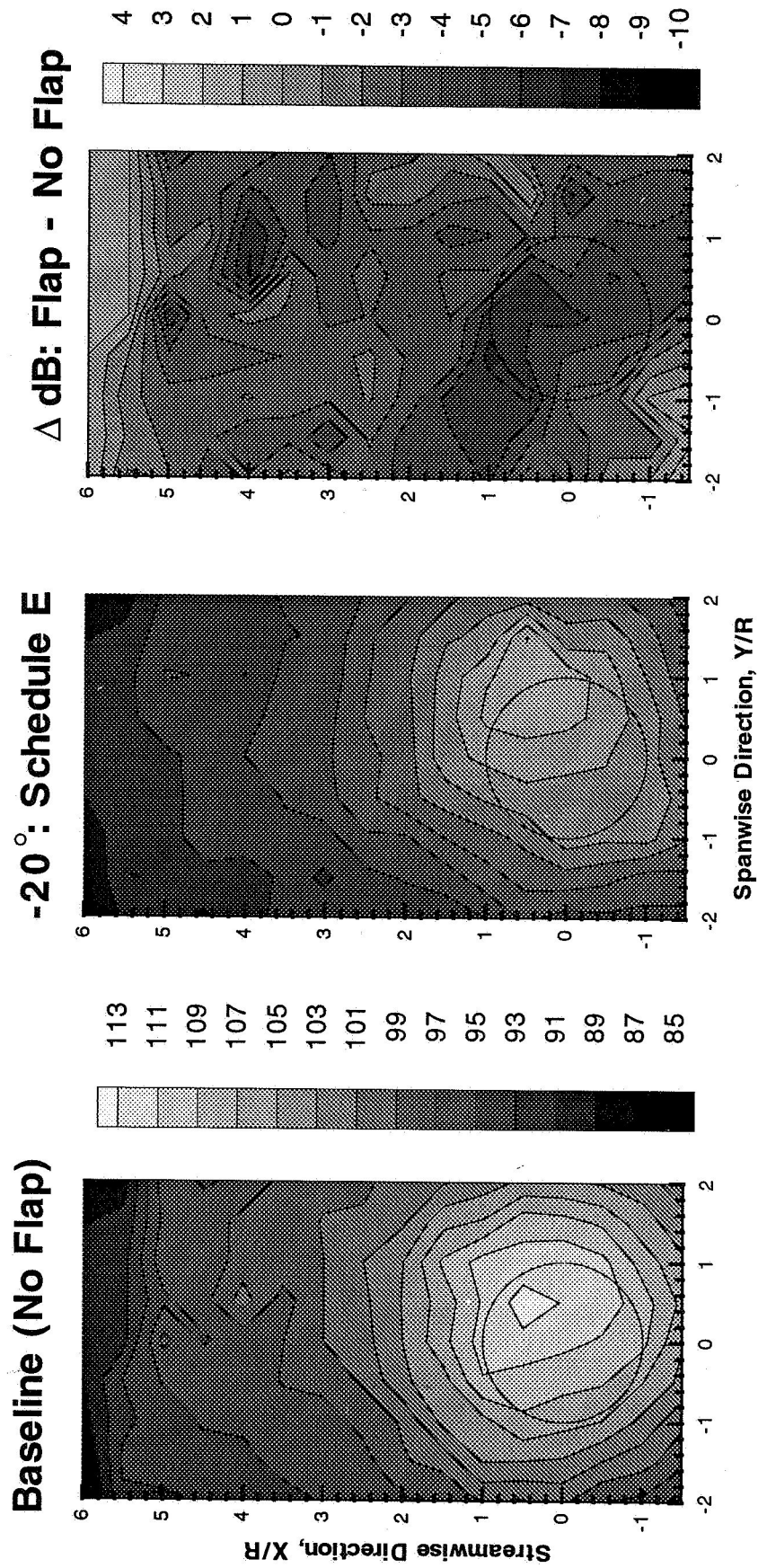
Fig. (75) Effects of the trailing edge flap on the predicted BVI directivity and noise levels for the OLS model rotor (Schedule E, Mtip = 0.666, Mu = 0.147)

176
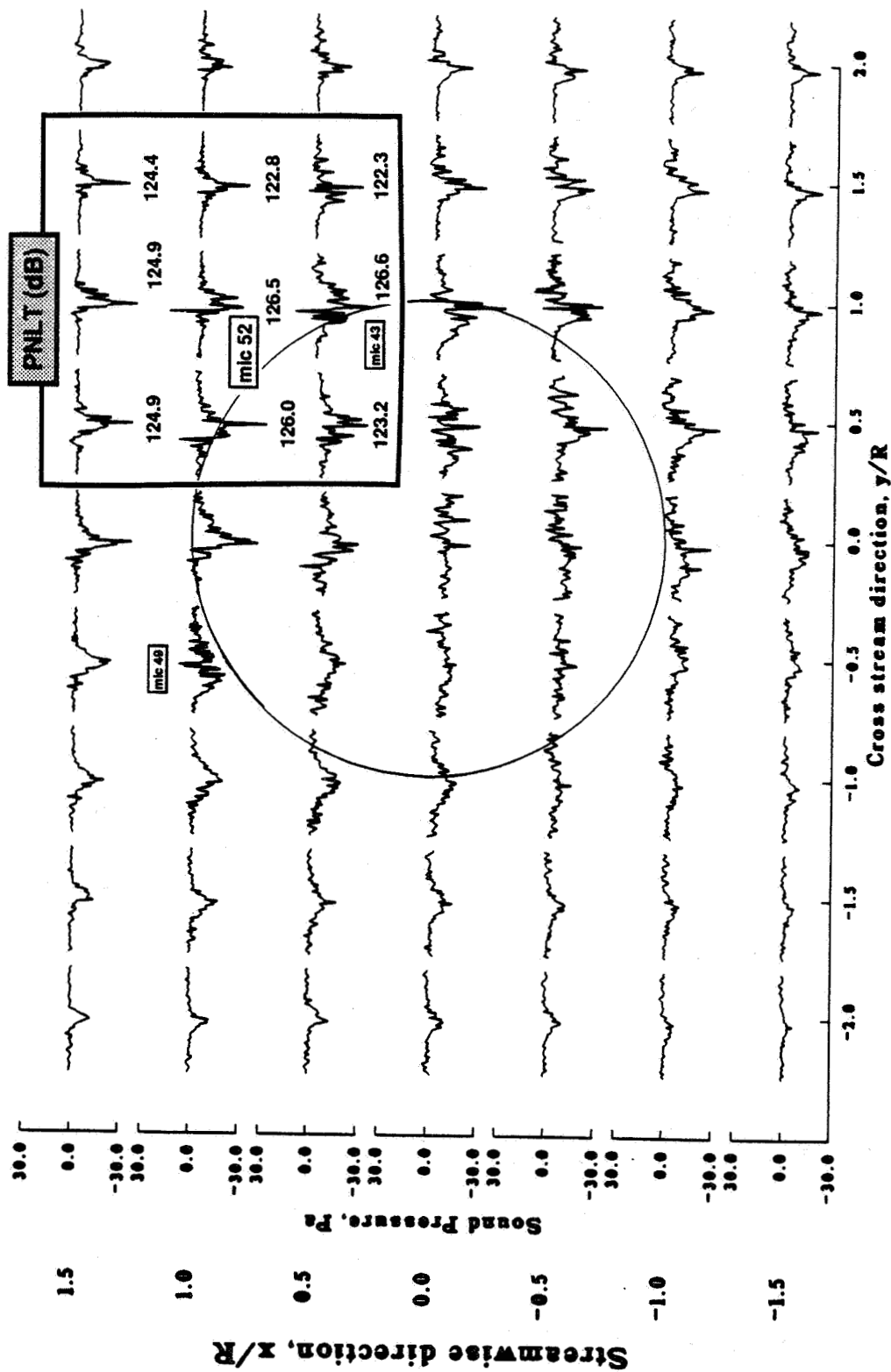
Total Noise

Fig. (76) Predicted acoustic time histories for one blade passage (baseline OLS model rotor, Mtip = 0.666, Mu = 0.147, TPP = 1.5 degrees aft)
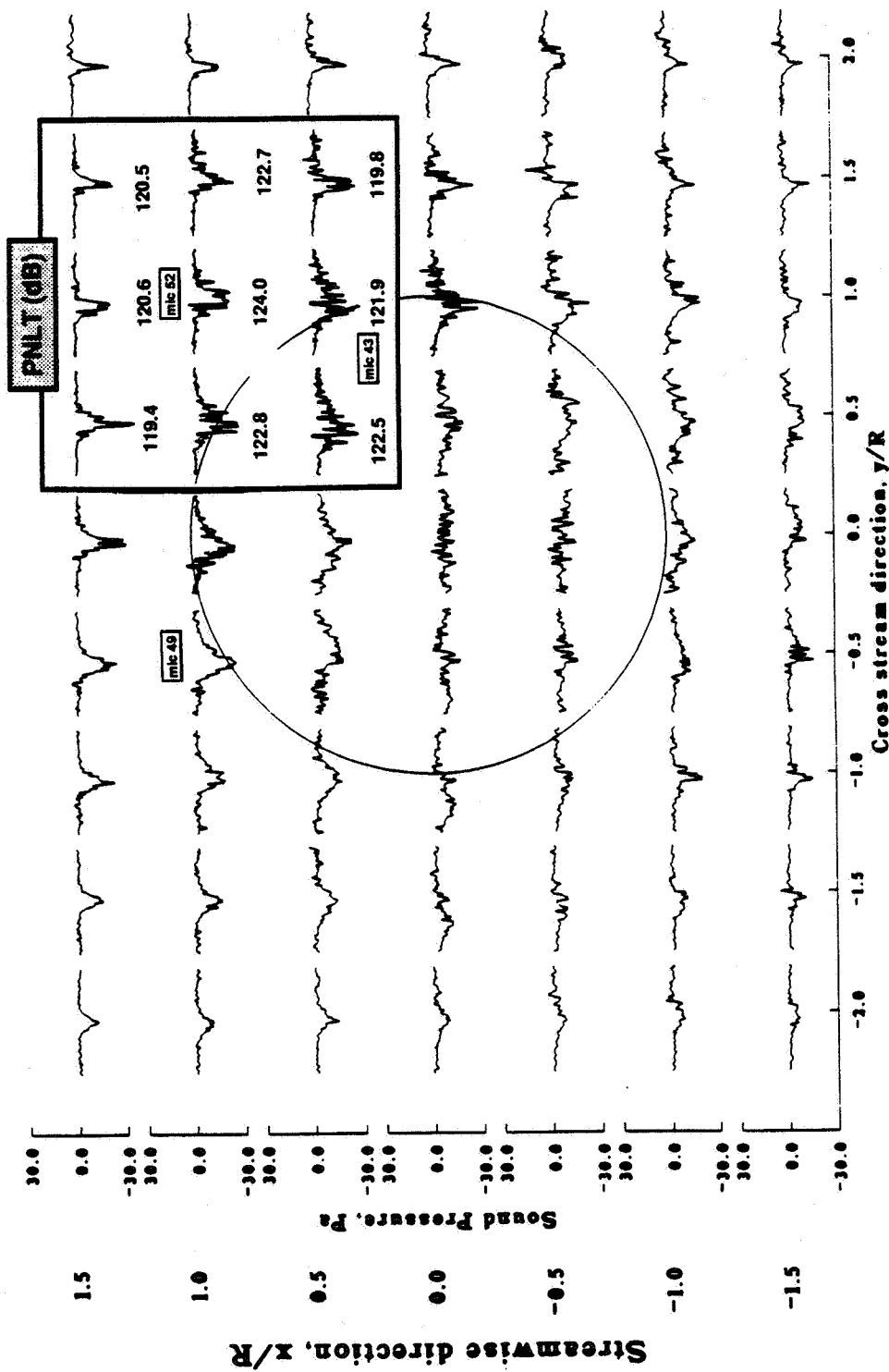
Total Noise

Fig. (77) Predicted acoustic time histories for one blade passage (flapped OLS model rotor, schedule E, Mtip = 0.666, Mu = 0.147, TPP = 0.12 degrees aft)

178
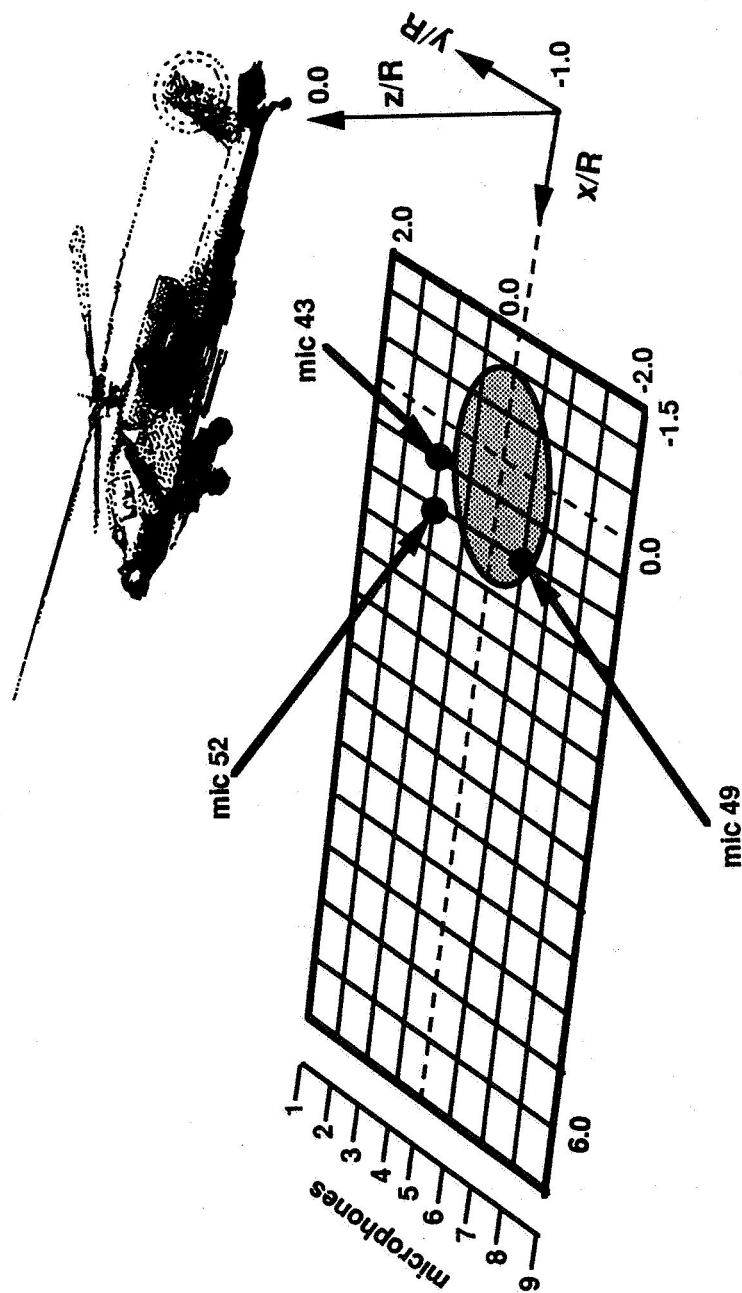
Fig. (78) Schematic depicting the selected microphone positions for spectral analyses (two-bladed OLS model rotor)
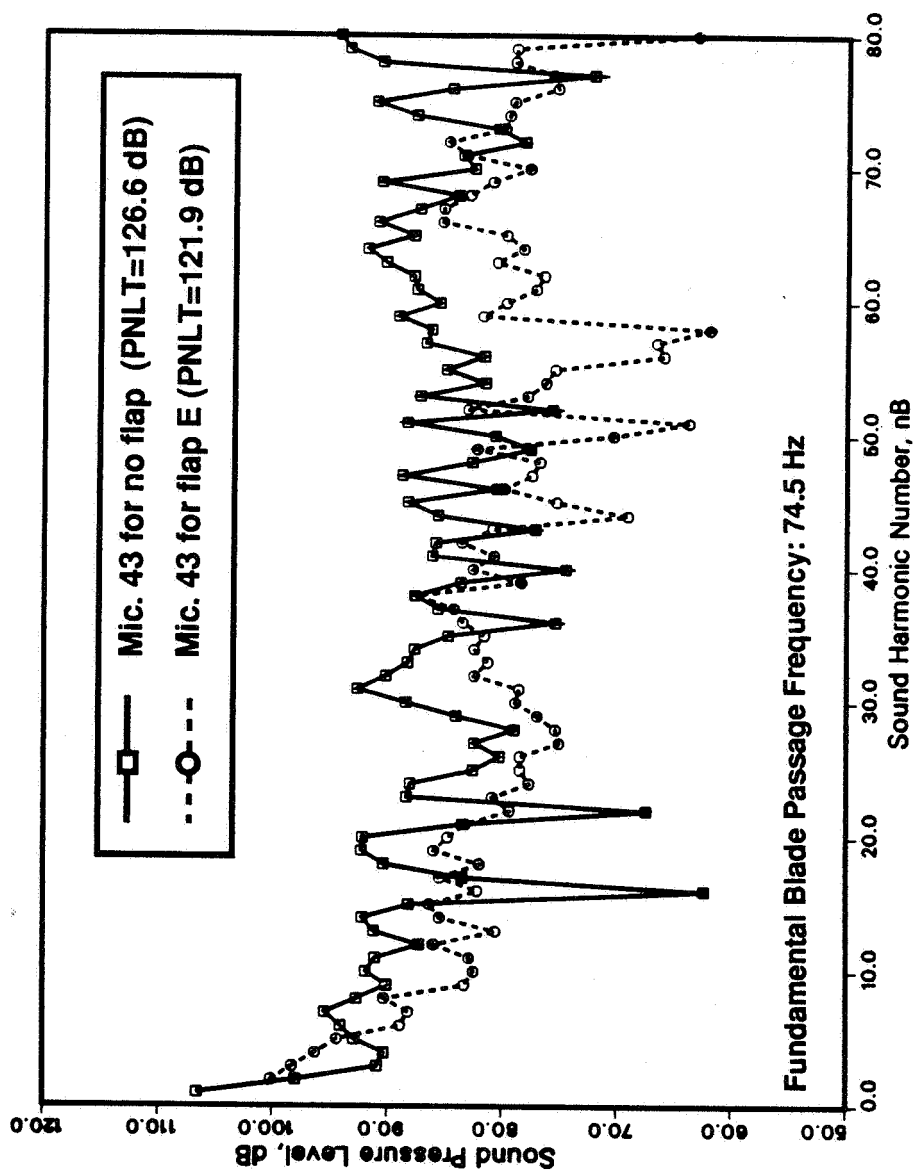
Fig. (79) A comparison between the predicted spectra for the baseline OLS rotor and for the flapped OLS rotor utilizing schedule E (microphone 43, observer location: x/R = 0.5, y/R = 1.0, z/R = -1.0; Mtip = 0.666, Mu = 0.147)

180
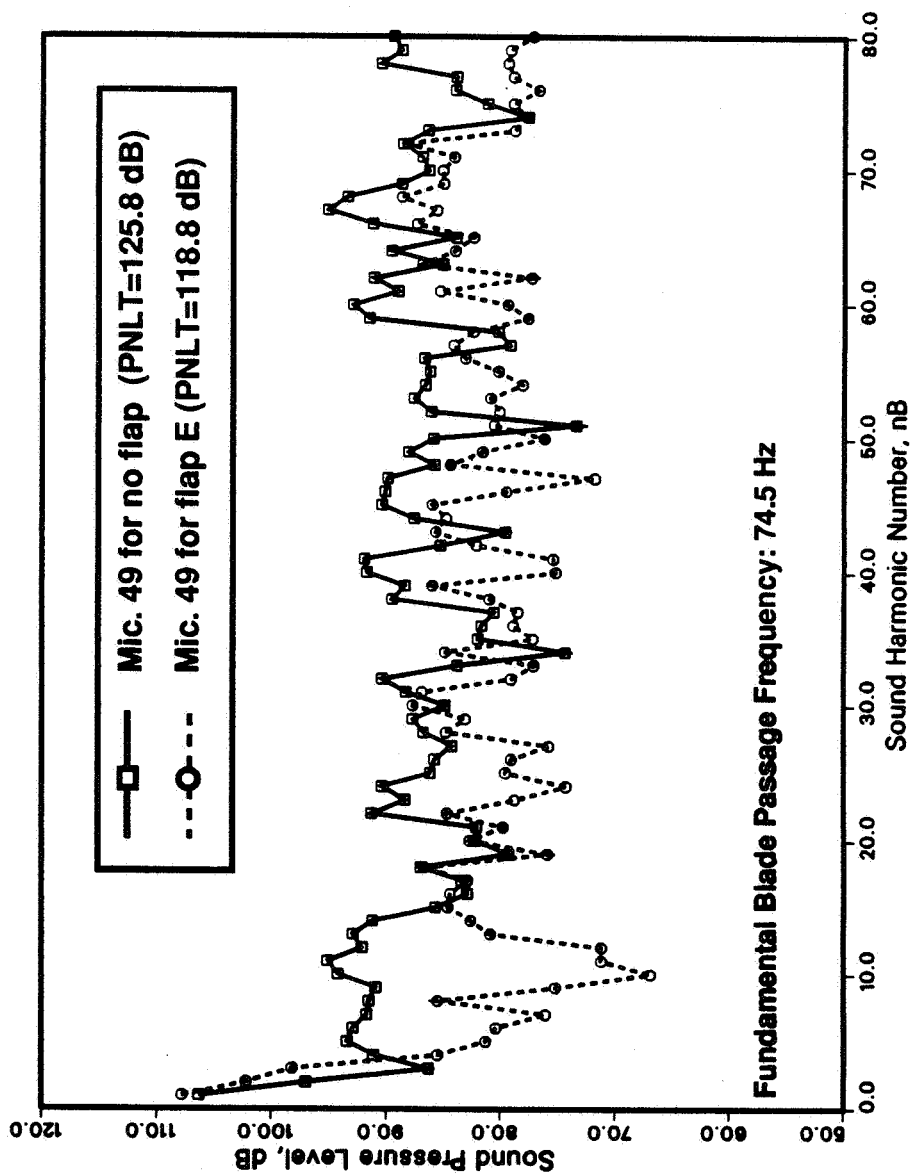
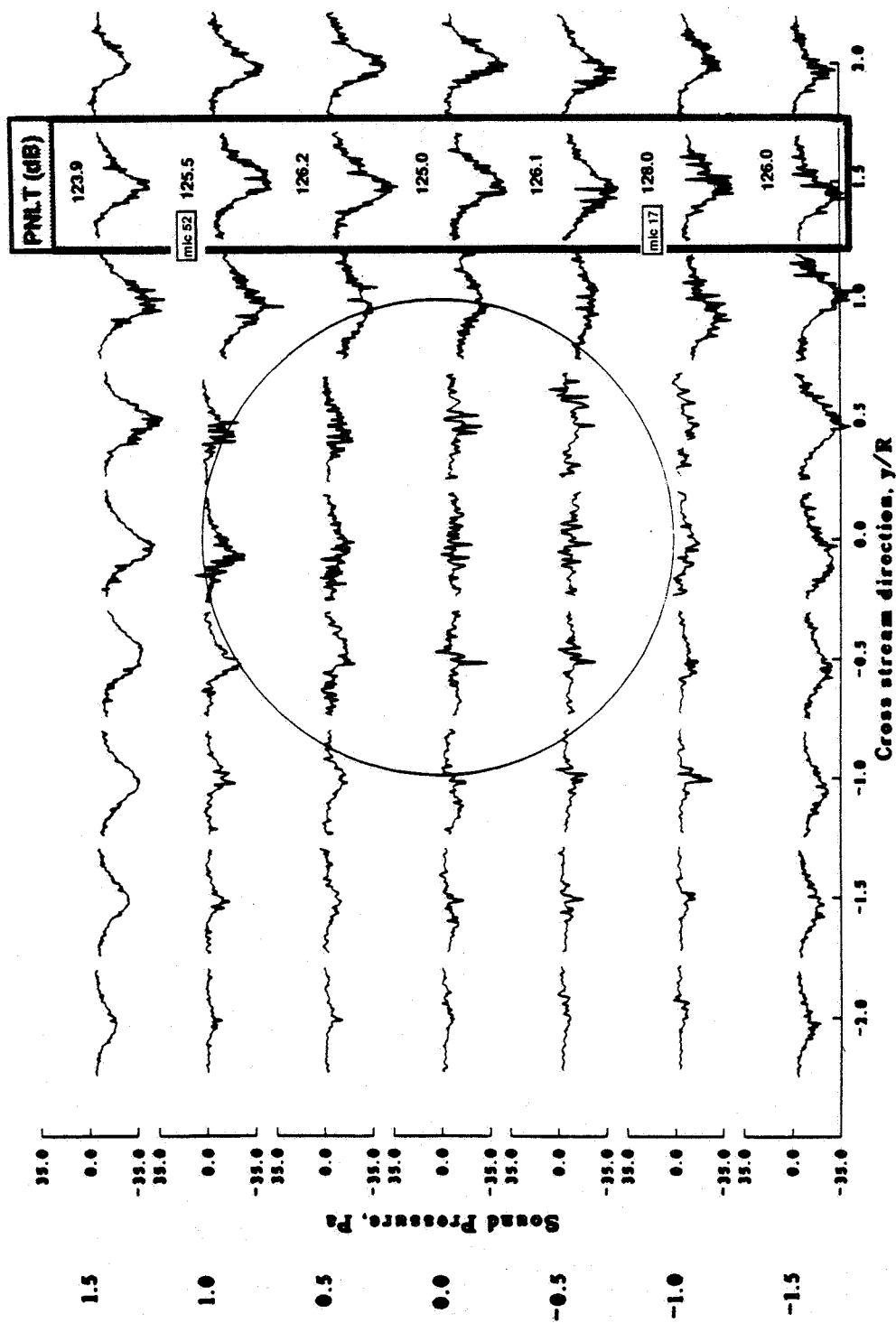Fig. (80) A comparison between the predicted spectra for the baseline OLS rotor and for the flapped OLS rotor utilizing schedule E (microphone 49, observer location: x/R = 1.0, y/R = -0.5, z/R = -1.0; Mtip = 0.666, Mu = 0.147)
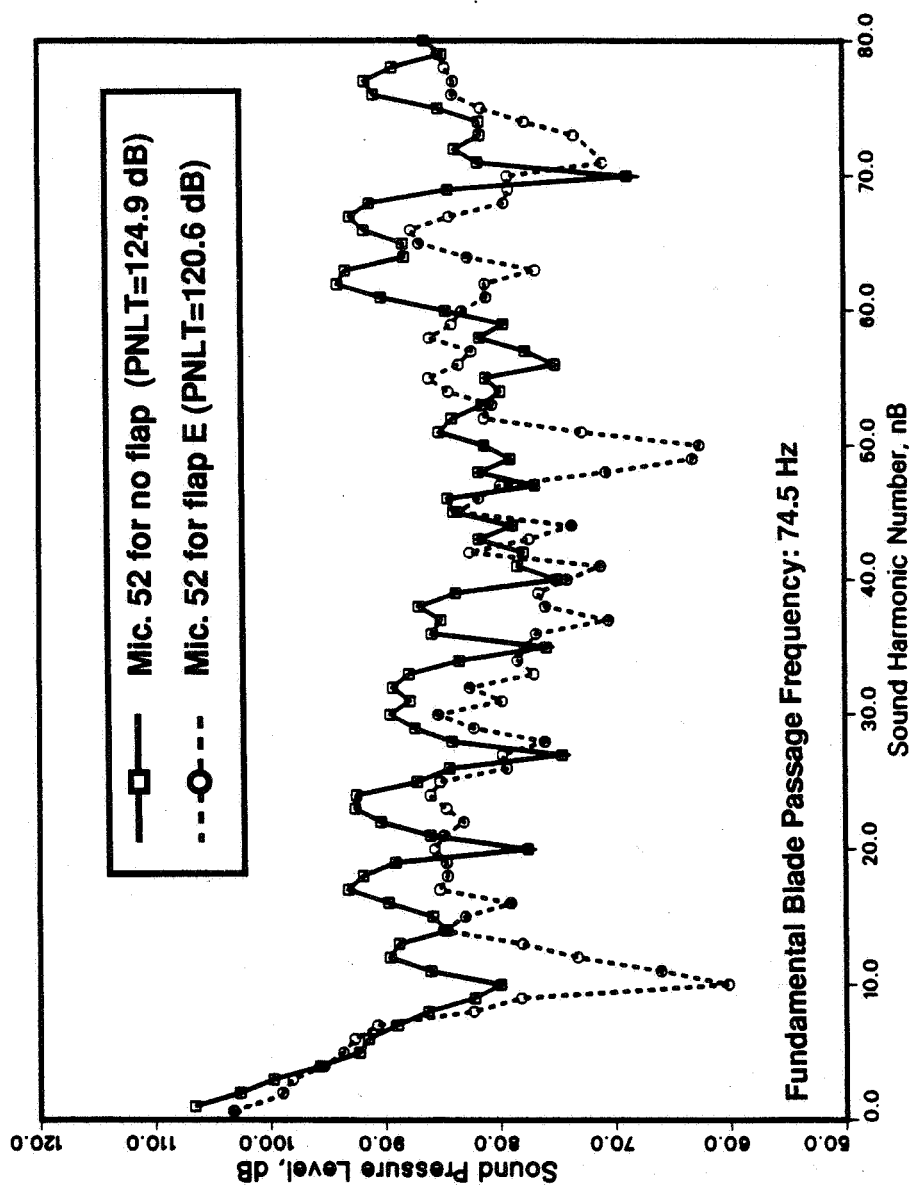
Fig. (81) A comparison between the predicted spectra for the baseline OLS rotor and for the flapped OLS rotor utilizing schedule E (microphone 52, observer location: x/R = 1.0, y/R = 1.0, z/R = -1.0; Mtip = 0.666, Mu = 0.147)
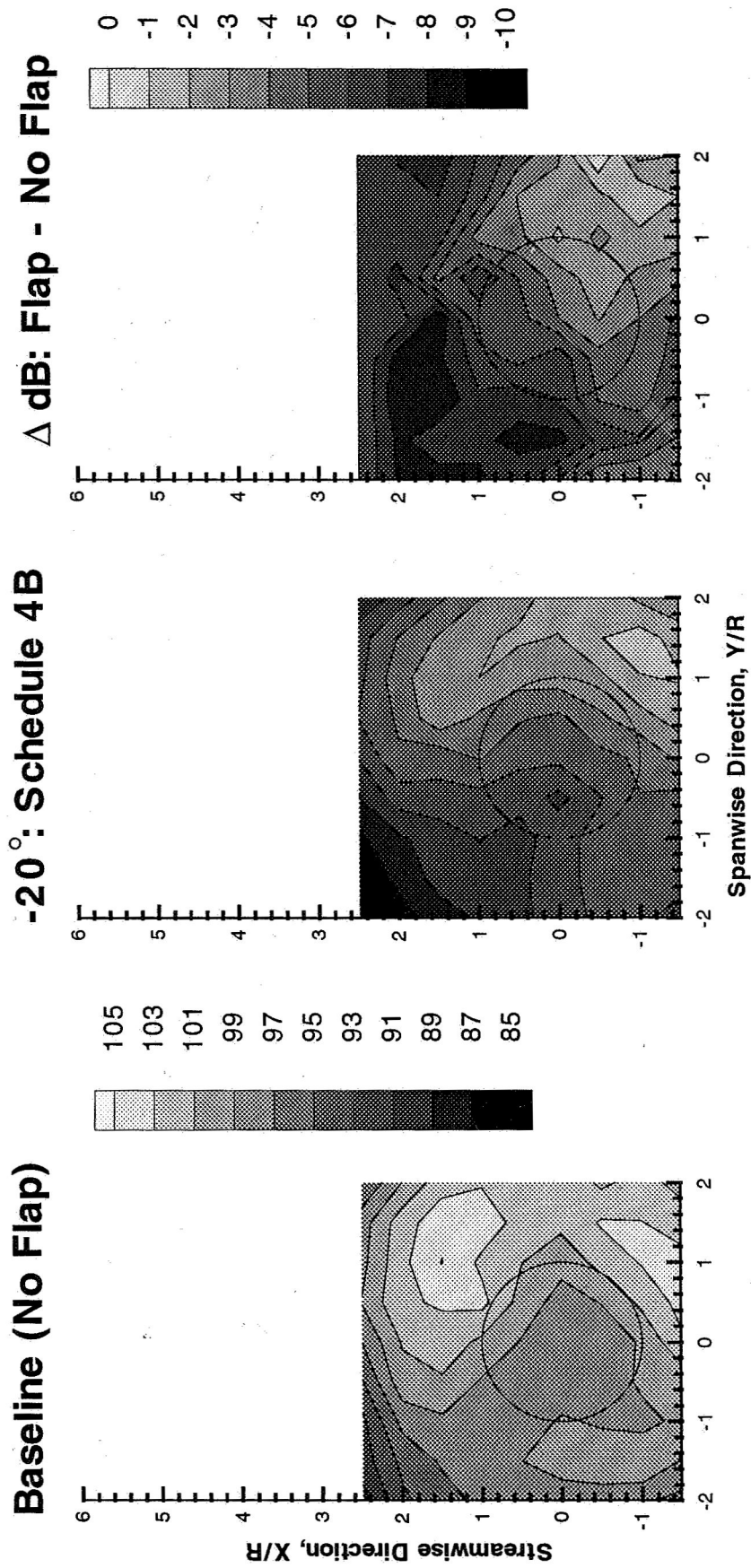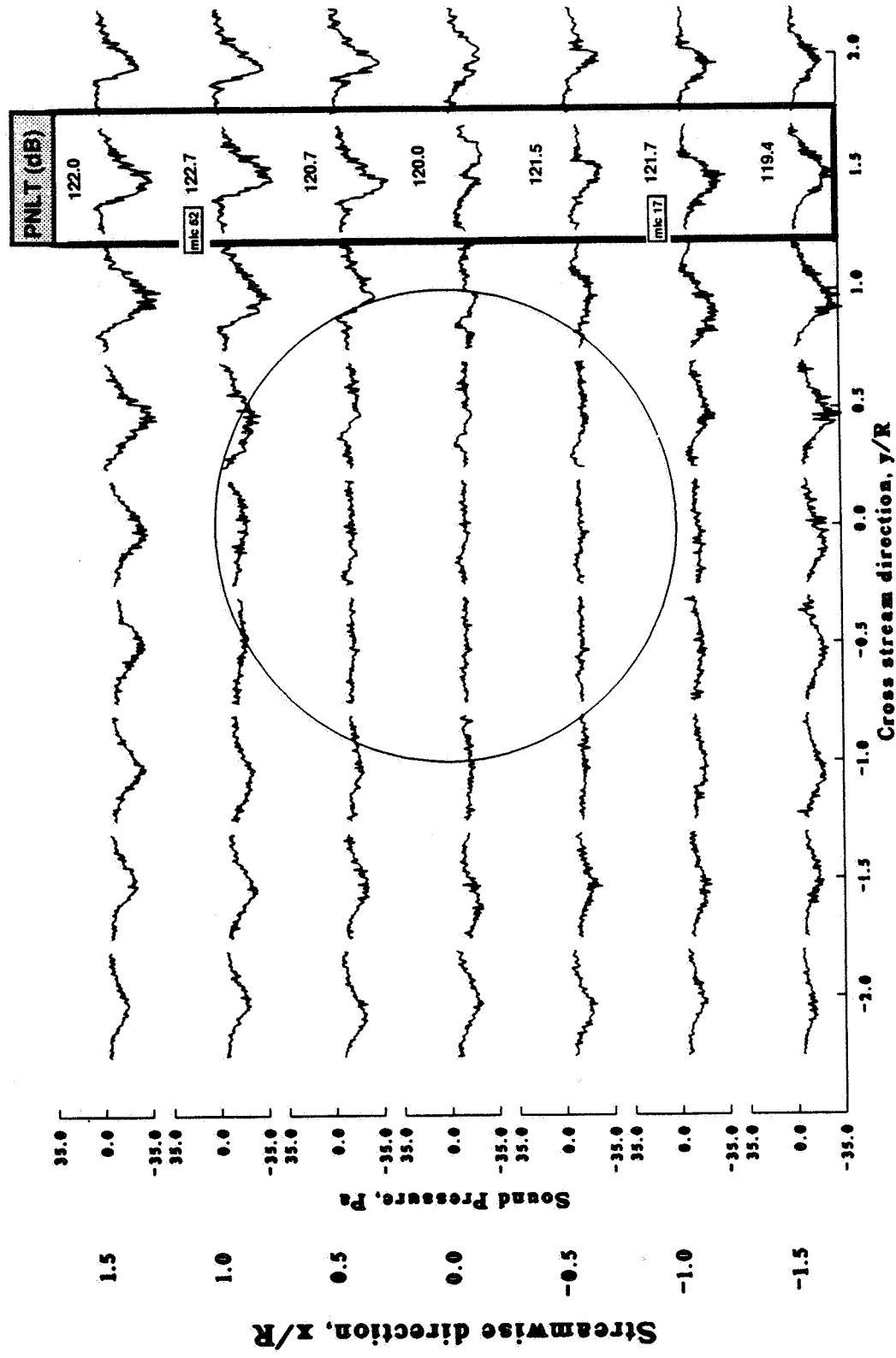
Fig. (82) Effects of the trailing edge flap on the predicted BVI directivity and noise levels for the generic four-bladed model rotor (Schedule 4B, Mtip = 0.627, Mu = 0.15)

183

Total Noise

Fig. (83) Predicted acoustic time histories for one blade passage (baseline four-bladed model rotor, Mtip = 0.627, Mu = 0.15, TPP = 2.0 degrees aft)

Total Noise

Fig. (84) Predicted acoustic time histories for one blade passage (flapped four-bladed model rotor, schedule 4B, Mtip = 0.627, Mu = 0.15, TPP = 1.64 degrees aft)

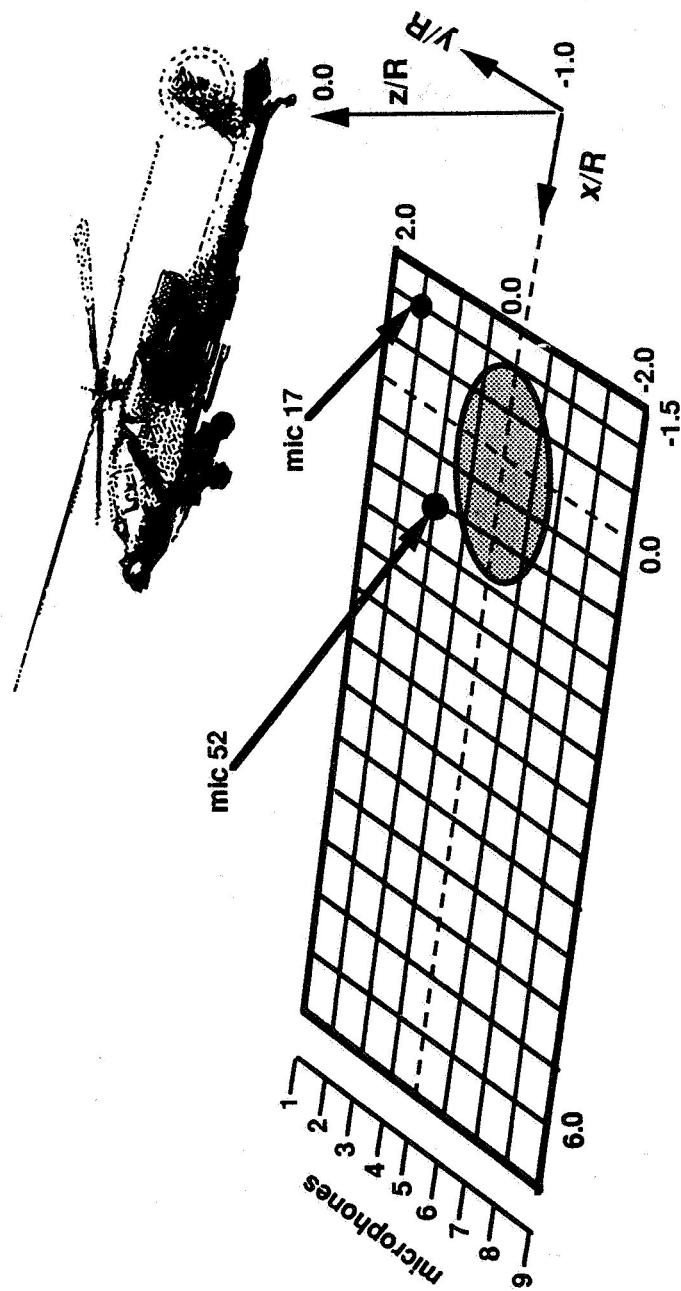Fig. (85) Schematic depicting the selected microphone positions for spectral analysis (generic four-bladed model rotor)
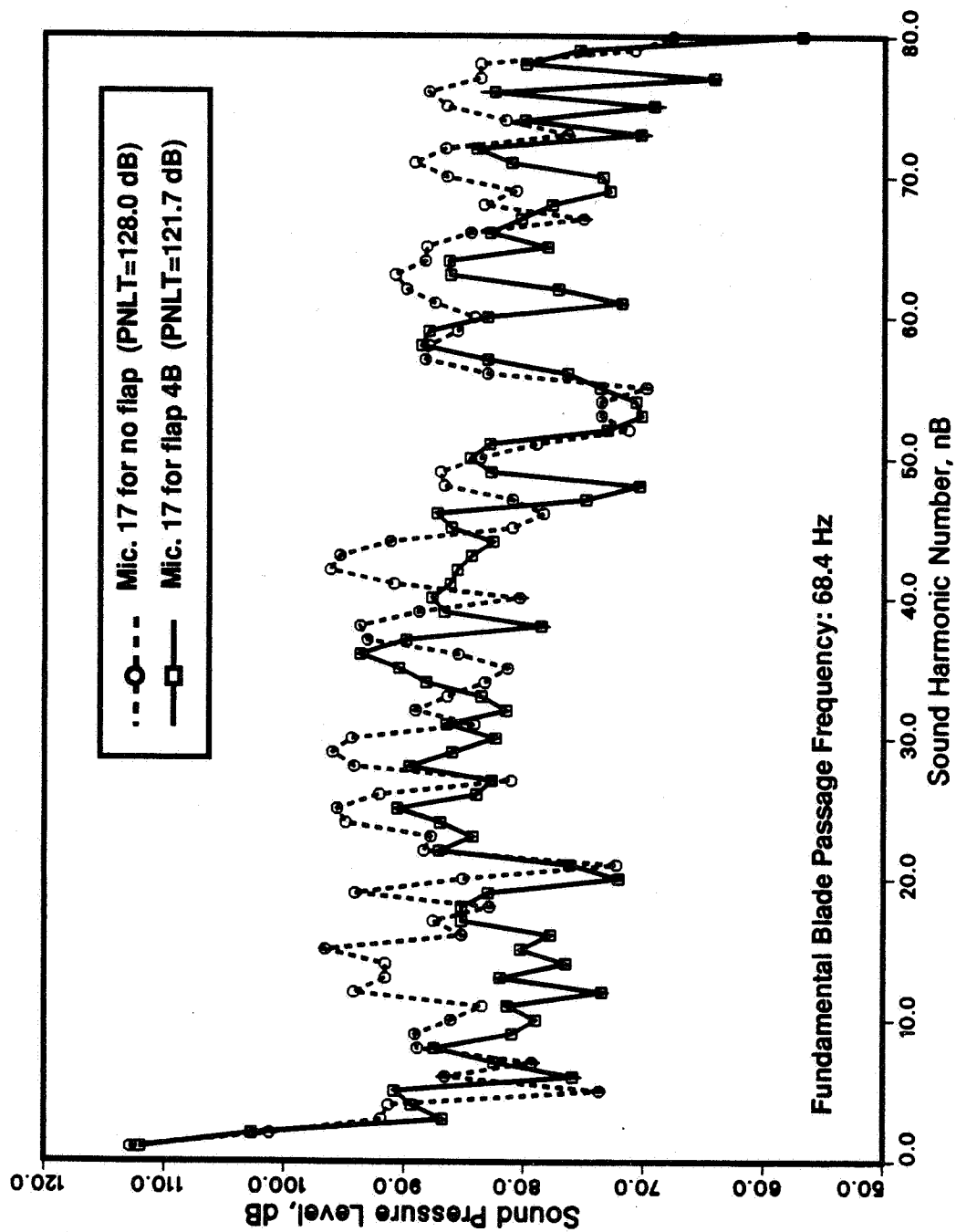
Fig. (86) A comparison between the predicted spectra for the baseline four-bladed rotor and for the flapped four-bladed rotor utilizing schedule 4B (microphone 17, observer location: x/R = -1.0, y/R = 1.0, z/R = -1.0; Mtip = 0.627, Mu = 0.15)
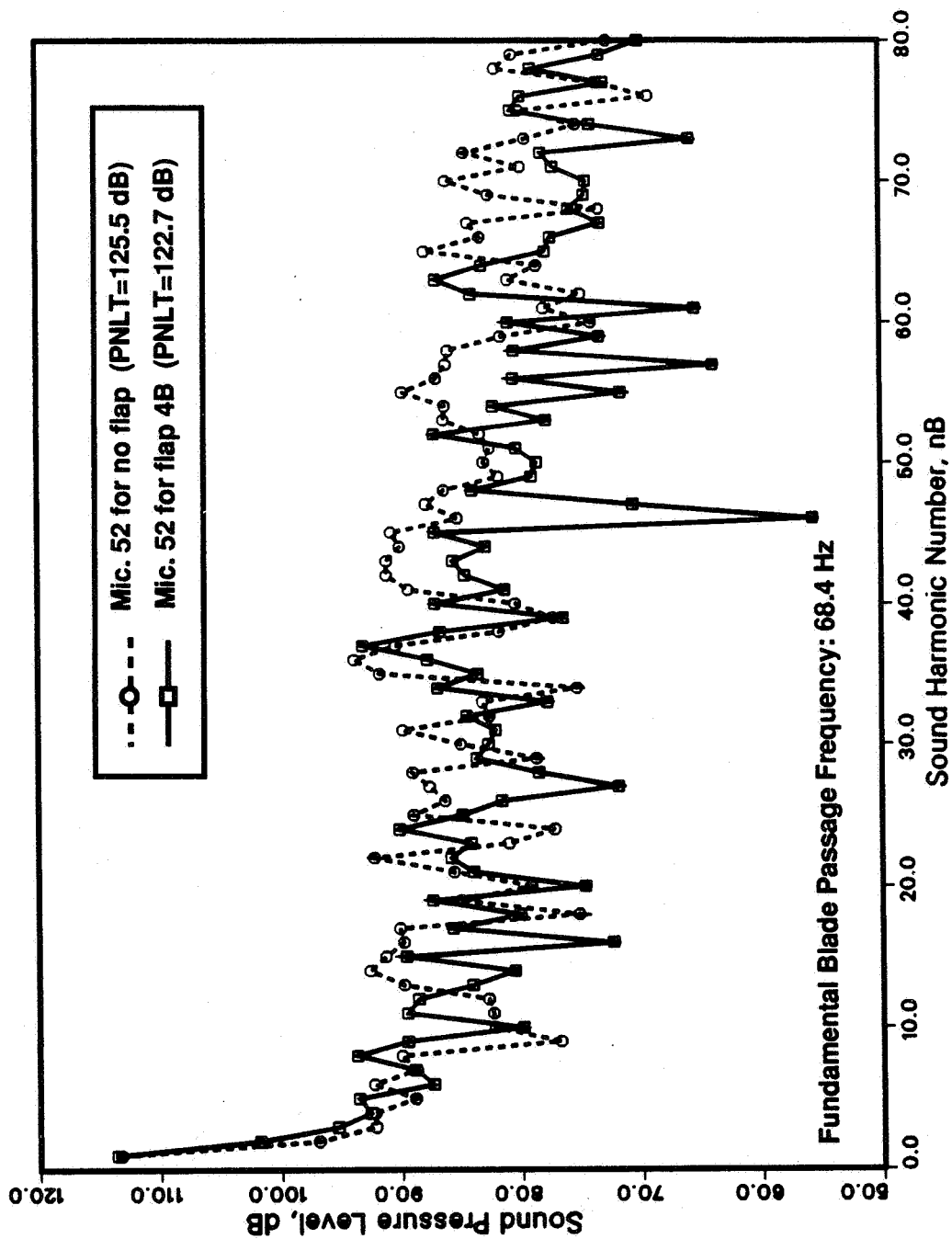
187

Fig. (87) A comparison between the predicted spectra for the baseline four-bladed rotor and for the flapped four-bladed rotor utilizing schedule 4B (microphone 52, observer location: x/R = 1.0, y/R = 1.0, z/R = -1.0; Mtip = 0.627, Mu = 0.15)

188

REPORT DOCUMENTATION PAGE

Form Approved
OMB No. 0704-0188

1. AGENCY USE ONLY (Leave blank)	2. REPORT DATE	3. REPORT TYPE AND DATES COVERED
	February 1992	Contractor Report

4. TITLE AND SUBTITLE

Blade-Mounted Trailing Edge Flap Control for BVI Noise Reduction

5. FUNDING NUMBERS

C NAS1-19136

WU 505-63-36

6. AUTHOR(S)

A. A. Hassan, B. D. Charles, H. Tadghighi, and L. N. Sankar

7. PERFORMING ORGANIZATION NAME(S) AND ADDRESS(ES)

McDonnell Douglas Helicopter Company
5000 East Mcdowell Road
Mesa, Arizona 85205-9797

8. PERFORMING ORGANIZATION REPORT NUMBER

9. SPONSORING/MONITORING AGENCY NAME(S) AND ADDRESS(ES)

National Aeronautics and Space Administration
Langley Research Center
Hampton, Virginia 23665-5225

10. SPONSORING/MONITORING AGENCY REPORT NUMBER

NASA CR-4426

11. SUPPLEMENTARY NOTES Langley Technical Monitor: Michael Marcolini   Final Report

Hassan, Charles, and Tadghighi: McDonnell Douglas Corp., Mesa, AZ
Sankar: Georgia Institute of Technology, Atlanta, GA

12a. DISTRIBUTION/AVAILABILITY STATEMENT

Unclassified - Unlimited

Subject Category 71

12b. DISTRIBUTION CODE

13. ABSTRACT (Maximum 200 words)

Numerical procedures based on the two- and three-dimensional full potential equations and the two-dimensional Navier-Stokes equations have been developed to investigate the effects of leading and trailing edge flap motions on the aerodynamics of parallel airfoil-vortex interactions and on the aerodynamics and acoustics of the more general self-generated rotor blade-vortex interactions (BVI). For subcritical interactions, our two-dimensional results indicate that the trailing edge flap can be used to alleviate the impulsive loads experienced by the airfoil. For supercritical interactions, our results demonstrate the necessity of using a leading edge flap, rather than a trailing edge flap, to alleviate the interaction. Results for various time-dependent flap motions and their effect on the predicted temporal sectional loads, differential pressures, and the free vortex trajectories are presented. For the OLS model rotor, contours of a BVI noise metric were employed to quantify the effects of the trailing edge flap on the size and directivity of the high/low intensity noise region(s). Average reductions in the BVI noise levels on the order of 5 dB with moderate power penalties on the order of 18% for a four-bladed rotor and 58% for a two-bladed rotor were obtained for a number of flap schedules. Examples illustrating the acoustic benefits arising from the use of the trailing edge flap for the two-bladed OLS model rotor and for a generic four-bladed model rotor are presented.

14. SUBJECT TERMS	15. NUMBER OF PAGES
Blade-Vortex Interactions, Noise Control, Flaps, Aerodynamics Fluid Dynamics, Acoustics	188
	16. PRICE CODE A09

17. SECURITY CLASSIFICATION OF REPORT	18. SECURITY CLASSIFICATION OF THIS PAGE	19. SECURITY CLASSIFICATION OF ABSTRACT	20. LIMITATION OF ABSTRACT
Unclassified	Unclassified		